Early Paleozoic Ocean Redox Dynamics: Perspectives from Uranium Isotopes of Sedimentary Rocks

by

Xinze Lu

A thesis

presented to the University of Waterloo

in fulfillment of the

thesis requirement for the degree of

Doctor of Philosophy

in

Earth Sciences

Waterloo, Ontario, Canada, 2022

Examining Committee Membership

The following served on the Examining Committee for this thesis. The decision of the Examining Committee is by majority vote.

External Examiner	Dr. Natascha Riedinger Associate Professor, Boone Pickens School of Geology, Oklahoma State University
Supervisor	Dr. Brian Kendall Associate Professor, Department of Earth and Environmental Sciences, University of Waterloo
Internal Member 1	Dr. Shaun Frape Professor, Department of Earth and Environmental Sciences, University of Waterloo
Internal Member 2	Dr. Martin Ross Associate Professor, Department of Earth and Environmental Sciences, University of Waterloo
Internal-external Examiner	Dr. Roland I. Hall Professor, Department of Biology, University of Waterloo

Author's Declaration

This thesis consists of material all of which I authored or co-authored: see Statement of Contributions included in the thesis. This is a true copy of the thesis, including any required final revisions, as accepted by my examiners.

I understand that my thesis may be made electronically available to the public.

Statement of Contributions

This thesis consists of three research chapters, written as three manuscripts for journal publication. Contributions for each chapter are described below.

Chapter 2 has been published as a research article in *Geochimica et Cosmochimica Acta* (Lu et al., 2020). Drs. Tais W. Dahl (second author) and Brian Kendall (last author, supervisor) provided samples. Su Wang (fourth author) digested samples and purified U isotopes. I measured elemental concentrations. Dr. Wang Zheng (third author) analyzed U isotope compositions. Drs. Brian Kendall (last author, supervisor) and Tais W. Dahl (second author) guided and helped with data analyses. I wrote and revised the manuscript, with contributions from all the co-authors.

Citation: Lu, X., Dahl, T. W., Zheng, W., Wang, S. and Kendall, B. (2020) Estimating ancient seawater isotope compositions and global ocean redox conditions by coupling the molybdenum and uranium isotope systems of euxinic organic-rich mudrocks. *Geochimica et Cosmochimica Acta*, 290, 76-103. doi:10.1016/j.gca.2020.08.032

Chapter 3 has not yet been submitted to an academic journal. Approximately half of the samples were collected by Ryan Truong and digested by Isabella Bowman. I collected the other half of samples and did the digestion. Dr. Geoffrey J. Gilleaudeau extracted three Fe phases for Fe speciation. I purified all the U isotopes. I measured the elemental concentrations for all samples. Dr. Brian Kendall (supervisor) and I measured U isotope compositions from bulk samples (fully digested) and leached samples (leached with 1N hydrochloric acid), respectively. Dr. Brian Kendall (supervisor) guided and helped with data analyses.

Chapter 4 has been submitted as a research article to *Geochimica et Cosmochimica Acta* (Lu et al., submitted) and is now under review. Dr. Cole T. Edwards (second author) provided samples and helped with geological background. I did wet chemistry and measured elemental concentrations and U isotope compositions for all samples. Dr. Brian Kendall (last author, supervisor) guided and helped with data analyses. As the leading author, I was responsible for writing and revising the manuscript, with inputs from all the co-authors.

Citation: Lu, X., Edwards, C. T., and Kendall, B. submitted. No evidence for expansion of global ocean euxinia during the base Stairsian mass extinction event (Tremadocian, Early Ordovician). Geochimica et Cosmochimica Acta.

Abstract

The trajectory of global ocean oxygenation could have greatly influenced the metazoan evolutions because O_2 could provide valuable energy to support biological activities. Remarkable metazoan diversifications occurred during the Late Neoproterozoic (i.e., Ediacaran; 635–539 Ma) and Early Paleozoic (i.e., Cambrian, Ordovician, and Silurian; ca. 538–419 Ma), such as the appearance of Ediacaran Biota and the "Cambrian Explosion". However, an increasing number of studies suggest that a near-modern level of Earth's surface oxygenation was not established during the Late Neoproterozoic (ca. 680 Ma), but rather during the Devonian (ca. 419–359 Ma). Therefore, it is of great importance to understand the co-evolution of global ocean redox conditions and metazoan diversifications during the Early Paleozoic (ca. 538–419 Ma).

The uranium isotope compositions ($\delta^{238}U$) from sedimentary rocks (e.g., organic-rich mudrocks, carbonates) have been used as a global ocean redox proxy and provided insights on ocean redox dynamics. Understanding the local bottom water redox conditions is crucial to interpret $\delta^{238}U$ values, as different $\delta^{238}U$ offsets occur under various redox settings. Relatively larger $\delta^{238}U$ offsets are observed in sediments from modern euxinic basins compared with the other redox settings, suggesting seawater $\delta^{238}U$ values are sensitive to the extent of global euxinic seafloor area. Uranium isotope mass balance modelling could be further used to quantitatively estimate the areal extent of euxinic seafloor in the oceans. In this thesis, U isotopes from sedimentary rocks are used to investigate ocean redox conditions, with a focus during the Ordovician Period (ca. 487–443 Ma) when there is rapid evolutionary change.

The coupled use of molybdenum and uranium isotope compositions from euxinic organic-rich mudrocks are investigated to better reconstruct ancient ocean redox conditions. Local depositional conditions of each formation were firstly examined by sedimentary Fe speciation, covariations between Mo and TOC, and between Mo and U enrichment factors. The Mo and U isotope compositions from individual formations were observed to exhibit negative, positive, and no correlations, suggesting different controlling mechanisms (e.g.,

bottom water H_2S concentrations, basin restrictions, global ocean redox conditions). This study provides a general framework of using coupled Mo-U isotopes from the same euxinic organic-rich mudrocks to disentangle the effects of local depositional environment and global ocean redox states. Specifically for the Ordovician, a positive correlation of Mo-U isotope data from the late Katian Fjäcka Shale suggests an episodic ocean oxygenation event prior to the Hirnantian.

The Late Ordovician mass extinction event (LOME; ca. 445–443 Ma) wiped out 85% of species. However, metazoan biodiversity started to decline during the Katian (ca. 453–445 Ma; prior to the LOME) and coeval global ocean redox conditions are not well understood. The Katian organic-rich sedimentary rocks in southern Ontario, namely the Collingwood Member (upper Lindsay Formation) and succeeding Rouge River Member (lower Blue Mountain Formation), were deposited during the Taconic Orogeny. Samples of both units were collected from several drillcores that cover southern Ontario. Paleosalinity (strontium/barium and sulfur/total organic carbon) and paleoredox (redox sensitive trace metals, Fe speciation, and C_{org} : P ratios) proxies were used to constrain the local depositional environment of both units. In addition, the $\delta^{238}U$ of both units were used to deduce coeval ocean redox conditions. Lower estimated seawater $\delta^{238}U$ during deposition of the Collingwood Member suggests an expansion of global ocean euxinia, whereas higher seawater $\delta^{238}U$ during deposition of the Rouge River Member represents a contraction of ocean euxinia. A three-sink U isotope mass balance model suggests a global ocean euxinic seafloor area of 0.5–31.6% and 0.2–2.0% during deposition of the Collingwood Member and Rouge River Member, respectively. Combined with other studies, fluctuating ocean redox conditions occurred during a decline of biodiversity prior to the LOME.

The base Stairsian mass extinction event (BSME; ca. 482 Ma), accompanied with a positive carbon isotope excursion (CIE), is one of the best studied mass extinction events in the Tremadocian, Early Ordovician (ca. 487–471 Ma). New trace metal concentrations and $\delta^{238}U$ of carbonates from three sections (along a proximal-to-distal transect: Ibex area, Shingle Pass, Meiklejohn Peak, respectively) in the Great Basin (western USA) were analyzed to

quantitatively constrain the role of global ocean euxinia on the mass extinction event. Carbonate $\delta^{238}U$ data show different trends among the three sections. The proximal Ibex section shows a negative $\delta^{238}U$ excursion during the CIE, whereas the distal Shingle Pass section only has one sample with unusually low $\delta^{238}U$ and the Meiklejohn Peak section does not have any samples with unusually low $\delta^{238}U$. The lowest $\delta^{238}U$ values from each of the Ibex and Shingle Pass sections are associated with the highest Mn/Sr ratios in those sections, suggesting diagenetic overprints. Carbonate $\delta^{238}U$ data from the other two distal sections likely record the open ocean $\delta^{238}U$ signals and limited variations in these sections suggest no significant change in global ocean euxinia during the BSME. A three-sink U isotope mass balance model suggests 0.2–15.8% global euxinic seafloor area during the studied interval. Although there was no expansion of euxinia, there is evidence of expanded ocean suboxia-anoxia based on concurrent positive carbon and sulfur isotope excursions during the BSME. Limited changes in global ocean euxinia are further proposed during the post-SPICE Cambrian and Early Ordovician because other carbon isotope perturbations during this time are smaller than that associated with the BSME.

Combined with previous studies, fluctuating ocean redox conditions were possibly the key character during the Early Paleozoic (ca. 538–419 Ma), though limited non-traditional metal isotope data are available for the Early-Middle Ordovician (ca. 487–458 Ma) and Silurian (ca. 443–419 Ma). The notable "Cambrian Explosion" has been suggested to coincide with pulses of ocean oxygenation, however, several recent studies proposed that this metazoan radiation could be facilitated by overall dynamic Cambrian ocean redox conditions. Nonetheless, more studies are needed to better understand the Early Paleozoic ocean redox conditions and the co-evolution of metazoans. For example, there is a great potential to study marine redox conditions during the "Great Ordovician Biodiversification Event" as metal isotope data during this event have not been reported.

Acknowledgements

Life is a journey of adventure that consists of surprises and challenges. I am so grateful to be surrounded by a group of people when pursuing a Ph.D. First and foremost, I would like to express my deepest gratitude to my supervisor Dr. Brian Kendall for his mentorship, encouragement, understanding, patience, and support. This thesis could not be even possible without you. Thank you for always being available to answer my questions and providing valuable guidance in lab experiments and data interpretation. Thank you for the countless lessons in the office and lab that considerably benefit me. I am greatly indebted to you.

I sincerely thank my committee members Drs. Shaun Frape, Martin Ross, and Thai Phan for feedback and support over the years. Thanks to Dr. Natascha Riedinger for being external examiner and Dr. Roland I. Hall for being internal-external examiner. I would like to thank Jordan Clark and Catherine Béland-Otis for assistance during sampling. Many thanks to my collaborators Dr. Cole T. Edwards, Dr. Tais W. Dahl, Dr. Geoffrey J. Gilleaudeau, Dr. Wang Zheng, and Su Wang for criticism and encouragement on manuscript preparations. Shout out to staff at the Environmental Isotope Laboratory with special mentions to Rhys Gwynne, William (Bill) Mark, and Humam El Mugammar for sample analyses.

Many thanks to my friends for always being there with me, including but not limited to Jiangyue Ju, Lingyi Kong, Jiangyu Li, Kai Liu, Ning Luo, Shinong Mao, Xin Tong, Jieying Wang, Xiaomeng Xu, and Tian Yu. Sincere thanks go out to the colleagues in our research group with special mentions to Natasha Bell, Alex Kunert, and Shuai Yang. I also thank Dr. Liyan Xing and Sarah McCaugherty for technical assistance in the lab.

This thesis is supported by fundings from the Canada Research Chairs Program (Tier 2 Canada Research Chair in Redox-Sensitive Metal Isotope Geochemistry), Natural Sciences and Engineering Research Council Discovery Grants, and an Ontario Early Researcher Award to Dr. Brian Kendall. I appreciate support from a Student Research Grant from the Geological Society of America, Ontario Graduate Scholarship, and University of Waterloo.

Dedication

To my parents and parents-in-law, for your unwavering encouragement and support.

To my wife Xiangnan Liu, for brighten up my life with love, understanding, and support.

To my son Yimou Lyu, for all the joy you bring to our family.

Table of Contents

List of Figures

List of Tables

Chapter 1 Introduction

1.1 Introduction

Understanding the evolution of the Earth's surface oxygenation has long been an interest to many geologists and biologists as O_2 plays important roles in biological metabolisms and metazoan evolutions (e.g., Nursall, 1959; Sperling et al., 2013; Reinhard et al., 2016). The complex multicellular animals did not emerge until the "Neoproterozoic Oxygenation Event" (NOE; 0.8-0.54 Ga; Och and Shields-Zhou, 2012; Lyons et al., 2014). Notable metazoan radiations occurred during the Late Neoproterozoic and Early Paleozoic, such as the appearance of the Ediacaran Biota, the "Cambrian Explosion", and the "Great Ordovician Biodiversification Event" (e.g., Narbonne, 2005; Xiao and Laflamme, 2009; Erwin et al., 2011; Harper et al., 2015; Servais and Harper, 2018; Fan et al., 2020). These metazoan radiations have been associated with episodic oxygenation events (e.g., Chen et al., 2015; Edwards et al., 2017; Zhang et al., 2019; Cao et al., 2020). A growing number of studies suggests that relatively stable and near-modern level of Earth's atmosphere-ocean oxygenation was not reached until the Devonian (~400 Ma; e.g., Dahl et al., 2010; Kendall et al., 2015; Sperling et al., 2015; Wallace et al., 2017; Krause et al., 2018; Lu et al., 2018; Elrick et al., 2022). On the other hand, four of the major Phanerozoic mass extinction events (i.e., during the end-Ordovician, end-Devonian, end-Permian, and end-Triassic) have been suggested to be accompanied with expanded ocean anoxia/euxinia (e.g., Sheehan, 2001; Meyer and Kump, 2008; Brennecka et al., 2011a; Zhou et al., 2012; Hammarlund et al., 2012; Lau et al., 2016; Jost et al., 2017; White et al., 2018; Zhang et al., 2018a, 2018b, 2018c; Zou et al., 2018; Dahl et al., 2021). Therefore, it is of great importance to understand the co-evolution of metazoans and environment.

The trajectory of the Earth's oxygenation is often inferred from geochemical proxies, such as iron speciation, cerium anomaly, iodine/calcium (I/Ca) ratios, redox sensitive trace metals concentrations (e.g., Mo and U) and their isotope compositions (Fig. 1.1; see a review by Kendall, 2021). The iron speciation is based on relationships among total Fe, pyrite Fe, and other Fe phases that are reactive with sulfides and provide valuable information on local

bottom water redox conditions for organic-rich mudrocks (ORM) (and potentially also for carbonates; e.g., Poulton and Canfield, 2011; Clarkson et al., 2014; Sperling et al., 2015). Cerium anomaly from carbonates as a local redox proxy is rooted from the oxidative removal of Ce^{4+} by Fe-Mn oxides, whereas the adjacent rare earth elements (forming trivalent ions) do not show such behavior (Bau and Koschinsky, 2009). The use of I/Ca ratios (and I/[Ca+Mg] ratios) from carbonates is founded on the basis that oxidized iodate (IO_3^-) substitutes carbonate ion (CO_3^{2-}) and incorporates into carbonate whereas reduced iodide (I^-) cannot (Lu et al., 2010; Hardisty et al., 2017). With sufficient data, the above discussed local proxies could provide redox information on a regional scale (e.g., continental margins, epicontinental seas) during the Late Neoproterozoic and Early Paleozoic (e.g., Sperling et al., 2015, 2021; Wallace et al., 2017; W. Lu et al., 2017, 2018; Liu et al., 2021). For example, compilation of Ce anomaly data suggests an episodic ocean oxygenation across the Neoproterozoic-Paleozoic boundary, a return of ocean anoxia in the Early Paleozoic, and a near-modern level of ocean oxygenation during the Devonian (Fig. 1.1; Wallace et al., 2017).

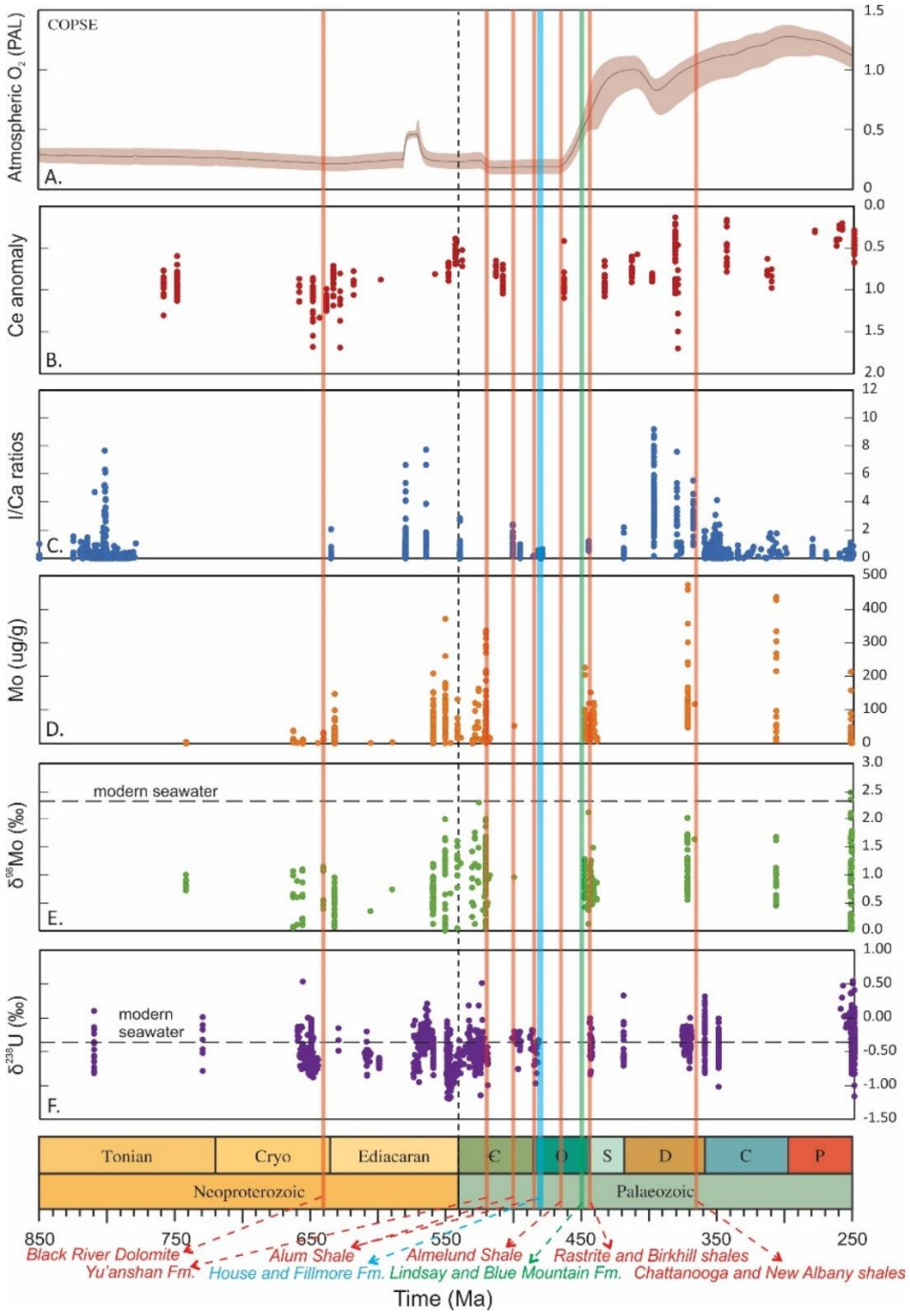

Figure 1.1 Atmospheric O_2 level predicted by COPSE model (A) and compiled geochemical redox proxies through the Neoproterozoic and Paleozoic: Ce anomaly (B) from carbonates

(Wallace et al., 2017 and references therein), I/Ca ratios (C) from carbonates (Hardisty et al., 2017; W. Lu et al., 2017, 2018), Mo concentrations (D) and isotope compositions (E) from euxinic ORMs (Ye et al., 2021 and references therein), and U isotope compositions (F) from carbonates (Liu et al., 2022; X. Chen et al., 2021 and references therein). Orange, green, and blue intervals represent the depositional age of samples in Chapter 2, 3, and 4, respectively. Fm. = Formation.

The enrichments of redox sensitive trace metals (RSTM; e.g., Mo, U, Re, V) are useful to reconstruct paleocean redox conditions (see Algeo and Li, 2020 and Bennett and Canfield, 2020 for a review). In general, these RSTMs are soluble in oxygenated water and can be removed into sediments under anoxic conditions via different mechanisms. For example, the removal of Mo is strongly associated with the existence of hydrogen sulfide (H_2S) in the water columns, whereas U and Re removal could occur under euxinic, ferruginous, and suboxic bottom waters. In addition, the ORM units have low permeability and thus the remobilization of RSTMs is commonly limited during diagenesis. Therefore, combined use of RSTM enrichments of the ORMs could effectively reveal local bottom water redox conditions (e.g., Algeo and Tribovillard, 2009; Algeo and Li, 2020).

The enrichments of RSTMs (e.g., Mo, U, Re, V) in ORMs could be used to infer global ocean redox conditions because they have longer oceanic residence times ($\geq$ 90 kyr for these four metals) than the ocean mixing time (1–2 kyr) in the modern oceans (e.g., Scott et al., 2008; Miller et al., 2011; Sahoo et al., 2012; Partin et al., 2013; Sheen et al., 2018). Prior to inferring global ocean redox conditions, it is of great importance to constrain local depositional environment and use RSTM data from various localities (e.g., Scott et al., 2008; Sahoo et al., 2012; Partin et al., 2013; Sheen et al., 2018; Kendall, 2021). Authigenic enrichments of RSTMs under locally anoxic/euxinic conditions broadly reflect the size of global dissolved seawater metal reservoirs, which are mainly controlled by the oceanic input flux and relative distribution of each redox sink in the oceans (Algeo and Lyons, 2006; Scott et al., 2008; Partin et al., 2013;

Sheen et al., 2018). For example, during an expanded ocean anoxia/euxinia, RSTMs would be greatly removed from the oceans via increased burial into anoxic/euxinic sediments, resulting in smaller seawater RSTM reservoirs and thus a temporal shift to lower enrichment of RSTMs in ORMs. Conversely, compilations of several RSTMs from anoxic/euxinic ORMs (i.e., Mo, U, Re, V) suggest episodic ocean oxygenation events during 635-551 Ma (Sahoo et al., 2016) and propose a stepwise increase of ocean oxygenation by at least ~551 Ma (Scott et al., 2008; Sahoo et al., 2012; Partin et al., 2013; Sheen et al., 2018).

With the use of multi-collector inductively coupled plasma mass spectrometry (MC-ICP-MS), the isotope compositions of some RSTMs have been developed (e.g., δ^{98}Mo, δ^{238}U; e.g., Anbar et al., 2001; Barling et al., 2001; Siebert et al., 2001, 2003; Stirling et al., 2017; Weyer et al., 2008). Long oceanic residence time in the modern oceans and redox sensitive behavior make them ideal global ocean redox proxies (e.g., see reviews by Andersen et al., 2017 for δ^{238}U and Kendall et al., 2017 for δ^{98}Mo). As such, their seawater isotope compositions are driven by relative distribution of ocean seafloor covered by water columns with different redox conditions. Therefore, the application of these non-traditional metal isotopes could provide important insights on the evolution of marine redox conditions.

Taking Mo as an example, modern oceans have a homogeneous δ^{98}Mo of 2.34 ± 0.10‰ (Nägler et al., 2014) and a long Mo oceanic residence time of ~440 kyr (Miller et al., 2011). The largest δ^{98}Mo offset between sediment and seawater ($\Delta^{98}Mo_{sediment-seawater} \approx -3$‰) is found in oxic sediments (e.g., Fe-Mn crusts) in well-oxygenated settings through Mo adsorption to Fe-Mn oxides (Barling and Anbar, 2004), whereas there are much smaller δ^{98}Mo offsets (≈ -0.3–0‰) for sediments deposited under strong euxinic settings ($[H_2S]_{aq} > 11\mu M$) due to near quantitative Mo removal from bottom waters to sediments (Neubert et al., 2008; Bura-Nakić et al., 2018). Intermediate and variable δ^{98}Mo offsets occur for sediments deposited under suboxic, ferruginous, and weakly euxinic bottom waters (Poulson Brucker et al., 2009; Goldberg et al., 2012). During an expanded ocean euxinia, less isotopically light Mo would be removed to oxic sediments, thus resulting in a lower seawater Mo isotope composition. Therefore, seawater δ^{98}Mo values could reflect the status of global ocean redox conditions.

Although the δ^{98}Mo of euxinic ORMs have the potential to record the seawater-like δ^{98}Mo, these δ^{98}Mo values could only be regarded as a conservative minimum estimate of the coeval seawater Mo isotope compositions because no technique is available to distinguish between weakly and strongly euxinic conditions (Kendall et al., 2017). Nevertheless, compilations of δ^{98}Mo from euxinic ORMs suggest several episodic ocean oxygenation events during the Late Ediacaran and Early Cambrian and a more stable and widespread ocean oxygenation was not reached until the Devonian (Fig. 1.1; Dahl et al., 2010; Chen et al., 2015; Kendall et al., 2015; Cheng et al., 2020; Qin et al., 2022).

Uranium isotope compositions from sedimentary rocks (e.g., ORMs, carbonates) have been used as another powerful global ocean redox proxy in recent decades (see Andersen et al., 2017 and Zhang et al., 2020a for a review). The δ^{238}U data have been extensively applied to the Late Neoproterozoic-Early Paleozoic, especially the Ediacaran and Cambrian (e.g., Dahl et al., 2014, 2017, 2019; Lau et al., 2017; G. Wei et al., 2018, 2021; Zhang et al., 2018c, 2019; Cao et al., 2020). Transient oxygenation events have been suggested after the Sturtian Glaciation (ca. 650 Ma; Lau et al., 2017) and during the Shuram Anomaly (a globally correlated negative carbon isotope excursion at ca. 570 Ma; Zhang et al., 2019; Cao et al., 2020; Rooney et al., 2020). Extensive global ocean euxinia occurred after a negative carbon isotope excursion at ca. 550 Ma (Kendall et al., 2015; Zhang et al., 2018c, Tostevin et al., 2019; Yang et al., 2021). Highly dynamic ocean redox conditions are suggested during the Cambrian (Dahl et al., 2017, 2019; G. Wei et al., 2018, 2020). A major increase in ocean oxygenation is proposed at the Emsian-Eifelian boundary, Devonian (ca. 395 Ma; Elrick et al., 2022).

The Ordovician Period in the Early Paleozoic is also quite fascinating due to the rapid changes in metazoan evolutions. The Cambrian-Ordovician boundary is characterized by several mass extinction events (e.g., Bambach et al., 2004; Saltzman et al., 2015). The base Stairsian mass extinction event (Tremadocian, Early Paleozoic) is one example and is accompanied with a globally correlated positive carbon isotope excursion (e.g., Miller et al., 2003; Adrain et al., 2009, 2014; Saltzman et al., 2015). The major pulse of the "Great Ordovician Biodiversification Event" (GOBE) and the first major Phanerozoic mass extinction

event occurred during the Middle and Late Ordovician, respectively (e.g., Algeo et al., 2016; Edwards, 2019; Goldberg et al., 2021). However, the global ocean redox conditions during the Ordovician are not well understood and only a few studies utilize $\delta^{238}U$ to reconstruct ocean redox conditions during the Ordovician (Azmy et al., 2015; Lu et al., 2017b; Bartlett et al., 2018; Dahl et al., 2021; Li et al., 2022; Liu et al., 2022).

In this dissertation, the U isotope system is applied for sedimentary rocks (ORMs and carbonates) to constrain global ocean redox conditions. Specifically, the $\delta^{238}U$ coupled with previously published $\delta^{98}Mo$ from the same euxinic ORMs is explored to better estimate the seawater Mo and U isotope compositions and global ocean redox conditions (Chapter 2). The $\delta^{238}U$ is applied to the Katian calcareous and siliciclastic organic-rich sedimentary rocks in southern Ontario (Canada) that were deposited during the Taconic Orogeny to constrain global ocean redox conditions prior to the Late Ordovician mass extinction event (LOME) (Chapter 3). The $\delta^{238}U$ of carbonates from the Great Basin (western USA) are used to constrain the role of global ocean euxinia during the base Stairsian mass extinction event in the Early Ordovician (Chapter 4).

1.2 Background: uranium isotope geochemistry

Uranium naturally occurs in two oxidation states as U(VI) and U(IV). Uranium is mainly derived from the oxidative weathering of upper continental crust, and dissolved U is then transported to the oceans via rivers. Riverine input is the major source of modern oceanic uranium (Dunk et al., 2002; Partin et al., 2013; Tissot and Dauphas, 2015; Andersen et al., 2016, 2017; Noordmann et al., 2016). Groundwaters could also be an oceanic U source, but the fluxes are poorly understood. Soluble U(VI) shows conservative behavior in oxygenated seawaters with an average concentration of ~14 nM (Ku et al., 1977), commonly combined with bicarbonate ions and existing as Ca/Mg-UO_2-CO_3 complexes (Langmuir, 1978; Endrizzi et al., 2016). Under anoxic conditions, soluble U(VI) is diffused into porewaters and reduced to insoluble U(IV) at sediment surface by organic floccule layer or below the sediment-water interface (SWI) via either abiotic or biotic reduction, and then sequestered in organic-rich

sediments and/or carbonates (Anderson et al., 1989; Barnes and Cochran, 1991; Klinkhammer and Palmer, 1991; Morford and Emerson, 1999; Dunk et al., 2002; McManus et al., 2006; Tribovillard et al., 2006; Partin et al., 2013; Romaniello et al., 2013; Andersen et al., 2017; Brown et al., 2018; Andersen et al., 2020). Uranium major oceanic sinks include sediments underlying anoxic and suboxic bottom waters and carbonates (Barnes and Cochran, 1990; Dunk et al., 2002; Partin et al., 2013). In addition, sediments deposited under well-oxygenated bottom water conditions and altered basalt are minor U sinks (Barnes and Cochran, 1990; Dunk et al., 2002; Partin et al., 2013).

The uranium isotope system has been extensively used as a global ocean redox proxy in recent years (see reviews in Andersen et al., 2017 and Zhang et al., 2020a). Uranium in the modern seawater has a long oceanic residence time (400–500 kyr) compared with ocean mixing time (1–2 kyr) (Ku et al., 1977; Dunk et al., 2002). Modern U abundance and isotope cycles are at steady state, and thus the average $\delta^{238}U$ of modern seawater (−0.39 ± 0.04‰) reflects the balance of $\delta^{238}U$ between U inputs and sinks in the ocean (Fig. 1.2; Dunk et al., 2002; Stirling et al., 2007; Weyer et al., 2008; Partin et al., 2013; Tissot and Dauphas, 2015; Andersen et al., 2016, 2017; Noordmann et al., 2016). The average $\delta^{238}U$ of rivers is estimated between −0.34‰ and −0.24‰, which is similar to the upper continental crust (−0.29 ± 0.03‰; Stirling et al., 2007; Weyer et al., 2008; Telus et al., 2012; Tissot and Dauphas, 2015; Andersen et al., 2016; Noordmann et al., 2016; Wang et al., 2018).

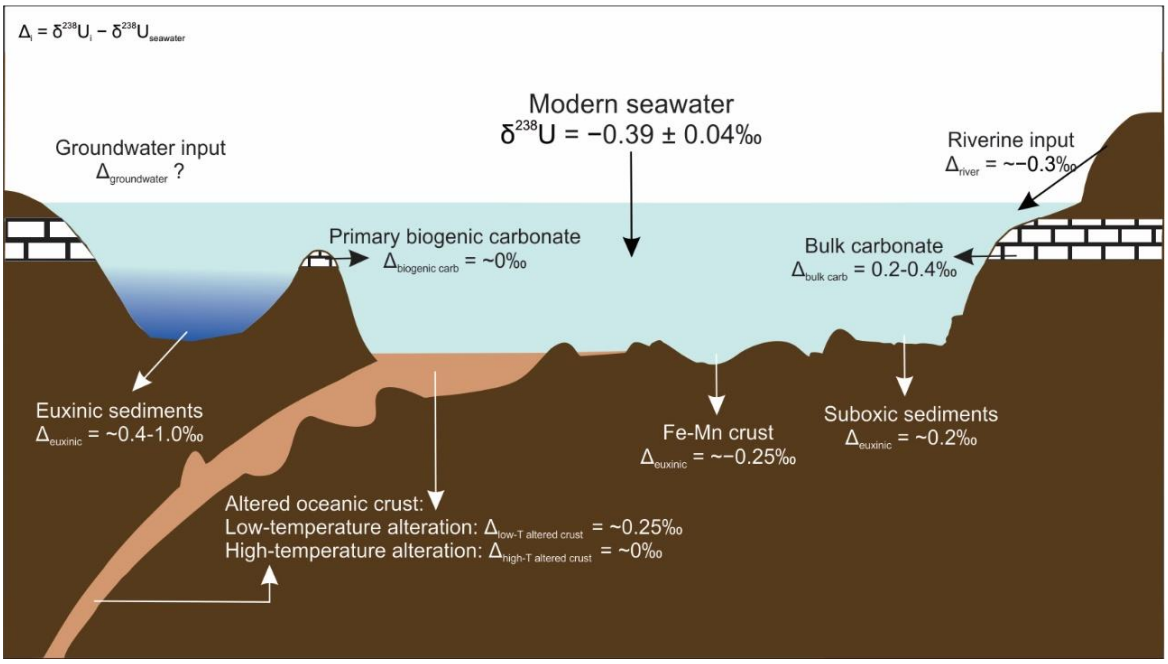

Figure 1.2 Uranium isotope distribution in modern oceans (modified from Zhang et al., 2020a; see references in the main text).

Abiotic and biotic U(VI) reduction could result in a large intrinsic U isotope fractionation (~1.0–1.3‰) with heavy ^{238}U enriched in solid U(IV) phases, which is associated with the nuclear volume effect (Base et al., 2014; Stirling et al., 2015; Brown et al., 2018). A large effective $\delta^{238}U$ offset (~0.6–0.8‰) between sediments and local bottom water, as observed in several modern euxinic settings, is approximately half of the intrinsic U isotope fractionation (e.g., the Black Sea, Cariaco Basin, Saanich Inlet, Lake Rogoznica, and Kyllaren Fjord; Stirling et al., 2007; Weyer et al., 2008; Andersen et al., 2014, 2016; Holmden et al., 2015; Noordmann et al., 2015; Rolison et al., 2017; Bura-Nakić et al., 2018; Brüske et al., 2020a). The discrepancy could be attributed to the U diffusive-reactive process. Theoretical calculations for selenium removal that is also characterized by this process suggest the effective isotope offset is approximately half of the intrinsic isotope fractionation (Clark and Johnson, 2008). However, it is noted that the $\delta^{238}U$ offsets between euxinic sediments and open

ocean seawater are rather variable (0.4–1.0‰), which is related to local depositional environment (e.g., bottom water sulfide concentration, basin restriction, sedimentation rate, productivity; Andersen et al., 2014, 2016, 2017; Holmden et al., 2015; Noordmann et al., 2015; Rolison et al., 2017; Bura-Nakić et al., 2018; Brüske et al., 2020a; Lau et al., 2020, 2022).

Ferruginous settings are rather rare in the modern, largely well-oxygenated oceans and the understanding of $\delta^{238}U$ offsets in such an environment is not well understood. Cole et al. (2020) analyzed $\delta^{238}U$ of sediments and bottom waters from two modern ferruginous lakes. They found variable $\delta^{238}U$ offsets between sediments and ferruginous bottom waters and the average $\delta^{238}U$ of ferruginous sediments is indistinguishable from sediments under oxic bottom waters (Cole et al., 2020). Nevertheless, more studies are needed to better constrain $\delta^{238}U$ in ferruginous settings.

The $\delta^{238}U$ offsets are smaller in oxic and suboxic settings compared with euxinic settings (Fig. 1.2; Weyer et al., 2008; Tissot and Dauphas, 2015; Andersen et al., 2016; Abshire et al., 2020; Cole et al., 2020; He et al., 2021; Bruggmann et al., 2022). The oxygenated Fe-Mn crusts contain $\delta^{238}U$ values that are ~0.25‰ lower than that of seawater due to the adsorption of isotopically light U on the Fe-Mn oxides (Goto et al., 2014). Suboxic sediments from the Peru continental margins, Namibian continental margins, and west coast of Washington State (United States) typically have slightly higher $\delta^{238}U$ values and the $\delta^{238}U$ offsets between sediments and seawater are generally less than 0.4‰ (Weyer et al., 2008; Andersen et al., 2016; Abshire et al., 2020; Cole et al., 2020; He et al., 2021; Bruggmann et al., 2022). Primary biogenic carbonates have minimal $\delta^{238}U$ offsets from seawater (Chen et al., 2018a; Livermore et al., 2020). However, shallow water platform carbonates from the modern Bahamas bank, deposited under oxygenated bottom waters, have $\delta^{238}U$ values that are on average ~0.27 ± 0.14‰ heavier than the modern seawater, which results from authigenic U enrichment in anoxic and sulfidic pore waters and preferential incorporation of charged isotopically heavy aqueous U(VI) species (Romaniello et al., 2013; Chen et al., 2016, 2018b; Tissot et al., 2018). In addition, negligible $\delta^{238}U$ offset is observed between high-temperature hydrothermal alteration of oceanic crust and seawater possibly due to near-quantitative U

removal, whereas the crust altered by low-temperature hydrothermal fluids have $\delta^{238}U$ value that is ~0.25‰ higher than seawater due to authigenic U(IV) enrichments (Tissot and Dauphas et al., 2015; Andersen et al., 2015, 2016; Noordmann et al., 2016).

Based on the above observations, the $\delta^{238}U$ of seawater is sensitive to the extent of euxinic seafloor area. For example, during an expanded ocean euxinia, more of the heavier ^{238}U would be preferentially removed to euxinic sediments, thus leaving more ^{235}U in the seawater and resulting in a lower seawater $\delta^{238}U$ value (Fig. 1.3). By contrast, during a widespread ocean oxygenation, less ^{238}U would be removed to euxinic sediments, leading to a higher seawater $\delta^{238}U$ value (Fig. 1.3).

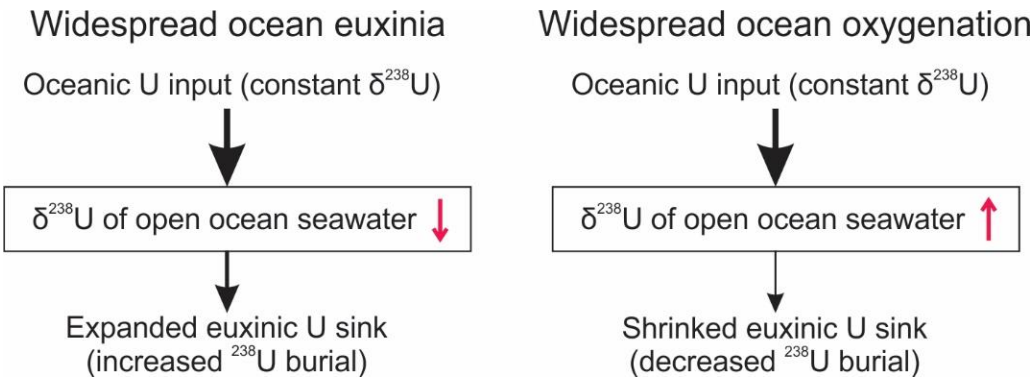

Figure 1.3 Changes in seawater $\delta^{238}U$ in response to the scenario of ocean euxinia and oxygenation.

Using $\delta^{238}U$ of sedimentary rocks (i.e., ORMs and carbonates) to reconstruct coeval seawater redox conditions should be done with caution. For the ORMs, although relatively low permeability of the ORM units could result in limited remobilization of U and the preserved $\delta^{238}U$ signals are resistant to diagenetic alteration, the local depositional environment (e.g., basin restrictions, bottom water redox conditions, and productivity) could influence the $\delta^{238}U$ offsets between the ORMs and coeval seawater (e.g., Andersen et al., 2016; Lau et al., 2020). With respect to carbonates, although a relatively small $\delta^{238}U$ offset is observed between

carbonate sediments and seawater, carbonates are more susceptible to diagenetic alteration and thus the preserved $\delta^{238}U$ signals could be potentially changed from the original depositional values (e.g., Zhang et al., 2020a). Therefore, a thorough understanding of local depositional environment during deposition of ORMs and a careful evaluation of diagenetic effects on carbonate $\delta^{238}U$ values are required before using $\delta^{238}U$ to reconstruct coeval ocean redox conditions.

1.3 Uranium isotope mass balance model

A uranium isotope mass balance model can be used to quantitatively constrain the areal extent of global ocean euxinic seafloor for the late Neoproterozoic and Phanerozoic (ca. 680–0 Ma) because extreme ocean anoxia in the Archean and early-middle Proterozoic would significantly shorten U oceanic residence time (e.g., similar or below ocean mixing time; X. Chen et al., 2021). A few assumptions have to be made before using the model: 1) similar $\delta^{238}U$ of the oceanic U inputs as today (~−0.3‰) because of the narrow $\delta^{238}U$ range of crustal igneous rocks (Telus et al., 2012; Andersen et al., 2015; Tissot and Dauphas, 2015), and 2) similar $\delta^{238}U$ offsets between each redox sink and coeval seawater as observed in the modern environment because similar U removal mechanisms in anoxic sediments that resulted in a similar magnitude of $\delta^{238}U$ offset in the modern anoxic environment could have been occurred since the Late Neoproterozoic (ca. 680 Ma; X. Chen et al., 2021). The model follows Stockey et al. (2020) and is summarized below. Firstly, the global seawater U concentration equals to total riverine input minus total U output into each sink (see equation (1); Goto et al., 2014; Wang et al., 2016; Stockey et al., 2020). The $\delta^{238}U$ of the global ocean can be expressed in a similar way as shown in equation (2):

$$dU_{SW}/dt = F_r - \sum F_i \quad (1)$$

$$dU_{SW}\delta_{SW}/dt = F_r\delta_r - \sum F_i\,(\delta_{SW} + \Delta_i) \quad (2)$$

where U_{SW} represents total U mass in the ocean; F_r refers to U riverine flux; F_i refers to U output flux, namely, the euxinic (eux), reducing (red; e.g., suboxic, ferruginous), and oxic (oxic; e.g., Fe-Mn oxides) sinks; δ_{SW} and δ_r represent seawater and riverine U isotope

composition, respectively; Δ_i refers to U isotope fractionation between seawater and each U sink (oxic, red, eux). Moreover, fluxes of each sink are defined as below (following Reinhard et al., 2013; Stockey et al., 2020):

$$F_i = A_i b_i \alpha_i ([U]_{SW}/[U]_{M.SW}) \quad (3)$$

where A_i is the seafloor area that is covered by each redox sink, b_i represents the burial flux of each sink, α_i is the pseudospatial scaling coefficient that scales the U burial rate to the effects of organic carbon remineralization as a function of water depth (Menard and Smith, 1966; Middelburg et al., 1996; following Stockey et al., 2020), $[U]_{SW}$ is the modeled average U concentrations of ancient seawater, and $[U]_{M.SW}$ is the average U concentration of modern seawater.

Burial scaling coefficient (α) is used to take the influence of organic carbon remineralization into consideration for euxinic and reducing U sinks (assuming $\alpha = 1$ for the oxic sink). Burial scaling coefficients in those two U sinks follow the remineralization model as a function of water depth and is expressed as below (Reinhard et al., 2013; Stockey et al., 2020).

$$\alpha_{eux} = \frac{\sum_{min(z_{eux})}^{max(z_{eux})} 1.58\text{-}0.16ln(z_{eux})}{N(z_{eux})\{1.58\text{-}0.16ln(\,min(z_{eux}))\}} \quad (4)$$

$$\alpha_{red} = \frac{\sum_{min(z_{red})}^{max(z_{red})} 1.58 - 0.16ln(z_{red} + maxln(z_{eux}))}{N(z_{red})\{1.58\text{-}0.16ln(\,min(z_{eux}))\}} \quad (5)$$

This U isotope mass balance model estimated seawater U isotope compositions as a function of global euxinic seafloor area (Fig. 1.4; see parameters in Table 3.5 and 4.3; Stockey et al., 2020). For the modern ocean with a seawater $\delta^{238}U$ of −0.39 ± 0.04‰ (Weyer et al., 2008; Tissot and Dauphas, 2015), the model reveals a euxinic seafloor area of 0.2–0.3% (32^{th}–68^{th} percentile; median = 0.2%). This result is generally consistent with previous estimations of modern euxinic seafloor area (0.1–0.3%; Reinhard et al., 2013; Tissot and Dauphas, 2015). The model result is founded on the steady state conditions. If the seawater U isotope compositions were significantly changed in a relatively short time interval (e.g., a few million

years or less), using a dynamic U isotope mass balance model would be more appropriate (e.g., end-Permian; Zhang et al., 2020a; Clarkson et al., 2021; Kendall, 2021).

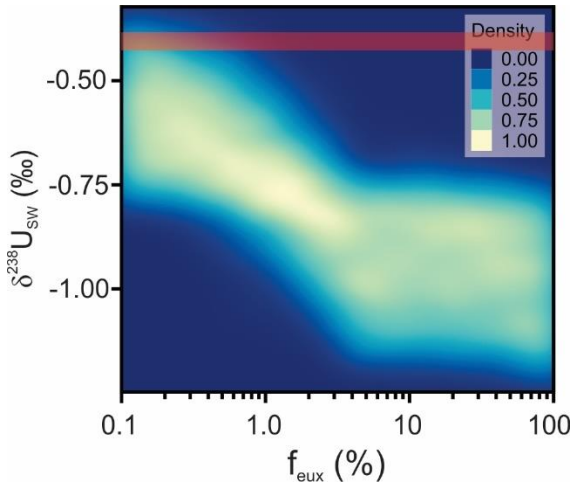

Figure 1.4 Uranium isotope mass balance model result that shows the frequency distribution of seawater U isotope compositions ($\delta^{238}U_{SW}$) as a function of global ocean euxinic seafloor area (f_{eux}). The pink bar represents the range of $\delta^{238}U$ in the modern seawater.

1.4 Thesis objectives

The overall objective of the thesis is: 1) to better estimate seawater isotope compositions using coupled Mo-U isotope data from the same euxinic ORM samples (Chapter 2), and 2) constrain ancient seawater U isotope composition and global ocean redox conditions using U isotope data from sedimentary rocks and U isotope mass balance modelling, respectively, for specific timeframes during the Early (Chapter 4) and Late Ordovician (Chapter 3). This work would contribute to the understanding of co-evolution of metazoans and environment, especially during the Ordovician when there were rapid changes in metazoan biodiversification. Specific objectives of this thesis are to investigate:

1) combined use of both $\delta^{98}Mo$ and $\delta^{238}U$ from the same euxinic ORMs to differentiate effects from local depositional environment versus global ocean redox state (Chapter 2);
2) a general framework of using coupled $\delta^{98}Mo$-$\delta^{238}U$ data from the same euxinic

ORMs to estimate ancient seawater isotope compositions (Chapter 2);

3) spatiotemporal variations in local hydrographic and ocean redox conditions of the Katian (Late Ordovician) calcareous and siliciclastic ORMs deposited during the Taconic Orogeny in southern Ontario (Chapter 3);
4) the extent of global ocean anoxia/euxinia during the Katian calcareous and siliciclastic organic-rich sedimentary rocks deposition and potential relationship with the concurrent Taconic Orogeny and a biodiversity decline prior to the LOME (Chapter 3);
5) the quantitative extent of global ocean euxinia during the base Stairsian mass extinction event (Chapter 4);
6) the role of global ocean euxinia on the base Stairsian (Tremadocian, Early Ordovician) mass extinction event (Chapter 4);

To approach these objectives, sedimentary rock samples have been obtained from either collaborators or drillcore libraries in Ontario (the Oil, Gas and Salt Resources Library at London and the Ontario Geological Survey at Sudbury). Bulk samples were carefully selected and powdered by an automated agate ball mill at the University of Waterloo. Wet chemistry was mainly carried out in the clean lab of the Metal Isotope Geochemistry Laboratory at the University of Waterloo. Elemental concentrations were measured on an Agilent 8800 triple quadrupole inductively coupled plasma mass spectrometer (QQQ-ICP-MS) at the Metal Isotope Geochemistry Laboratory, University of Waterloo. Uranium isotope compositions were measured on a Thermo Scientific Neptune multi-collector ICP-MS at the W.M. Keck Foundation Laboratory for Environmental Biogeochemistry, Arizona State University, for Chapter 2, and a Nu Plasma II multi-collector ICP-MS at the Metal Isotope Geochemistry Laboratory, University of Waterloo, for Chapters 3 and 4.

1.5 Organization of thesis

Following this introductory chapter, the thesis consists of three main research chapters (2–4) and a concluding chapter (5). Each research chapter is written as a stand-alone paper

meant to be published in a peer-reviewed journal. The chapters are organized to provide a comprehensive understanding of using the U isotope system in sedimentary rocks to better reconstruct and constrain the global ocean redox conditions in the deep time. References and appendices for all chapters are compiled and presented at the end of the thesis.

Chapter 2 deals with the topic that using coupled δ^{98}Mo-δ^{238}U from the same euxinic organic-rich mudrocks can better reconstruct the ancient ocean redox conditions. As each proxy has its own drawbacks, the combined use of different isotope systems would be a better approach to infer seawater isotope compositions and thus global ocean redox conditions. In this study, U isotope compositions were measured for the same euxinic organic-rich mudrocks during the late Neoproterozoic and middle Paleozoic that have been previously analyzed for δ^{98}Mo values (and TOC and Fe speciation data; Dahl et al., 2010; Kendall et al., 2015). This chapter has been published in *Geochimica et Cosmochimica Acta* in 2020 (volume 290, pages 76–103).

Chapter 3 focuses on the local depositional environment and contemporaneous ocean redox conditions during the deposition of Katian (Late Ordovician) organic-rich sedimentary rocks in southern Ontario (Canada), namely the calcareous Collingwood Member (upper Lindsay Formation) and the overlying siliciclastic Rouge River Member (lower Blue Mountain Formation) (Russell and Telford, 1983). Both units were deposited during the Taconic Orogeny and a period of biodiversity decline prior to the LOME. However, the local depositional environment and global redox conditions during the deposition of both units have not been well understood. In this study, elemental concentrations and U isotope compositions were analyzed for both units from several drillcores that spatially cover southern Ontario. This would provide valuable information about the spatiotemporal variations in local depositional environment of both units and constrain the coeval Katian global ocean redox conditions prior to the LOME during the Hirnantian.

Chapter 4 is mainly concerned with the global ocean redox conditions during the base Stairsian (Tremadocian, Early Ordovician) mass extinction event (Adrain et al., 2009, 2014). Edwards et al. (2018) provides geochemical evidence of expanded local and global ocean

anoxia during this mass extinction event from three carbonate sections in the Great Basin (western United States). Coincidently, this mass extinction event is accompanied by a globally correlated positive carbon isotope excursion (CIE, ~1–2‰) (Saltzman et al., 2015; Edwards et al., 2018) and eustatic fall (Miller et al., 2003, 2012). However, different characteristics of geochemical proxies (e.g., I/Ca ratios) during the CIE are observed among three sections and are not well understood. Moreover, the extent of coeval global ocean euxinia is not quantitatively constrained. In this study, trace metal concentrations and U isotope compositions were analyzed for the same carbonate samples in Edwards et al. (2018) to test the role of global ocean euxinia on the base Stairsian mass extinction event. This chapter has been submitted to *Geochimica et Cosmochimica Acta* (now under review).

Chapter 2 Estimating ancient seawater isotope compositions and global ocean redox conditions by coupling the molybdenum and uranium isotope systems of euxinic organic-rich mudrocks

Published on Geochimica et Cosmochimica Acta.

Citation: Lu, X., Dahl, T. W., Zheng, W., Wang, S. and Kendall, B. (2020) Estimating ancient seawater isotope compositions and global ocean redox conditions by coupling the molybdenum and uranium isotope systems of euxinic organic-rich mudrocks. *Geochimica et Cosmochimica Acta*, 290, 76–103. doi:10.1016/j.gca.2020.08.032

2.1 Introduction

Changes in Earth's atmosphere-ocean redox conditions are likely intertwined with the evolution of the overall Earth system, including the biosphere, crust, and mantle (e.g., Holland, 2006; Canfield et al., 2007; Dahl et al., 2010; Lyons et al., 2014; Kendall et al., 2015; Reinhard et al., 2016; Wallace et al., 2017; Lu et al., 2018). Although the modern atmosphere and ocean are well-oxygenated, the environment of the Precambrian was likely different – more widespread anoxic conditions (e.g., Scott et al., 2008; Partin et al., 2013; Lyons et al., 2014; Lu et al., 2017a; Lu et al., 2018; Sheen et al., 2018; Wang et al., 2018). Both environmental (e.g., oxygen level, climate change) and ecological/genetic factors (e.g., arms race) could influence metazoan evolution (e.g., Rhoads and Morse, 1971; Diaz and Rosenberg, 1995; Dahl et al., 2010; Mills and Canfield, 2014; Planavsky et al., 2014; Reinhard et al., 2016). It has been demonstrated a physiological control of O_2 on the body size of species, diversity of carnivory, and complexity of food webs (e.g., Dahl and Hammarlund, 2011; Payne et al., 2011; Sperling et al., 2013; Mills and Canfield, 2014). Therefore, exploring the Earth's surface oxygenation through time greatly helps to understand how metazoans diversified through time and how the Earth evolved as a complex system (e.g., Holland, 2006; Canfield et al., 2007; Butterfield, 2009; Dahl et al., 2010, 2017b, 2019; Reinhard et al., 2013; Lyons et al., 2014; Kendall et al., 2015; Wallace et al., 2017; Lu et al., 2018; Zhang et al., 2019).

Tracking the Earth's oxygenation history is not straightforward and is often inferred from geochemical redox proxies, such as the concentrations and isotopic compositions of redox-sensitive trace metals (e.g., Scott et al., 2008; Partin et al., 2013; Kendall et al., 2015; Lu et al., 2017a; Sheen et al., 2018). The molybdenum and uranium isotope compositions of euxinic organic-rich mudrocks (ORM) have been widely used as novel global ocean redox tracers (e.g., Barling et al., 2001; Arnold et al., 2004; Stirling et al., 2007; Weyer et al., 2008; Kendall et al., 2009, 2015, 2020; Dahl et al., 2010, 2011; Asael et al., 2013; Lu et al., 2017b; Yang et al., 2017; Wang et al., 2018; Gilleaudeau et al., 2019; Ostrander et al., 2019a). Both Mo and U have much longer modern oceanic residence times (Mo: 440 kyr; U: 400-500 kyr)

than the ocean mixing time (~1-2 kyr) (Ku et al., 1977; Dunk et al., 2002; Miller et al., 2011). These metals are soluble and show conservative behavior in oxygenated waters and can be removed to sediments under anoxic conditions via different mechanisms (see Section 2.2; Anderson, 1989; Barnes and Cochran, 1990; Helz et al., 1996, 2011; Morford and Emerson, 1999; Erickson and Helz, 2000; Dunk et al., 2002; McManus et al., 2006; Algeo and Tribovillard, 2009). The Mo and U isotope compositions of ORMs are sensitive to the extent of global ocean euxinia, and geochemical models have been developed to quantitatively constrain the contemporaneous global ocean redox conditions (e.g., Dahl et al., 2011; Goldberg et al., 2016; Gilleaudeau et al., 2019).

Depending on only Mo isotope compositions of euxinic ORM leads to uncertainty when reconstructing paleocean redox conditions (e.g., Arnold et al., 2004; Neubert et al., 2008; Gordon et al., 2009). Only under strongly euxinic bottom water conditions ($[H_2S]_{aq}$ > 11µM) and near-quantitative removal of Mo from bottom waters can the Mo isotope compositions of modern euxinic sediments approach the global seawater Mo isotope composition (Barling et al., 2001; Arnold et al., 2004; Neubert et al., 2008; Nägler et al., 2011; Noordmann et al., 2015; Bura-Nakić et al., 2018). In contrast, much larger and variable Mo isotope fractionations (0.5-3.0‰) between modern seawater and sediments occur when bottom waters are non-euxinic or weakly euxinic ($[H_2S]_{aq}$ < 11µM) (Arnold et al., 2004; Neubert et al., 2008; Poulson et al., 2006; Poulson Brucker et al., 2009; Goldberg et al., 2012; Kendall et al., 2017). However, there is no valid method to distinguish between strongly and weakly euxinic conditions for ancient ORM. Therefore, it is challenging to determine how much seawater Mo isotope variation occurred during deposition of a euxinic ORM stratigraphic unit. Because of this difficulty, the heaviest Mo isotope compositions of a euxinic ORM stratigraphic unit are commonly regarded as a conservative lower limit of coeval seawater Mo isotope compositions for the entire unit (Barling et al., 2001; Arnold et al., 2004; Neubert et al., 2008; Gordon et al., 2009; Dahl et al., 2010; Nägler et al., 2011; Kendall et al., 2015; Brüske et al., 2020). However, doing so limits the utility of the Mo isotope system as a global ocean redox tracer.

Inferring ancient global ocean redox conditions solely based on the U isotope compositions of euxinic ORM can also be ambiguous (e.g., Andersen et al., 2014; Rolison et al., 2017; Wang et al., 2018; Brüske et al., 2020; Kendall et al., 2020). A large apparent U isotope fractionation factor between bottom waters and euxinic sediments ($\geq$ 0.6‰) is found to be accompanied by both abiotic and biotic U reduction (U[VI] to U[IV]) and removal, resulting in the preferential accumulation of ^{238}U in U(IV) in sediments as observed in modern euxinic basins (Stirling et al., 2007; Weyer et al., 2008; Montoya-Pino et al., 2010, 2011; Andersen et al., 2014, 2017; Holmden et al., 2015; Noordmann et al., 2015; Rolison et al., 2017; Bura-Nakić et al., 2018; Brüske et al., 2020). This process is explained as the nuclear field shift fractionation (e.g., Bigeleisen, 1996; Schauble, 2007; Abe et al., 2008). However, the effective U isotope fractionation between euxinic bottom waters and sediments can be variable due to changes in the local depositional environment (e.g., aqueous U species, site of U reduction (above, at, or below sediment-water interface [SWI]), the efficiency of U removal, U diffusive-reactive process, sedimentation rate, productivity), limiting the use of U isotope compositions from ancient ORM to reconstruct global paleocean redox conditions (Andersen et al., 2014, 2017; Noordmann et al., 2015; Rolison et al., 2017; Brown et al., 2018; Bura-Nakić et al., 2018; Brüske et al., 2020; Lau et al., 2020).

Using a single metal isotope system can lead to significant uncertainties; however, the combined use of multiple metal isotope systems is a better approach to more robustly infer ancient seawater metal isotope compositions and thus infer global ocean redox conditions. In this study, we use new and previously published data to further develop the coupled use of Mo and U isotope compositions from Proterozoic and Phanerozoic euxinic ORM to reconstruct global ocean redox conditions. Different patterns of covariation between Mo and U isotope data from individual ORM units are observed, shedding light on the relative influence of local depositional effects versus global redox controls. In addition, the potential ranges of contemporaneous seawater Mo and U isotope compositions during ORM deposition are estimated using a coupled Mo-U isotope model developed from observations of modern marine sediments.

2.2 The molybdenum and uranium isotope systems as global ocean redox tracers

2.2.1 The Mo isotope proxy

Molybdenum is mainly sourced from the oxidative weathering of the upper continental crust and delivered to the oceans via rivers, and low-temperature seafloor hydrothermal systems contribute a small amount of Mo (~5–10%) to the oceans (McManus et al., 2002; Miller et al., 2011; Reinhard et al., 2013). In the oxygenated surface waters, Mo mainly exists as soluble molybdate (MoO_4^{2-}), which can be slowly adsorbed on the surface of Mn oxides (Barling et al., 2001; Siebert et al., 2003; Barling and Anbar, 2004). In anoxic and sulfidic environments, the soluble molybdate can efficiently react with aqueous hydrogen sulfide ($[H_2S]_{aq}$) to form particle reactive thiomolybdate and polysulfide species that are scavenged by organic matter and solid sulfide minerals (Helz et al., 1996, 2011; Morford and Emerson, 1999; Erickson and Helz, 2000; Dahl et al., 2013, 2017a). The Mo removal rates in euxinic settings are much higher than in oxic settings (Bertine and Turekian, 1973; Emerson and Huested, 1991; Scott et al., 2008). The redox sensitive behavior and long oceanic residence time (~440 kyr today) make Mo an ideal tracer for global ocean redox conditions (Barling et al., 2001; Miller et al., 2011; Kendall et al., 2017).

The modern ocean has a homogenous δ^{98}Mo of ~2.34 ± 0.10‰ (2SD; Barling et al., 2001; Nakagawa et al., 2012; Nägler et al., 2014). The δ^{98}Mo of low-temperature seafloor hydrothermal systems is estimated around 0.8‰, but is still poorly understood (McManus et al., 2002; Kendall et al., 2017). The weight-averaged δ^{98}Mo of large rivers is estimated to be ~0.7‰ (Archer and Vance, 2008). However, groundwater could potentially contribute a larger amount of Mo to the rivers than previously thought (Moore, 1996). Taking the groundwater input into consideration, the newly estimated average δ^{98}Mo of the riverine inputs is similar to the estimated average composition of the upper continental crust (0.3–0.6‰; Voegelin et al., 2014; King et al., 2016; Willbold and Elliott, 2017; King and Pett-Ridge, 2018). Neely et al. (2018) estimated a δ^{98}Mo value of ~0.5‰ for the overall oceanic Mo inputs, including contributions from rivers, groundwaters, and low-temperature hydrothermal systems.

Under well-oxygenated bottom waters, Fe-Mn oxides are characterized by an average δ^{98}Mo of −0.7‰, indicating a large Mo isotope fractionation of ~3‰ during Mo adsorption to Fe-Mn oxides (Barling et al., 2001; Siebert et al., 2003; Barling and Anbar, 2004). By contrast, continental margin sediments, deposited under weakly oxygenated and anoxic bottom waters where aqueous hydrogen sulfide is restricted to the porewaters, have a much heavier δ^{98}Mo value of 1.6–2.1‰ (Poulson et al., 2006; Siebert et al., 2006; Poulson Brucker et al., 2009; Eroglu et al., 2020). Sediments deposited in mildly oxygenated environments have intermediate δ^{98}Mo values between −1.0‰ and +1.6‰, which are influenced by the different compositions of Fe and Mn oxides and the levels of $[H_2S]_{aq}$ in the porewaters (Siebert et al., 2006; Goldberg et al., 2009, 2012).

When the bottom water is strongly euxinic ($[H_2S]_{aq}$ > 11 µM, "active point of switch" [APS]), molybdate can be completely converted to trithiomolybdate ($MoOS_3^{2-}$) or tetrathiomolybdate (MoS_4^{2-}) (Helz et al., 1996; Erickson and Helz, 2000). If quantitative Mo removal was further achieved, the authigenic Mo isotope composition of the euxinic sediment is close to that of the open-ocean seawater value as observed in the deep Black Sea and the Kyllaren Fjord (Barling et al., 2001; Neubert et al., 2008; Helz et al., 2011; Noordmann et al., 2015). However, if Mo removal was incomplete (e.g., bottom water renewal rate > Mo burial rate), a small Mo isotopic offset (0.5 ± 0.3‰) between seawater and the euxinic sediments could still occur even in a strongly euxinic environment (Nägler et al., 2011; Bura-Nakić et al., 2018). In contrast, large and variable Mo isotope fractionations (up to ~3‰) could occur under weakly euxinic bottom water conditions ($[H_2S]_{aq}$ < 11 µM) due to the formation of intermediate thiomolybdate species and non-quantitative Mo removal from bottom waters (Arnold et al., 2004; Neubert et al., 2008; Nägler et al., 2011). Short-term redox fluctuations (possibly associated with eustatic sea-level change, occasional inflow of oxygenated waters) could stimulate cycling of the Fe-Mn oxides that shuttle isotopically light Mo to deeper waters or the sediment surface, which can also cause lower δ^{98}Mo in these euxinic sediments as observed in the Cariaco Basin and the Baltic Sea (Gotland Deep and Landsort Deep) (Huckriede and

Meischner, 1996; Dellwig et al., 2010, 2012; Arnold et al., 2004; Goldberg et al., 2009, 2012; Nägler et al., 2011; Scholz, 2013, 2018; Noordmann et al., 2015).

In this framework, during expanded ocean euxinia, the seawater would be characterized by a relatively lower Mo isotope composition due to less removal of isotopically light Mo to oxic sediments. In contrast, a widespread oxygenated ocean would have a higher Mo isotope composition.

2.2.2 The U isotope proxy

Riverine input is the only known major source of U to the oceans (Dunk et al., 2002). Groundwaters, as an important source of Mo to the oceans, might contribute to oceanic U although it is currently a knowledge gap. Uranium mainly exists as the Ca/Mg-UO_2-CO_3 complexes in oxygenated waters (Langmuir, 1978; Anderson et al., 1989; Dunk et al., 2002; Endrizzi et al., 2016). Unlike Mo removal that can occur in a euxinic water column, U removal typically involves the diffusion of seawater U(VI) into porewaters and subsequent reduction of soluble U(VI) to insoluble U(IV) at the SWI or within the sediments under anoxic conditions (Anderson et al., 1989; Barnes and Cochran, 1990, 1993). The strong negative correlation (r^2 = 0.99) between dissolved U concentrations and hydrogen sulfide concentrations in the Black Sea water column indicates U removal is more efficient when euxinia is more intense (Rolison et al., 2017). It has also been demonstrated that the U reduction and removal rate is proportional to the sulfate reduction rate (Barnes and Cochran, 1993). The U burial rates in euxinic settings are much higher than in oxic settings (Barnes and Cochran, 1990; Morford and Emerson, 1999; Dunk et al., 2002). Oxygenated modern seawater has an average $\delta^{238}U$ of -0.39 ± 0.04‰ (2SD; Stirling et al., 2007; Weyer et al., 2008; Tissot and Dauphas, 2015; Andersen et al., 2016; Noordmann et al., 2016). The weighted average $\delta^{238}U$ of rivers has been estimated between −0.34‰ and −0.24‰, which is similar to the upper continental crust (−0.3‰; Stirling et al., 2007; Weyer et al., 2008; Tissot and Dauphas, 2015; Andersen et al., 2016; Noordmann et al., 2016).

The U reduction and removal process below the SWI is accompanied by a large and variable U isotope fractionation (typically 0.6–0.8‰) between modern euxinic sediments and bottom waters (Stirling et al., 2007; Weyer et al., 2008; Montoya-Pino et al., 2010; Andersen et al., 2014, 2016; Holmden et al., 2015; Noordmann et al., 2015, 2016; Rolison et al., 2017; Bura-Nakić et al., 2018; Brüske et al., 2020). This diffusive-reactive process for U has been fully explained in previous studies (Clark and Johnson, 2008; Andersen et al., 2014; Rolison et al., 2017; Wang et al., 2018), and thus is only briefly described here. When dissolved U(VI) diffuses across the SWI from bottom waters to sediments, partial U reduction and removal will cause authigenic U accumulation and preferential enrichment of ^{238}U in the sediments, leading to lower U concentrations and lower $\delta^{238}U$ in the porewaters. When U reduction occurs at greater depths below the SWI, there will be progressively less U isotopic offset from overlying seawater because of less dissolved U(VI) in the porewaters (Clark and Johnson, 2008; Andersen et al., 2014; Rolison et al., 2017; Wang et al., 2018).

The full range of intrinsic U isotope fractionation during reduction of U^{6+} to U^{4+} is not well determined. Theoretical calculations based on ab initio molecular orbital modeling suggest an intrinsic U isotope fractionation of 0.95‰ (Abe et al., 2008). Laboratory experimental studies yield a similar value of ~1.0–1.3‰ for abiotic and biotic U reduction (Basu et al., 2014; Stirling et al., 2015; Stylo et al., 2015; Brown et al., 2018). Based on a model that describes Se diffusion and reduction below the SWI, the effective Se isotope fractionation between the dissolved phase and reduced phase is calculated to be half of the intrinsic Se isotope fractionation (Clark and Johnson, 2008). Similarly, this diffusive-reactive approach can be used for U (Andersen et al., 2014). An effective U isotope fractionation of ~0.6‰ between euxinic bottom waters and sediments is observed in several modern anoxic basins (e.g., the Black Sea, Cariaco Basin, Saanich Inlet, Kyllaren Fjord, Lake Rogoznica; Andersen et al., 2014; Noordmann et al., 2015; Holmden et al., 2015; Rolison et al., 2017; Bura-Nakić et al., 2018; Brüske et al., 2020). This value also matches calculations by a simple Rayleigh model based on studies of modern anoxic basins (Andersen et al., 2014; Rolison et al., 2017; Bura-Nakić et al., 2018; Brüske et al., 2020). Therefore, the intrinsic U isotope

fractionation could reach 1.2‰ using an effective U isotope fractionation of 0.6‰ (Clark and Johnson, 2008; Andersen et al., 2014). This intrinsic U isotope fractionation value (1.2‰) is similar to theoretical predictions (Abe et al., 2008) and laboratory studies (Basu et al., 2014; Stirling et al., 2015; Stylo et al., 2015; Brown et al., 2018). In addition, a few anomalously high U isotope compositions were reported for ancient ORMs, such as the Neoarchean Albitibi Formation (up to 0.81‰, leaches; Wang et al. 2018) and Paleoproterozoic Zaonega Formation (up to 0.79‰, whole rock; Mänd et al. 2020), implying large U isotope fractionations (likely > 0.6‰) from coeval seawater. In this study, an intrinsic U isotope fractionation of 1.2‰ is tentatively used.

The depositional environment significantly influences the effective U isotope fractionation factor associated with U reduction and removal to sediments. Taking the U reduction pathway as an example, if U reduction primarily occurred on the sediment surface and was less affected by diffusive-reactive process, the effective U isotope fractionation would be close to the intrinsic U isotope fractionation (Andersen et al., 2017). In addition, generally smaller U isotopic offsets occur in more severely restricted basins due to basin reservoir effect (Andersen et al., 2017; Rolison et al., 2017; Lau et al., 2020). Besides the U reduction pathway and basin reservoir effect, the magnitude of U isotope fractionation in euxinic settings is influenced by several other factors, such as aqueous U species, aqueous major ion chemistry, basin geometry, bottom water chemistry, sedimentation rate, and productivity (e.g., Andersen et al., 2014, 2018; Noordmann et al., 2015; Rolison et al., 2017; Brown et al., 2018; Bura-Nakić et al., 2018; Tissot et al., 2018; Brüske et al., 2020; Lau et al., 2020).

Ferruginous settings, which were prevalent in the Precambrian (e.g., Planavsky et al., 2011; Poulton and Canfield, 2011; Lowenstein et al., 2014), could be an important sink of U (Cole et al., 2020). A recent study suggests highly variable $\delta^{238}U$ in ancient and modern ferruginous settings, but the average U isotope composition of modern ferruginous sediments is indistinguishable from the adjacent oxic settings (Cole et al., 2020). More studies are needed to further constrain U behavior in ferruginous settings.

In modern oxic and suboxic settings, the U isotope fractionations are much smaller compared with those in euxinic settings (Weyer et al., 2008; Tissot and Dauphas, 2015; Andersen et al., 2016; Cole et al., 2020). The oxygenated Fe-Mn crusts have lighter $\delta^{238}U$ (−0.59‰ to −0.69‰) that is ~0.25‰ on average lower than that of seawater (Goto et al., 2014; Wang et al., 2016). It indicates that ^{235}U is preferentially adsorbed to Fe-Mn crusts, leaving seawater enriched in^{238}U. In the continental margin of Peru and Washington State (United States), sediments deposited under suboxic bottom waters contain $\delta^{238}U$ that are only 0.1-0.2‰ heavier than seawater (Weyer et al., 2008; Tissot and Dauphas, 2015; Andersen et al., 2016). Primary biogenic carbonates contain $\delta^{238}U$ values that approach the modern seawater value, with a small isotope fractionation of < 0.1‰ (Weyer et al., 2008; Romaniello et al., 2013; Chen et al., 2018b). However, modern shallow-water carbonate sediments from the Bahamas bank have higher U concentrations and isotopic compositions (0.24 ± 0.14‰, 1SD) mainly due to U reduction in the sulfidic sediment pore fluids and aqueous U speciation-dependent isotope fractionations (Romaniello et al., 2013; Chen et al., 2018a, Tissot et al., 2018, Dahl et al., 2019). Negligible U isotope fractionation is observed between seawater and high-temperature hydrothermal alteration of oceanic crust, whereas the $\delta^{238}U$ of crust altered by low-temperature hydrothermal fluids is approximately 0.25‰ higher than that of seawater (Tissot and Dauphas, 2015; Andersen et al., 2015, 2016; Noordmann et al., 2016).

The basic logic of interpreting $\delta^{238}U$ from ORM for the extent of ancient ocean oxygenation/euxinia is based on the modern marine U isotope cycle. During an expansion of ocean euxinia, ^{238}U is preferentially removed to sediments, thus leading to a lighter seawater U isotope composition (enriched in ^{235}U). On the contrary, with increased ocean oxygenation, the preferential removal of ^{238}U from the oceans to euxinic sediments is largely reduced, resulting in a heavier seawater U isotope composition.

2.2.3 Covariations of $\delta^{98}Mo$ and $\delta^{238}U$ in modern euxinic sediments

Bura-Nakić et al. (2018) compiled sedimentary authigenic average Mo and U isotope compositions of euxinic organic-rich sediments from modern basins and observed an overall

negative correlation between the Mo and U isotope data (Fig. 2.1). The apparent ratio of the isotopic fractionation factors of Mo to U (Δ^{98}Mo : Δ^{238}U ≈ −0.9‰ : 0.6‰ ≈ −3 : 2) in the euxinic sediments from Kyllaren Fjord, Lake Rogoznica, Cariaco Basin, and Saanich Inlet is approximately −1.5 (Bura-Nakić et al., 2018). This pattern is not suitable for the Black Sea sediments (Unit I), which may be due to sluggish ventilation and renewal of the strongly euxinic deep bottom waters (Bura-Nakić et al., 2018). This causes more efficient Mo removal relative to U such that the Mo isotope compositions of euxinic sediments in the Black Sea approaches global seawater whereas there are still U isotope fractionations due to kinetically slower U removal (than Mo) and diffusive-reactive processes (Andersen et al., 2014; Rolison et al., 2017; Brüske et al., 2020; Lau et al., 2020).

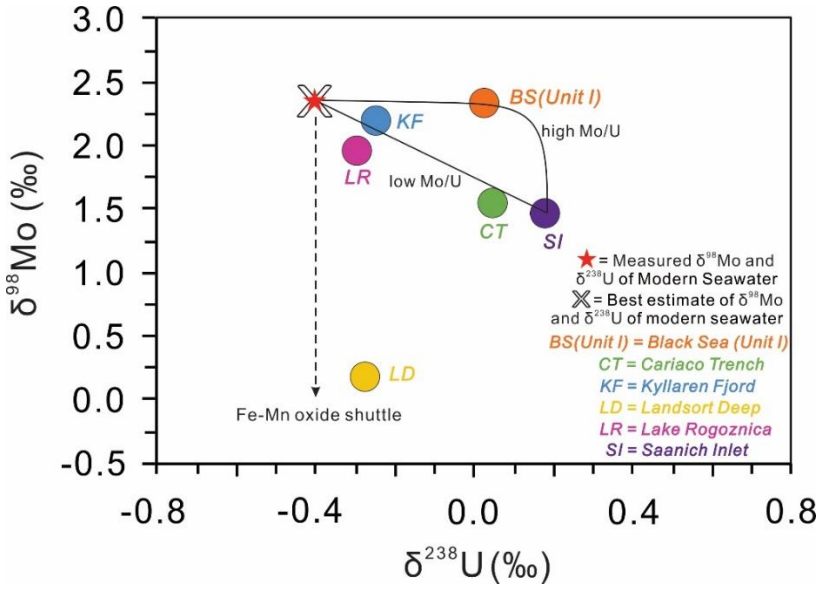

Figure 2.1 Covariations of Mo and U isotope compositions of sediments from modern euxinic basins (modified from Bura-Nakić et al., 2018). Circled points represent the averaged δ^{98}Mo-δ^{238}U of the euxinic basins (modified from Bura-Nakić et al. 2018 and see references therein). Other sources: Black Sea Unit I (Barling et al., 2001; Weyer et al., 2008; Arnold et al., 2012), Landsort Deep (Noordmann et al., 2015).

The inverse correlations between Mo and U isotope compositions are also shown in sediments from several individual euxinic basins (Andersen et al., 2018; Brüske et al., 2020). The $\Delta^{98}Mo : \Delta^{238}U$ ratios of the coupled Mo-U isotope data in sediments from the Black Sea (the Unit I, II, and core 32MUC24 sediments), the Cariaco Basin (> 10 cm below the SWI), and the Eastern Mediterranean Sea (Sapropel S5) are −1.19 ± 0.32 (1SE), −1.74 ± 0.33 (1SE), and −2.63 ± 0.57 (1SE), respectively (Barling et al., 2001; Weyer et al., 2008; Montoya-Pino et al., 2010, 2011; Arnold et al., 2012; Andersen et al., 2018; Brüske et al., 2020). The ratios yielded from the Black Sea and Cariaco Basin sediments (Brüske et al., 2020) are close to the ratio inferred from Bura-Nakić et al. (2018), whereas the Sapropel S5 of Eastern Mediterranean Sea has a lower ratio (Andersen et al., 2018). These observations suggest that different depositional conditions for each basin can cause different individual $\Delta^{98}Mo : \Delta^{238}U$ ratios. Overall, the local depositional environment (e.g., particulate shuttle, the degree of basin restriction, basin geometry, and dissolved sulfide concentrations) is the major control on the Mo-U isotope data in modern euxinic basins such that the observed negative correlations between the two isotope systems are not related to changes in global ocean redox conditions (Fig. 2.1; Andersen et al., 2018; Bura-Nakić et al., 2018; Brüske et al., 2020).

The Fe-Mn oxide shuttle should also be mentioned because it can significantly influence the $\delta^{98}Mo$ but has little influence on the $\delta^{238}U$ of the sediments (Fig. 2.1; Barling et al., 2001; Weyer et al., 2008; Noordmann et al., 2015; Scholz et al., 2018). For example, the Landsort Deep sediments deposited < 6 cm below the SWI and Gotland Deep sediments deposited > 20 cm below the SWI of the Baltic Sea were strongly affected by the delivery of Fe-Mn oxides to the seafloor during the inflow of oxygenated waters, and have low $\delta^{98}Mo$ of −0.03 ± 0.20‰ (1SD) and −0.15 ± 0.22‰ (1SD), respectively (Noordmann et al., 2015; Scholz et al., 2018). Although the Fe-Mn oxide shuttle also operates in the Cariaco Basin, the influence of the shuttle is weaker because the $\delta^{98}Mo$ (> 0.9‰) of the sediments in the basin are generally higher than that of the Baltic Sea sediments (Arnold et al., 2004; Brüske et al., 2020).

2.3 Samples and analytical methods

We report new U isotope data for 28 samples of late Neoproterozoic to middle Paleozoic ORM formations that were previously measured for Mo isotope compositions and sedimentary Fe speciation (Dahl et al., 2010; Kendall et al., 2015). These samples are from the: ca. 640 Ma Black River Dolomite, ca. 520 Ma Yu'anshan Formation, ca. 500-485 Ma Alum Shale, ca. 465 Ma Almelund Shale, ca. 442 Ma Rastrites Shale, ca. 442 Ma Birkhill Shale, ca. 365 Ma Chattanooga Shale, and ca. 365 Ma New Albany Shale (see Appendix A2 for geological backgrounds). In this study, we also revisit the coupled Mo-U isotope compositions (i.e., measured on the same samples) reported previously for several other ORM formations, including the ca. 372 Ma Kettle Point Formation (Kendall et al., 2020), ca. 442 Ma Tanezzuft Formation (Stockey et al., 2020), ca. 448 Ma Fjäcka Shale (Lu et al., 2017b), ca. 555 Ma Member IV of the Doushantuo Formation (Kendall et al., 2015), ca. 1360 Ma Velkerri Formation (Kendall et al., 2009; Yang et al., 2017), and ca. 2050 Ma Zaonega Formation (Asael et al., 2013). This compilation of new and previously published data is used in our coupled Mo-U isotope mass-balance model (section 2.5.2).

Trace element concentrations and uranium isotope separations were carried out in the clean lab of the Metal Isotope Geochemistry Laboratory at the University of Waterloo. The sample dissolutions and purification of U from the digested sample solutions followed the protocols of Weyer et al. (2008) and Kendall et al. (2013), which are briefly described as follows. A small amount (~100mg) of rock powders were ashed at 550°C for at least 24 hours to remove organic matter. Subsequently, samples were digested by concentrated HF-HNO_3-HCl. Samples were then diluted in 2% HNO_3 and elemental concentrations were measured on an Agilent 8800 triple quadrupole inductively coupled plasma mass spectrometer (QQQ-ICP-MS). The SBC-1 (Brush Creek Shale) and SGR-1b (Eocene Green River Shale) were processed along with the samples to verify instrument accuracy. The Al-normalized enrichment factors (EF) of Mo and U were calculated relative to the post-Archean Australian

Shale (PAAS) (EF = $[metal/Al]_{sample}$ / $[metal/Al]_{PAAS}$). The PAAS values for Al, U, and Mo are 10 wt.%, 3.1 µg/g, and 1.0 µg/g, respectively (Taylor and McLennan, 1985).

A weighted amount of ^{236}U-^{233}U double spike (IRMM-3636) was added to each digested sample solution to correct for instrumental mass bias and any U isotope fractionation during the column chemistry. Eichrom® UTEVA resin was used to separate U from sample-spike solutions. The U isotope compositions were measured on a Thermo Scientific Neptune multi-collector ICP-MS at the W.M. Keck Foundation Laboratory for Environmental Biogeochemistry, School of Earth and Space Exploration, Arizona State University. The U isotope compositions are reported against the CRM145 standard:

$$\delta^{238}U\ (‰) = \left[\frac{\left({}^{238}U/_{235}U\right)_{sample}}{\left({}^{238}U/_{235}U\right)_{CRM145}} - 1\right] \times 1000 \qquad \text{(I)}$$

Three U isotope standards CRM145, CRM129a, and Ricca were measured during the study and have average $\delta^{238}U$ values of 0.00 ± 0.07‰ (2SD, n = 31), −1.69 ± 0.12‰ (2SD, n = 6), and −0.21 ± 0.05‰ (2SD, n = 6), respectively. The measured average $\delta^{238}U$ for the CRM129a and Ricca standards in this study agree with the long-term average $\delta^{238}U$ reported for CRM129a (−1.71 ± 0.09‰, 2SD, n = 237) and Ricca (−0.22 ± 0.07‰, 2SD, n = 243) at Arizona State University (Yang et al., 2017). The 2SD uncertainty of a sample is reported as either the 2SD uncertainty of sample replicate measurements or 0.08‰ (the average long-term 2SD uncertainty of CRM129a and Ricca), whichever is greater. The reference materials SBC-1 and SGR-1b that were processed through chemistry in the same way along with our samples have $\delta^{238}U$ values of −0.20 ± 0.05‰ (2SD, n = 3) and −0.18 ± 0.09‰ (2SD; n = 3), respectively. The measured $\delta^{238}U$ of SBC-1 is identical to the value of −0.24 ± 0.10‰ (2SD, n = 3) reported by Yang et al. (2017) and −0.21 ± 0.04‰ (2SD, n = 3) reported by Rolison et al. (2017), and the measured $\delta^{238}U$ of SGR-1b is indistinguishable from the value of −0.19 ± 0.05‰ (2SD, n = 3) reported by Yang et al. (2017). Three sample duplicates have statistically identical $\delta^{238}U$ values given 2SD uncertainties.

Detrital contamination could affect the bulk Mo and U isotope compositions of the samples. Therefore, authigenic δ^{98}Mo ($\delta^{98}Mo_{auth}$, relative to NIST 3134 = 0.25‰) and δ^{238}U ($\delta^{238}U_{auth}$, relative to CRM 145) are calculated relative to PAAS:

$$\delta^{98}Mo_{auth} = \delta^{98}Mo_{sample} - (Al/Mo)_{sample} \times \frac{\delta^{98}Mo_{PAAS} - \delta^{98}Mo_{sample}}{(Al/Mo)_{PAAS} - (Al/Mo)_{sample}} \quad \text{(II)}$$

$$\delta^{238}U_{auth} = \delta^{238}U_{sample} - (Al/U)_{sample} \times \frac{\delta^{238}U_{PAAS} - \delta^{238}U_{sample}}{(Al/U)_{PAAS} - (Al/U)_{sample}} \quad \text{(III)}$$

The Al (10 wt.%), Mo (1.0 µg/g), and U (3.1 µg/g) concentrations of PAAS are assumed to be the detrital Al, Mo, and U concentrations, respectively (Taylor and McLennan, 1985). The detrital δ^{98}Mo and δ^{238}U endmembers are assumed to be 0.3‰ and –0.3‰, respectively (Weyer et al., 2008; Voegelin et al., 2014; Tissot and Dauphas, 2015; Andersen et al., 2016, 2017; Noordmann et al., 2016; Kendall et al., 2017; Wang et al., 2018).

2.4 Results

The trace metal concentrations and isotope compositions for each ORM sample are shown in Table 2.1. The Neoproterozoic (Cryogenian) Black River Dolomite has an average $\delta^{238}U_{auth}$ of 0.01 ± 0.04‰ (1SD, n = 5). The Cambrian Yu'anshan Formation (520 Ma) and Alum Shale (500 Ma) have similar $\delta^{238}U_{auth}$ values of −0.01 ± 0.07‰ (1SD, n = 5) and −0.01 ± 0.08‰ (1SD, n = 5), respectively. By contrast, the average $\delta^{238}U_{auth}$ of the Ordovician ORM formations is variable: higher $\delta^{238}U_{auth}$ is observed for the 485 Ma Alum Shale (0.15 ± 0.05‰, 1SD, n = 4) and 442 Ma Birkhill Shale & Rastrites Shale (0.05 ± 0.11‰, 1SD, n = 3) whereas lower $\delta^{238}U_{auth}$ is observed for the 465 Ma Almelund Shale (−0.29 ± 0.00‰, 1SD, n = 2). The Devonian New Albany Shale and Chattanooga Shale have an average $\delta^{238}U_{auth}$ of −0.04 ± 0.08‰ (1SD, n = 3).

In order to provide a complete view of the covariation of Mo and U isotope compositions during euxinic ORM deposition, we compiled the coupled Mo-U isotope data from ancient ORM formations in this (number of formations "m" = 8; Table 2.1) and previous studies (m = 6; Table A1; Fig. 2.2; the Zaonega Formation [Asael et al., 2013], upper Velkerri Formation [Kendall et al., 2009; Yang et al., 2017], Doushantuo Formation Member IV

[Kendall et al., 2015], Fjäcka Shale [Lu et al., 2017b], Tanezzuft Formation [Stockey et al., 2020], and Kettle Point Formation [Kendall et al., 2020]). Archean ORM samples are not included in this compilation because oxidative weathering and thus the riverine Mo flux to the oceans was much smaller in the Archean and increased significantly following the Great Oxidation Event (GOE) (e.g., Farquhar et al., 2000; Pavlov and Kasting, 2002; Scott et al., 2008; Bekker and Holland, 2012; Lyons et al., 2014). Samples with Mo EF < 2 or U EF < 2 could have large uncertainties in their authigenic δ^{98}Mo or δ^{238}U values, thus these isotope data (left blank) are not considered in the following discussion (Table A1).

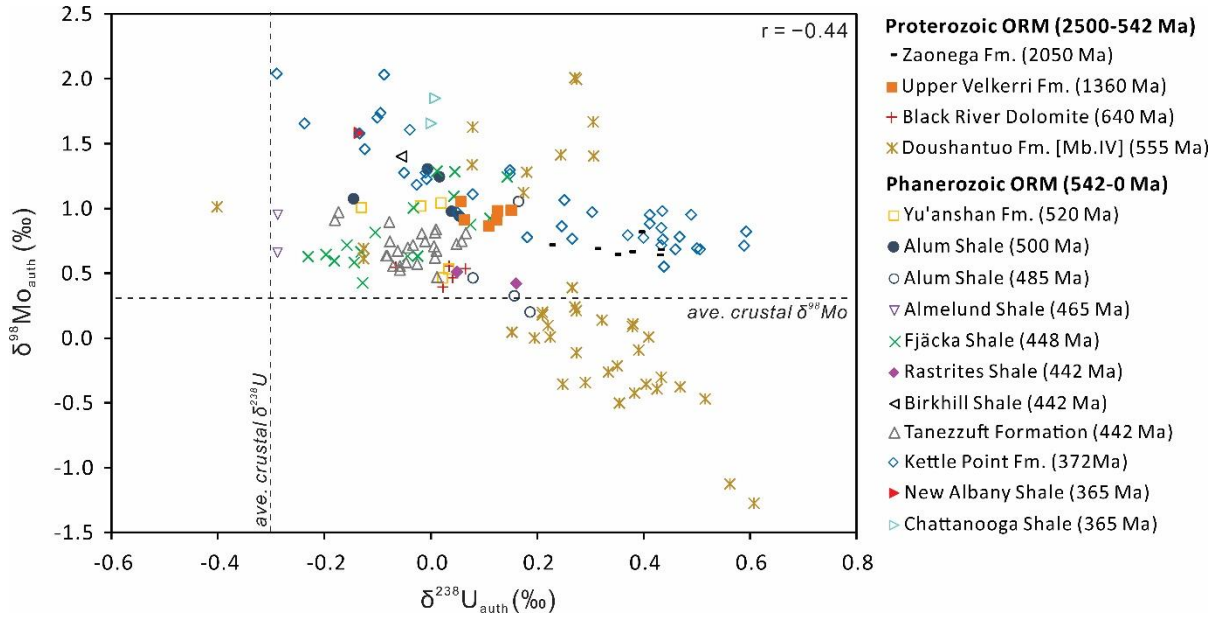

Figure 2.2 Covariations of the Mo and U isotope compositions of the euxinic organic-rich mudrocks from this study and previous publications. Horizontal and vertical dashed lines represent average upper crustal δ^{98}Mo (0.3‰; Voegelin et al., 2014; Willbold and Elliott, 2017) and δ^{238}U (−0.3‰; Andersen et al., 2015; Tissot and Dauphas, 2015), respectively. See Table 2.1 and Table A1 for references.

Table 2.1 Geochemical data for the euxinic ORM samples from eight formations in this study.

Sample [a]	Depth (m)	TOC [b] (wt.%)	Al (wt.%)	Mo (µg/g)	Mo EF [e]	U (µg/g)	U EF [e]	$\delta^{98}Mo$ [c] (‰)	$\delta^{98}Mo_{auth}$ [e] (‰)	2SD measured	n [f]	$\delta^{238}U$ [d] (‰)	$\delta^{238}U_{auth}$ [e] (‰)	2SD measured	n [f]	Fe_{HR}/Fe_T	Fe_{py}/Fe_{HR}
New Albany & Chattanooga Shale, outcrop, USA 365 Ma																	
Clegg 873-B8+22		12.3	6.5	200.1	308.5	57.8	28.7	1.58	1.58	0.18	3	-0.14	-0.13	0.12	3	0.68	0.78
Chattanoga K8/7/94-22		13.6	5.6	236.5	425.0	76.5	44.3	1.65	1.66	0.10	3	-0.01	0.00	0.03	3	0.71	0.80
Chattanoga K8/7/94-23		14.7	5.3	257.9	489.9	81.7	50.1	1.85	1.85	0.13	2	0.00	0.01	0.09	3	0.66	0.70
Birkhill Shale, Dobs Linn outcrop, Scotland 442 Ma																	
DL6	13.3	1.4	6.0	17.7	29.7	8.2	4.4	1.36	1.40	0.17	3	-0.11	-0.06	0.11	3	0.44	0.73
Rastrites Shale, Billegrav-1 core, Sweden 442 Ma																	
BG-4	26.55	2.0	8.4	15.4	18.3	6.7	2.6	0.50	0.51	0.36	3	-0.09	0.05	0.08	3	0.45	0.78
Rastrites Shale, Lönstorp-1 core, Sweden 442 Ma																	
Lön97154	64.9	3.8	8.3	17.8	21.3	8.2	3.2	0.41	0.42	0.08	2	0.01	0.16	0.01	3	0.52	0.74
Lön97154 rep[g]	64.9		8.9	18.0	20.4	7.7	2.8					0.04	0.22	0.07	3		
Lön79002	72.4	1.0	7.8	5.6	7.2	4.3	1.8	0.69	0.75	0.23	2	-0.15		0.01	3	0.42	0.72
Almelund Shale, Albjära-1 core, Sweden 465 Ma																	
Alb79013	50.1	2.1	8.7	5.4	6.3	7.2	2.7	0.85	0.96	0.33	4	-0.29	-0.29	0.04	3	0.36	0.73
Alb79016	94.9	1.9	9.0	4.4	4.9	6.0	2.2	0.58	0.66	0.26	3	-0.29	-0.29	0.03	3	0.90	0.71
Alum Shale Formation, Albjära-1 core, Sweden 485 Ma																	
Alb97160	139.03	4.6	7.8	37.8	48.3	98.9	40.7	1.04	1.05	0.19	3	0.15	0.17	0.12	3	0.93	0.73
Alum Shale Formation, Gislövhammar-2 core, Sweden 485 Ma																	
Gis89934	24.03	7.3	7.6	69.4	91.7	45.9	19.6	0.46	0.46		1	0.06	0.08	0.01	3	0.44	0.71
Gis89933	26	8.7	7.7	132.1	170.9	44.4	18.5									0.55	0.74
Gis89933 rep[g]	26		7.9	136.8	173.5	44.8	18.3	0.20	0.20		1	0.16	0.19	0.04	3		
Gis89931	28	7.3	8.3	119.9	143.7	37.6	14.5	0.33	0.33	0.33	3	0.13	0.16	0.05	3	0.54	0.70

Alum Shale Formation, Andrarum-3 core, Sweden 500 Ma																	
Alum0760	7.6	12.4	7.5	111.1	148.4	132.2	57.0	1.07	1.07	0.09	3	-0.15	-0.14	0.07	3	1.25	0.78
Alum1178	11.78	7.1	7.4	51.2	69.1	28.5	12.4	0.93	0.94	0.17	2	0.03	0.05	0.06	3	1.35	0.75
Alum1200	12	9.1	7.4	60.1	80.8	33.3	14.5	0.97	0.98	0.10	2	0.02	0.04	0.13	4	1.35	0.80
Alum1300	13	9.1	7.3	44.6	61.2	20.6	9.1	1.23	1.24	0.06	2	-0.02	0.02	0.05	3	1.22	0.73
Alum1370	13.7	7.5	7.1	53.4	75.8	18.7	8.6	1.29	1.30	0.06	3	-0.04	-0.01	0.04	3	1.31	0.74
Yu'anshan Formation, Ma'fang core, China, 520 Ma																	
Cheng485	48.5	1.5	7.1	18.6	26.3	14.5	6.6	0.46	0.46	0.34	3	-0.03	0.02	0.08	3	0.51	0.85
Cheng476	47.6	1.3	7.2	7.6	10.6	8.8	4.0	0.51	0.53	0.17	4	-0.05	0.03	0.12	3	0.44	0.89
Cheng456	45.6	1.5	7.2	7.8	10.8	6.8	3.0	0.94	1.01	0.24	4	-0.19	-0.13	0.10	3	0.41	0.83
Cheng442	44.2	2.3	7.1	19.9	28.0	10.9	5.0	0.99	1.01	0.18	5	-0.08	-0.02	0.07	3	0.55	0.89
Cheng438	43.8	2.0	7.0	16.2	23.2	10.8	5.0	1.01	1.04	0.17	3	-0.04	0.02	0.05	3	0.50	0.85
Black River Dolomite, Forest-1 core, Tasmania, 640 Ma																	
RC06-FOR02-B	828.11-828.15	6.5	7.8	31.5	40.5	7.5	3.1	0.53	0.54	0.10	3	-0.05	0.07	0.03	3	0.79	0.93
RC06-FOR02-B rep[g]	828.11-828.15		6.6	26.4	40.2	6.6	3.2					-0.10	-0.01	0.07	3		
RC06-FOR02-D	828.23-828.27	6.6	11.3	43.5	38.5	11.7	3.3	0.55	0.56	0.18	6	-0.07	0.03	0.07	3	0.80	0.93
RC06-FOR02-G	828.37-828.40	6.5	7.1	29.3	41.2	6.9	3.1	0.46	0.46	0.21	6	-0.07	0.04	0.09	3	0.80	0.93
RC06-FOR02-H	828.48-828.50	6.4	6.8	28.6	41.8	6.9	3.2	0.39	0.39	0.10	3	-0.08	0.02	0.03	3	0.90	0.93
RC06-FOR02-H rep[g]	828.48-828.50		6.9	28.9	41.8	7.1	3.3					-0.10	-0.02	0.03	3		
RC06-FOR02-I	828.55 - 828.58	6.8	7.5	27.5	36.6	8.0	3.4	0.54	0.55	0.12	4	-0.13	-0.07	0.07	3	0.81	0.90

[a] Sample depth, Mo isotope data, TOC, and Fe speciation data are from Dahl et al. (2010)
[b] TOC = total organic carbon
[c] Mo isotope data reported relative to NIST SRM 3134 = 0.25‰
[d] U isotope data reported relative to CRM 145
[e] See calculation methods in section 2.3 of the main text
[f] Number of replicate analyses of the same sample solution
[g] rep = replicate samples

Correlation coefficients (r, $-1 \leq r \leq +1$) are calculated to show the relationship between the coupled Mo-U isotope data. We interpret r values between ±0.5 and ±1 as datasets as exhibiting negative (−) or positive (+) correlations between authigenic δ^{98}Mo and δ^{238}U data, whereas no specific correlations if $-0.5 < r < 0.5$. It should be noted that the number of samples in each ORM formation are not equal, thus correlation coefficients could be influenced by an ORM formation if it contains a relatively large number of samples and show specific relationships (e.g., the Doushantuo Formation Member IV). In addition, ORM formations with limited number of samples ($n \leq 5$) do not yield robust correlations even if r is between ±0.5 and ±1 (e.g., the Almelund Shale).

There is an overall lack of correlation between the compiled Mo and U isotope data from these euxinic ORM formations ($r = -0.44$, Fig. 2.2). However, for individual ORM units, the coupled Mo-U isotope data show negative (e.g., the Devonian Kettle Point Formation, $r = -0.88$), positive (e.g., the Ordovician Fjäcka Shale, $r = +0.75$), and no correlations (e.g., the Rhuddadian Tanezzuft Formation [$r = -0.22$], the Paleoproterozoic Zaonega Formation [$r = -0.12$]), suggesting different controlling mechanisms at local and global scales that influenced the preservation of sedimentary Mo and U isotope compositions. The correlation coefficient of the Ediacaran Doushantuo Formation Member IV is −0.54, suggesting an overall negative correlation. However, the Doushantuo samples can be stratigraphically divided into three groups based on different characteristics of the coupled Mo-U isotope data, implying different controls on the Mo and U isotope compositions for each group.

2.5 Discussion

2.5.1 Inferring the seawater Mo and U isotope compositions from the coupled Mo-U isotope data of euxinic sediments

Here, we build upon a method from Dahl et al. (2017b) to estimate potential ranges of seawater Mo and U isotope compositions through the combined use of a coupled Mo-U isotope

mass balance model and covariations of the coupled Mo-U isotope compositions observed in modern euxinic sediments.

2.5.1.1 A coupled Mo and U isotope mass balance model

The coupled Mo-U isotope mass balance model can be used to not only quantitatively constrain the relative proportion of each Mo and U oceanic sink but also to estimate the seawater Mo and U isotope compositions under various global ocean redox conditions, respectively. Assuming a steady state mass-balance for Mo (e.g., Goldberg et al., 2016; Ostrander et al., 2019b) and U (e.g., Andersen et al., 2016; Gilleaudeau et al., 2019) for the modern ocean, the Mo and U input fluxes (F_{IN}) and isotope compositions (δ_{IN}) should be equal to that of the Mo and U outputs (F_{OUT}, δ_{OUT}), respectively:

$$F_{IN} = F_{OUT} \quad \text{(IV)}$$

$$\delta_{IN} \times F_{IN} = \delta_{OUT} \times F_{OUT} \quad \text{(V)}$$

Assuming a three-sink model for Mo (euxinic [EUX], sulfidic at depth [SAD], and oxic [OX] sinks) and a two-sink model for U (euxinic [EUX] and other [OTHER] sinks), the isotope mass balance [equation (V)] can be expressed as:

$$\delta_{OUT} \times F_{OUT} = \sum(\delta_i \times F_i) \quad \text{(VI)}$$

where "i" represents each specific sink for Mo and U. Defining "f" as the burial fraction of the total Mo or U sinks [equation (VII)], the sum of "f_i" is 1 [equation (VIII)] and equation (VI) can be rewritten as equation (IX):

$$f_i = F_i/F_{OUT}\,, (0 \le f_i \le 1) \quad \text{(VII)}$$

$$\sum f_i = 1 \quad \text{(VIII)}$$

$$\delta_{OUT} = \sum(\delta_i \times f_i) \quad \text{(IX)}$$

Further, the isotope composition of each sink i is related to that of the contemporaneous seawater, as shown in equation (X):

$$\delta_{OUT} = \sum[(\delta_{SW} + \Delta_i) \times f_i] \quad \text{(X)}$$

where "δ_{SW}" represents the isotope composition of the seawater, and "Δ_i" represents the net isotopic offset between seawater and each sink i. Combining equations V-X, the Mo and U

isotope composition of seawater can be calculated as shown in equations (XI) and (XII), respectively:

$$\delta^{98}Mo_{SW} = \delta^{98}Mo_{IN} - \Delta^{98}Mo_{OX} - (\Delta^{98}Mo_{EUX} - \Delta^{98}Mo_{OX}) \times f_{Mo\_EUX} - (\Delta^{98}Mo_{SAD} - \Delta^{98}Mo_{OX}) \times f_{Mo\_SAD} \quad \text{(XI)}$$

$$\delta^{238}U_{SW} = \delta^{238}U_{IN} - \Delta^{238}U_{OTHER} - (\Delta^{238}U_{EUX} - \Delta^{238}U_{OTHER}) \times f_{U\_EUX} \quad \text{(XII)}$$

Rivers, groundwaters, and low-temperature seafloor hydrothermal inputs are the sources of Mo to the oceans. The δ^{98}Mo of the overall modern Mo inputs was estimated to be ~0.5‰ (Neely et al., 2018). Here, we use an average δ^{98}Mo of 0.5 ± 0.2‰ for the oceanic Mo inputs, which is similar to the average upper crust (0.3–0.6‰; Voegelin et al., 2014; Willbold and Elliott, 2017). Assigning an average Mo isotopic offset for the euxinic settings is difficult because sediments deposited under strongly and weakly euxinic environments are characterized by different Mo isotope fractionations (see Section 2.1). Here, we tentatively assume an average Mo isotopic offset of 0.5 ± 0.3‰ for euxinic settings (Table 2.2). In the oxic settings, a Mo isotope fractionation of 3.0 ± 0.1‰ is observed and is used in this model (Table 2.2; Siebert et al., 2003; Barling and Anbar, 2004; Wasylenki et al., 2008). The sulfidic at depth sink is used to describe the environment where dissolved sulfide is restricted to the shallow sediment porewaters and either does not occur or rarely occurs in the bottom waters above the SWI (e.g., the Peru continental margin). The SAD sink consists of both the anoxic sink and mildly oxygenated sink, which are characterized by a Mo isotopic offset of ~0.2–0.8‰ and ~0.8–3.0‰, respectively (Poulson et al., 2006; Siebert et al., 2006; Goldberg et al., 2009, 2012; Poulson Brucker et al., 2009; Eroglu et al., 2020). Molybdenum removal to the anoxic sink is more efficient than Mo removal to the mildly oxygenated sink, indicating a dominant role of the anoxic sink for the SAD sink (Poulson Brucker et al., 2009). Therefore, an average Mo isotopic offset of 0.9 ± 0.2‰ is tentatively used for Mo burial in sediments associated with the SAD sink (Poulson et al., 2006; Siebert et al., 2006; Poulson Brucker et al., 2009).

Table 2.2 Parameters used in the Mo and U isotope mass balance models for the modern seawater (see main text for references).

Parameters for the Mo isotope mass balance model		Parameters for the U isotope mass balance model	
δ_{input}	0.5 ± 0.2‰	δ_{input}	−0.29 ± 0.03‰
Δ^{a}_{EUX-SW}	−0.5 ± 0.3‰	Δ_{EUX-SW}	0.60 ± 0.20‰
Δ_{SAD-SW}	−0.9 ± 0.2‰	$\Delta_{OTHER-SW}$	0.05 ± 0.09‰
Δ_{OX-SW}	−3.0 ± 0.1‰	--	--
$f^{b}_{Mo\_EUX}$	5 ± 3%	f_{U_EUX}	9 ± 6%
f_{Mo_SAD}	50 ± 10%	f_{U_OTHER}	91 ± 6%
f_{Mo_OX}	45 ±10%	--	--
Modeled $\delta^{98}Mo_{SW}$	2.33 ± 0.24‰	Modeled $\delta^{238}U_{SW}$	−0.39 ± 0.10‰
Measured $\delta^{98}Mo_{SW}$	2.34 ± 0.10‰	Measured $\delta^{238}U_{SW}$	−0.39 ± 0.04‰

[a] Δ = the net Mo and U isotopic offsets between each sink and seawater

[b] f = the fractions of Mo and U removal into each sink

By using the parameters above, euxinic settings should approximately account for less than 8% of total Mo removal to achieve the modern global seawater Mo isotope composition of 2.34‰. Otherwise, the modern seawater Mo isotope composition can only be achieved by increasing Mo removal to the oxic and euxinic sinks while decreasing Mo removal into the SAD sink, which is unrealistic because the intermediate SAD sink should generally expand along with the expansion of the euxinic sink. Here, 45 ± 10%, 50 ± 10%, and 5 ± 3% of total Mo removal in the modern ocean is used for the oxic, SAD, and euxinic sinks, respectively. These values are generally consistent with estimates from previous studies (Siebert et al., 2003; Scott et al., 2008; Poulson Brucker et al., 2009; Kendall et al., 2009, 2017; Dahl et al., 2011; Reinhard et al., 2013; Chen et al., 2015). Therefore, applying these parameters (Table 2.2) in equation (XI), the predicted modern seawater Mo isotope composition is 2.33 ± 0.24‰, which

is identical to the measured seawater Mo isotope composition of 2.34 ± 0.10‰ (Barling et al., 2001; Nakagawa et al., 2012; Nägler et al., 2014).

The riverine input is the major U source to the oceans and has an average $\delta^{238}U$ value between −0.34‰ and −0.24‰ that is similar to the average upper crust (Dunk et al., 2002; Tissot and Dauphas, 2015; Andersen et al., 2016, 2017; Noordmann et al., 2016; Wang et al., 2018). Therefore, we use an average $\delta^{238}U$ of −0.29 ± 0.03‰ for the U input. Several factors influence U reduction and removal such that variable U isotope fractionations between sediments and bottom waters are observed in modern euxinic settings (see Section 2.2; Andersen et al., 2014, 2017; Holmden et al., 2015; Noordmann et al., 2015; Rolison et al., 2017; Bura-Nakić et al., 2018; Brüske et al., 2020). We tentatively use 0.60 ± 0.20‰ as the U isotopic offset for the euxinic sink because this value is generally consistent with modern euxinic basins (Holmden et al., 2015; Noordmann et al., 2015; Rolison et al., 2017; Bura-Nakić et al., 2018; Brüske et al., 2020). The "other sink" comprises several sinks, including other reducing environments (suboxic settings, anoxic/ferruginous settings, carbonates with dissolved sulfide in sediment pore fluids, biogenic carbonates, oceanic crust altered by high- and low-temperature hydrothermal fluids, and oxic sediments) (Table 2.3; Tissot and Dauphas, 2015; Andersen et al., 2016, 2017; Noordmann et al., 2016; Wang et al., 2016; Cole et al., 2020). According to the relative fraction of U removal into each sink (Table 2.3), an overall weighted U isotopic offset of 0.05 ± 0.09‰ is calculated for the other sink [OTHER], which agrees with previous studies (Weyer et al., 2008; Montoya-Pino et al., 2010; Andersen et al., 2016; Wang et al., 2016; Dahl et al., 2017b; Yang et al., 2017; Zhang et al., 2018; Gilleaudeau et al., 2019; Stockey et al., 2020).

Table 2.3 Fractions of U burial and corresponding isotope fractionations of each U sink in the modern seawater.

Sinks		Fraction of U burial flux into each sink (%)	Fractionation factors [$\Delta_{sink\text{-}SW}$ (‰)]	References
Euxinic		9 ± 6	0.60 ± 0.20	1-6
Other reducing (Ferruginous sediments*)		40 ± 10	0.15 ± 0.16	1,3,6-11
Bio-carbonate		30 ± 10	0.01 ± 0.13	1,3,7,12,13
Hydrothermal alteration of crust	High-T	3 ± 3	0.00 ± 0.02	1,14-17
	Low-T	6 ± 6	0.25 ± 0.02	1,14-17
Oxic sediments		12 ± 6	−0.25	1,6,15-18
Weighted average of OTHER sink			0.05 ± 0.09%	

References: 1. Dunk et al. (2002); 2. Andersen et al. (2014); 3. Andersen et al. (2017); 4. Holmden et al. (2015); 5. Bura-Nakić et al. (2018); 6. Weyer et al. (2008); 7. Romaniello et al. (2013); 8. Andersen et al. (2016); 9. Chen et al. (2018a); 10. Tissot et al. (2018); 11. Noordmann et al. (2016); 12. Partin et al. (2013); 13. Chen et al. (2018b); 14. Andersen et al. (2015); 15. Barnes and Cochran (1990); 16. Morford and Emerson (1999); 17. Tissot and Dauphas (2015); 18. Cole et al. (2020);

* Ferruginous setting is not well understood.

Using the above parameters, the modern seawater $\delta^{238}U$ of −0.39‰ can be achieved when the euxinic and other sinks comprise 9% and 91% of U removal, respectively. These values are consistent with previous estimates of 5–25% for the euxinic sink and 75–95% for the other sink (Barnes and Cochran, 1990; Morford and Emerson, 1999; Dunk et al., 2002; Tissot and Dauphas, 2015; Andersen et al., 2016). Here, we use 9 ± 6% of U removal for the euxinic sinks and 91 ± 6% for the other sinks (Table 2.2). Applying these values in equation (XII), the modeled modern seawater has a $\delta^{238}U$ of −0.39 ± 0.10‰ (Table 2.2), which is in good agreement with the measured $\delta^{238}U$ of modern seawater (−0.39 ± 0.04‰; Weyer et al., 2008; Tissot and Dauphas, 2015; Andersen et al., 2016, 2017; Noordmann et al., 2016).

In order to couple the Mo and U isotope mass balance models, we assume that there is a general correlation between the Mo and U euxinic burial fractions (Dahl et al., 2017b), which can be described as:

$$f_{Mo\_EUX} = {f_{U\_EUX}}^{\gamma} \quad \text{(XIII)}$$

Two end-member criteria should be fulfilled for the above equation: 1) if $f_{Mo\_EUX} = 0$, then $f_{U\_EUX} = 0$; 2) if $f_{Mo\_EUX} = 1$, then $f_{U\_EUX} = 1$. Here, $\gamma = 1.24 \pm 0.38$ is calculated using 5 ± 3% and 9 ± 6% as the euxinic burial fraction of Mo and U in the modern ocean, respectively (Table 2.2; see Fig. A1 for sensitivity analysis). This is identical to the previously reported value of 1.34 ± 0.38 by Dahl et al. (2017b), who assumed the fractions of anoxic Mo and U removal in the modern ocean are 6–15% and 12–25%, respectively. Combining equations (XI)-(XIII), the covariations of the seawater Mo and U isotope compositions under various redox conditions are shown in Figure 2.3a. Each black dot in Figure 2.3a represent specific seawater Mo and U isotope compositions that correspond to specific fractions of U removal into the euxinic sink (vertical black dashed lines) and Mo removal into the SAD sink (curved colorful lines).

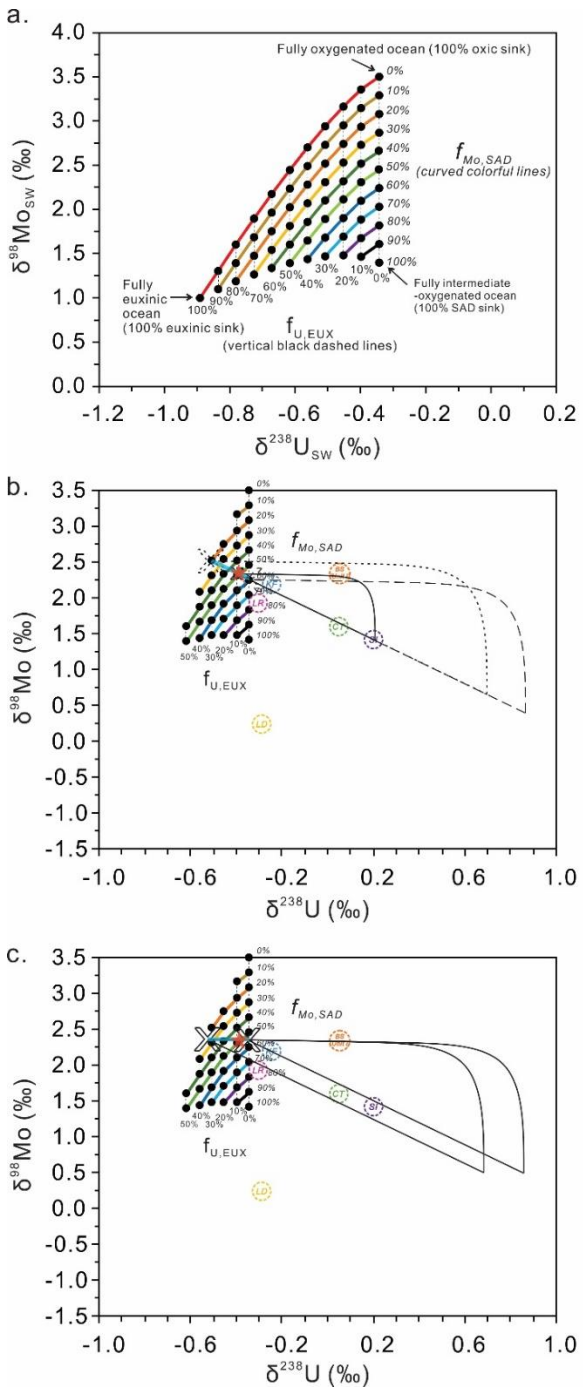

Figure 2.3 a) The modeled seawater (SW) Mo and U isotope compositions under different redox conditions from a coupled Mo-U isotope mass balance model (see Section 2.5.1.1). The

points on the same vertical black dashed lines have the same euxinic U burial fractions. The euxinic U burial fraction is 100% for the leftmost sample ($f_{U\_EUX} = f_{Mo\_EUX} = 1$) and decreases by 10% for each point towards its right (i.e. 90%, 80%, 70%, etc.). The curved colorful lines connect points that have the same SAD Mo burial fractions. The SAD Mo burial fraction is 100% for the lower right sample ($f_{Mo\_SAD} = 1$, $f_{U\_EUX} = 0$) and decreases by 10% for each line radiating outwards (i.e., 90%, 80%, 70%, etc.). b) Estimated potential ranges of modern seawater Mo and U isotope compositions (highlighted blue line) using samples deposited in modern euxinic basins (except the severely restricted Black Sea). Unrealistic solutions (e.g., EUX > SAD for Mo removal) of modern seawater are excluded. Data points of sediments are the averaged authigenic $\delta^{98}Mo$ and $\delta^{238}U$ for modern euxinic basins (see Fig. 2.1 and references therein). Solid curve is from Bura-Nakić et al. (2018) and has a $\Delta^{98}Mo : \Delta^{238}U \approx -3 : 2$, $\Delta^{98}Mo \approx 0.9‰$, and $\Delta^{238}U \approx 0.6‰$. The dotted and dashed curves have the same $\Delta^{98}Mo : \Delta^{238}U$ ratios ($-3 : 2$) but $\Delta^{98}Mo = 1.8‰$ and $\Delta^{238}U = 1.2‰$, covering possible seawater-sediment U isotopic offsets up to the intrinsic U isotope fractionation factor of 1.2‰ associated with U^{6+} reduction. c) Estimated potential ranges of modern seawater Mo and U isotope compositions (highlighted blue line) using samples deposited under strong basin restrictions (the Black Sea). Unrealistic solutions (e.g., EUX > SAD for Mo removal) are excluded. The solid curves move horizontally to estimate the modern seawater isotope compositions (see Section 2.5.1.2 for details).

2.5.1.2 Estimating the modern seawater Mo and U isotope compositions from the coupled Mo-U isotope mass balance model

The estimation of modern seawater Mo and U isotope compositions here is based on the coupled Mo-U isotope data from modern euxinic settings and the coupled Mo-U isotope mass balance model. Although an effective U isotope fractionation of ~0.6‰ has been proposed for euxinic settings (e.g., Andersen et al., 2014; Bura-Nakić et al., 2018; Brüske et al., 2020), several factors could influence the effective U isotope fractionations and the full range of intrinsic U isotope fractionations is still uncertain (see Section 2.2). Here, we tentatively use 1.2‰ as the intrinsic U isotope fractionation during U^{6+} reduction in euxinic

settings (see Section 2.2) because this value is generally consistent with theoretical ab initio modeling calculations (Abe et al., 2008) and laboratory experiments (Stirling et al., 2015; Stylo et al., 2015; Brown et al., 2018). Assuming the inverse correlation between Mo and U isotope compositions in modern euxinic settings ($\Delta^{98}Mo : \Delta^{238}U \approx -3 : 2$; Bura-Nakić et al., 2018) is still effective at the full range of intrinsic U isotope fractionation of 1.2‰, the corresponding range of Mo isotope fractionation would be 1.8‰. We acknowledge that this linear relationship is not confirmed by experiments and needs further studies.

This linear relationship is used to account for variable U isotope fractionations between open ocean seawater and euxinic sediments caused by local depositional environments (e.g., dotted and dashed lines in Fig. 2.3b; see Section 2.2). For the curve, symbol "X" represents the best estimate of modern seawater Mo and U isotope compositions. The regression line with a negative slope is defined by Mo-U isotope data from euxinic basins without severe restriction from the open ocean, whereas the line that intersects the Black Sea sediments represents the case of strong basin restriction (Fig. 2.3b and 2.3c).

Our approach for estimating the $\delta^{98}Mo$ and $\delta^{238}U$ of modern seawater is to extrapolate the curve inferred from modern euxinic environments (Bura-Nakić et al., 2018) to the coupled Mo-U isotope mass balance model solutions, in which unrealistic solutions for the modern ocean (e.g., Mo removal in EUX is larger than SAD) are excluded (Fig. 2.3b). Two scenarios are applicable here: samples deposited in non- or weakly-restricted basins vs strongly restricted basins. Using the Mo-U isotope data of sediments deposited with no severe basin restrictions and no significant influence of the Fe-Mn particulate shuttle (e.g., the Cariaco Basin), the symbol "X" of the dotted and dashed curves should be moved along the negative regression line to reach the model solution space. The dotted and dashed curves represent maximum and minimum U isotope fractionations, respectively (Fig. 2.3b). Therefore, the modern seawater Mo and U isotope compositions are estimated to be 2.25‰ to 2.55‰ and −0.51‰ to −0.34‰, respectively (Fig. 2.3b). On the other hand, if there was strong basin restriction during sediment deposition (e.g., Black Sea Unit I), the euxinic sediments potentially have seawater-like Mo isotope compositions and the curve should be moved horizontally to reach the model solution

space (solid curves in Fig. 2.3c; Bura-Nakić et al., 2018). In this case, the modern seawater is estimated to have δ^{98}Mo of ~2.37‰ and δ^{238}U from −0.50‰ to −0.34‰. The estimated δ^{98}Mo and δ^{238}U of modern seawater from both cases are similar to the measured δ^{98}Mo (2.34 ± 0.10‰) and δ^{238}U (−0.39 ± 0.04‰) values of modern seawater, respectively (Barling et al., 2001; Weyer et al., 2008; Nakagawa et al., 2012; Nägler et al., 2014; Tissot and Dauphas, 2015; Andersen et al., 2016; Noordmann et al., 2016; Bura-Nakić et al., 2018).

2.5.1.3 Estimating the ancient seawater Mo and U isotope compositions based on euxinic ORMs from the coupled Mo-U isotope mass balance model

To reconstruct ancient seawater Mo and U isotope compositions, there are a few assumptions for the use of the coupled Mo-U isotope mass balance model. We assume that: 1) steady state conditions were achieved during ancient ORM deposition, particularly for a long period of geologic time and not perturbed by post-depositional processes; 2) the post-Archean Mo and U oceanic inputs have similar δ^{98}Mo (0.5 ± 0.2‰) and δ^{238}U (−0.29 ± 0.03‰) values as today; 3) the magnitudes of net Mo and U isotopic difference between each defined sink and coeval seawater are similar to those observed in modern observations; 4) the relationship between Mo and U isotope compositions of ancient euxinic ORM are similar to that inferred from multiple modern euxinic basins, though inverse Mo-U isotope correlations can have slopes that are different in the individual basins.

Applying the coupled Mo-U isotope mass balance model to ancient euxinic ORMs needs to be discussed in two cases: ORMs (not affected by a Fe-Mn oxide shuttle) deposited in non- or weakly-restricted basins (Fig. 2.4a) vs strongly restricted basin (Fig. 2.4b). Before interpreting the coupled Mo-U isotope data, the local depositional environment should be carefully evaluated. For the conceptual illustrations shown in Figure 2.4, it is assumed that the ORMs were deposited under euxinic conditions and were not significantly affected by a particulate Fe-Mn oxide shuttle. If the ORMs were deposited when basin restriction was not severe, then the negative regression line (curve 1 and 2) should be placed at sample A (the lowest $\Delta^{238}U/\Delta^{98}Mo$ ratio) and then extrapolated to solution boundaries (yellow area, Fig.

2.4a). Curve 1 and 2 represent the minimum and maximum isotope fractionations from coeval seawater, respectively (Fig. 2.4a). The U isotopic offset between samples and the best estimate for seawater $\delta^{238}U$ (symbol "X") should be within the range of the intrinsic U isotope fractionation for euxinic settings (1.2‰). Curve 3 is by moving curve 2 up vertically and stopping at where the negative regression line crosses the sample B (the highest $\Delta^{238}U/\Delta^{98}Mo$ ratio) (Fig. 2.4a). This movement ensures that all samples are bracketed between the two negative regression lines and the U isotopic offsets between the samples and seawater are within 1.2‰. The model solution space (highlighted area) encompassed between the two negative regression lines represents the potential range of contemporaneous seawater Mo and U isotope compositions during ORM deposition. Because the highest $\delta^{98}Mo$ from a set of euxinic samples from the same formation represents the most conservative estimate of seawater Mo isotope composition (white dotted horizontal line), in this case, the upper highlighted blue area (above the white dotted line) in Figure 2.4a represents the potential range of coeval seawater isotope compositions. For the ORMs deposited in strongly restricted basins, assuming there was no variation in seawater $\delta^{98}Mo$ during deposition, only the sample with the highest $\delta^{98}Mo$ is used because this $\delta^{98}Mo$ value likely approached the coeval seawater Mo isotope composition (Fig. 2.4b). Therefore, curve 1' is moved laterally to curve 2' and the best estimate of the seawater U isotope composition is between the "X" symbols of both curves (Fig. 2.4b). However, with a data distribution that is shown in Figure 2.4b, it is not possible to know if seawater $\delta^{98}Mo$ was constant or variable because a combination of local and global changes could cause a scattered data distribution. For simplicity, only curve 1 and 3 in Figure 2.4a and curve 2' in Figure 2.4b (assuming there were no seawater $\delta^{98}Mo$ variations during deposition) are used for weak and strong basin restrictions, respectively, when discussing application of the model to ancient ORM.

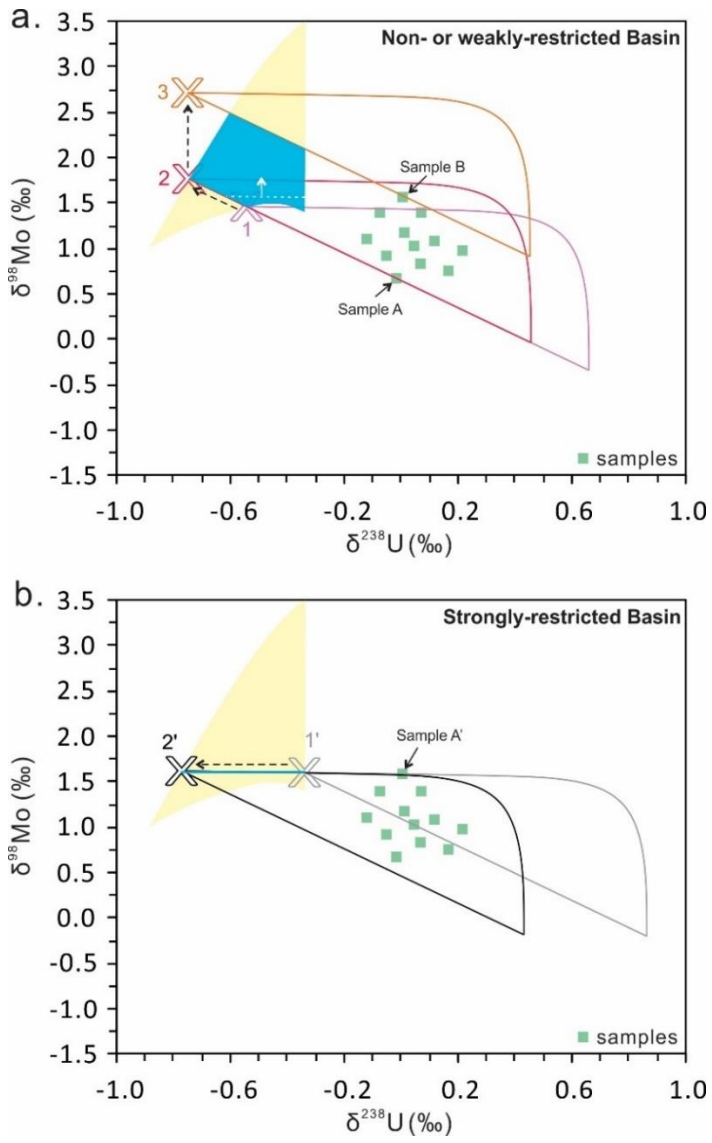

Figure 2.4 Illustration of the reconstruction of ancient seawater Mo and U isotope compositions based on coupled Mo-U isotope data of euxinic ORMs assuming deposition under a) non- or weakly-restricted basins and b) strongly-restricted basins. Yellow area represents the model solutions of seawater Mo and U isotope compositions and blue area represents the estimated seawater Mo and U isotope compositions using the proposed approach (see Section 2.5.1.3 for details). The curves (1, 2, 3 in a and 1', 2' in b) have the same $\Delta^{98}Mo$: $\Delta^{238}U$ ratios (−3 : 2) and $\Delta^{98}Mo$ = 1.8‰ and $\Delta^{238}U$ = 1.2‰.

2.5.2 Covariations of Mo and U isotope compositions in the individual ancient euxinic ORM units: Influence of local depositional environment versus global ocean redox conditions

Although there is no overall correlation between δ^{98}Mo and δ^{238}U of the compiled euxinic ORM formations ($r = -0.44$), the individual euxinic ORM units exhibit various patterns of coupled Mo and U isotope compositions: a negative correlation for the Devonian Kettle Point Formation ($r = -0.88$; Kendall et al., 2020), a positive correlation for the Ordovician Fjäcka Shale ($r = 0.75$; Lu et al., 2017b), and no or weak correlations for the other ORM units (e.g., the Rhuddadian Tanezzuft Formation [$r = -0.22$; Stockey et al., 2020], the Paleoproterozoic Zaonega Formation [$r = -0.12$; Asael et al., 2013], the Ediacaran Doushantuo Formation Member IV [$r = -0.54$; Kendall et al., 2015]). To decipher global ocean redox conditions using the sedimentary Mo and U isotope compositions of ORMs, the local depositional environment needs to be analyzed and understood (e.g., Dahl et al., 2010; Scholz et al., 2013, 2018; Andersen et al., 2014, 2017; Noordmann et al., 2015; Kendall et al., 2015, 2017, 2020; Rolison et al., 2017; Bura-Nakic et al., 2018; Ostrander et al., 2019a; Brüske et al., 2020). Here, the geochemical data, including the Mo/TOC ratios, Mo/U EF ratios, and Fe speciation, together with geological background (e.g., paleogeographic maps), are used to interpret the local depositional environment of ORM formations from this ($n = 8$; Dahl et al., 2010) and previous studies ($n = 6$; Kendall et al., 2009, 2015, 2020; Asael et al., 2013; Lu et al., 2017b; Yang et al., 2017; Stockey et al., 2020).

The local bottom water redox condition can be inferred from sedimentary Fe speciation (Poulton and Raiswell, 2002; Poulton and Canfield, 2005, 2011; Canfield et al., 2007; Planavsky et al., 2011; Raiswell et al., 2018). Highly reactive Fe (Fe_{HR}) consists of pyrite Fe (Fe_{py}) as well as the carbonate Fe (Fe_{carb}), ferric oxide Fe (Fe_{ox}), and magnetite Fe (Fe_{mag}) that could react with sulfide during deposition and early diagenesis (Poulton and Canfield, 2005, 2011; Raiswell et al., 2018). The ratio of highly reactive Fe over total Fe (Fe_T) can be used to indicate anoxic ($Fe_{HR}/Fe_T > 0.38$) or oxic ($Fe_{HR}/Fe_T < 0.22$) water columns (Poulton and

Canfield, 2011; Raiswell et al., 2018). The Fe_{HR}/Fe_T ratios between 0.22 and 0.38 represent an ambiguous zone of bottom water redox environment. In anoxic bottom waters, the ratio of pyrite Fe over total Fe can further distinguish euxinic (Fe_{py}/Fe_{HR} > 0.7–0.8) and ferruginous (Fe_{py}/Fe_{HR} < 0.7–0.8) conditions (Poulton and Canfield, 2011; Raiswell et al., 2018).

The Mo/TOC ratios of modern euxinic sediments are suggested to mimic aqueous Mo concentrations in the bottom waters and reflect the rate of bottom water renewal by open-ocean seawater (Algeo and Lyons, 2006). In the modern anoxic basins, euxinic sediments from the strongly restricted Black Sea, the moderately restricted Framvaren Fjord, the less restricted Cariaco Basin, and the relatively open Saanich Inlet have average Mo/TOC ratios of 4.5 μg/g/wt.%, 9 μg/g/wt.%, 25 μg/g/wt.%, and 45 μg/g/wt.%, respectively (Algeo and Lyons, 2006). Therefore, the comparison of sedimentary Mo/TOC between ancient ORM and modern basins can be used to indicate the degree of basin restriction. However, other factors complicate the use of sedimentary Mo/TOC as a tracer of basin restriction, such as global ocean redox conditions, sedimentation rates, and thermal maturity (e.g., Algeo and Lyons, 2006; Scott et al., 2008; Ardakani et al., 2016; Dickson et al., 2020). For example, a fast sedimentation rate could dilute Mo concentrations in euxinic sediments and cause lower Mo/TOC ratios, thus leading to an incorrect interpretation of a more restricted depositional environment (Sageman and Lyons, 2003). Less oxygenated ancient oceans could have a smaller Mo reservoir than the well-oxygenated modern ocean such that the deposited ORMs contain lower Mo/TOC ratios without basin restriction (Scott et al., 2008; Asael et al., 2013). The maturation of ORM could cause the loss of TOC, thus leading to an increase of Mo/TOC ratios (Dickson et al., 2020) and scattered Mo-TOC relationships on a cross plot of Mo vs TOC (Ardakani et al., 2016).

The patterns of Mo and U enrichments in sediments can be used to infer the local depositional environment due to the different removal mechanisms of the two metals (Algeo and Tribovillard, 2009). The efficiency of Mo removal to sediments is influenced by the amount of hydrogen sulfide ($[H_2S]_{aq}$) in the water column and the operation of a particulate Fe-Mn oxyhydroxide shuttle (Helz et al., 1996, 2011; Morford and Emerson, 1999; McManus et al., 2006; Algeo and Tribovillard, 2009). In contrast, the efficiency of U removal to

sediments is less dependent on dissolved H_2S availability and is more associated with abiotic/biotic reduction and the diffusive-reactive process below the SWI (Anderson, 1989; Barnes and Cochran, 1990; Dunk et al., 2002; McManus et al., 2006; Algeo and Tribovillard, 2009). Therefore, the covariations of Al-normalized Mo and U EF can be used to infer the importance of the Fe-Mn particulate shuttle, bottom water redox conditions, and hydrographic controls on metal enrichment in ORM (Algeo and Tribovillard, 2009). However, the early and middle Proterozoic ORMs have relatively low U concentrations because of dominantly anoxic deep oceans and widespread U removal into anoxic (both euxinic and ferruginous) sediments (Partin et al., 2013). By contrast, Mo removal is mainly associated with the euxinic waters. Therefore, those euxinic ORM could have overall less enrichments of Mo and U but still high Mo/U ratios, which can be incorrectly interpreted as the effect of the particulate shuttle.

After determining the local depositional environment, the contemporaneous ancient seawater Mo and U isotope compositions during ORM deposition can be estimated based on the coupled δ^{98}Mo-δ^{238}U data of each ORM unit. Applying the curve to fully cover the coupled δ^{98}Mo-δ^{238}U data points of each ORM, the potential ranges of the coeval seawater Mo and U isotope compositions can be revealed by the coupled Mo-U isotope mass balance model (see Section 2.5.1.3).

2.5.2.1 Negative correlation between δ^{98}Mo and δ^{238}U: The Kettle Point Formation

The Devonian Kettle Point Formation was deposited in the Appalachian Foreland Basin of an epeiric sea during the Acadian Orogeny (Hamblin, 2010). It is preserved in the "Chatham Sag", which is a structural depression between the Appalachian Basin and Michigan Basin (Hamblin, 2010). The Kettle Point Formation is informally subdivided into units 1 to 4 from the stratigraphic bottom to the top of the formation. Interbedded organic-rich and poor mudstones are found in units 1 and 3 and more uniform intervals of organic-rich mudstones are found in units 2 and 4 (Bingham-Kozlowski et al., 2016). The samples have an average Mo/TOC ratio of 16.1 ± 8.1 μg/g/wt.% (1SD) that is between the Framvaren Fjord (~9 μg/g/wt.%) and the Cariaco Basin (~25 μg/g/wt.%) (Fig. 2.5a; Algeo and Lyons, 2006). High

Mo/U EF ratios, together with high Mo and U enrichments (Mo EF: 51.5–644.1, U EF: 3.4–26.7; Fig. 2.5b), suggest a relatively good connection between open-ocean seawater and the local waterbody during the deposition of the Kettle Point Formation (Table A1; Kendall et al., 2020). Although there are no Fe speciation data available, a euxinic depositional environment is indicated by the consistently high Mo/U EF ratios that are three times the modern seawater Mo/U ratio (Algeo and Tribovillard, 2009). In addition, upper unit 4 samples with vanadium EF > 5 may reflect the operation of the Fe-Mn oxide shuttle that is associated with the brackish conditions during deposition (Table A1; Kendall et al., 2020).

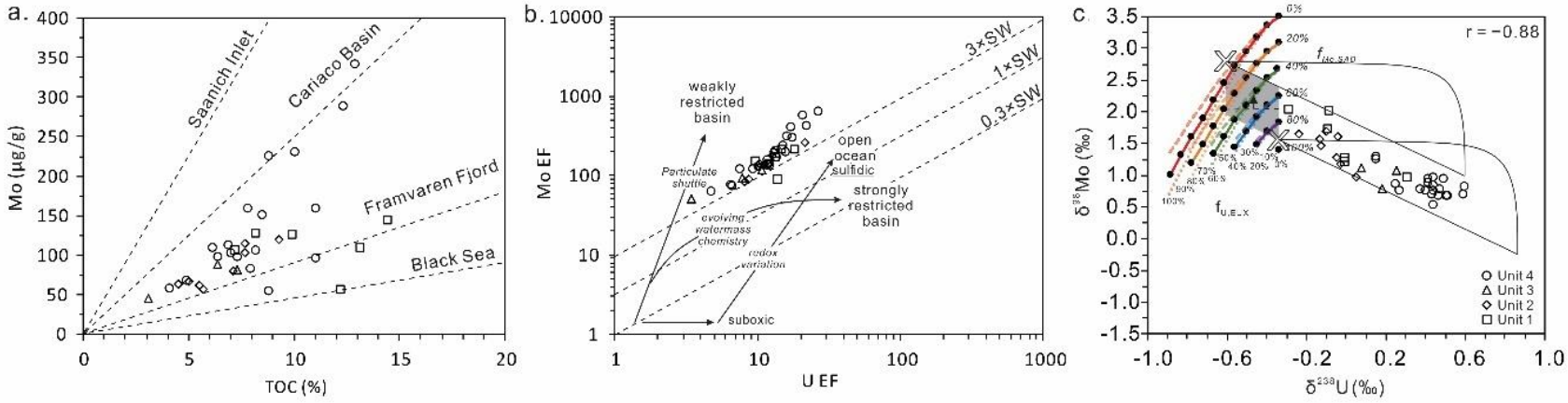

Figure 2.5 Geochemical data of the Devonian Kettle Point Formation showing a) Mo vs TOC, b) Mo EF vs U EF, and c) δ^{98}Mo vs δ^{238}U (Table A1; Kendall et al., 2020). Dashed lines in a) represent regression slopes for four modern basins from Algeo and Lyons (2006) (Black Sea: 4.5 ± 1; Framvaren Fjord: 9 ± 2; Cariaco Basin: 25 ± 5; Saanich Inlet: 45 ± 5; in µg/g/wt.%). Dashed lines in b) represent the Mo/U ratios of modern seawater (1 × SW; Algeo and Tribovillard, 2009), and fractions of modern seawater (0.3 × SW and 3 × SW). The covariations of Mo and U enrichments and controlling mechanisms in b) are plotted following Algeo and Tribovillard (2009). Shaded area in c) represents the estimated ranges of coeval seawater Mo and U isotope compositions. Authigenic δ^{98}Mo and δ^{238}U data of euxinic samples are used. The dashed and dotted lines represent a Mo isotopic offset of −0.8‰ and −0.2‰ between the euxinic sink and seawater, respectively, by keeping all other parameters unchanged. This approach is applied to the following figures (Fig. 2.6-2.10).

The coupled Mo-U isotope data of the Kettle Point Formation ORM show a negative correlation ($r = -0.88$) with a slope of -1.36 ± 0.12 (1SE), which is similar to the proposed negative regression line (a slope of −1.5) based on modern environments (Fig. 2.5c; Bura-Nakić et al., 2018). This observation indicates that changes in local depositional factors (e.g., bottom water sulfide concentrations) influenced the Mo and U isotope compositions of these ORM at a time of relatively stable global seawater redox conditions (Kendall et al., 2020). Upper unit 4 samples that are potentially affected by the Fe-Mn particulate shuttle show a general horizontal trend (relatively invariable δ^{98}Mo and variable δ^{238}U) with a slope of -0.23 ± 0.31 (1SE). However, the influence of a particulate shuttle on the observed low δ^{98}Mo (0.79 ± 0.11‰) of upper unit 4 may not be that significant because the Landsort Deep (-0.03 ± 0.20‰, 1SD; sediments deposited < 6 cm below the SWI) and Gotland Deep sediments (-0.15 ± 0.22‰, 1SD; sediments deposited > 20 cm below the SWI) that are significantly affected by the particulate shuttle have lower Mo isotope compositions (Noordmann et al., 2015; Scholz et al., 2018). In addition, there is no vertical jump of δ^{98}Mo between the upper unit 4 and units 1–3 & lower unit 4, implying that the particulate shuttle does not significantly alter the sedimentary δ^{98}Mo record. Therefore, it is possible that relatively lower and constant bottom water sulfide concentrations associated with increased mixing with fresh waters (brackish conditions) led to a relatively constant Mo isotopic offset between sediment and seawater during upper unit 4 deposition. At the same time, the variable δ^{238}U values of the same samples indicate that the U isotope fractionations are influenced by several other factors such as the aqueous U species and the rates of U reduction and removal (Andersen et al., 2014, 2017; Rolison et al., 2017; Kendall et al., 2020). By contrast, units 1–3 and lower unit 4 samples show a negative correlation between the Mo and U isotope compositions with a slope of -1.78 ± 0.33 (1SE) that is similar to the modern Cariaco Basin (-1.74 ± 0.33, 1SE; Brüske et al., 2020). Dissolved sulfide levels in the bottom waters likely control the efficiency of Mo and U removal into sediments, thus resulting in the observed negative correlation between the Mo and U isotope compositions (Kendall et al., 2020).

The Kettle Point Formation samples are used to estimate the ancient seawater Mo and U isotope compositions during ORM deposition by extrapolating the inverse correlation to the coupled Mo-U isotope mass balance model solution space. Applying our proposed method to all samples, the best estimate of coeval seawater Mo and U isotope compositions during ORM deposition is 2.04‰ to 2.75‰ and −0.61‰ to −0.34‰, respectively (Fig. 2.5c). Similar seawater isotope compositions (δ^{98}Mo: 2.04‰ to 2.75‰, δ^{238}U: −0.70‰ to −0.34‰) are obtained if only units 1–3 and lower unit 4 samples are used. Our predictions are consistent with the estimations (δ^{98}Mo ≥ 2.0‰, δ^{238}U ≤ −0.3‰) from Kendall et al. (2020), which are suggestive of a generally oxygenated global ocean during deposition of the largely Famennian Kettle Point Formation. This interpretation is also consistent with the proposed increase in atmosphere-ocean oxygenation during the Devonian (Dahl et al., 2010; Wallace et al., 2017; Lu et al., 2018).

2.5.2.2 Positive correlation between δ^{98}Mo and δ^{238}U: The Fjäcka Shale

The Fjäcka Shale is preserved in the Siljan Ring area of central Sweden and was deposited on the margin of the Baltica continent, which was at the equator during the (Katian) Late Ordovician (Cocks and Torsvik, 2005). The Mo/TOC ratios of the Fjäcka Shale (13.2 ± 10.8 μg/g/wt.%, 1SD) are generally between that of the Black Sea (~4.5 μg/g/wt.%) and Cariaco Basin (~25 μg/g/wt.%) (Fig. 2.6a; Table A1; Lu et al., 2017b). A relatively smaller oceanic Mo reservoir in a less oxygenated Katian world compared to today likely resulted in overall lower Mo/TOC ratios of Katian ORM compared to modern euxinic sediments (Lu et al., 2017b). Therefore, the depositional environment of the Fjäcka Shale is probably no more than moderately restricted, which is in line with high Mo and U enrichments (Mo EF: 14.1–226.9, U EF: 6.2–10.4; Lu et al., 2017b). Euxinic bottom water redox conditions during Fjäcka Shale deposition are inferred from the Fe speciation data, which agrees with the high Mo/U EF ratios (Fig. 2.6b; Table A1; Lu et al., 2017b).

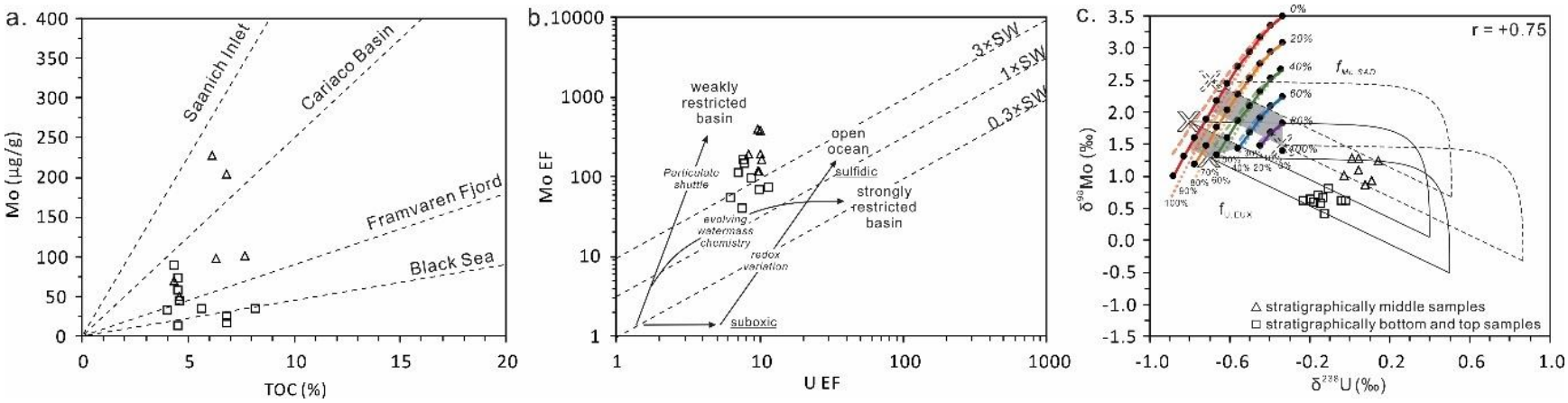

Figure 2.6 Geochemical data of the Ordovician Fjäcka Shale showing a) Mo vs TOC, b) Mo EF vs U EF, and c) δ^{98}Mo vs δ^{238}U (Table A1; Lu et al., 2017b). The dotted and solid lines in c) are used to estimate ancient seawater isotope compositions for stratigraphically middle samples and stratigraphically higher & lower samples, respectively.

The Fjäcka Shale is an example of an ORM unit with a positive correlation between Mo and U isotope compositions (r = +0.75; Fig. 2.6c). In contrast to a negative correlation that is controlled by changes in the local depositional environment, a positive correlation between Mo and U isotope compositions is best explained by a changing global ocean redox state, which shifts seawater Mo and U isotope compositions and thus the sedimentary Mo and U isotope compositions of euxinic ORM in the same direction (see Section 2.2). Other explanations seem unlikely. The stratigraphically lower and higher Fjäcka Shale samples are characterized by lower δ^{98}Mo (0.42‰ to 0.81‰) and δ^{238}U (−0.23‰ to −0.02‰), whereas samples with higher δ^{98}Mo (0.87‰ to 1.28‰) and δ^{238}U (0.03‰ to 0.14‰) are stratigraphically in the middle (Table A1). Samples with higher δ^{98}Mo and δ^{238}U are from the Stumsnäs #1 core (more continuous sampling over ~4 m) but not the Solberga #1 core (more discrete sampling over ~2 m) possibly because samples from the Solberga #1 core with the same features were missed during sampling (Lu et al., 2017b).

Applying our method, the coeval seawater could have δ^{98}Mo of 1.31‰ to 1.75‰ and δ^{238}U of −0.80‰ to −0.54‰ during the deposition of stratigraphically higher and lower Fjäcka Shale, whereas the global seawater δ^{98}Mo and δ^{238}U could be 1.48‰ to 2.37‰ and −0.69‰ to −0.34‰, respectively, during deposition of the stratigraphically middle Fjäcka Shale (Fig. 2.6c). Therefore, a transient ocean oxygenation event likely occurred during the deposition of Fjäcka Shale. These seawater estimations assume that the inverse correlation of Mo-U isotope compositions for Ordovician euxinic basins is identical to the overall slope defined by modern euxinic basins. Because individual modern euxinic basins have yielded different slopes between the Mo and U isotope compositions (see Section 2.2.3), there is some uncertainty associated with estimates of global seawater Mo and U isotope compositions based on ORM data that show a positive Mo-U isotope correlation. By comparison, Lu et al. (2017b) estimated Late Ordovician (Katian) seawater δ^{98}Mo of 1.4‰ to 2.1‰ and δ^{238}U of −0.85‰ to −0.60‰ during Fjäcka Shale deposition. Their estimations were made individually with assumed isotopic offsets. However, they did not recognize the changing global ocean redox conditions

through the positively correlated Mo and U isotope compositions. An episode of increased global ocean oxygenation during the Katian Fjäcka Shale deposition is suggested in this study based on the coupled Mo-U isotopes, implying dynamic ocean redox conditions during the Ordovician (and more generally throughout the Early Paleozoic; Dahl et al., 2017b, 2019; Bartlett et al., 2018; Wei et al., 2018).

2.5.2.3 No correlation between δ^{98}Mo and δ^{238}U

Unlike the two previous examples of negative and positive correlations of Mo-U isotope data for euxinic ORM that are mainly controlled by changes in the local depositional environment and global ocean redox conditions, respectively, the absence of a correlation between δ^{98}Mo and δ^{238}U suggests distinctive local depositional conditions, a more complex combination of local and global controlling mechanisms or is an artifact of limited data. The Tanezzuft Formation, Zaonega Formation, and Doushantuo Formation Member IV have sufficient data and thus will be discussed in detail, whereas the other ORM units with limited data will only be briefly described.

2.5.2.3.1 The Tanezufft Formation: relatively stable local and global ocean redox conditions

The (Rhuddanian) early Silurian Tanezzuft Formation was deposited in the intracratonic Murzuq Basin (Libya) during a marine transgression caused by the melting of the Late Ordovician ice sheets (Desio, 1936; Davidson et al., 2000; Lüning et al., 2000). The Mo/TOC ratios of the Tanezzuft Formation (7.2 ± 2.6 μg/g/wt.%, 1SD) are mostly between that of the Black Sea (~4.5 μg/g/wt.%) and Framvaren Fjord (~9 μg/g/wt.%) (Fig. 2.7a; Table A1; Stockey et al., 2020). This low Mo/TOC ratio does not necessarily represent a limited connection between the local watermass and the open ocean because a smaller oceanic Mo reservoir is expected during the ocean anoxic events (e.g., Algeo, 2004; Montoya-Pino et al., 2010), in this case, the Hirnantian-Rhuddanian ocean anoxic event (Hammarlund et al., 2012; Melchin et al., 2013; Bartlett et al., 2018; Zou et al., 2018). The average Mo EF and U EF are 54.3 (8.3–127.7) and 8.2 (2.5–23.3), respectively. The high Mo/U EF ratios that are nearly

three times the modern seawater Mo/U ratio suggest a relatively good connection between the local watermass and the open ocean (Fig. 2.7b). Euxinic bottom water conditions are inferred from sedimentary Fe speciation, which is in an agreement with high Mo/U EF ratios (Stockey et al., 2020).

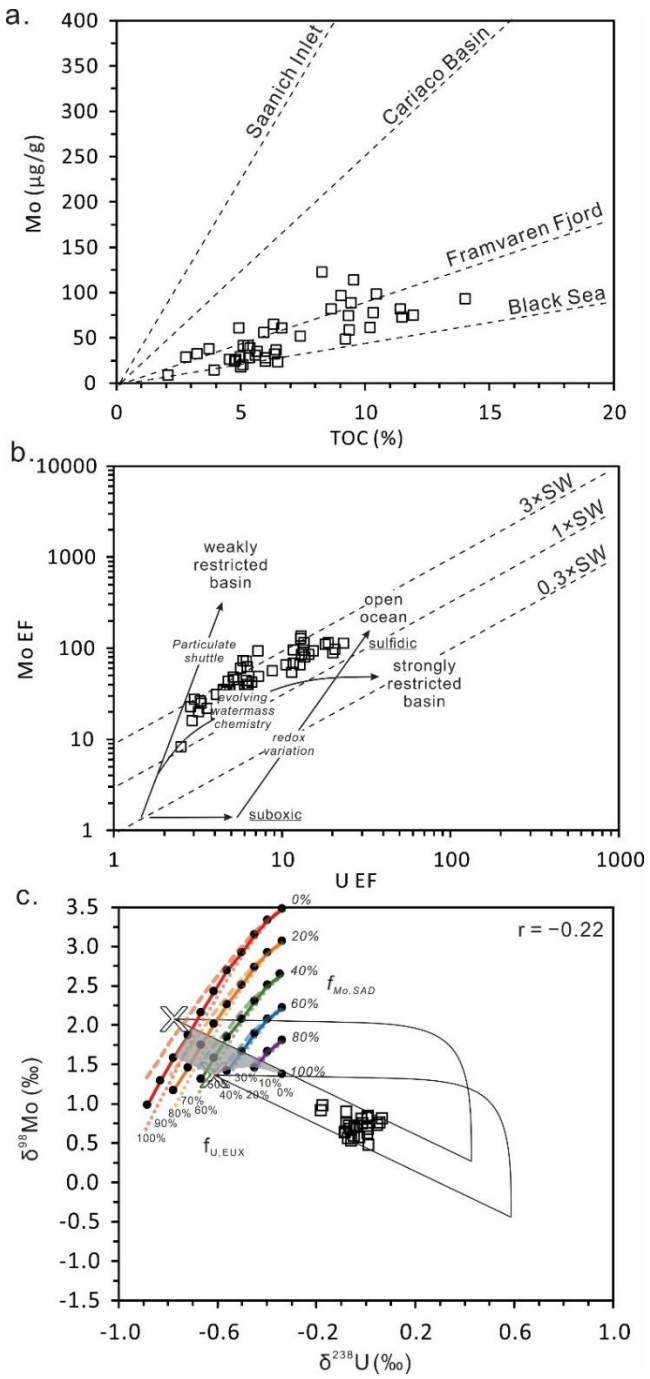

Figure 2.7 Geochemical data of the Silurian Tanezzuft Formation showing a) Mo vs TOC, b) Mo EF vs U EF, and c) δ^{98}Mo vs δ^{238}U (Table A1; Stockey et al., 2020).

Covariations of the Mo and U isotope compositions of the Tanezzuft Formation are examined (Fig. 2.7c). Narrow ranges are observed for both $\delta^{98}Mo_{auth}$ (0.51 to 0.97‰) and $\delta^{238}U_{auth}$ (−0.18‰ to 0.07‰), suggesting relatively constant Mo and U isotopic offsets between the euxinic ORM and seawater (Stockey et al., 2020). This observation further implies a relatively stable local depositional environment (e.g., bottom water redox conditions, basin restriction). The coupled $\delta^{98}Mo_{auth}$ and $\delta^{238}U_{auth}$ data of the Tanezzuft Formation do not exhibit a negative or positive correlation ($r = -0.22$), indicating no significant changes in global ocean redox conditions at the time.

The contemporaneous seawater Mo and U isotope compositions during deposition of the Tanezzuft Formation are estimated by the proposed model and compared with previous studies (Bartlett et al., 2018; Stockey et al., 2020). Applying our method, Rhuddanian seawater is characterized by $\delta^{98}Mo$ of 1.32‰ to 1.95‰ and $\delta^{238}U$ of −0.78‰ to −0.34‰ during deposition of the Tanezzuft Formation (Fig. 2.7c). By comparison, Stockey et al. (2020) did not clearly predict a coeval seawater $\delta^{238}U$ value but estimated Rhuddadian seawater $\delta^{98}Mo$ to be ~0.69 ± 0.13 (1SD) assuming no Mo isotope fractionations between local euxinic ORMs and the open ocean. The broadly co-deposited carbonates (the Becscie Formation) on Anticosti Island (Canada) have an average $\delta^{238}U$ of ~ −0.45‰ (Bartlett et al., 2018). Applying a modern $\delta^{238}U$ offset of 0.24‰ between shallow-water carbonates and seawater to the carbonates of the Becscie Formation, the Rhuddadian seawater likely had a $\delta^{238}U$ value of ~ −0.69‰. Therefore, the $\delta^{238}U$ offset of ~0.67‰ between euxinic Tanezzuft Formation (−0.02 ± 0.07‰, 1SD; Stockey et al., 2020) and the Rhuddadian seawater (~ −0.69‰) inferred from carbonates is generally consistent with observed U isotope fractionations between modern euxinic sediments and open-ocean seawater (e.g., Andersen et al., 2014, 2017; Noordmann et al., 2015; Rolison et al., 2017; Bura-Nakić et al., 2018; Brüske et al., 2020). In summary, our estimated $\delta^{98}Mo$ of Rhuddanian seawater (1.32-1.95‰) is higher than that (~0.69‰) from Stockey et al. (2020) mainly because they assumed no Mo isotopic offset between euxinic ORMs and seawater, whereas our model predicts there was a Mo isotopic offset. Our estimated Rhuddadian seawater

$\delta^{238}U$ value has a large range (−0.78‰ to −0.34‰) and is consistent with the estimation (−0.69‰) based on carbonates of the Becscie Formation (Bartlett et al., 2018).

2.5.2.3.2 The Zaonega Formation: potentially variable extent of basin restriction

The Zaonega Formation (~2.05 Ga) was deposited in the Onega Basin in a rifted continental marginal area and was deformed and metamorphosed (to low greenschist facies) during the 1.98-1.79 Ga Svecofennian Orogeny (Hannah et al., 2008; Melezhik et al., 1999, 2015). It is still not well understood if the basin was relatively well connected to the open ocean (e.g., Asael et al., 2013; Scott et al., 2014; Mänd et al., 2020) or not (e.g., Qu et al., 2012; Paiste et al., 2018) during deposition of the Zaonega Formation. The Zaonega Formation has low Mo/TOC ratios that are mostly below the modern Black Sea average (4.5 μg/g/wt.%), suggesting a severely restricted environment (Fig. 2.8a; Table A1). However, the low Mo/TOC ratios are also expected for ORM deposited in the less oxygenated Paleoproterozoic oceans where a smaller seawater Mo reservoir than the modern ocean was likely (Scott et al., 2008; Asael et al., 2013; Reinhard et al., 2013). The average Mo and U enrichment factors are 33.9 (6.0–114.8) and 3.1 (1.5–7.2), respectively (Fig. 2.8b). The high Mo/U EF ratios are mostly three times the modern seawater Mo/U ratio, suggesting euxinic bottom waters with the potential effect of an Fe-Mn particulate shuttle on Mo enrichment (Fig. 2.8b). It was previously suggested that the stratigraphically lower part of the section (Unit A and B) was affected by metamorphism, which caused alteration of pyrite to pyrrhotite, whereas the stratigraphically higher part of the section (Unit C) is less metamorphosed (Asael et al., 2013). Euxinic bottom water redox conditions were inferred for samples from Unit C (Asael et al., 2013). Detailed analysis of each specific Fe pool and the similar Mo isotope compositions of all samples raises the possibility that the more metamorphosed samples were also deposited under euxinic bottom waters (Asael et al., 2013). It has been shown that ancient ORMs that have undergone low greenschist facies metamorphism can still provide robust depositional information, such as precise and accurate Re-Os depositional ages (Kendall et al., 2004; Rooney et al., 2011). Considering the similar redox sensitive behavior between Mo & U and Re & Os, it is likely

that the Mo and U isotope compositions of such ORMs (especially less metamorphosed samples in Unit C) reflect the depositional environment.

The coupled Mo-U isotope data from the euxinic samples in less metamorphosed Unit C are used to ensure a more reasonable interpretation of global seawater redox conditions (Fig. 2.8c). The euxinic samples define a horizontal trend of δ^{98}Mo (0.72 ± 0.09‰, 1SD) with a slope of −0.10 ± 0.38 (1SE). This trend is similar to upper unit 4 (δ^{98}Mo = 0.79 ± 0.11‰, 1SD) of the Kettle Point Formation (−0.23 ± 0.31, 1SE), suggesting that Mo isotope compositions were mainly controlled by relatively lower and constant bottom water sulfide concentrations with a potentially minor effect from the Fe-Mn particulate shuttle, whereas the variable U isotope fractionations were influenced by several processes. However, there is one euxinic sample that shows a higher δ^{98}Mo of 1.40 ± 0.11‰ (2SD) compared with other euxinic samples, though the U EF is less than 2 (Fig. 2.8c). The high δ^{98}Mo value could be caused by more quantitative Mo removal when the bottom water renewal rate was slower (Mo/TOC = 1.8 μg/g/wt.%; Asael et al., 2013), which is indicative of a transient period of stronger basin restriction. Therefore, the degree of basin restriction was likely variable during the deposition of Zaonega Formation.

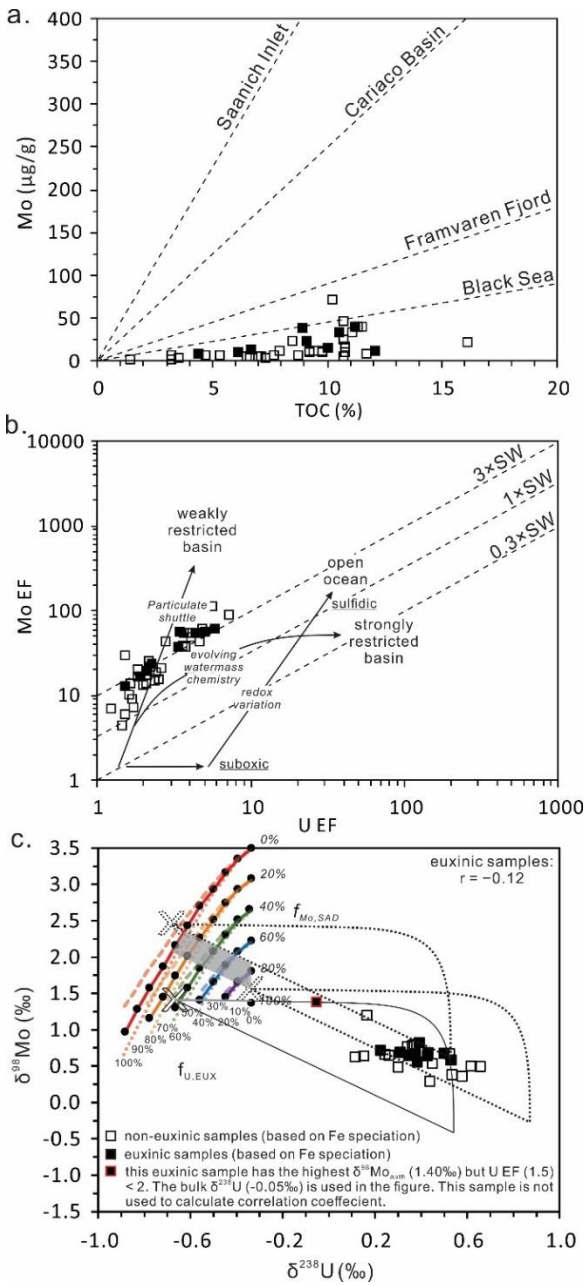

Figure 2.8 Geochemical data of the Paleoproterozoic Zaonega Formation showing a) Mo vs TOC, b) Mo EF vs U EF, and c) δ^{98}Mo vs δ^{238}U using euxinic samples only (Table A1; Asael et al., 2013). The dotted and solid lines in c) are used to estimate ancient seawater isotope compositions for an open marine environment and local basin restriction, respectively.

The coeval seawater Mo and U isotope compositions during deposition of the Zaonega Formation is estimated and compared with previous studies (Asael et al., 2013, 2018). Two possible scenarios are examined because of potential changes in the extent of basin restriction: 1) stronger basin restriction for the euxinic sample that has a δ^{98}Mo of 1.40‰; and 2) relatively open marine environment for the rest of the euxinic samples that have an average δ^{98}Mo of 0.72 ± 0.09‰ (1SD). Applying our method, the first scenario suggests a global seawater δ^{98}Mo of 1.40‰ (horizontal extrapolation to the model curves assuming the local bottom waters were strongly euxinic) and δ^{238}U of −0.66‰ to −0.34‰ (solid line in Fig. 2.8c). By comparison, the second scenario suggests a global seawater δ^{98}Mo of 1.57‰ to 2.37‰ and δ^{238}U of −0.68‰ to −0.34‰ by extrapolating to the model solution space using a curve whose slope is similar to the average slope defined by data from modern euxinic basins (dotted lines in Fig. 2.8c). The current dataset does not allow us to further justify which case best reflects the coeval global ocean redox conditions and it remains possible that both cases may have occurred. In comparison, Asael et al. (2013) estimated that the ca. 2.05 Ga global seawater δ^{98}Mo and δ^{238}U were 0.75 ± 0.21‰ and −0.18 ± 0.15‰, respectively. Recently, more δ^{98}Mo data were obtained for the Zaonega Formation from two additional drillcores and suggested a coeval seawater δ^{98}Mo of 0.70 ± 0.21‰ (Asael et al., 2018), which is identical to the values from Asael et al. (2013). Our estimated seawater δ^{98}Mo in both scenarios are higher than that of Asael et al. (2013) and Asael et al. (2018). The estimated δ^{238}U of contemporaneous seawater in this study has significant uncertainty (a relatively large range of ~0.32‰) and is generally lower than that of Asael et al. (2013).

2.5.2.3.3 The Doushantuo Formation Member IV: influence of the particulate Fe-Mn oxide shuttle and the potential change of global ocean redox conditions

The Ediacaran Doushantuo Formation was deposited on a passive continental margin (shelf lagoon and shelf margin-slope transition area) of the Yangtze Block (Wang and Li, 2003; Jiang et al., 2003, 2011). The ORM samples of Doushantuo Formation Member IV have an average Mo/TOC ratio of 28.3 ± 14.2 μg/g/wt.% (except one outlier with a Mo/TOC value of

290.0 µg/g/wt.%) that is higher than the modern Cariaco Basin (25 µg/g/wt.%) (Fig. 2.9a, Table A1, Kendall et al., 2015). The samples are also enriched in Mo (EF: 65.1–592.1, outlier: 960.8) and U (EF: 6.0–59.0), suggesting a relatively good connection between the local watermass and the open ocean during ORM deposition (Fig. 2.9b; Table A1; Kendall et al., 2015). The Mo/U EF ratios of these samples are mostly greater than three times the modern seawater Mo/U ratio, indicating a euxinic depositional environment that led to efficient Mo removal to the sediments relative to U (Fig. 2.9b; Kendall et al., 2015). This interpretation is confirmed by Fe speciation data (Kendall et al., 2015). It is possible that some samples with high Mo/U EF ratios were influenced by the Fe-Mn particulate shuttle (Fig. 2.9b; Algeo and Tribovillard, 2009).

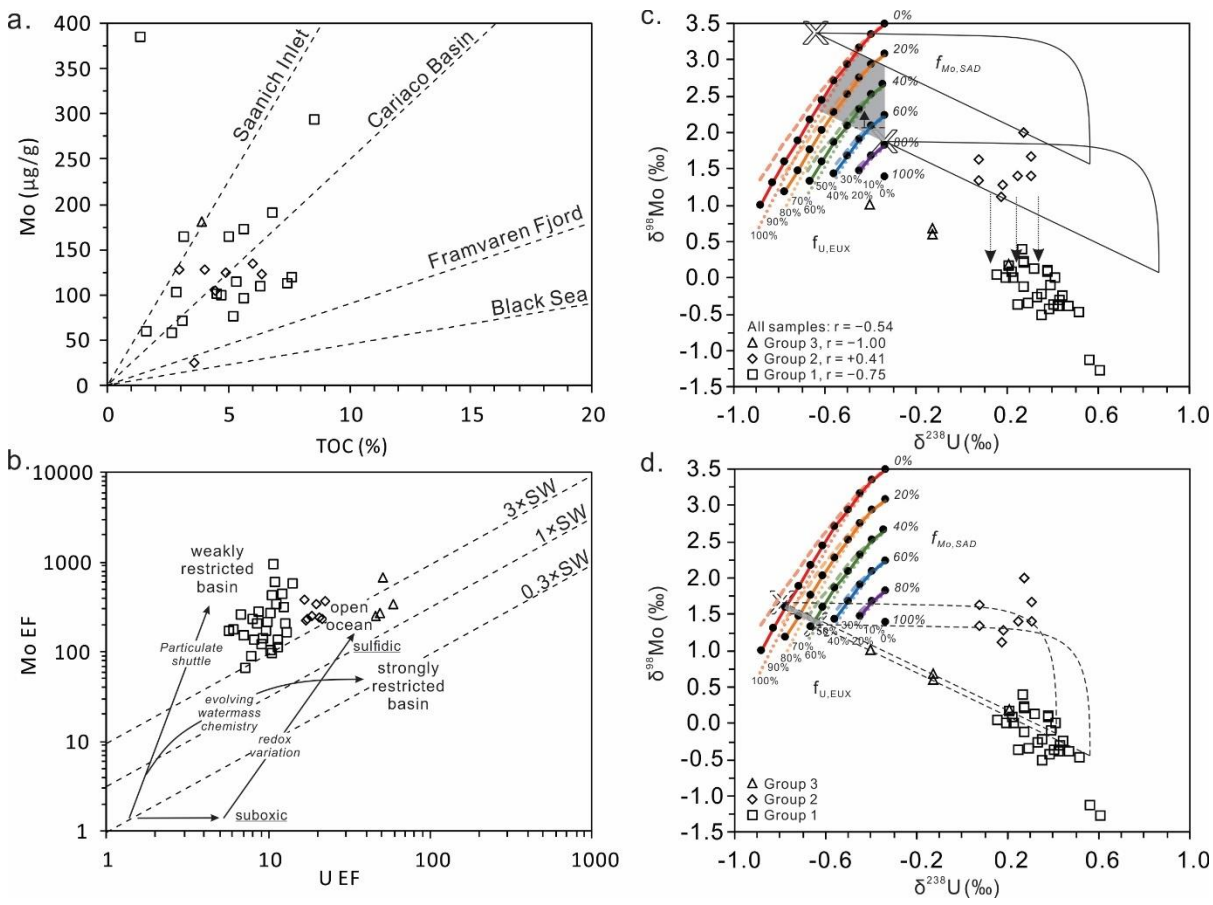

Figure 2.9 Geochemical data of the Ediacaran Doushantuo Formation Member IV showing a) Mo vs TOC, b) Mo EF vs U EF, and c) δ^{98}Mo vs δ^{238}U (group 1 and 2), and d) δ^{98}Mo vs δ^{238}U (group 3) (Table A1; Kendall et al., 2015). The vertical jump revealed between group 1 and 2 likely reflects that group 1 was significantly affected by a particulate Fe-Mn oxide shuttle.

In this study, rather than use the overall trend (r = –0.54), we subdivided the ORM samples into three stratigraphic groups (1–3) from the bottom to top of Member IV based on their different Mo and U isotope compositions. Group 1 contains lower δ^{98}Mo (< 0.40‰) and variable δ^{238}U (0.15–0.61‰) (r = −0.75, n = 27), group 2 has higher δ^{98}Mo (1.12–2.01‰) and a relatively smaller range of δ^{238}U (0.08-0.31‰) (r = +0.41, n = 8), and group 3 is characterized

by moderate δ^{98}Mo (0.20–1.01‰) and variable but generally lower δ^{238}U (−0.40‰ to 0.21‰) ($r = -1.00$, $n = 4$; Fig. 2.9c and 2.9d). These stratigraphic divisions suggest multiple controlling mechanisms on the isotopic compositions of euxinic ORM during deposition of Member IV.

Group 1 and 2 samples overlap in δ^{238}U but have different δ^{98}Mo. The overlapping δ^{238}U ranges between these two groups likely reflect different local depositional effects (that influence the efficiency of U removal to sediments) but generally similar global ocean redox states. The more variable δ^{238}U in group 1 could be caused by different U reduction and removal rates under weakly euxinic bottom waters, whereas the more uniform δ^{238}U in group 2 is indicative of relatively more efficient U reduction and removal under more strongly euxinic bottom waters. In addition, the δ^{238}U of group 2 (0.21 ± 0.09‰, 1SD) are similar to those of sediments from the modern Cariaco Basin and Saanich Inlet, indicating a near modern-level of ocean oxygenation if a U isotope fractionation of 0.6‰ was expressed locally between seawater and the euxinic sediments (Andersen et al., 2014; Holmden et al., 2015; Kendall et al., 2015; Brüske et al., 2020). The interpretation of widespread ocean oxygenation is also consistent with high δ^{98}Mo of the same samples (up to 2.01‰; Kendall et al., 2015). These high δ^{98}Mo values can be explained by efficient Mo removal under intensified euxinic bottom waters (Kendall et al., 2015).

By contrast, the much lower δ^{98}Mo of group 1 (−0.19 ± 0.38‰, 1SD) are similar and comparable to that of the sediments from the Landsort Deep (−0.03 ± 0.20‰, 1SD; sediments deposited < 6 cm below SWI) and Gotland Deep (−0.15 ± 0.22‰, 1SD; sediments deposited > 20 cm below SWI) in the Baltic Sea, which reflects Fe-Mn oxide delivery to the sediments during local transient oxygenation events (Noordmann et al., 2015; Scholz et al., 2018). Therefore, it is likely that the Fe-Mn particulate shuttle contributes to the observed low δ^{98}Mo in group 1 as this process can explain different δ^{98}Mo but generally similar δ^{238}U for groups 1 and 2 (Fig. 2.9c). There is a negative correlation between Mo and U isotope compositions in group 1 that suggests changes in the dissolved sulfide concentrations of bottom waters simultaneously affected the Mo and U isotopic offsets between sediments and seawaters (Brüske et al., 2020). The slope (−2.56 ± 0.45, 1SE) of this negative correlation is similar to

that of Sapropel S5 from the Eastern Mediterranean Sea (−2.63 ± 0.57, 1SE), which was related to changing bottom water renewal rates with different extents of basin restriction (Andersen et al., 2018). Hence, both an Fe-Mn particulate shuttle and bottom water sulfide concentrations (possibly associated with variable basin restriction) may play important roles on the covariation of Mo and U isotope compositions in group 1.

Similar and lower δ^{98}Mo values were recently reported for other Doushantuo Formation Members (II, III, IV) (Ostrander et al., 2019a). Bottom water redox conditions, the operation of an Fe-Mn (oxy)hydroxide shuttle, and sea-level changes (that influence the extent of basin restriction) are proposed to influence Mo isotope fractionations between sediments and overlying seawater (Ostrander et al., 2019a).

To sum up, the global ocean redox state was more oxygenated and remained generally the same during the deposition of group 1 and 2, even though the δ^{98}Mo of the two groups are significantly different. Because group 1 samples were significantly influenced by the Fe-Mn particulate shuttle, the group 2 samples are used to estimate the coeval seawater isotope compositions for both group 1 and 2 (Fig. 2.9c). The coeval global seawater δ^{98}Mo and δ^{238}U are estimated from 2.01‰ to 3.10‰ and from −0.64‰ to −0.34‰, respectively (Fig. 2.9c).

The stratigraphically highest group 3 contains only three samples, which have intermediate δ^{98}Mo (0.20-1.01‰) and generally lower δ^{238}U (−0.40‰ to 0.21‰). The Mo and U isotope compositions of these samples exhibit a clear negative correlation (−1.33 ± 0.09, 1SE) that is close to the proposed average negative correlation observed for modern euxinic basins, reflecting a dominant local depositional control on group 3 Mo-U isotope systematics (Fig. 2.9d; Bura-Nakić et al., 2018; Brüske et al., 2020). Applying our method, the contemporaneous seawater during group 3 deposition could have δ^{98}Mo and δ^{238}U of 1.32‰ to 1.60‰ and −0.78‰ to −0.61‰, respectively (Fig. 2.9d). These values suggest an expansion of ocean anoxia (group 3) following an episode of widespread ocean oxygenation (group 1 and 2). Although there are only three samples in this group, this interpretation is in an agreement with the low δ^{238}U (−1.2‰ to −0.8‰) reported for carbonates from the overlying Dengying Formation (South China; Zhang et al., 2018) and co-deposited Nama Group (Namibia;

Tostevin et al., 2019). The exceptionally low $\delta^{238}U$ values of the carbonates point to widespread global ocean anoxia during the terminal Ediacaran (Zhang et al., 2018; Tostevin et al., 2019).

2.5.2.3.4 The rest of the ORM formations

The rest of the euxinic ORM formations have small Mo-U isotope datasets, which significantly limits efforts to distinguish the influences of changes in local depositional conditions from global ocean redox variations because only a small part of the whole coupled Mo-U isotopes covariation pattern would be observed. The Almelund Shale was potentially deposited in a restricted environment based on the low Mo/TOC ratios ($\leq$ 2.6 μg/g/wt.%]), low Mo EF ($\leq$ 6.3) and U EF ($\leq$ 2.7), and Fe speciation evidence for locally euxinic bottom waters, but data come from only two samples (Table 2.1). Except this formation, we tentatively suggest the rest of the ORM units with small datasets were deposited under euxinic bottom waters with no severe basin restrictions and were not significantly affected by an Fe-Mn particulate shuttle, based on geological background and geochemical data (Fig. 2.10; Appendix A2; Kendall et al., 2009, 2015; Dahl et al., 2010; Yang et al., 2017). The estimated ranges of global seawater Mo and U isotope compositions at the time of ORM deposition were plotted in Fig. 2.10 and summarized in Table 2.4. If the local depositional environment of each ORM were interpreted correctly, the estimated $\delta^{98}Mo$ of coeval seawater are generally higher than that of the contemporaneous euxinic ORM units, implying appreciable Mo isotope fractionation from coeval seawater. However, it is difficult to determine the exact Mo isotopic offset between sediments and seawater because both a weakly euxinic environment and the particulate shuttle are possible influencing factors that can not be fully distinguished and quantitatively constrained using small datasets. In addition, the estimated ranges of seawater $\delta^{238}U$ are relatively large for most of these small datasets, which makes it difficult to predict the ancient seawater $\delta^{238}U$ due to several influencing factors on effective U isotope fractionations (e.g., bottom water chemistry, aqueous U species, productivity, U diffusion-reactive process; Andersen et al., 2017; Lau et al., 2020).

Table 2.4 A summary of estimated ranges of global seawater Mo and U isotope compositions based on the coupled Mo-U isotope compositions of euxinic ORMs

Time (Ma)	ORM interval	Estimated δ^{98}Mo of coeval seawater	Estimated δ^{238}U of coeval seawater
2050	Zaonega Formation[1]	Scenario 1: 1.40‰ Scenario 2: 1.57‰ to 2.37‰	Scenario 1: −0.66‰ to −0.34‰ Scenario 2: −0.68‰ to −0.34‰
1360	upper Velkerri Formation[2, 3]	1.50‰ to 2.23‰	−0.70‰ to −0.34‰
640	Black River Dolomite[4]	1.45‰ to 1.75‰;	−0.78‰ to −0.55‰
555	Doushantuo Formation Member IV[4]	2.01‰ to 3.10‰ (Group 1 and 2); 1.32‰ to 1.60‰ (Group 3)	−0.64‰ to −0.34‰ (Group 1 and 2); −0.78‰ to −0.61‰ (Group 3)
520	Yu'anshan Formation[5, 6]	1.43‰ to 2.10‰	−0.77‰ to −0.34‰
500	Alum Shale[5, 6]	1.37‰ to 2.25‰	−0.72‰ to −0.34‰
485	Alum Shale[5, 6]	1.37‰ to 2.27‰	−0.78‰ to −0.34‰
465	Almelund Shale[5, 6, #]	N/A	N/A
448	Fjäcka Shale[7]	1.31‰ to 1.75‰ (early and late stage); 1.48‰ to 2.37‰ and, (middle stage)	−0.80‰ to −0.54‰, (early and late stage); −0.69‰ to −0.34‰ (middle stage)
442	Rastrite Shale[5, 6] and Birkhill Shale[5, 6, *]	1.37‰ to 2.27‰	−0.75‰ to −0.34‰
442	Tanezzuft Formation[9]	1.32‰ to 1.95‰	−0.78‰ to −0.34‰
372	Kettle Point Formation[8]	2.04‰ to 2.75‰ and	−0.61‰ to −0.34‰
365	Chattanooga Shale[5, 6] and New Albany Shale[5, 6, *]	1.82‰ to 2.25‰	−0.63‰ to −0.34‰

References: [1] Asael et al. (2013); [2] Kendall et al. (2009); [3] Yang et al. (2017); [4] Kendall et al. (2015); [5] Dahl et al. (2010); [6] This study;[7] Lu et al. (2017b); [8] Kendall et al. (2020); [9] Stockey et al., (2020).

[#] For the Almelund Shale, the coeval global seawater Mo and U isotope compositions are not estimated due to limited samples (n = 2).

*Because there is only one sample for the Birkhill Shale and New Albany Shale, the shales that were broadly co-deposited are used together to estimate the coeval seawater Mo and U isotope compositions.

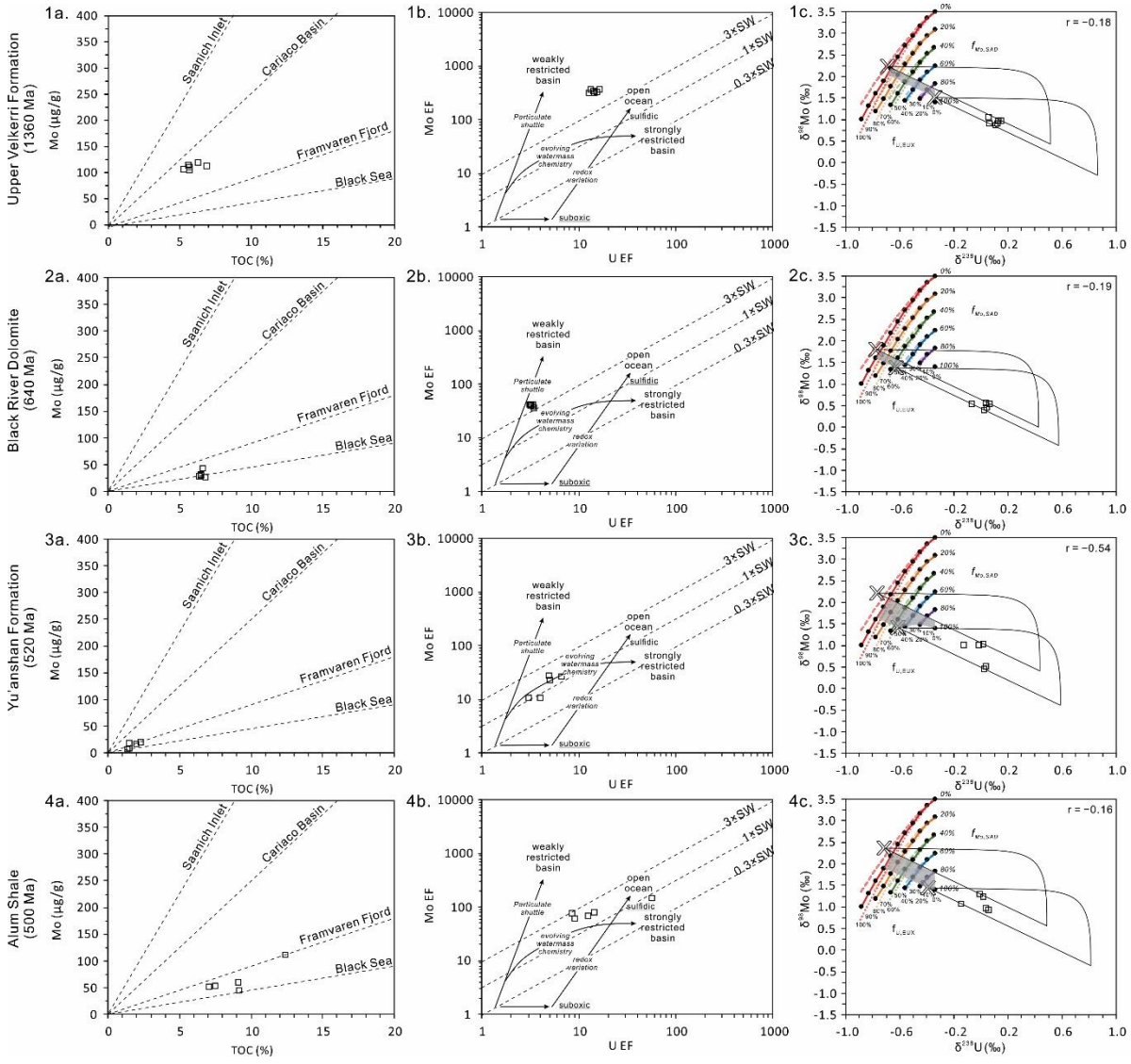

Figure 2.10 Geochemical data of the rest of the ORM units that have no correlations between Mo and U isotope compositions. Plots of (a) Mo vs TOC, (b) Mo EF vs U EF, and (c) δ^{98}Mo vs δ^{238}U are shown for each of these ORM units (Table A1; Kendall et al., 2009, 2015; Dahl et al., 2010; Yang et al., 2017; Sheen et al., 2018; This study).

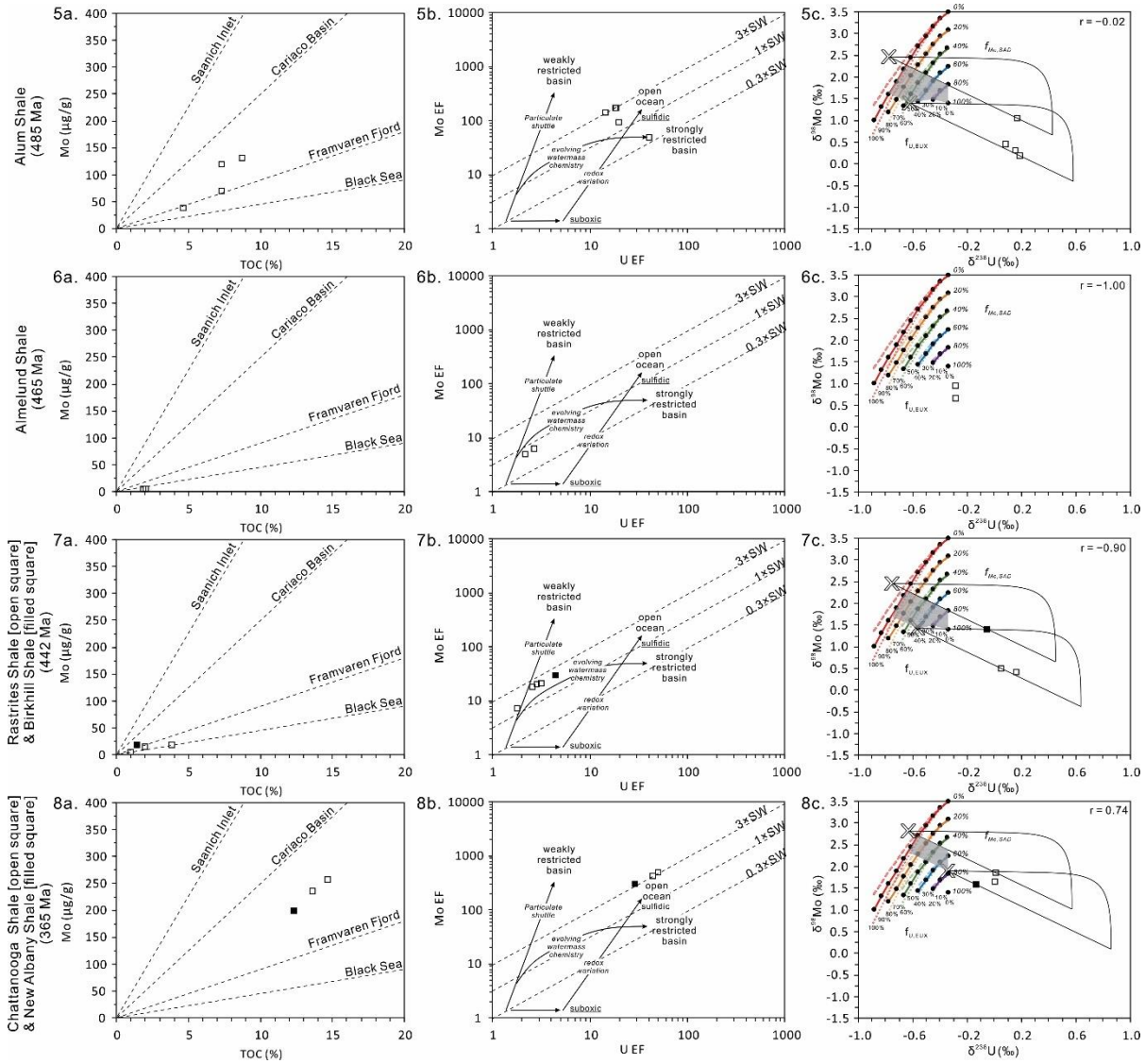

Figure 2.10 Continued.

Even though a larger dataset would be more helpful, there are a few exceptions where limited Mo-U isotope data could still be useful to reveal global ocean redox conditions. For example, the Late Devonian Chattanooga Shale and New Albany Shale contain high Mo (EF: 308.5–489.5) and U (EF: 28.7–50.1) enrichments, high δ^{98}Mo (e.g., ~2.0‰), and δ^{238}U (e.g., ~0.2‰). This combination of geochemical signatures represents compelling evidence of

widespread ocean oxygenation at the time of ORM deposition. The ~1.36 Ga Velkerri Formation is worth mentioning as well. The contemporaneous seawater Mo isotope composition is estimated to be at least 1.5‰ in this study, which is higher than previous estimates of ~1.0‰ (Arnold et al., 2004; Kendall et al., 2009). If it is correct, then the global ocean at the time may be relatively more oxygenated than previously thought (e.g., Arnold et al., 2004; Kendall et al., 2009; Planavsky et al., 2011). This hypothesis is generally consistent with the interpretation of high Mo (105–112 μg/g; Kendall et al., 2009) and Re (39.0–52.7 ng/g; Sheen et al., 2018) concentrations in bulk samples and pyrite trace element abundances (Mukherjee and Large, 2016), which are suggestive of an episode of ocean oxygenation at 1.36 Ga. In addition, recent studies of δ^{98}Mo and $\delta^{34}S_{py}$ from the ~1.40 Ga Xiamaling Formation (Zhang et al., 2016; Diamond et al., 2018; Wang et al., 2020) and I/Ca from the ~1.44 Ga Tieling Formation (Hardisty et al., 2017) suggest an episode of transient ocean oxygenation around ~1.4 Ga.

2.6 Conclusions

The coupled use of Mo and U isotope compositions from euxinic ORMs is further developed in this study to better infer ancient global ocean redox conditions. A lack of overall correlation between δ^{98}Mo and δ^{238}U is observed from a compilation of coupled Mo-U isotope data from the same samples of euxinic post-Archean ORMs, indicating that both local depositional factors and global ocean redox states exert significant influence on the sedimentary Mo and U isotope compositions. Negative, positive, and no correlations are observed from the covariations of the coupled Mo-U isotope data in the individual euxinic ORM units. Hence, each euxinic ORM unit must be carefully evaluated on a case-by-case basis to disentangle changes in local depositional conditions from global ocean redox variations.

A negative correlation between the Mo and U isotope compositions, similar to the observations from modern euxinic basins, is observed for the Upper Devonian Kettle Point Formation. This negative correlation most likely reflects changes in local depositional conditions with a generally stable global ocean redox state that, in the case of the Late

Devonian (Famennian), was only slightly less oxygenated than the modern oceans. A lack of correlation between the Mo-U isotope compositions for upper unit 4 of the Kettle Point Formation implies relatively constant bottom water sulfide concentrations. The Fe-Mn particulate shuttle could contribute to but is not the main cause of the low Mo isotope compositions.

A positive correlation between Mo and U isotope compositions points to a change in global ocean redox conditions during deposition of euxinic ORM. Such a positive correlation is observed for the Upper Ordovician (Katian) Fjäcka Shale, suggesting a transient episode of increased ocean oxygenation that simultaneously shifted the euxinic sediment Mo and U isotope compositions to higher values. This interpretation supports previous studies that suggested dynamic ocean redox conditions occurred during the Early Paleozoic Era.

No correlations are observed in many ORM units, which may be related to relatively stable depositional environment at local and global scales, specific changes in the local depositional environment, a combination of changes in local depositional conditions and global ocean redox state, or may simply be an artifact of limited data.

The Tanezzuft Formation represents a case of relatively constant local depositional conditions and global ocean redox conditions. This interpretation is supported by no directional stratigraphic changes of various geochemical proxies and narrow ranges of Mo and U isotope compositions of the euxinic shales from this formation.

The Doushantuo Formation Member IV is an excellent example that shows the combined effects of local (e.g., Fe-Mn particulate shuttle, changing bottom water sulfide concentrations, bottom water renewal rates associated with basin restrictions) and global variations (e.g., changing ocean redox conditions). Detailed analyses of the geochemical data suggest widespread ocean oxygenation throughout much of Member IV time, whereas an expansion of ocean anoxia is inferred during uppermost Member IV time.

The Zaonega Formation represents potentially variable extents of basin restriction during deposition. The coupled Mo-U isotope data exhibits a generally horizontal trend that is similar to upper unit 4 of the Kettle Point Formation with only one sample that has a higher

δ^{98}Mo value. This lone sample with a higher δ^{98}Mo might be deposited during a transient period of strong basin restriction that caused sluggish bottom water ventilation and renewal, whereas the horizontal trend defined by the other samples suggests that relatively constant bottom water sulfide concentrations resulted in similar magnitudes of Mo isotope fractionations and several processes (e.g., U reduction pathways, efficiency of U reduction and removal, aqueous U species) caused variable U isotope fractionations.

For the ORMs with limited data, there are large uncertainties associated with inferring global seawater Mo and U isotope compositions. Nevertheless, the coupled high δ^{98}Mo (nearly similar to modern seawater) and high δ^{238}U of the Upper Devonian Chattanooga Shale and New Albany Shale represents strong evidence of widespread ocean oxygenation at that time.

Building upon recent studies of modern euxinic basins, our study highlights the potential of using coupled Mo-U isotope data from euxinic ORM units to disentangle the effects of the local depositional environment and global ocean redox states. Using this approach, we have revealed some features that were not identified in previous studies. We have also demonstrated how the contemporaneous global seawater Mo and U isotope compositions during euxinic ORM deposition can be estimated through a coupled Mo-U isotope mass balance model. Our study demonstrates the necessity of carefully determining the local depositional environment (e.g., basin restriction, bottom water redox conditions, operation of an Fe-Mn particulate shuttle) before interpreting global ocean redox tracers (e.g., δ^{98}Mo and δ^{238}U) and highlights the necessity of using large datasets of coupled Mo and U isotope data to better infer local and global ocean redox dynamics.

Chapter 3 Ocean redox conditions during the Katian Taconic Orogeny, Late Ordovician

3.1 Introduction

The Late Ordovician (ca. 458–443 Ma) witnessed significant changes in metazoan biodiversity, with the culmination of the Great Ordovician Biodiversification Event (GOBE) at the Sandbian–Katian boundary (ca. 453 Ma) and the occurrence of the Late Ordovician Mass Extinction (LOME) during the Hirnantian (ca. 445–443 Ma; e.g., Sheehan 2001; Weber et al., 2004; Harper et al., 2014, 2015; Algeo et al., 2016; Servais and Harper, 2018; Rasmussen et al., 2019; Stigall et al., 2019; Cocks and Torsvik, 2021). The LOME wiped out ~85% of species and significant environmental changes are suggested to be associated with its two extinction phases. The first extinction phase (LOME1) is commonly associated with global cooling, volcanism, ocean anoxia, and eustatic fall whereas the second phase (LOME2) is often related to widespread ocean anoxia (e.g., Sheenhan et al., 2001; Zhang et al., 2009; Finnegan et al., 2011, 2012; Hammarlund et al., 2012; Melchin et al., 2013; Ghienne et al., 2014; Algeo et al., 2016; Jones et al., 2017; Bartlett et al., 2018; Zou et al., 2018; Edwards, 2019; Albanesi et al., 2020; Bond and Grasby, 2020; Hu et al., 2020; Young et al., 2020; Goldberg et al., 2021; Kozik et al., 2022). It has been noted that metazoan biodiversity started to decline during the Katian (e.g., Kröger, 2017; Rasmussen et al., 2019) and the associated environmental changes are not well understood prior to the abrupt occurrence of LOME.

Regarding global ocean redox conditions during the Katian, only a few studies that utilized novel metal isotope systems (e.g., δ^{98}Mo, δ^{238}U) are available (Zhou et al., 2012, 2015; Lu et al., 2017; Dahl et al., 2021). The δ^{98}Mo of euxinic (anoxic and sulfidic) Katian black shales, which are all below 1.50‰ (Dahl et al., 2010, 2021; Zhou et al., 2012, 2015; Lu et al., 2017), provide a minimum estimate of the coeval global seawater δ^{98}Mo as lighter Mo isotopes are preferentially removed to sediments (see review by Kendall et al., 2017). A positive correlation between δ^{98}Mo and δ^{238}U from the euxinic Katian Fjäcka Shale (Sweden) suggests a transient ocean oxygenation event (Lu et al., 2017, 2020). The inferred coeval seawater δ^{98}Mo is 1.48–2.37‰ and 1.31–1.75‰ during the oxygenation event and before/after the event, respectively (Lu et al., 2017, 2020). Compared with the modern well-oxygenated

seawater δ^{98}Mo of 2.34‰ (e.g., Nägler et al., 2014), the estimated Katian seawater δ^{98}Mo values are generally lower and suggest contemporaneously more extensive ocean anoxia (Dahl et al., 2010, 2021; Lu et al., 2017, 2020).

The Taconic Orogeny on Laurentia could have profoundly influenced the climate, ocean chemistry, and biological events during the Late Ordovician. A sharp decrease in seawater strontium isotope ratios ($^{87}Sr/^{86}Sr$) across the Middle–Late Ordovician boundary is suggested to reflect a significant volcanic Sr flux related to the exhumation and weathering of mafic/ultramafic rocks (Young et al., 2009; Saltzman et al., 2014; Edwards et al., 2015). A concurrent increase in neodymium isotope ratios ($^{143}Nd/^{144}Nd$) from the Appalachian margin shales (Swanson-Hysell and Macdonald, 2017) and the Great Basin margin carbonates (Conwell et al., 2022) could have resulted from the weathering of juvenile crust. Both isotopic changes could be explained by the increased tropical weathering of volcanic arcs due to the Taconic Orogeny (Young et al., 2009; Swanson-Hysell and Macdonald, 2017). This process could result in the climate cooling, as evidenced by oxygen isotope data from bulk carbonate and fossils (i.e., brachiopod and conodont; Trotter et al., 2008; Goldberg et al., 2021), because atmospheric CO_2 can effectively react with the Mg and Ca enriched mafic/ultramafic rocks and form solid carbonate minerals (e.g., calcite, dolomite; Kelemen et al., 2020). Low-latitude arc-continent collisions during the Late Ordovician (e.g., the Taconic Orogeny, Central Asia Orogenic Belt) are proposed to cause the effective exhumation and eroding of mafic/ultramafic rocks and thus contribute to climate cooling and glaciation (Macdonald et al., 2019), which is regarded as a potential trigger for the LOME1 (e.g., Finnegan et al., 2011; Melchin et al., 2013; Ghienne et al., 2014; Algeo et al., 2016). Moreover, the Taconic Orogeny was associated with the "Richmondian Invasion", which reflects a large-scale immigration of extra-basinal taxa into the warmer environment of the Cincinnati region during the Katian (e.g., Holland and Patzkowsky, 1996; Wright and Stigall, 2013).

The Collingwood Member (upper Lindsay Formation) and Rouge River Member (lower Blue Mountain Formation) are the Katian organic-rich sedimentary rocks (ORS) in southern Ontario, Canada (e.g., Russell and Telford, 1983; Churcher et al., 1991; Armstrong

and Carter, 2010; Béland-Otis, 2015; Hamblin, 2018). The deposition of both ORS units is related to the concurrent Taconic Orogeny, thus providing a rare opportunity to explore the ocean redox dynamics accompanied by an orogeny event between the GOBE and LOME. In this study, the Collingwood Member and Rouge River Member samples collected from multiple drill cores throughout southern Ontario were measured for elemental concentrations and uranium isotope compositions to examine local depositional environments and coeval global ocean redox dynamics, respectively.

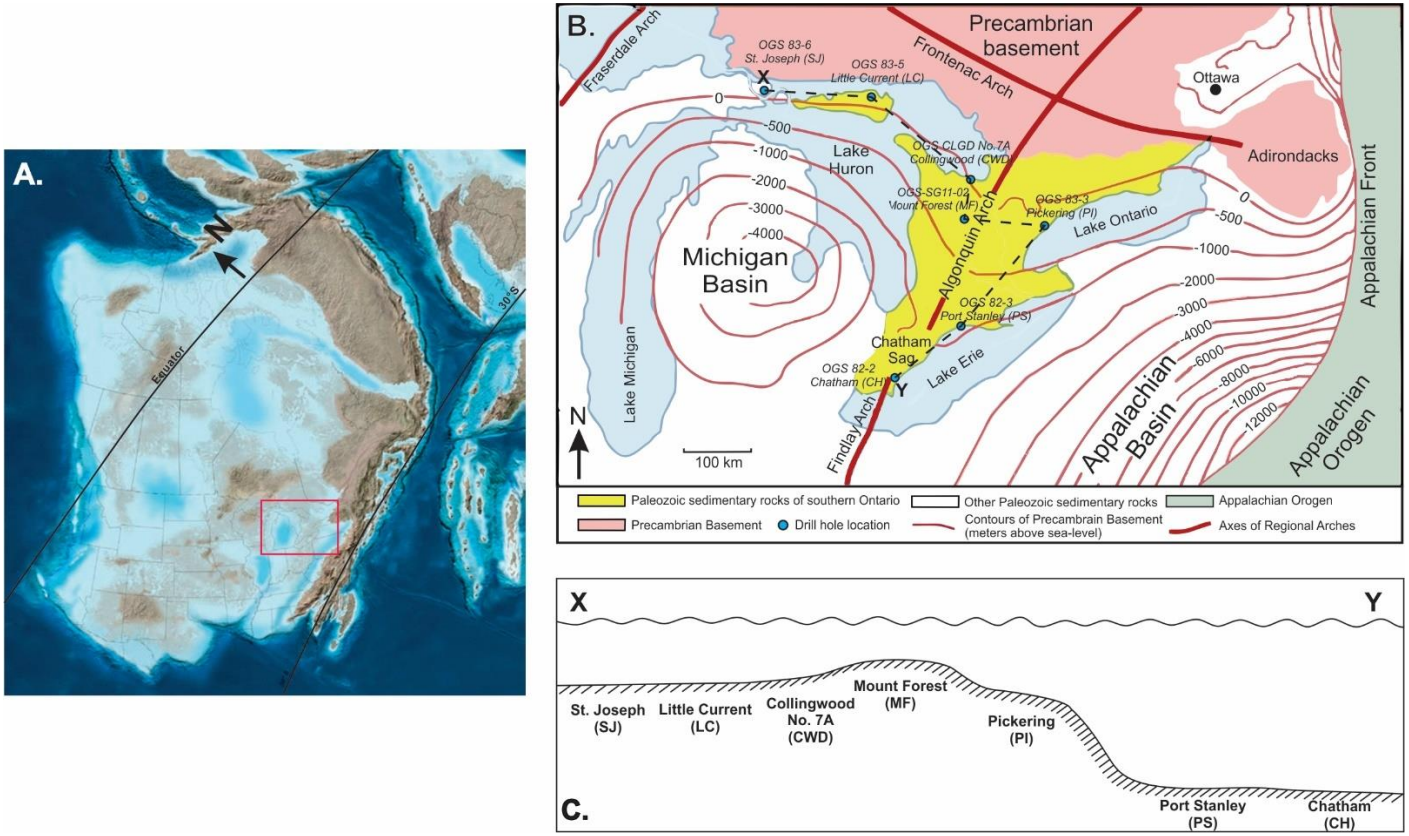

Figure 3.1 The paleogeography of Laurentia during the Late Ordovician (~450 Ma; modified from Blakey and Ranney, 2018); B) A regional map showing the tectonic elements around southern Ontario (Canada) and the drill core locations in this study (modified from Johnson et al., 1992); C) a schematic view of cross-section (X–Y shown in B) that illustrates basin geometry (modified from Lehmann et al., 1995; Rancourt, 2009; Brookfield and Hannigan, 2021).

3.2 Background

3.2.1 Geological background

During the Late Ordovician, eastern Laurentia was situated in the equatorial area (Fig. 3.1; Blakey and Ranney, 2018; Cocks and Torsvik, 2021) and a shallow marine carbonate platform developed in the Michigan Basin and along the continental margin (Howell and van der Pluijm, 1990). The Taconic Orogeny represents collisions between eastern Laurentia and island arcs/microcontinents, which resulted in the deformation of lithosphere and creation of a peripheral foreland basin (the Appalachian Basin; e.g., Cisne et al., 1982; Quinlan and Beaumont, 1984; Bradley and Kidd, 1991; Niocaill et al., 1997; van Staal and Barr, 2012). The Taconic Orogeny led to intensified weathering and increased sediment loading, reflected by the lithologic transition from carbonates to siliciclastic sediments in both the Appalachian Basin and Michigan Basin (Howell and van der Pluijm, 1990; Lehmann et al., 1995; Béland-Otis, 2015; Hamblin, 2018). In southern Ontario, increased sediment flux is reflected by a transition from the Trenton Group carbonates, through calcareous shales of the Collingwood Member (the uppermost Trenton Group), to the succeeding siliciclastic-dominated Nottawasaga Group (in ascending stratigraphic order: the Blue Mountain Formation, Georgian Bay Formation, and Queenston Formation) (Fig. 3.2; Johnson et al., 1992; Armstrong and Carter, 2010; Hamblin, 2018). Mineralogical analysis suggests that the Collingwood Member mainly consists of calcites (50–59%) and clays (29–36%) with smaller amounts of other minerals such as quartz, dolomite, and pyrite (Béland-Otis, 2015). In contrast, the succeeding Blue Mountain Formation and Georgian Bay Formation are mainly composed of clays (62–71%) and quartz (19–25%) with subordinate calcite, dolomite, and pyrite (Béland-Otis, 2015). Despite differences in carbonate content, relatively constant proportions of clays versus quartz are observed for the Collingwood Member and succeeding Nottawasaga Group, suggesting similar siliciclastic sediment sources for these strata (Béland-Otis, 2015).

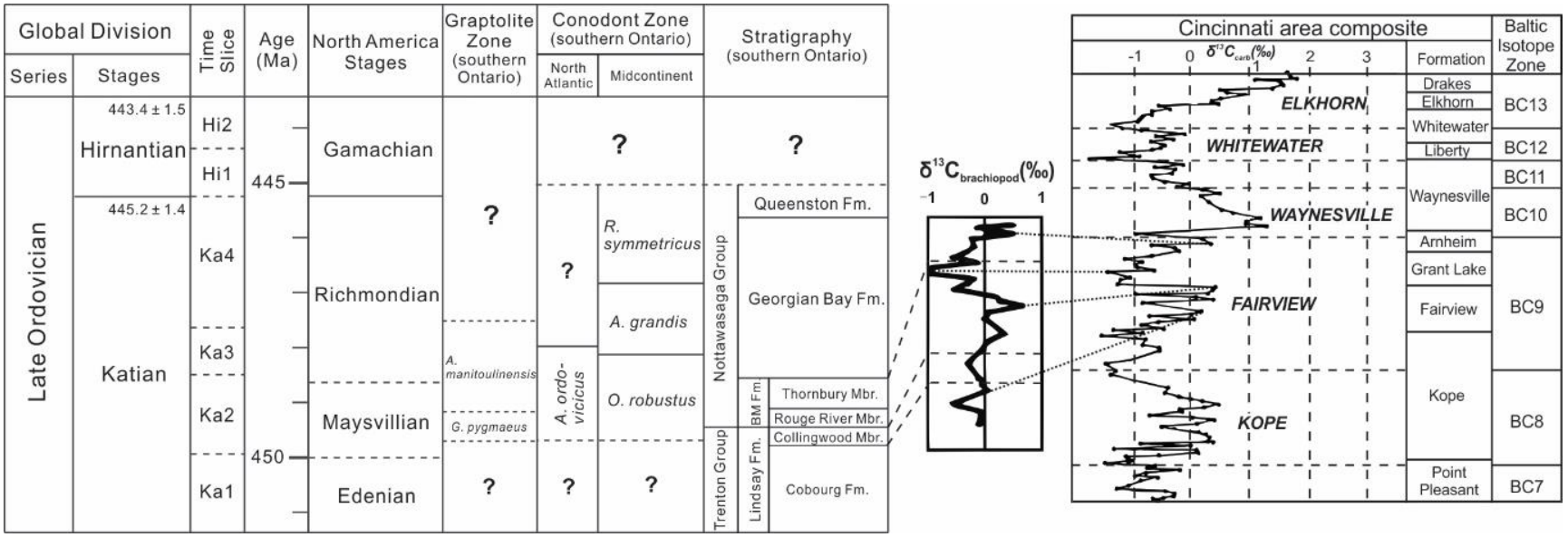

Figure 3.2 The Late Ordovician stratigraphic units and associated biozones in southern Ontario (Canada), and correlations with the $\delta^{13}C$ from Cincinnati area composite (modified from Armstrong and Carter, 2010; Zhang et al., 2011; Bergström et al., 2010, 2015; Brookfield et al., 2021). Conodont zone is from Zhang et al. (2011); graptolite zone is from Riva (1974), Goldman and Bergström (1997), and Sharma et al. (2003); stratigraphy and lithology are from Armstrong and Carter (2010) and Hamblin (2018); stage slice of the Late Ordovician is from Ogg et al. (2016) and Bergström et al. (2020b). The brachiopod $\delta^{13}C$ data are from Brookfield and Hannigan (2021) (samples from the Little Current core, Ontario). The $\delta^{13}C$ from Cincinnati area composite and formation names are from Bergström et al. (2015) and Baltic isotope zones are from Ainsaar et al. (2010).

The Collingwood Member (ca. 449 Ma), defined as the upper member of the Lindsay Formation (Trenton Group), comprises brownish to black, organic-rich, calcareous shales with some fossiliferous interbeds (Fig. 3.2; Russell and Telford, 1983; Johnson et al., 1992; Armstrong and Carter, 2010). It gradationally overlies the limestones of the Cobourg Formation (lower member of the Lindsay Formation) (Liberty, 1969; Russell and Telford, 1983; Armstrong and Carter, 2010). The Collingwood Member is within the *Geniculograptus pygmaeus* graptolite zone (Riva, 1974; Goldman and Bergström, 1997; Sharma et al., 2003) and *Amorphognathus ordovicicus* conodont zone (Zhang et al., 2011). The Collingwood Member was deposited below storm wave base during the drowning of a carbonate ramp associated with the Taconic Orogeny (Howell and van der Pluijm, 1990, 1999; Johnson et al., 1992; Rancourt, 2009). Although the ancient carbonate ramp commonly represents the locality where carbonate material accumulated rather than precipitated, low energy environment suggests the transportation distance may not be far from the site of precipitation, thus preserved geochemical data should reflect local/regional depositional environment. Sedimentological data suggested cyclical deposition of carbonates and clastic sedimentary rocks for the Collingwood Member (outcrop near the towns of Craigleith, south shore of Georgian Bay, and Bowmanville, north shore of Lake Ontario), which may result from short term variations in sea level or climate (Brett et al., 2006). The Collingwood Member is the thickest (up to ~12 m) on Manitoulin Island and the north-central part of southern Ontario and thins towards the south and east (Rancourt, 2009; Armstrong and Carter, 2010; Chen et al., 2021). Its stratigraphically equivalent stratum in eastern Ontario is the Eastview Member of the Lindsay Formation (Russell and Telford, 1983; Williams, 1991; Armstrong and Carter, 2010).

The Rouge River Member is the lower member of the Blue Mountain Formation (ca. 449 Ma) and is characterized by dark grey to black, non-calcareous siliciclastic shales with some carbonate-rich interbeds (Fig. 3.2; Russell and Telford, 1983; Armstrong and Carter, 2010). It is in gradational contact with the overlying Thornbury Member (upper Blue Mountain Formation), which consists of bluish to greyish, siliciclastic shales with interbeds of carbonates and siltstones (Johnson et al., 1992; Armstrong and Carter, 2010; Hamblin, 2018). The lower

contact of the Rouge River Member with the Collingwood Member is either gradational or sharp (Russell and Telford, 1983; Lehmann et al., 1995; Armstrong and Carter, 2010). A phosphatic bed sometimes can be observed at the contact and could represent a maximum flooding surface (Russell and Telford, 1983; Sharma et al., 2003; Brett et al., 2006; Béland-Otis, 2015). The Rouge River Member is within the *Geniculograptus pygmaeus* graptolite zone (Riva, 1974; Goldman and Bergström, 1997; Sharma et al., 2003) and the *Amorphognathus ordovicicus* conodont zone (Zhang et al., 2011). The Rouge River Member was deposited below storm wave base, marking the first major arrival of clastic sediments from the concurrent Taconic Orogeny (Russell and Telford, 1983; Johnson et al., 1992). The thickness of the Rouge River Member reaches ~60 m in the southwest of southern Ontario and thins towards the northeast (Johnson et al., 1992; Armstrong and Carter, 2010; Béland-Otis, 2015). The Blue Mountain Formation is equivalent to the Billings Formation in eastern Ontario and the Utica Shale in Quebec and the United States (Williams, 1991; Lehmann et al., 1995; Lavoie et al., 2008). A K-bentonite bed, observed between the lower and upper Billings Formation in drill core Russell-GSC #2 (Russell County, eastern Ontario), yields an age range of 440–450 Ma by Ar-Ar dating (Sharma et al., 2005), which is generally consistent with the biostratigraphy (Riva, 1974; Goldman and Bergström, 1997; Sharma et al., 2003; Zhang et al., 2011). However, the K-bentonite bed has not been reported for the Blue Mountain Formation in southern Ontario.

Both the Collingwood Member and Rouge River Member have been extensively studied using organic geochemistry (e.g., Rock-Eval pyrolysis) and some remarkable differences are observed (e.g., Macauley and Snowdon, 1984; Churcher et al., 1991; Obermajer et al., 1999; Armstrong and Carter, 2010; Béland-Otis, 2015). First, the Collingwood Member generally contains higher total organic carbon (TOC; 3–10%) than the Rouge River Member (1–3%; Russell and Telford, 1983; Macauley and Snowdon, 1984; Churcher et al., 1991; Obermajer et al., 1999; Béland-Otis, 2015). Second, the thermal maturity patterns are different. An increasing thermal maturity towards the southeast is observed for the Collingwood Member, from immature on St. Joseph Island, through marginally mature on Manitoulin Island

and in the Georgian Bay area, to moderately mature in the Toronto area (Macauley and Snowdon, 1984; Obermajer et al., 1999; Béland-Otis, 2015). By comparison, the Rouge River Member is predominantly early mature in southern Ontario (Macauley and Snowdon, 1984; Obermajer et al., 1999; Béland-Otis, 2015). Third, the Collingwood Member contains type I–II kerogen that suggests a marine source, whereas the Rouge River Member has type II–II/III kerogen that represents a mixed marine and terrestrial source (Macauley and Snowdon, 1984; Obermajer et al., 1999; Béland-Otis, 2015).

Only a few studies utilized inorganic geochemistry to understand the depositional environment of the two ORS units in southern Ontario (Sharma et al., 2003; Hannigan et al., 2010; Brookfield and Hannigan, 2021). Sharma et al. (2003) suggested intensified anoxic bottom water conditions during Collingwood Member deposition and suboxic conditions for the Blue Mountain Formation based on trace metal redox proxies (i.e., V, Mo, and U) of samples from drill core GSC DDH2-Elizabeth (Manitoulin Island). Hannigan et al. (2010) analyzed $^{87}Sr/^{86}Sr$ ratios of brachiopods preserved in the Upper Ordovician strata in southern Ontario (drill core OGS 83-5 Little Current, Manitoulin Island) and compared these data with the global seawater $^{87}Sr/^{86}Sr$ curve inferred from Ordovician brachiopods and carbonates (Shields et al., 2003). Similar $^{87}Sr/^{86}Sr$ ratios from the Collingwood Member and lower-middle Blue Mountain Formation suggest a primary seawater $^{87}Sr/^{86}Sr$ signal, whereas an abrupt increase of $^{87}Sr/^{86}Sr$ ratios from the middle-upper Blue Mountain Formation and Georgian Bay Formation is explained by basin isolation from the open oceans and significant freshwater influx due to the Taconic Orogeny (Hannigan et al., 2010). The change of $^{87}Sr/^{86}Sr$ ratios also corresponds to gradual cooling from ~30–35°C to ~28°C based on brachiopod oxygen isotope data (Brookfield and Hannigan, 2021), which may have caused the coeval "Richmondian Invasion" (Wright and Stigall, 2013). In addition, inorganic brachiopod carbon isotope compositions of the Collingwood Member and Rouge River Member are correlated to the Fairview positive carbon isotope excursion (CIE) observed in the Cincinnati region (Fig. 3.2; Bergström et al., 2009, 2015, 2020b; Brookfield and Hannigan, 2021). However, the global significance of the Fairview CIE remains uncertain because it is only correlated with a CIE

observed in China but not other continents (e.g., Baltoscandia; Ainsaar et al., 2010; Bergström et al., 2009, 2010, 2015, 2020a, 2020b; Jing et al., 2019).

3.2.2 Geochemical proxy background

3.2.2.1 Paleosalinity proxies

Strontium/barium ratios (Sr/Ba) from organic-rich siliciclastic sedimentary rocks have been applied as a paleosalinity proxy (e.g, W. Wei et al., 2018; Wei and Algeo, 2020). Compilations of Sr/Ba ratios in modern sediments with different watermass salinities show that freshwater, brackish, and marine sediments have Sr/Ba ratios of < 0.2, 0.2–0.5, and > 0.5, respectively (Wei and Algeo, 2020). The application of this paleosalinity proxy can be affected by several factors, such as high Sr concentrations in carbonate-rich sediments due to substitution of Sr^{2+} for Ca^{2+} or K^{+} and high Ba concentrations from biogenic source(s) and diagenetic remobilization (e.g., Wei and Algeo, 2020).

The sulfur/total organic carbon ratio (S/TOC) is another useful paleosalinity proxy (e.g., W. Wei et al., 2018; Wei and Algeo, 2020; Remírez and Algeo, 2020). Wei and Algeo (2020) suggested S/TOC ratios of < 0.1, 0.1–0.5, and > 0.5 represent fresh, brackish, and marine conditions, respectively. However, brackish and marine conditions cannot be effectively differentiated by S/TOC ratios due to active microbial sulfate reductions in both settings (Wei and Algeo, 2020). Samples with at least 1% TOC are recommended for inferring paleosalinity using S/TOC (Berner, 1984; Berner and Raiswell, 1984; Wei and Algeo, 2020).

3.2.2.2 Paleoredox proxies

Redox-sensitive trace metals (Mo, U, Re), sedimentary Fe speciation, and C_{org} : P (molar) ratios are used to decipher local bottom water redox conditions of the Collingwood Member and Rouge River Member. These proxies have been reviewed in recent publications (Raiswell et al., 2018; Algeo and Li, 2020; Kendall, 2021), thus being briefly introduced here. Molybdenum removal is more efficient to sediments in euxinic settings, whereas U removal

does not depend on aqueous H_2S in bottom waters and can occur in suboxic settings (Barnes and Cochran, 1990; Crusius et al., 1996; Helz et al., 1996; Morford and Emerson, 1999; Algeo and Tribovillard, 2009). A particulate Fe-Mn oxyhydroxide shuttle could accelerate Mo enrichment over U in sediments (e.g., the Cariaco Basin; Algeo and Tribovillard, 2009). In comparison, Re behaves similar to U and is a robust indicator of suboxic conditions due to less detrital input from the upper continental crust (e.g., Crusius et al., 1996; Morford et al., 2005; Rudnick and Gao, 2014). Unlike Mo, the effects of Fe-Mn oxyhydroxides on U and Re are much weaker (Morford et al., 2005; Algeo and Tribovillard, 2009). For the sedimentary Fe speciation, the ratio of highly reactive Fe over total iron (Fe_T) is used to distinguish anoxic (> 0.38) from oxic (< 0.22) bottom water conditions (Poulton and Canfield, 2011; Clarkson et al., 2014; Raiswell et al., 2018). The Fe_{HR}/Fe_T ratios between 0.22 and 0.38 are more ambiguous and reflects either oxic or anoxic conditions (Poulton and Canfield, 2011; Raiswell et al., 2018). The ratio of Fe_{py}/Fe_{HR} can be further used to infer if the anoxic water column is dominated by dissolved iron (< 0.7–0.8, ferruginous) or sulfide (> 0.7–0.8, euxinic) (März et al., 2008; Poulton and Canfield, 2011; Raiswell et al., 2018). However, a recent study suggests Fe speciation may reflect diagenetic processes (Pasquier et al., 2022). The C_{org} : P molar ratios of ORS (TOC > 1%) that are < 50 and > 50 are suggestive of oxic-suboxic and anoxic conditions, respectively (Algeo and Ingall, 2007; Algeo and Li, 2020).

3.2.2.3 U isotopes as a global ocean redox tracer

The $\delta^{238}U$ of sedimentary rocks (e.g., organic-rich shales, carbonates) have been used as a novel proxy to reconstruct paleocean redox conditions (see recent reviews in Andersen et al., 2017, Zhang et al., 2020a, and Kendall, 2021). Uranium is mainly derived from the oxidative weathering of the upper continental crust and is transported to the oceans via rivers (Dunk et al., 2002; Partin et al., 2013). In the modern well-oxygenated seawater, U mainly exists as $Ca/Mg\text{-}UO_2\text{-}CO_3$ complexes and has a long oceanic U residence time of ~400–500 kyr (Langmuir, 1978; Dunk et al., 2002; Endrizzi et al., 2016). The modern seawater has an average $\delta^{238}U$ of -0.39 ± 0.04‰ (Stirling et al., 2007; Weyer et al., 2008; Tissot and Dauphas,

2015; Andersen et al., 2016; Noordmann et al., 2016). The average $\delta^{238}U$ of rivers is estimated between −0.34‰ and −0.24‰, which is indistinguishable from that of the upper continental crust (−0.29 ± 0.09‰; Stirling et al., 2007; Weyer et al., 2008; Telus et al., 2012; Tissot and Dauphas, 2015; Andersen et al., 2016; Noordmann et al., 2016; Wang et al., 2018). Groundwaters could potentially contribute U to the oceans, but the flux is not known. The major U sinks in the oceans are euxinic settings (9 ± 6% of U removal), other O_2-deficient settings (e.g., suboxic, ferruginous; 40 ± 10%), biogenic carbonates (30 ± 10%), oxic sediments (12 ± 6%), and altered oceanic crust at high (3 ± 3%) and low (6 ± 6%) temperatures (Barnes and Cochran, 1990; Morford and Emerson, 1999; Dunk et al., 2002; Tissot and Dauphas, 2015; Andersen et al., 2016, 2017; Noordmann et al., 2016).

Different oceanic U sinks exhibit different $\delta^{238}U$ offsets from open ocean seawater. In modern euxinic settings, heavy ^{238}U is preferentially removed to euxinic sediments, leading to large $\delta^{238}U$ offsets from open ocean seawater (~0.60 ± 0.20‰; Stirling et al., 2007; Weyer et al., 2008; Andersen et al., 2014; Holmden et al., 2015; Noordmann et al., 2015; Rolison et al., 2017; Bura-Nakić et al., 2018; Brüske et al., 2020). The large and variable $\delta^{238}U$ offsets in euxinic settings could be associated with several factors, such as bottom water H_2S concentrations and basin restrictions (e.g., Andersen et al., 2017; Lau et al., 2020). Even larger U isotope offsets (approaching intrinsic U isotope fractionations of ~1.2‰) for some organic-rich sediments have been proposed to be associated with U reduction in the water column (Andersen et al., 2017) and/or an organic floccule layer (Andersen et al., 2020). Smaller U isotope offsets are observed in other U sinks. The areal extent of ferruginous settings is limited in the modern oceans and the U isotope offsets in such settings are reported to be variable, with an overall average of 0.25 ± 0.21‰ heavier than seawater (Cole et al., 2020). The $\delta^{238}U$ of suboxic sediments (e.g., the Peru and Namibian continental margins, Washington coast) is commonly ~0.1–0.3‰ heavier than the modern seawater (Weyer et al., 2008; Andersen et al., 2016; Cole et al., 2020; Abshire et al., 2020; He et al., 2021; Bruggmann et al., 2022). Biogenic carbonates have minimal U isotope offsets from the modern seawater (Chen et al., 2018a; Livermore et al., 2020), whereas shallow-water platform carbonates from the modern Bahamas

bank have small U isotope offsets (0.27 ± 0.14‰) due to U(VI) reduction in sulfidic porewaters below the SWI (Romaniello et al., 2013; Chen et al., 2018b; Tissot et al., 2018). The $\delta^{238}U$ offset between oxic Fe-Mn oxides and seawater is approximately −0.25 ± 0.05‰ due to preferential adsorption of lighter ^{235}U to the oxides (Stirling et al., 2007; Weyer et al., 2008; Goto et al., 2014; Jemison et al., 2016). The $\delta^{238}U$ offsets for the hydrothermal alteration of crust at high and low temperatures are 0.00 ± 0.02‰ and 0.25 ± 0.02‰, respectively (Andersen et al., 2015, 2016; Tissot and Dauphas, 2015; Noordmann et al., 2016).

Because of large U isotope offsets in the euxinic settings compared with the other redox conditions, seawater U isotope compositions are sensitive to the extent of global ocean euxinia. In an ocean where there is widespread euxinia on continental margins and in intracratonic basins, heavy ^{238}U would be preferentially removed from seawater, resulting in a lower seawater $\delta^{238}U$. In contrast, when the oceans become more oxygenated, less ^{238}U are removed from the oceans, leading to a higher $\delta^{238}U$ of seawater.

3.3 Samples and methods

3.3.1 Samples

A total of 233 Upper Ordovician sedimentary rocks was sampled from seven drill cores throughout southern Ontario (Fig. 3.1). Details on drill core locations, stratigraphy, and number of samples collected from each stratigraphic unit for each drill core are listed in Table 3.1. The OGS 82-2 Chatham (CH), OGS 82-3 Port Stanley (PS), OGS 83-3 Pickering (PI), OGS-SG11-02 Mount Forest (MF), and OGS CLGD No.7A Collingwood (CWD) cores are stored at the Ontario Oil, Gas and Salt Resources Library in London (Ontario), whereas the OGS 83-5 Little Current (LC) and OGS 83-6 St. Joseph (SJ) cores are stored at the Ministry of Energy, Northern Development and Mines in Sudbury (Ontario). Samples were collected from, in order of older to younger, the Cobourg Formation of the lower Lindsay Formation (n = 3), the Collingwood Member of the upper Lindsay Formation (n = 52), the Rouge River Member of the lower Blue

Mountain Formation (n = 156), and the Thornbury Member of the upper Blue Mountain Formation (n = 22) (Table 3.1).

Table 3.1 Drillhole locations, stratigraphic classifications, and sample collections in this study.

Well information		**Co-ordinates (NAD83 CNT)**		**Top of Unit (m)[#] [number of samples]**				**Total number of samples**
Name	Well Licence	Latitude (°North)	Longitude (°West)	Thornbury Mbr.	Rouge River Mbr.	Collingwood Mbr.	Cobourg Fm.	
OGS 82-2 Chatham	T006045	42.38782	-82.07989	848.7 [1]	872.9 [41]	N/A*	899.65 [1]	43
OGS 82-3 Port Stanley	T006078	42.67077	-81.16139	796.85 [1]	824.25 [56]	861.5	863.2	57
OGS 83-3 Pickering	T006124	43.81652	-79.05789	24.3 [6]	30.6 [17]	43.65** [5]	48.22	28
OGS 83-5 Little Current	T006305	45.94118	-81.94685	80	93	103.5 [15]	113	15
OGS 83-6 St. Joseph	T006311	46.09624	-83.92743	100 [2]	136 [17]	158.5 [11]	169.5	30
OGS-SG11-02 Mount Forest	T012100	43.95996	-80.63535	426	463.3 [16]	476.9 [15]	486.3 [2]	33
OGS CLGD No. 7A Collingwood^	N000255	44.46744	-80.27927	42.06^ [12]	61.50^ [8]	72.69^ [7]	?	27
TOTAL				22	155	53	3	233

Fm. = Formation; Mbr. = Member
[#] Based on Beland-Otis (2015).
* Unit absent from the well.
** From Churcher et al. (1991). It is consistent with abrupt high TOC and TIC data of the sample at 44.49 m from this study. Instead, Beland-Otis (2015) suggested the contact to be 46.84 m.
^ Depth of top of units for OGS CLGD No. 7A is inferred from borehole geophysical data in Johnson et al. (1983).

Salient observations of the Collingwood Member and Rouge River Member from these seven drill cores are summarized below. The Collingwood Member from the MF core is characterized by the cyclical deposition of TOC-poor and TOC-rich layers. By comparison, the Collingwood Member from the other drill cores (LC, SJ, PI, CWD) was more uniformly deposited as black to brown, organic-rich marls. The Rouge River Member from all drill cores was observed as grey to black, uniformly deposited siliciclastic shales. The sharp contact (phosphatic bed) between the Collingwood Member and Rouge River Member was observed in the CH, PS, and MF cores, whereas a gradational contact was present in the LC, SJ, CWD, and PI cores.

Our sampling resolution varies from 0.2 m to 3 m and is mostly 0.5–0.8 m, targeting uniformly deposited, organic-rich sedimentary rocks. Samples with macroscopic diagenetic pyrite nodules, carbonate/quartz veins and fossils were avoided. The collected samples were broken into chips (taking care to avoid metal contact) and then powdered by an automated agate ball mill at the University of Waterloo.

3.3.2 Analytical methods

3.3.2.1 Carbon analyses

Total carbon (TC), total inorganic carbon (TIC), and total organic carbon were analyzed at the Geoanalytical Laboratory, University of Western Ontario (CH, PS, and PI cores, and the Blue Mountain Formation from the MF core) and the Agriculture and Food Laboratory, University of Guelph (CWD, LC, and SJ cores, and the Lindsay Formation from the MF core). At the Geoanalytical Laboratory, TC contents were measured through combustion in a Leco CS-244 analyzer and TIC was analyzed through acid digestion. Reference standards AR-4005, AR-4006, and AR-4007 were measured along with samples and the accuracy is better than 95%. At the Agriculture and Food Laboratory, TC (without ashing) and TIC (with pre-ashing) contents were determined by combustion in an Elementar Vario Macro Cube CN combustion analyzer. The Brush Creek Shale (SBC-1) served as the

reference standard and the accuracy is generally better than 90%. The TOC contents were calculated as the difference between TC and TIC. The TIC data were converted to carbonate content by assuming that all inorganic carbon is present as calcium carbonate.

3.3.2.2 Sulfur analyses

Total sulfur contents were analyzed at the Geoanalytical Laboratory (CH, PS, and PI cores, and the Blue Mountain Formation from the MF core) and Activation Laboratories Ltd. (CWD, LC, and SJ cores, and the Lindsay Formation from the MF core). At the Geoanalytical Laboratory, the S contents were analyzed via combustion in a Leco CS-244 analyzer. Reference standards AR-4005, AR-4006, and AR-4007 were measured and the accuracy is > 95% compared to certified values. At Activation Laboratories Ltd., the S contents were determined by combustion in an ELTRA instrument. The SBC-1 standard was measured along with samples and the accuracy is > 95% compared to certified value.

3.3.2.3 Sedimentary iron speciation

Sedimentary iron speciation has been widely used to infer the local bottom water redox conditions (e.g., Dahl et al., 2010; Kendall et al., 2010, 2015; Hammarlund et al., 2012; Zou et al., 2018; Gilleaudeau et al., 2021). Highly reactive Fe (Fe_{HR}) is a sum of several iron phases (pyrite Fe [Fe_{py}] + carbonate Fe [Fe_{carb}] + ferric oxide Fe [Fe_{ox}] + magnetite Fe [Fe_{mag}]) that can react with sulfide in the water column or in sediments during early diagenesis (Poulton and Canfield, 2005, 2011). Except for the pyrite Fe, the other three Fe phases were extracted at George Mason University. The Fe_{carb}, Fe_{ox}, and Fe_{mag} phases were sequentially extracted by sodium acetate, dithionite, and ammonium oxalate solutions, respectively, following the protocols in Poulton and Canfield (2005). The extract solutions were dried and re-diluted in 2% HNO_3 and measured using an Agilent 8800 triple quadrupole inductively coupled plasma mass spectrometer (QQQ-ICP-MS) in the Metal Isotope Geochemistry Laboratory, University of Waterloo. Water standards (T207, T211, T225, T231) from the United States Geological Survey (USGS) served as reference standards and the accuracy is better than 95%.

Pyrite sulfur is traditionally extracted via chromium reduction (e.g., Canfield et al., 1986; Poulton and Raiswell, 2002; Poulton and Canfield, 2005). In this study, pyrite sulfur is assumed to be the difference between total sulfur and other forms of sulfur (from sulfate minerals and organic matter), which were combusted at 1450°C and 550°C, respectively, using ELTRA instruments at Activation Laboratories Ltd. Pyrite Fe is then calculated based on the pyrite sulfur content assuming a stoichiometry of FeS_2 (Poulton and Raiswell, 2002; Poulton and Canfield, 2005). This combustion method is mainly aimed for reduced sulfur phases, because some oxidized sulfur phases (e.g., barite) were potentially not combusted/extracted during total sulfur analyses. To test this method, we first selected 16 samples that have published Fe speciation data with Fe_{py} contents ranging from 0.1% to 6.5% as determined using the chromium reduction method (Kendall et al., 2010, 2015; Lu et al., 2017), and measured these samples for their pyrite sulfur contents via the combustion method. The obtained pyrite sulfur contents were used to calculate pyrite Fe contents and Fe_{HR}/Fe_T and Fe_{py}/Fe_{HR} ratios (using previously published Fe_{carb}, Fe_{ox}, and Fe_{mag} data). An excellent correlation ($R^2 = 0.98$, $p < 0.01$) is observed for Fe_{py} contents between the chromium reduction and combustion methods (Fig. 3.3). In addition, excellent correlations are observed between the two methods for both Fe_{HR}/Fe_T ($R^2 = 0.95$, $p < 0.01$) and Fe_{py}/Fe_{HR} ($R^2 = 0.97$, $p < 0.01$) ratios (Fig. 3.3). The average difference of Fe_{py} between the two methods is −0.20% (Fe_{py} content is slightly underestimated by combustion method) and does not significantly influence the Fe_{HR}/Fe_T and Fe_{py}/Fe_{HR} ratios, which only have average differences of −0.07 (1SD = 0.07) and −0.05 (1SD = 0.06), respectively. This test suggests that Fe_{py} data obtained via the combustion method can be used to get Fe_{HR}/Fe_T and Fe_{py}/Fe_{HR} ratios that are comparable to those determined using Fe_{py} data obtained via the chromium reduction method.

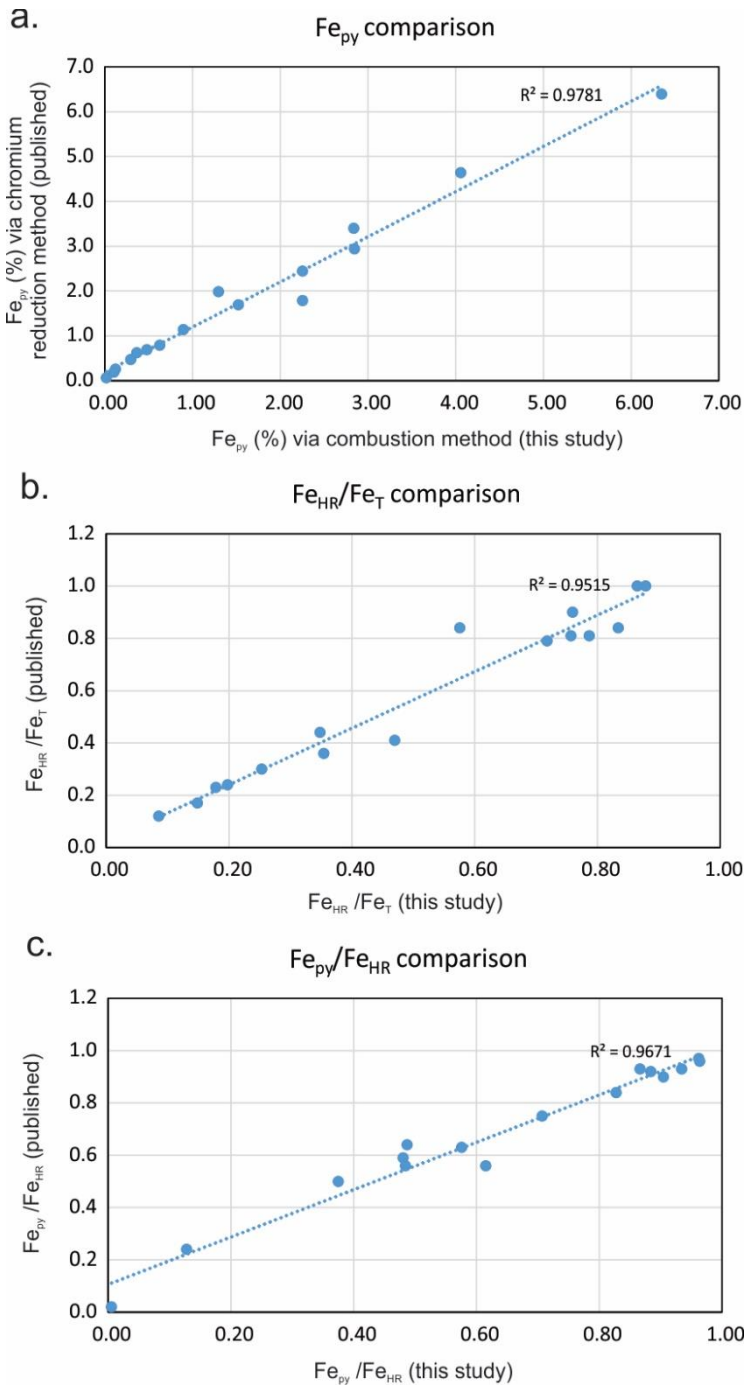

Figure 3.3 Sedimentary Fe speciation data comparison. a) comparison of Fe_{py} data between chromium reduction method (Kendall et al., 2010, 2015; Lu et al., 2017) and combustion

method (this study); b) comparison of Fe_{HR}/Fe_T between published data and this study (using Fe_{py} from the combustion method and previously published data for other Fe pools); c) comparison of Fe_{py}/Fe_{HR} between published data and this study (using the combustion method and previously published data for other Fe pools).

3.3.2.4 Elemental concentrations

Dissolution of samples and measurement of elemental concentrations were carried out at the Metal Isotope Geochemistry Laboratory, University of Waterloo. The analytical protocols followed Kendall et al. (2020) and are briefly described here. Approximately 100 mg of sample powder was ashed overnight in a furnace at 550°C to remove organic matter. The ashed sample was dissolved through several rounds of HNO_3-HCl-HF acid digestions in a clean laboratory. A split of the sample solutions was dried and then re-dissolved in 2% HNO_3 and measured for elemental concentrations on an Agilent 8800 QQQ-ICP-MS. The relative standard deviation (RSD) is typically < 5% and always < 10%. The RSD of Re is normally < 8% but sometimes was higher (up to 18%) when the sample Re concentration is similar to the average upper continental crust. The SGR-1b (Green River Shale) and SBC-1 standards were included as secondary reference standards and the accuracy is > 90% compared to reported Re concentrations of SGR-1b from Yin et al. (2017) and SBC-1 from Li and Yin (2019). The SBC-1 standard was used to verify the accuracy for Ba, whose measured values indicate > 92% accuracy compared to the certified value (we did not use SGR-1b because of considerable variations in Ba concentrations for that standard compared with SBC-1; see Kendall et al., 2020). Reproducibility of duplicate sample analyses agreed to within 10%. The procedural blanks are negligible (< 1%). Sample elemental abundances were corrected using the respective measured standard recovery rates to ensure data accuracy.

3.3.2.5 Carbon and oxygen isotope analyses

Carbon ($\delta^{13}C$) and oxygen ($\delta^{18}O$) isotope compositions were measured at the Environmental Isotope Laboratory, University of Waterloo. Samples were firstly ashed at 550°C to remove organic matter. The CO_2 produced from the carbonate fractions of samples via 100% phosphoric acid reaction was extracted automatically with a double-hole needle Gilson auto-sampler connected to a GVI MultiFlow and analyzed on a GVI IsoPrime continuous flow isotope ratio mass spectrometer. Three standards (EIL-21, IAEA-CO-1, and IAEA-CO-8) were measured and the analytical precisions of both $\delta^{13}C$ and $\delta^{18}O$ are ± 0.2‰ (2SD).

3.3.2.6 Uranium isotope analyses

Uranium isotope purifications and measurements were carried out at the Metal Isotope Geochemistry Laboratory, University of Waterloo. The procedure follows the protocols in Weyer et al. (2008) and Kendall et al. (2020). Before the purification of U by ion exchange chromatography, a weighed amount of ^{236}U-^{233}U double spike (IRMM-3636) was added to a portion of each fully digested sample solution (bulk) that contains 200–300 ng sample U. The Eichrom® UTEVA resin was used to purify U from sample-spike solutions. The U isotope compositions were measured on a Nu Plasma II multi-collector ICP-MS and reported against the CRM145 standard:

$$\delta^{238}U\ (‰) = (^{238/235}U_{\ sample} / {}^{238/235}U_{\ CRM145} - 1) \times 1000$$

Because the bulk $\delta^{238}U$ ($\delta^{238}U_{bulk}$) data could be affected by detrital U, and carbonate-associated $\delta^{238}U$ are likely to capture the coeval seawater $\delta^{238}U$ with generally small isotope offsets (Romaniello et al., 2013; Chen et al., 2018b; Tissot et al., 2018), some carbonate-rich Collingwood Member samples were leached to obtain carbonate $\delta^{238}U$ data ($\delta^{238}U_{carb}$). Three Collingwood Member samples, with TOC of 1–9% and $CaCO_3$ of 30–65%, were selected and leached with 0.8N acetic acid, 0.5N HCl, and 1N HCl. As no significant difference is found in $\delta^{238}U_{carb}$ with different leaching acids (see Table B5 in Appendix B), selected Collingwood Member samples from the MF and CWD cores were then leached with 1N HCl to obtain the

$\delta^{238}U_{carb}$ data following the same ion-exchange chromatography and mass spectrometry procedures used for bulk sample analyses.

During the measurements, double spiked CRM145 (analyzed every 2 samples) and CRM129a (analyzed every 8–10 samples) yielded average $\delta^{238}U$ values of 0.00 ± 0.08‰ (2SD, n = 196) and −1.42 ± 0.08‰ (2SD, n = 57), respectively. As the reported $\delta^{238}U$ data of CRM129a are heterogenous among different laboratories (Lau et al., 2016, 2017; Andersen et al., 2017), it is only used to monitor the long-term reproducibility of our instrument. The SBC-1, SDO-1 (Devonian Ohio Shale), and SGR-1b served as secondary rock standards and yielded measured $\delta^{238}U$ values of −0.29 ± 0.07‰ (2SD, n = 10), −0.12 ± 0.07‰ (2SD, n = 6), and −0.22 ± 0.09‰ (2SD, n = 11), respectively. These values are consistent with the published $\delta^{238}U$ data for these rock standards from several laboratories (Kendall et al., 2015, 2020; Tissot and Dauphas, 2015; Lu et al., 2017, 2020; Rolison et al., 2017; Yang et al., 2017; Brüske et al., 2020; Clarkson et al., 2021), demonstrating the reliability of U isotope data generated from our lab. The uncertainty of a sample is reported as either the 2SD of sample replicate measurements or the long-term-reproducibility of CRM145/CRM129a (0.08‰), whichever is greater.

3.3.3 Data normalization and local detrital background

The Al-normalized enrichment factors (EF) of elements are used to describe the relative enrichment or depletion of the element relative to that of a reference material and are calculated as below (Tribovillard et al., 2006):

$$X\ EF = (X / Al)_{sample} / (X / Al)_{reference\ material}$$

An X EF > 1 indicates element enrichment whereas X EF < 1 represents element depletion. An EF > 10 is regarded as substantial enrichment of the element (Algeo and Tribovillard, 2009). Several reference materials have been used for normalization, including PAAS (Post-Archean average Australian Shale; Taylor and McLennan, 1985), AS (Average Shale; Wedepohl, 1971, 2004), NASC (North American Shale Composite; Gromet et al., 1984), and AUCC (average upper continental crust; McLennan, 2001; Rudnick and Gao,

2014). Because the local detrital background can have different compositions compared with the above-mentioned reference materials, using local detrital background for normalization will be more reliable to reflect the enrichment/depletion of elements (e.g., Van der Weijden, 2002; Cole et al., 2017).

To estimate the local detrital background, covariations between several elements (i.e., Mo, U, Re, Fe, Ba, Sr) and Al concentrations of the Collingwood Member and Rouge River Member are plotted in Fig. 3.4. A strong positive correlation between an element and Al suggests a dominantly detrital source of the element, whereas a weak positive or negligible correlation is indicative of an authigenic elemental enrichment, at least for those samples with higher element/Al ratios. A negative correlation between an element and Al suggests that element is not closely associated with clay minerals and other Al-bearing minerals like feldspars. For example, both the Collingwood Member and Rouge River Member exhibit strong positive correlations between Ba and Al and negative correlations between Sr and Al (Fig. 3.4). The minimum element/Al ratios of samples are likely to represent the detrital backgrounds. As the mineralogical analyses suggest similar siliciclastic sediment components for the Collingwood Member and succeeding Nottawasaga Group (Béland-Otis, 2015) and the minimum element/Al ratios are similarly low among the different cores (except for the Collingwood Member), we regarded the average minimum element/Al ratios of these units from all cores as representing the local detrital backgrounds (bold in Table 3.2).

Samples with carbonate-related Sr and high biogenic Ba contents are corrected to ensure the effective use of Sr/Ba ratio as a paleosalinity proxy. Strong positive correlations between Ba and Al for both the Collingwood Member and Rouge River Member (Fig. 3.4) suggest that Ba is predominantly from terrestrial/detrital sources rather than biogenic sources. To correct for carbonate-related Sr, it is assumed that non-carbonate Sr equals the detrital background Sr/Al ratio multiplied by sample Al contents ($Sr_{carb\text{-}corrected} = [Sr/Al]_{background} \times Al_{sample}$; Table 3.3). The corrected Sr/Ba ratios are thus used to infer paleosalinity conditions during deposition (Fig. 3.13).

Table 3.2 Comparison of element/Al background ratios between local and reference materials. Local detrital backgrounds of each stratigraphic units are calculated as the average of minimum element/Al ratio from the wells containing the corresponding unit. Bolded values are used as the local detrital background.

	Mo/Al	U/Al	Re/Al	Fe/Al	Ba/Al	Sr/Al	References
PAAS	0.10	0.31		0.51	65.00	20.00	Taylor and McLennen, 1985
AS	0.15	0.42		0.54	65.61	33.94	Wedepohl, 1971, 2004
NASC		0.30		0.49	71.06	15.87	Gromet et al., 1984
AUCC	0.19	0.35	0.05	0.44	68.41	43.53	McLennen, 2001
AUCC	0.13	0.33	0.02	0.48	76.56	39.26	Rudnick and Gao, 2014
TB	0.17	0.46	0.16	0.54	35.96	14.54	
RR	0.12	0.42	0.16	0.48	32.91	13.12	
CW	0.36	0.80	1.30	0.44	**35.90**	69.29	This study
BM (TB+RR)	**0.09**	**0.42**	**0.11**	0.48	31.62	**12.91**	
CW+BM	0.16	0.46	0.31	**0.44**	31.80	14.50	

Units: ng/g/% for Re/Al, %/% for Fe/Al, and μg/g/% for the rest of element/Al ratios

BM = Blue Mountain Formation

TB = Thornbury Member

RR = Rouge River Member

CW = Collingwood Member

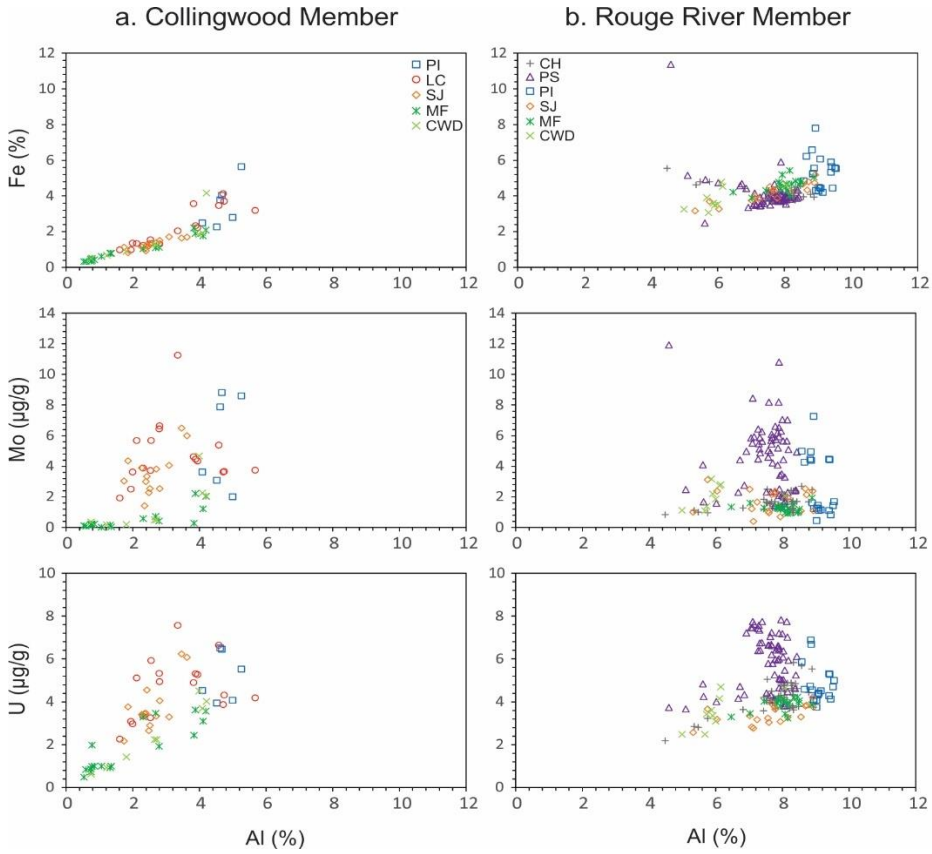

Figure 3.4 Cross plots between Al and selected major and trace elements for the Collingwood Member (a) and Rouge River Member (b).

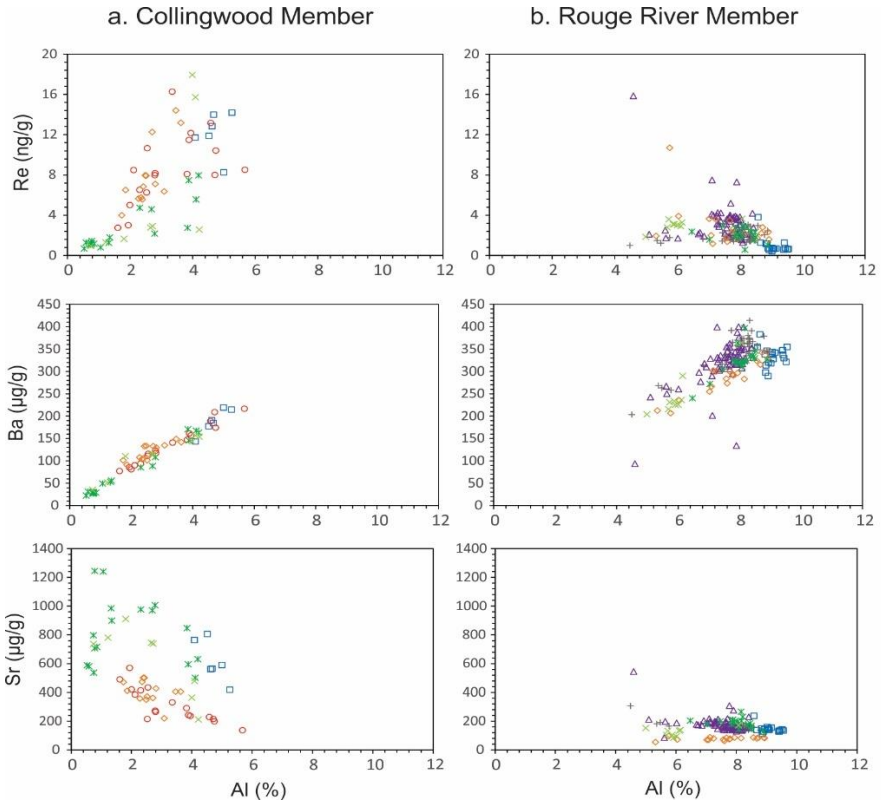

Figure 3.4 Continued.

3.4 Results

3.4.1 Carbon and sulfur contents and C_{org} : P ratios

Carbon and sulfur contents and C_{org} : P (molar) ratios of the Late Ordovician ORS units are summarized below (see Table B1 in Appendix B). The average TOC content of the Collingwood Member (4.52%) is higher than that of the Rouge River Member (2.25%) (Table 3.3; Fig. 3.5–3.11). The average $CaCO_3$ content of the Collingwood Member (55.65%) is higher than that of the Rouge River Member (10.69%). With respect to sulfur contents, the Collingwood Member has a lower average S content (0.92%) than the Rouge River Member (1.43%) (Table 3.3; Fig. 3.5–3.11). With respect to C_{org} : P ratio, the Collingwood Member has a higher average value (90.06) than the Rouge River Member (31.02; Table 3.3).

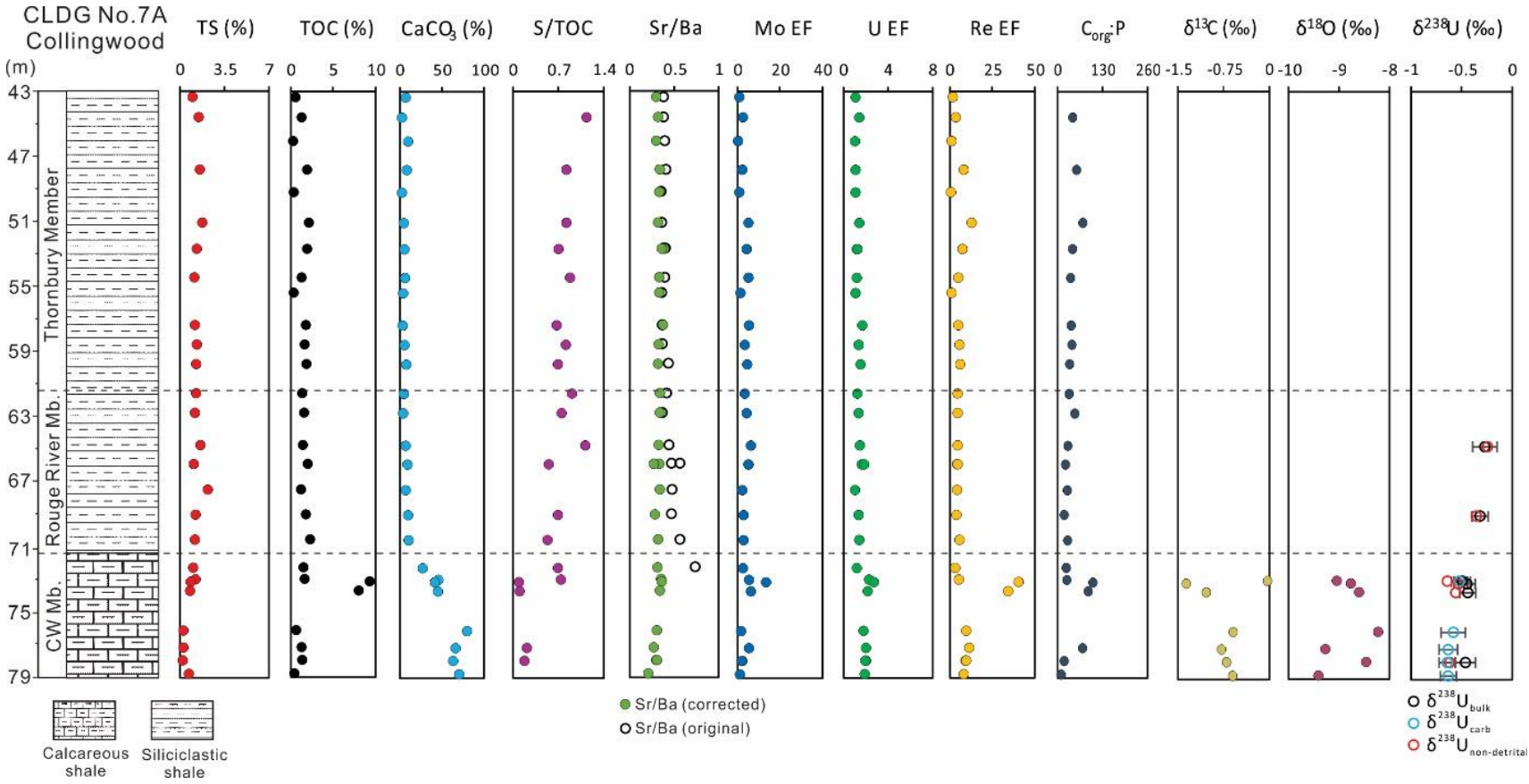

Figure 3.5 Geochemical profile of OGS CLGD No.7A Collingwood (CWD). CW Mb. = Collingwood Member and Fm. = Formation. Samples with original Sr/Ba ratios >1 are not showed in the figure (which applies for the Fig. 3.6–3.11)

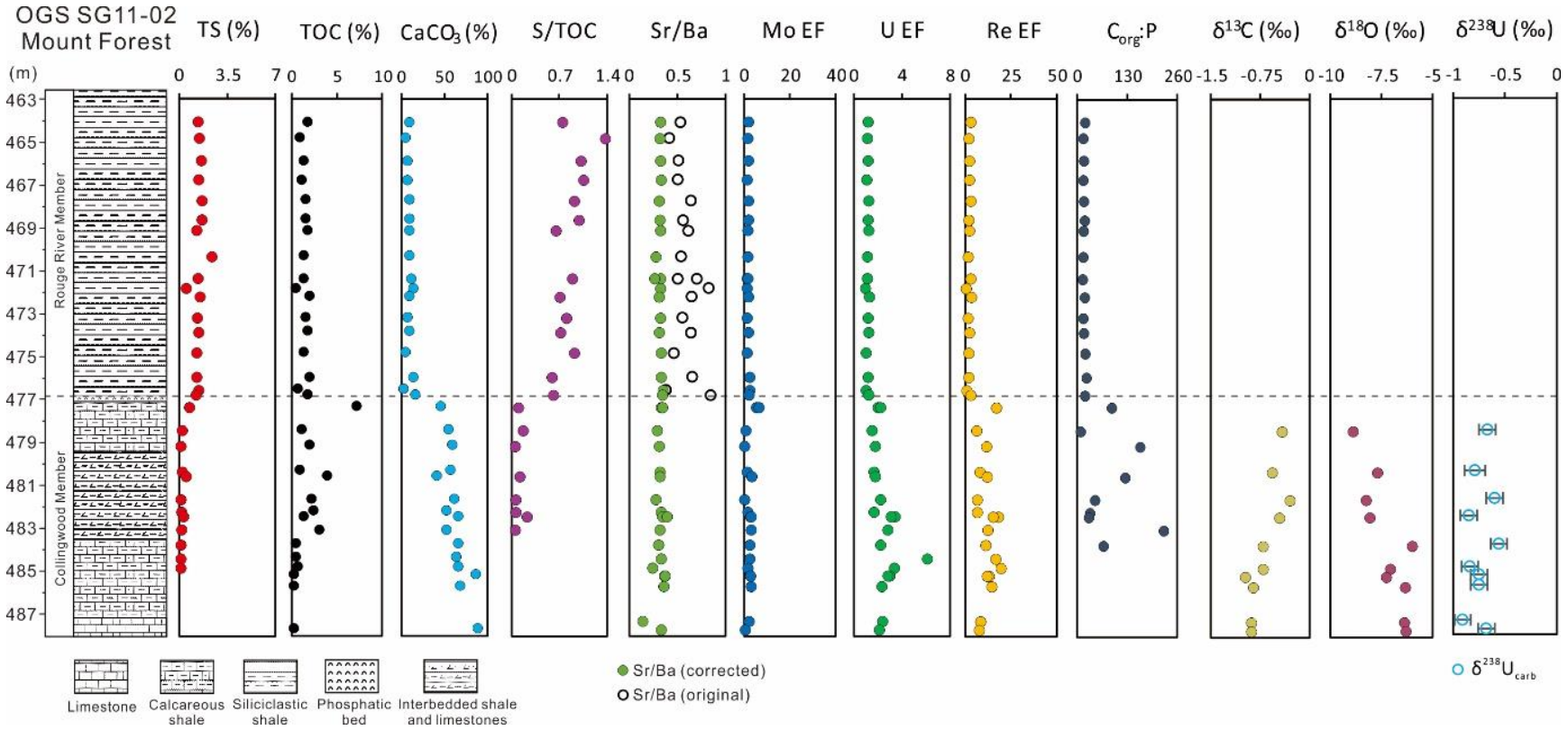

Figure 3.6 Geochemical profiles of OGS-SG11-02 Mount Forest (MF).

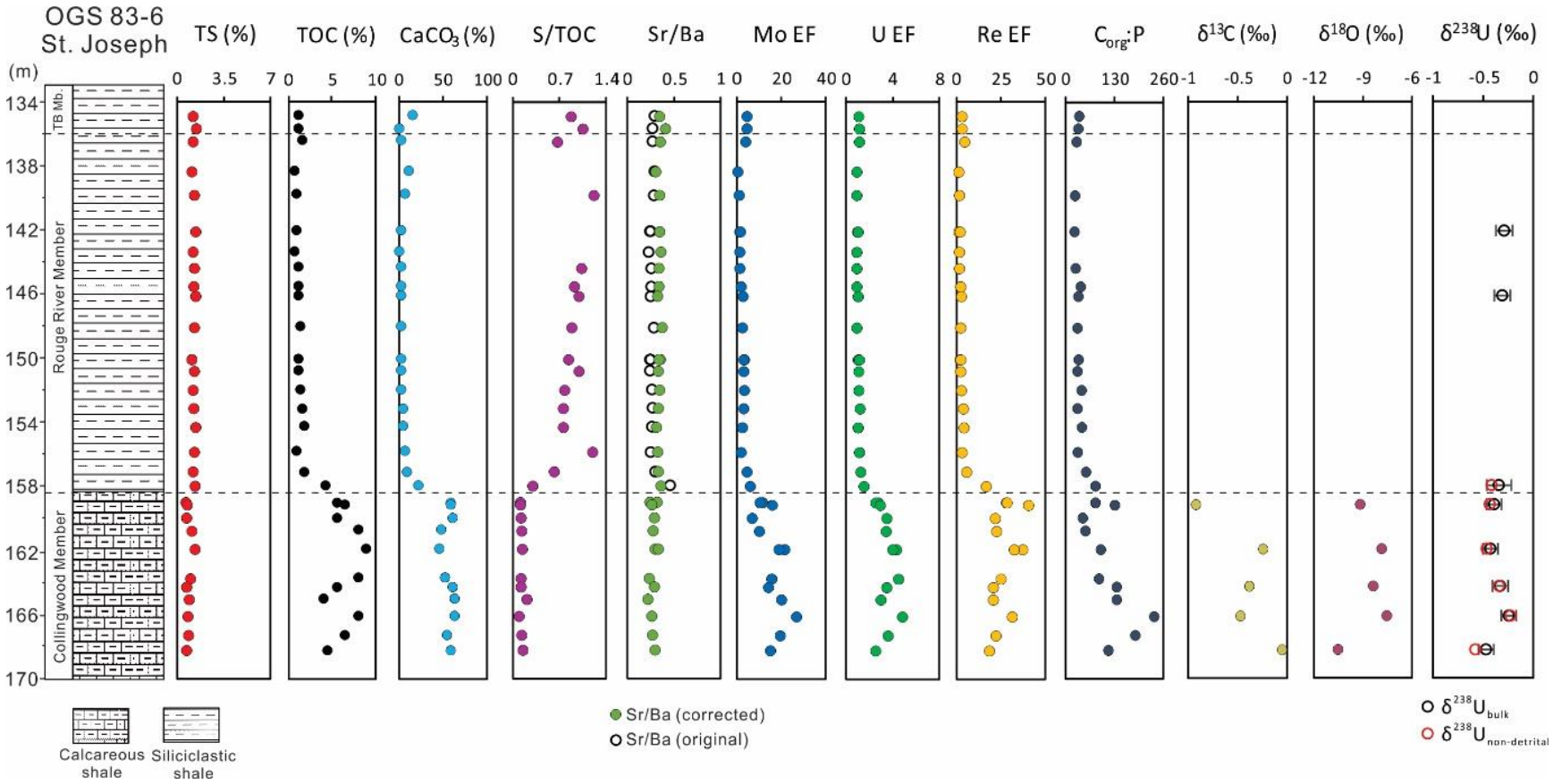

Figure 3.7 Geochemical profiles of OGS 83-6 St. Joseph (SJ). TB Mb. = Thornbury Member.

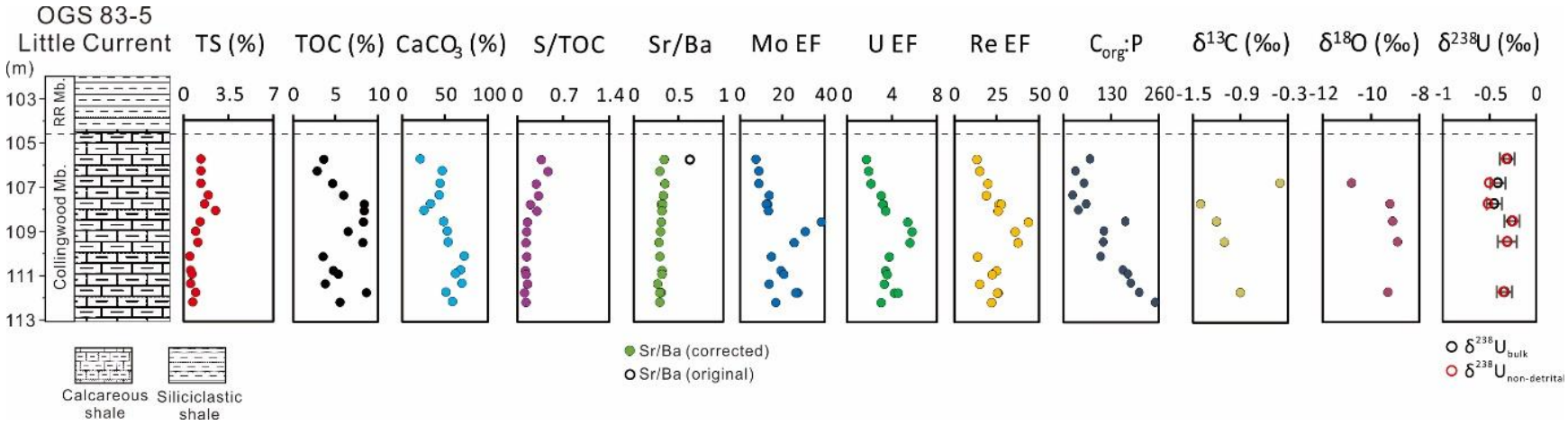

Figure 3.8 Geochemical profiles of OGS 83-5 Little Current (LC). RR Mb. = Rouge River Member.

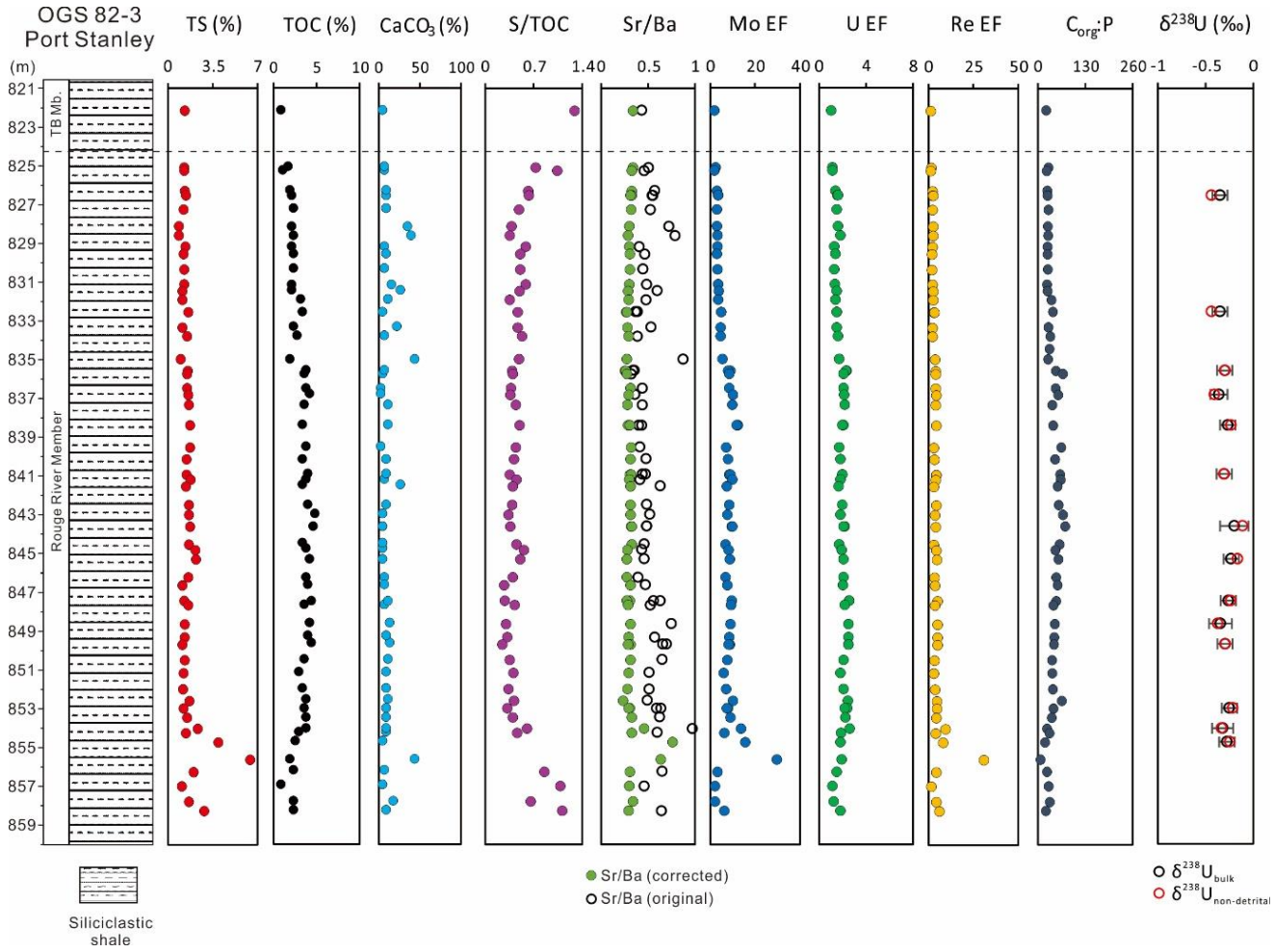

Figure 3.9 Geochemical profiles of OGS 82-3 Port Stanley (PS). TB Mb. = Thornbury Member.

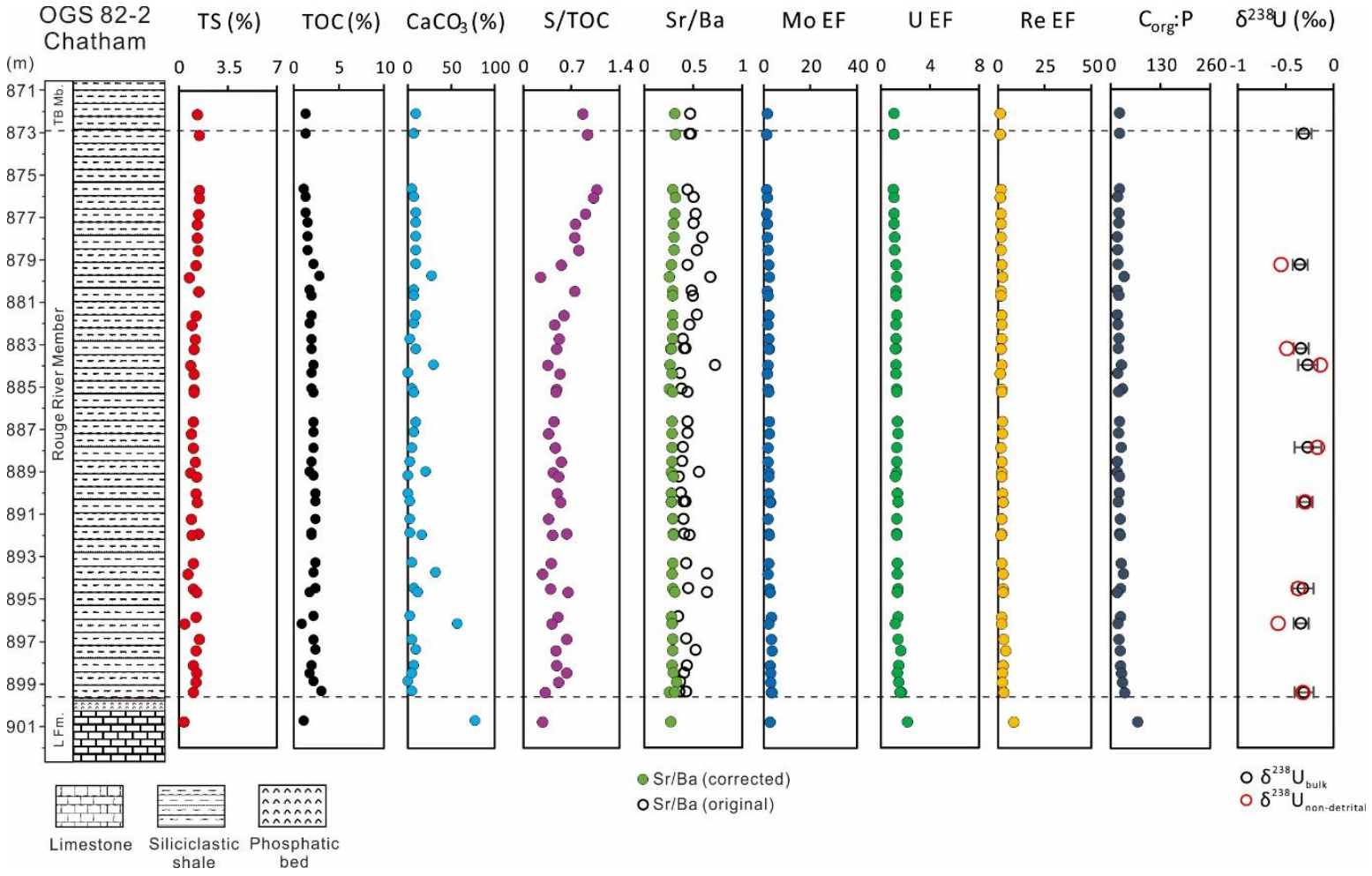

Figure 3.10 Geochemical profiles of OGS 82-2 Chatham (CH). TB Mb. = Thornbury Member and L Fm. = Lindsay Formation.

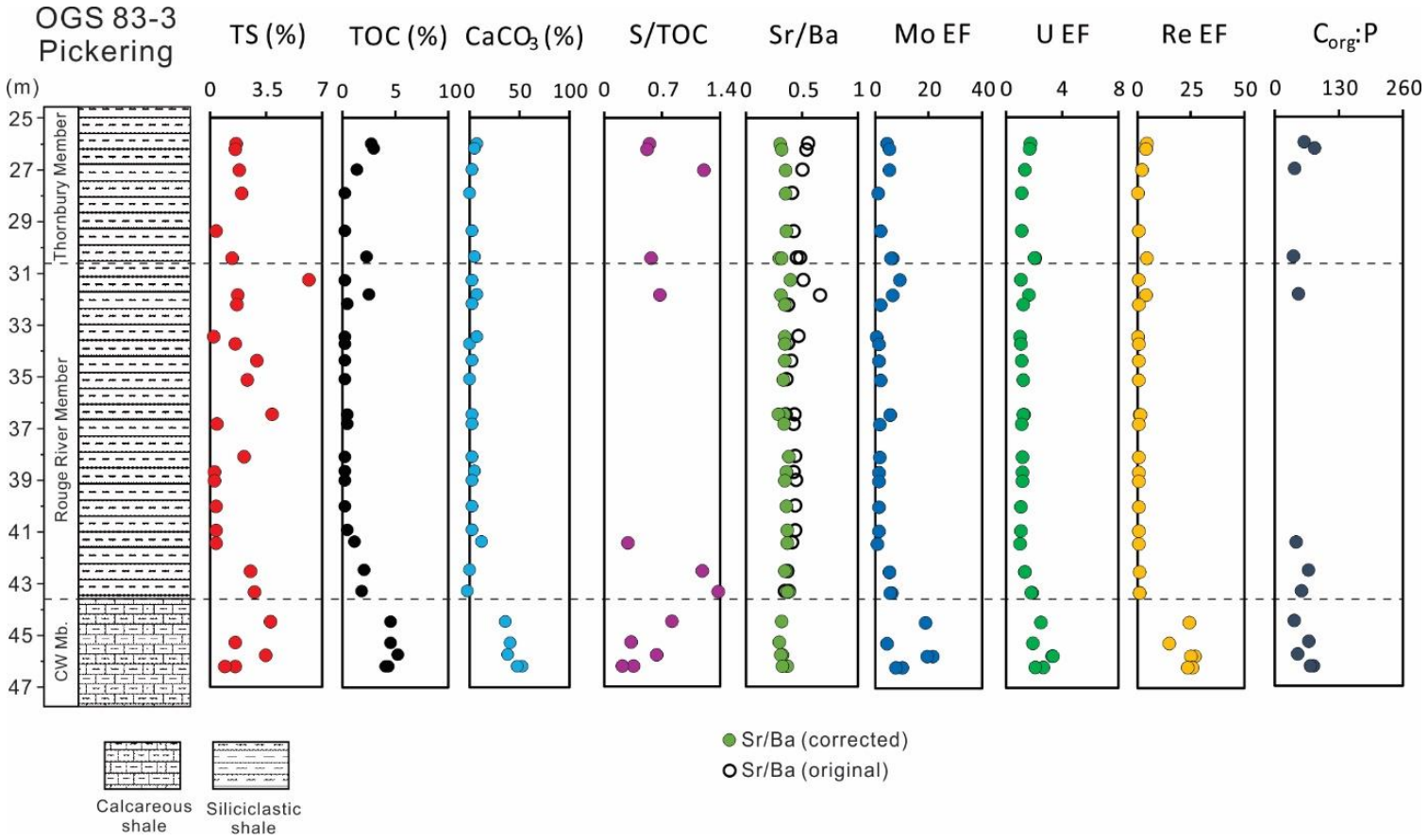

Figure 3.11 Geochemical profiles of OGS 83-3 Pickering (PI). CW Mb. = Collingwood Member.

Table 3.3 Summary of geochemical data among rocks units from each drill core

Stratigraphic Units	Drill cores	S			TOC			$CaCO_3$[p]		S/TOC[#]			C_{org}:P[m,#]		Sr/Ba[o]			Sr/Ba[c]		Mo EF[n]		U EF		Re EF		Ba EF	
		ave	1SD	n	ave	1SD	n[$]	ave	1SD	ave	1SD	n	ave	1SD	ave	1SD	n[^]	ave	1SD	ave	1SD	ave	1SD	ave	1SD	ave	1SD
Cobourg Formation	CH	0.39	N/A	1	1.36	N/A	1	78.36	N/A	0.29	N/A	1	70.70	N/A	4.08	N/A	1	0.27	N/A	2.95	N/A	2.20	N/A	8.45	N/A	1.52	N/A
	MF	N/A	N/A	0	0.44	N/A	1	90.00	N/A	N/A	N/A	0	N/A	N/A	14.92	9.83	2	0.24	0.13	1.38	1.04	2.24	0.19	8.30	0.47	2.07	1.17
	Total	0.39	N/A	1	0.90	0.65	2	84.18	8.23	0.29	N/A	1	70.70	N/A	11.31	9.35	3	0.25	0.10	1.91	1.17	2.23	0.14	8.35	0.35	1.88	0.89
Collingwood Member	PI	2.27	1.26	5	4.73	0.44	5	44.90	6.35	0.47	0.25	5	61.48	17.13	3.51	1.39	5	0.33	0.03	12.56	7.28	2.51	0.54	22.95	4.76	1.25	0.10
	LC	1.17	0.56	15	5.89	2.06	15	49.93	15.27	0.21	0.11	15	117.73	70.09	2.97	1.99	15	0.31	0.02	18.16	8.85	3.59	1.23	24.03	8.99	1.32	0.09
	SJ	0.87	0.21	11	6.55	1.56	11	58.33	5.73	0.14	0.03	11	118.57	56.42	3.59	0.99	11	0.28	0.03	16.19	5.61	3.55	0.74	26.31	7.25	1.50	0.17
	MF	0.26	0.20	12	2.03	1.85	14	61.79	11.19	0.11	0.06	8	91.00	75.73	17.91	10.83	14	0.32	0.03	2.31	1.40	2.57	1.20	12.57	4.36	1.29	0.14
	CWD	0.63	0.38	7	3.23	1.36	7	59.06	14.76	0.26	0.27	5	61.86	37.14	8.28	7.33	7	0.31	0.05	5.13	4.22	2.13	0.30	16.93	####	1.37	0.28
	Total	0.92	0.76	50	4.52	2.75	52	55.65	12.87	0.21	0.17	44	100.34	63.12	7.89	8.84	52	0.31	0.04	11.18	9.00	3.01	1.13	20.37	9.66	1.35	0.17
Rouge River Member	CH	1.15	0.24	41	2.13	0.39	42	11.67	10.70	0.56	0.18	41	22.70	4.57	0.49	0.18	42	0.29	0.01	2.26	0.55	1.28	0.12	2.16	0.53	1.41	0.07
	PS	1.61	0.82	55	3.26	0.92	55	13.02	9.51	0.55	0.41	55	40.79	15.02	0.66	0.75	55	0.32	0.08	7.19	4.36	1.86	1.40	4.24	3.94	1.33	0.19
	PI	1.77	1.61	17	0.87	0.69	17	5.01	3.26	0.88	0.50	4	53.55	10.64	0.44	0.07	17	0.36	0.02	3.03	2.58	1.22	0.22	0.91	0.82	1.15	0.07
	SJ	1.28	0.09	17	1.55	0.79	17	7.05	4.98	0.90	0.27	15	37.59	14.10	0.28	0.05	17	0.34	0.02	2.71	1.40	1.08	0.16	3.68	3.56	1.20	0.06
	MF	1.43	0.35	17	1.58	0.45	17	11.23	3.73	0.91	0.29	15	18.74	2.69	0.59	0.13	17	0.33	0.02	1.83	0.42	1.17	0.09	2.33	0.80	1.26	0.06
	CWD	1.35	0.38	8	1.63	0.35	8	10.28	7.28	0.89	0.43	8	29.72	9.16	0.51	0.12	8	0.33	0.02	3.70	1.39	1.34	0.18	4.45	0.65	1.26	0.08
	Total	1.43	0.76	155	2.25	1.08	156	10.69	8.70	0.66	0.37	138	32.49	14.62	0.53	0.47	156	0.32	0.05	4.17	3.59	1.45	0.41	3.07	2.89	1.31	0.15

Table 3. Continued.

Stratigraphic Units	Drill cores	S			TOC			$CaCO_3$[p]		S/TOC[#]			C_{org}:P[m,#]		Sr/Ba[o]			Sr/Ba[c]		Mo EF[n]		U EF		Re EF		Ba EF	
		ave	1SD	n	ave	1SD	n[$]	ave	1SD	ave	1SD	n	ave	1SD	ave	1SD	n[^]	ave	1SD	ave	1SD	ave	1SD	ave	1SD	ave	1SD
Thornbury Member	CH	1.33	N/A	1	1.53	N/A	1	11.07	N/A	0.87	N/A	1	23.59	N/A	0.47	N/A	1	0.31	N/A	1.63	N/A	1.10	N/A	1.48	N/A	1.31	N/A
	PS	1.33	N/A	1	1.03	N/A	1	6.17	N/A	1.29	N/A	1	22.64	N/A	0.44	N/A	1	0.34	N/A	1.85	N/A	1.06	N/A	1.38	N/A	1.20	N/A
	PI	1.47	0.56	6	1.84	1.17	6	5.91	2.23	0.71	0.33	4	54.99	20.10	0.48	0.06	6	0.33	0.03	4.11	2.04	1.54	0.38	2.73	1.89	1.24	0.11
	SJ	1.33	0.16	2	1.38	0.01	2	10.05	10.30	0.96	0.12	2	35.44	1.56	0.28	0.01	2	0.38	0.05	4.68	0.10	1.14	0.02	3.10	0.03	1.08	0.13
	CWD	1.34	0.24	9	1.29	0.70	12	5.77	2.35	0.82	0.15	8	46.14	12.38	0.39	0.02	12	0.33	0.03	3.01	1.90	1.26	0.22	4.87	3.61	1.24	0.09
	Total	1.39	0.34	19	1.45	0.81	22	6.40	3.36	0.84	0.23	16	44.14	15.97	0.41	0.07	22	0.34	0.03	3.34	1.88	1.31	0.29	3.82	3.04	1.23	0.10

[$] number of samples for TOC is the same for $CaCO_3$

[^] number of samples for Sr/Ba is the same for the following geochemical data

[#] samples with < 1% TOC are excluded from calculation

[o] Sr/Ba ratios are calculated based on elemental data from Table 1

[c] Sr/Ba ratios are corrected for carbonate-associated Sr by $Sr_{carb\text{-}corrected} = (Sr/Al)_{background} \times Al_{sample}$

[m] Molar ratios of C_{org}:P are calculated as C_{org}:P = (TOC/12.01)/(P/30.97)

[n] Trace element (TE) enrichment factors (EF) are calculated as: TE EF = (TE/Al)sample/(TE/Al)local detrital background; local detrital backgrounds are from Table 2 and see text for details.

3.4.2 Sedimentary iron speciation

Sedimentary Fe speciation yields Fe_{HR}/Fe_T ratios of 0.07–0.63 and Fe_{py}/Fe_{HR} ratios of 0.00–0.76 (Table B3). For the Collingwood Member, except two samples from the CWD core with high Fe_{HR}/Fe_T of 0.39–0.63 and Fe_{py}/Fe_{HR} of 0.69–0.76, all the other samples have Fe_{HR}/Fe_T values lower than 0.38 and Fe_{py}/Fe_{HR} lower than 0.7. All the Rouge River Member samples have Fe_{HR}/Fe_T values lower than 0.30 and Fe_{py}/Fe_{HR} values between 0.00 and 0.85.

3.4.3 Trace metal enrichment factors

Because of the dilution effect of carbonates, elemental concentrations, especially from the carbonate-rich Collingwood Member, do not reflect the actual enrichments of elements. Therefore, the Al-normalized enrichment factors of those elements are reported here (Fig. 3.5–3.11; Table 3.3 and B2). The Collingwood Member has higher average Mo (11.2), U (3.0), and Re (20.4) EF than the Rouge River Member (Mo EF = 4.2, U EF = 1.5; Re EF = 3.1). Spatially, the Collingwood Member from the PI, LC, and SJ cores has higher average Mo (> 12.6) and Re (> 23.0) EF than those from the MF and CWD cores (Mo EF < 5.2, Re EF < 17.0). The average U EF values of the Collingwood Member from the LC and SJ cores (> 3.5) are higher than those from other cores (< 2.6). For the Rouge River Member, except for similar average Re EF between the PS (4.2) and CWD (4.5) cores, relatively higher average Mo (7.2), U (1.9), and Re (4.2) EF are observed in the PS core than the other cores (Mo EF < 4.2, U EF < 1.5, Re EF < 3.7).

3.4.4 Carbon and oxygen isotope compositions

The carbon and oxygen isotope compositions of the Collingwood Member range from −1.4‰ to 0.0‰ and from −10.8‰ to −6.0‰, respectively (Table B4). The average $\delta^{13}C$ of the Collingwood Member from the MF, CWD, SJ, and LC cores are −1.4 ± 0.2‰ (1SD, n = 8), −0.8 ± 0.4‰ (1SD, n = 7), −0.4 ± 0.3‰ (1SD, n = 5), and −1.0 ± 0.4‰ (1SD, n = 5), respectively. The average $\delta^{18}O$ of the Collingwood Member from the MF, CWD, SJ, and LC cores are −7.4 ± 1.0‰ (1SD, n = 8), −8.6 ± 0.6‰ (1SD, n = 7), −8.7 ± 1.2‰ (1SD, n = 5), and −9.4 ± 0.8‰ (1SD, n = 5), respectively.

3.4.5 Uranium isotope compositions

The bulk $\delta^{238}U$ data were corrected for detrital materials based on local detrital background. Among the samples measured for bulk $\delta^{238}U$, three Rouge River samples (C43, SJ6, SJ10) have U EF less than 1.1, suggesting most U in these samples are in detrital minerals (Table B2 and B5). These samples have an average bulk $\delta^{238}U$ of −0.30 ± 0.01‰ (1SD, n = 3) that is indistinguishable from the upper continental crust (−0.29 ± 0.09‰, 1SD; Telus et al., 2012; Tissot and Dauphas, 2015; Wang et al., 2018). Therefore, this average $\delta^{238}U$ represents the best estimate of local detrital background in this study and is used to correct for detrital U following the equation below:

$$\delta^{238}U_{non-detrital} = \delta^{238}U_{sample} - (Al/U)_{sample} \times \frac{\delta^{238}U_{detrital} - \delta^{238}U_{sample}}{(Al/U)_{detrital} - (Al/U)_{sample}}$$

where detrital U/Al (0.42 µg/g/%) is the local background (Table 3.2). This correction is not applied for samples with carbonate $\delta^{238}U$ because 1N HCl was used to leach carbonate U with the least dissolution of detrital U.

The $\delta^{238}U$ data for the Collingwood Member and Rouge River Member are summarized below. The Collingwood Member (with TOC mostly > 3%) from each drill core does not show any specific trends in $\delta^{238}U_{non\text{-}detrital}$, with an overall average of −0.44 ± 0.13‰ (1SD, n = 15). The average $\delta^{238}U_{non\text{-}detrital}$ of the Collingwood Member from the CWD, SJ and LC cores are −0.59 ± 0.05‰ (1SD, n = 4), −0.41 ± 0.13‰ (1SD, n = 5), and −0.37 ± 0.11‰ (1SD, n = 6), respectively (Table B5). For the Collingwood Member samples that have both bulk and carbonate $\delta^{238}U$ data, the $\delta^{238}U_{carb}$ and $\delta^{238}U_{non\text{-}detrital}$ of the same sample yield identical values given the uncertainties (Fig. 3.12). Average $\delta^{238}U_{carb}$ values of the Collingwood Member from the MF and CWD cores (with TOC mostly < 2%) are −0.60 ± 0.05‰ (1SD, n = 5) and −0.73 ± 0.11‰ (1SD, n = 8), respectively (Table B7). Larger $\delta^{238}U_{carb}$ variations are observed in the MF core and there are no specific stratigraphic trends in $\delta^{238}U_{carb}$ for both cores. The overall average $\delta^{238}U_{non\text{-}detrital}$ of the Rouge River Member is −0.32 ± 0.12‰ (1SD, n = 25), except for three samples that represent detrital background. The Rouge River Member from the CH, PS,

SJ, and CWD cores has similar average $\delta^{238}U_{non\text{-}detrital}$ of −0.36 ± 0.12‰ (1SD, n = 8), −0.29 ± 0.10‰ (1SD, n = 13), −0.42 ± 0.12‰ (n = 1), and −0.30 ± 0.08‰ (1SD, n = 2), respectively (Table B7), with no obvious $\delta^{238}U_{non\text{-}detrital}$ stratigraphic trends in each drill core. Although the average $\delta^{238}U_{non\text{-}detrital}$ values of the Collingwood Member (−0.44 ± 0.13‰) and Rouge River Member (−0.32 ± 0.12‰) are similar, the Collingwood Member shows a positive correlation between $\delta^{238}U_{non\text{-}detrital}$ and elemental redox proxies whereas such correlation is absent for the Rouge River Member (Fig. 3.14 and 3.21). This suggests that variations in local redox conditions were significant enough to influence $\delta^{238}U_{non\text{-}detrital}$ of the Collingwood Member but were smaller and had less effect on the $\delta^{238}U_{non\text{-}detrital}$ of the Rouge River Member (see details in Section 3.5.2.1).

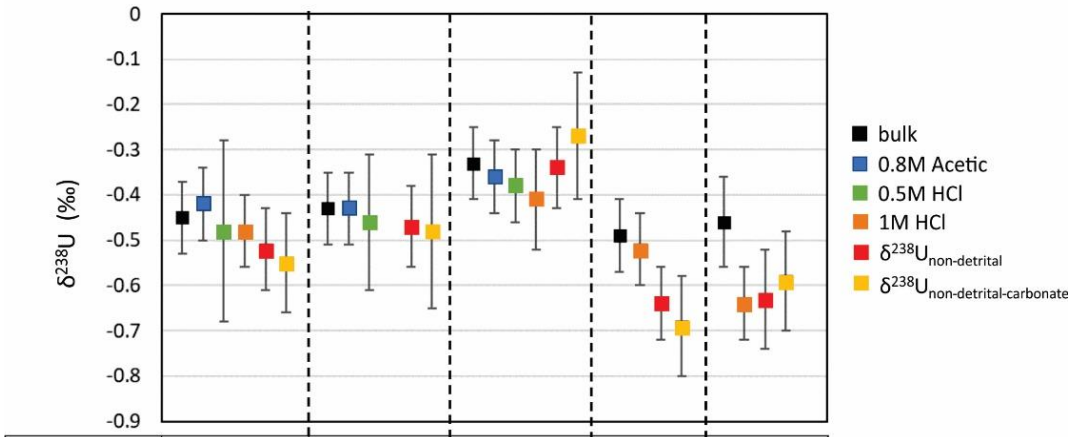

Sample	LC5	SJ24	SJ26	CW21	CW29
TOC (%)	8.41	8.99	5.77	1.67	1.36
$CaCO_3$ (%)	32.92	48.25	63.75	46.33	63.33
U EF	3.27	4.31	3.48	2.29	2.03

Figure 3.12 Leaching experiment of $\delta^{238}U$ in carbonate fractions (using 0.8N acetic acid, 0.5N and 1N HCl) and other fractions (non-detrital fraction and non-detrital-carbonate fraction).

3.5 Discussion

3.5.1 Reconstruction of local depositional environment

3.5.1.1 Paleosalinity conditions

Both Sr/Ba ratios and S/TOC ratios are used to constrain paleosalinity conditions during the deposition of Collingwood Member and Rouge River Member. The overall average corrected Sr/Ba ratios of the Collingwood Member and Rouge River Member from all cores are 0.31 ± 0.04 and 0.32 ± 0.05, respectively (Table 3.3). For both members, there is no significant difference in the corrected Sr/Ba ratios between cores (Table 3.3, Fig. 3.13). The corrected Sr/Ba ratios from both members indicate brackish conditions during deposition of the Collingwood Member and Rouge River Member (Wei and Algeo, 2020). With respect to S/TOC ratios, excluding samples with < 1% TOC, the Collingwood Member and Rouge River Member have average S/TOC ratios of 0.21 ± 0.17 (1SD) and 0.66 ± 0.37 (1SD), respectively (Table 3.3, Fig. 3.13), all of which are indicative of brackish/marine conditions during deposition (Wei and Algeo, 2020).

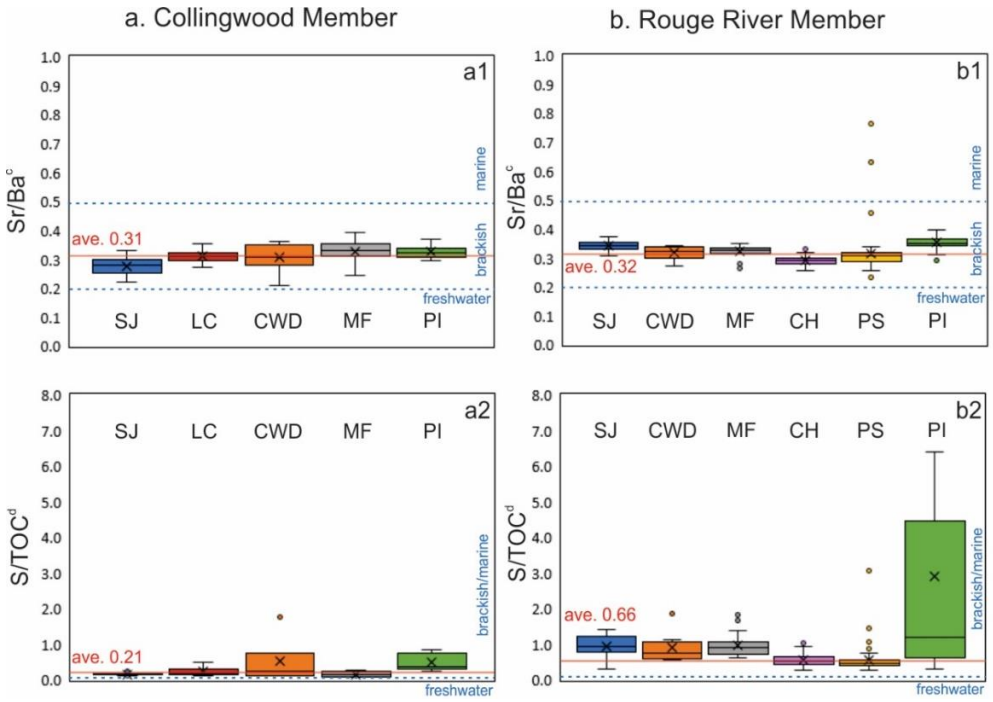

Figure 3.13 Boxplots of paleosalinity proxies (Sr/Ba and S/TOC) of samples from each drill core for the Collingwood Member (a) and Rouge River Member (b). Sr/Ba^c represents the Sr/Ba ratios were corrected for the carbonate-associated Sr and S/TOC^d represents the S/TOC ratios for samples with >1% TOC. Horizontal line and cross mark the median and average of the core, respectively. Red lines are the overall average (ave.) values of respective proxies of that unit. Blue dashed lines are the thresholds of freshwater, brackish, and marine conditions based on compilation of Sr/Ba and S/TOC ratios from modern environments in Wei and Algeo (2020).

The Sr/Ba and S/TOC paleosalinity proxies consistently suggest some water exchange between the local basin watermass and the open ocean during deposition of the Collingwood Member and Rouge River Member (brackish/marine conditions, Fig. 3.13). This conclusion is consistent with previous inorganic ($^{87}Sr/^{86}Sr$ data, Hannigan et al., 2010) and organic

geochemical studies (kerogen types, Macauley and Snowdon, 1984; Obermajer et al., 1999; Béland-Otis, 2015) that suggest marine conditions during deposition.

3.5.1.2 Paleoredox conditions

3.5.1.2.1 The Collingwood Member

Local water redox conditions are evaluated by trace metal EF vs TOC (and S), trace metal EF covariations, Fe speciation, and the C_{org} : P ratios. The relationships between multiple trace metal EF and TOC (and also S) are firstly examined for the Collingwood Member. It is noticed that ancient organic-rich sedimentary rocks with low trace metal enrichments and TOC contents (< 2.5%) were deposited under oxic-suboxic conditions, whereas those with high trace metal enrichments and TOC contents (> 10%) were under euxinic conditions (Algeo and Maynard, 2004). For the Collingwood Member, Mo, U, and Re EFs are relatively low and constant when TOC is below 3%, whereas there are increasing trace metal EFs with TOC > 3% (Fig. 3.14). Integrating the drill core information, these patterns suggest that the Collingwood Member was deposited from oxic-suboxic bottom waters in the shallower regions of the Michigan and Appalachian basins (core MF and CWD near the Algonquin Arch; Algeo and Maynard, 2004; Tribovillard et al., 2006). In contrast, the Collingwood Member from the deeper water environment was deposited under anoxic conditions (Algeo and Maynard, 2004; Tribovillard et al., 2006).

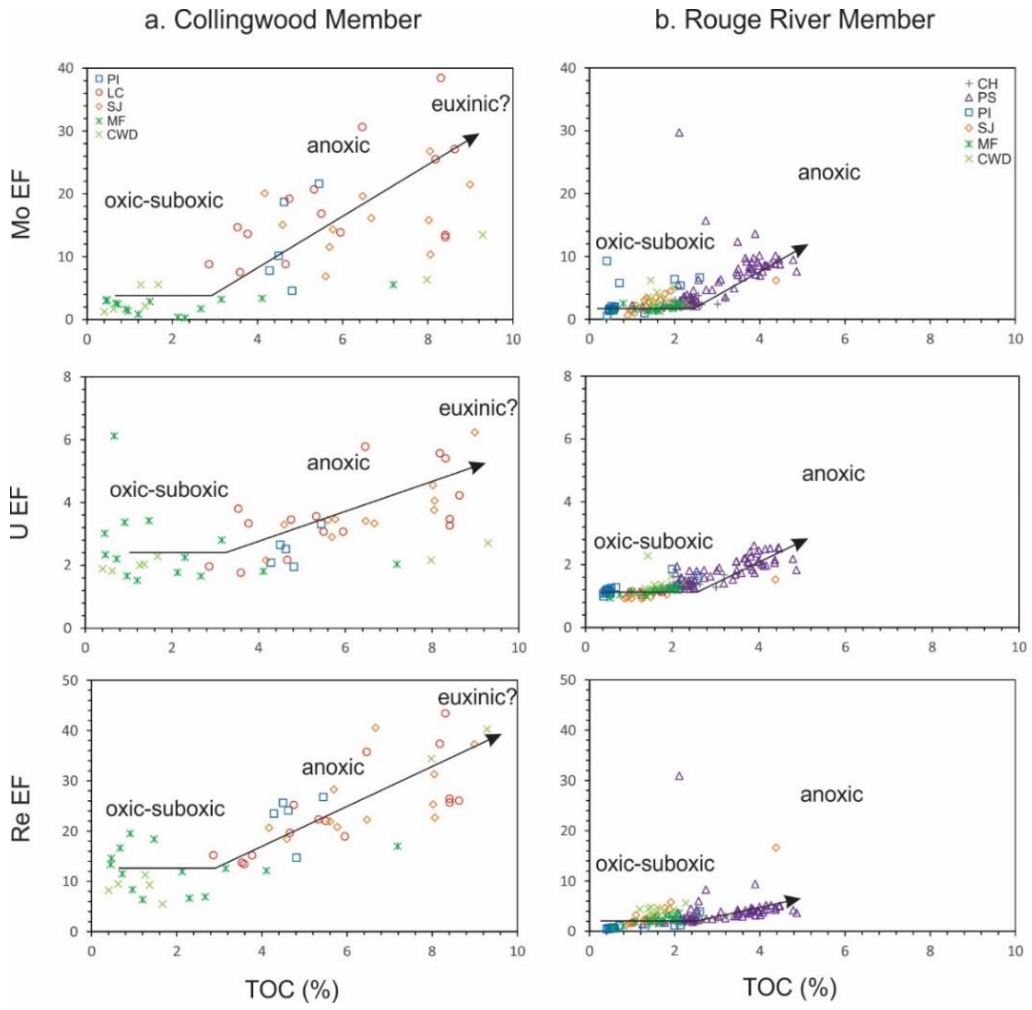

Figure 3.14 Diagrams showing trace metal enrichments (Mo, U, Re) versus TOC for a) Collingwood Member and b) Rouge River Member. Illustrations are from Tribovillard et al. (2006).

Two positive correlation trends with different slopes are observed between each trace metal EF and total S content, which are particularly obvious for samples from the LC core (Fig. 3.15). Stratigraphically lower samples from the LC core show a positive correlation with a steeper slope, whereas stratigraphically higher samples show a positive correlation with a shallower slope. This observation suggests that stratigraphically lower samples were likely

deposited under more reducing conditions. The deeper water Collingwood Member samples from the Michigan Basin (the SJ core) generally follow the one with a steeper slope and those from the Appalachian Basin (the PI core) mostly follow the one with a shallower slope, suggesting relatively more reducing deeper water redox conditions in the Michigan Basin than the Appalachian Basin. In contrast, samples from shallower waters of the basins (i.e., from the MF and CWD cores) have much less trace metal enrichments and do not follow either positive correlation, suggest predominantly oxic-suboxic bottom water conditions.

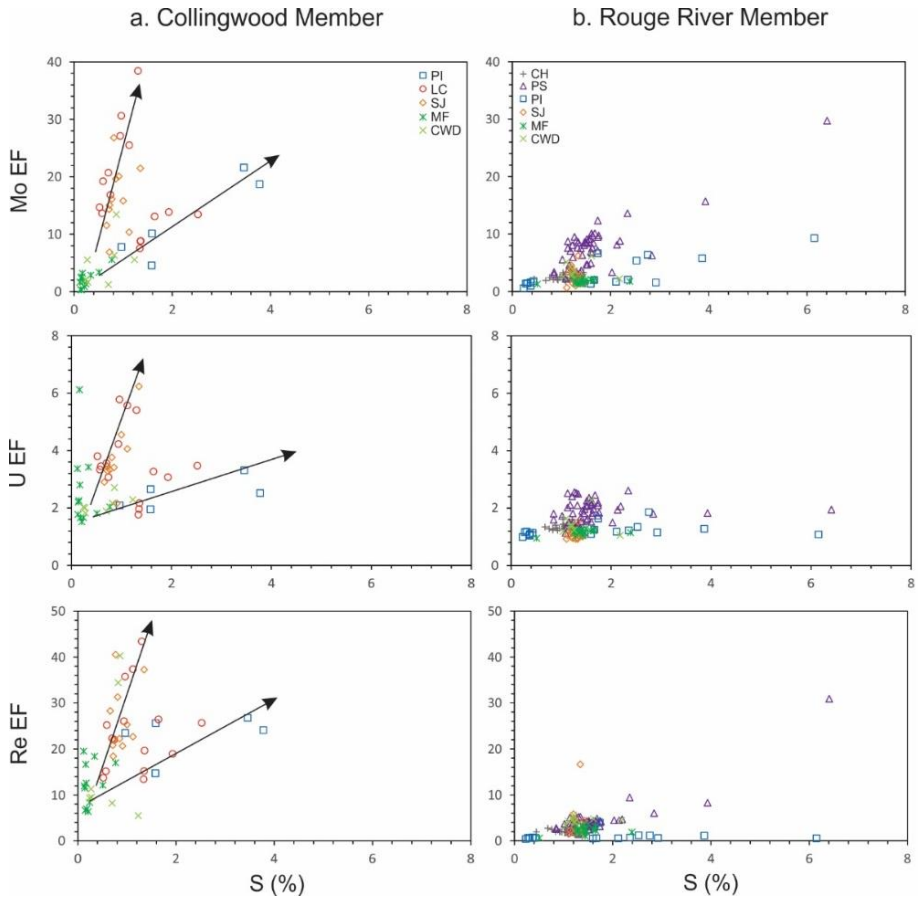

Figure 3.15 Diagrams showing trace metal enrichments (Mo, U, Re) versus S for a) Collingwood Member and b) Rouge River Member. Two positive correlations trends are observed and illustrated for each plot of the Collingwood Member.

Local bottom water redox conditions of the Collingwood Member are also revealed by the covariations of Mo-U EF and Mo-Re EF (Fig. 3.16). Faster accumulation of Mo over U exhibits a pattern that is similar to the modern Cariaco Basin, implying the operation of a particulate Fe-Mn shuttle that accelerates the Mo enrichments (Fig. 3.16; Algeo and Tribovillard, 2009). The shallower water Collingwood Member samples from the CWD and MF cores have Mo/U EF ratios that span 0.3× to 1× the modern seawater Mo/U ratio (Mo/U_{SW}), suggesting that the chemocline was mostly below the sediment-water interface (SWI) and the bottom waters were predominantly oxic to suboxic (Algeo and Tribovillard, 2009). In comparison, the deeper Collingwood Member samples from the PI, LC, and SJ cores have Mo/U EF ratios that are mostly ~1–3× Mo/U_{SW}, suggesting the chemocline was likely at or above the SWI (Algeo and Tribovillard, 2009). A positive correlation is observed between Mo and Re EFs (Fig. 3.16). Samples with higher Mo/U EF ratios (> 1× Mo/U_{SW}) have higher Mo and Re EFs than those with lower Mo/U EF ratios (<1× Mo/U_{SW}), suggesting more O_2-deficient deeper water conditions in the Michigan and Appalachian basins than shallower waters (Fig. 3.16).

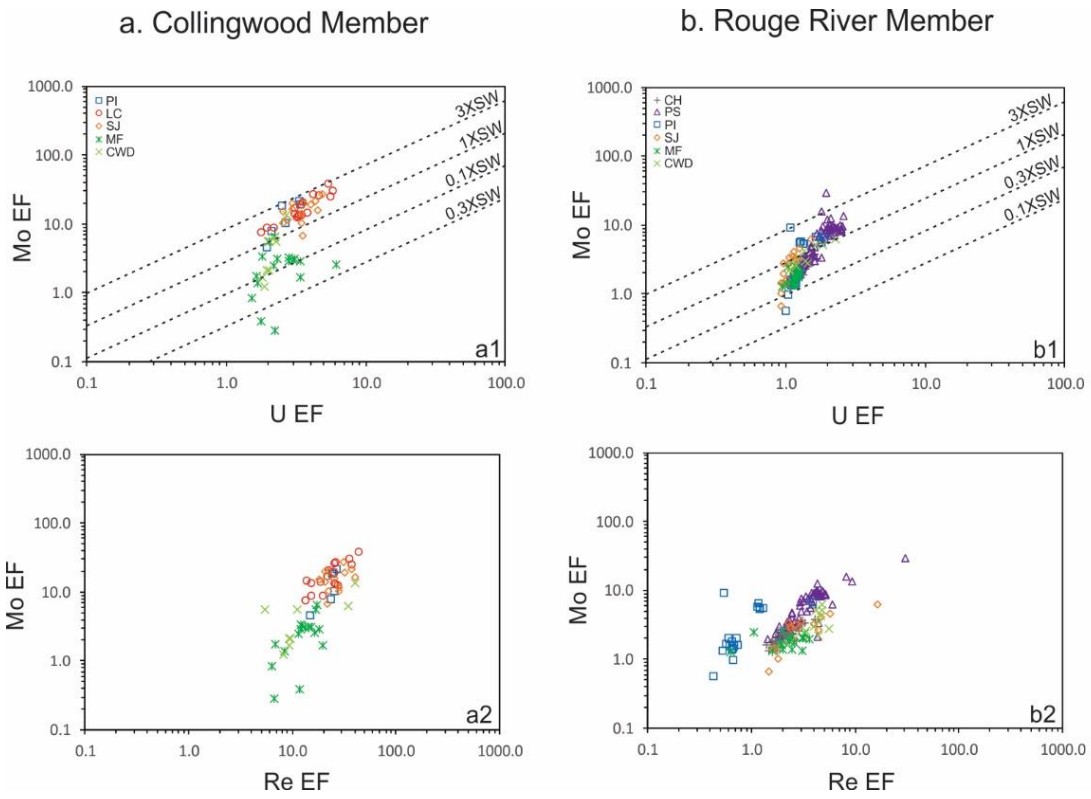

Figure 3.16 Redox sensitive trace metal covariations between Mo EF and U EF, and Mo EF and Re EF for the Collingwood Member (a) and Rouge River Member (b). Dashed lines represent fractions (0.1×, 0.3×, 1×, and 3×) of modern seawater (SW) Mo/U ratios (Algeo and Tribovillard, 2009).

Sedimentary Fe speciation data show that most Collingwood Member samples have Fe_{HR}/Fe_T between 0.12 and 0.36 (except for two samples from CWD) (Fig. 3.17). Because the Fe_{HR}/Fe_T ratios of samples are mostly equivocal (0.22–0.38; either oxic or anoxic conditions), other lines of evidence (e.g., trace metal EF) are needed to infer local redox conditions. Considering trace metal EF and covariation patterns that suggest predominantly anoxic for deeper water samples and oxic-suboxic for shallower water samples, the interpretation of Fe_{HR}/Fe_T ratios should be generally consistent with these interpretations. For the anoxic deeper

water samples, the low Fe_{py}/Fe_{HR} ratios (< 0.7) suggest ferruginous bottom waters. The two CWD samples with Fe_{HR}/Fe_T of 0.39 and 0.63 and Fe_{py}/Fe_{HR} of 0.69 and 0.76 could be deposited under either ferruginous or euxinic bottom waters. Considering their generally lower trace metal EF compared with those from the LC and SJ cores, non-euxinic bottom water redox conditions are preferred for the two CWD samples. Such high Fe_{py}/Fe_{HR} ratios might also reflect that sulfurization occurred during diagenesis and thus increased Fe_{py}/Fe_{HR} ratios (Pasquier et al., 2022).

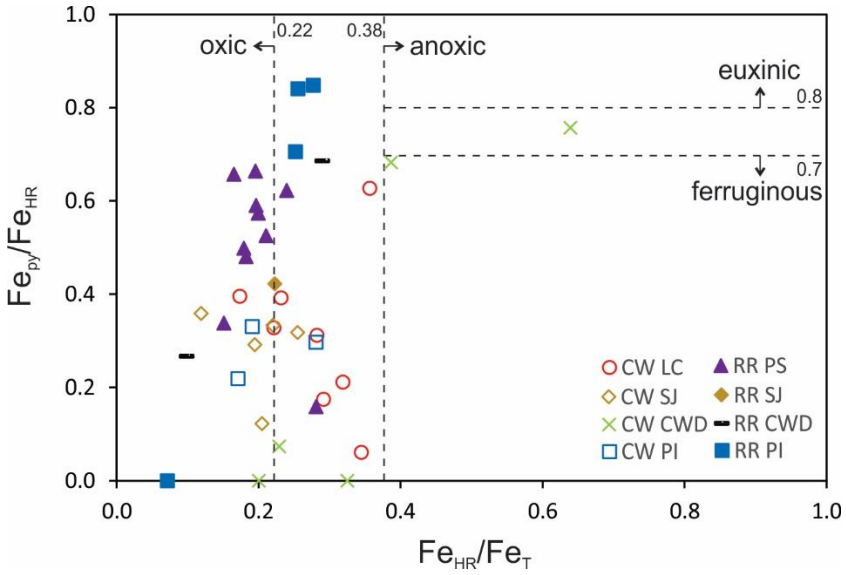

Figure 3.17 Sedimentary Fe speciation for the Collingwood Member and Rouge River Member. Boundaries (dashed lines) between oxic and anoxic and between ferruginous and euxinic are from Poulton and Canfield (2011).

The interpretations of the C_{org} : P ratios for the Collingwood Member are generally consistent with the above-mentioned redox proxies (Fig. 3.18; Algeo and Ingall, 2007; Algeo and Li, 2020). The overall average C_{org} : P ratio of the Collingwood Member is 100.34, which is larger than the threshold of 50 and thus suggests anoxic conditions. Among each cores, the

samples from the LC and SJ cores contains higher average C_{org} : P ratios (> 100) than those from the other cores, suggesting more reducing conditions. Collectively, the Collingwood Member was deposited under anoxic conditions (ferruginous at maximum) in the deeper waters of the basins and mostly under oxic-suboxic conditions in the shallower waters.

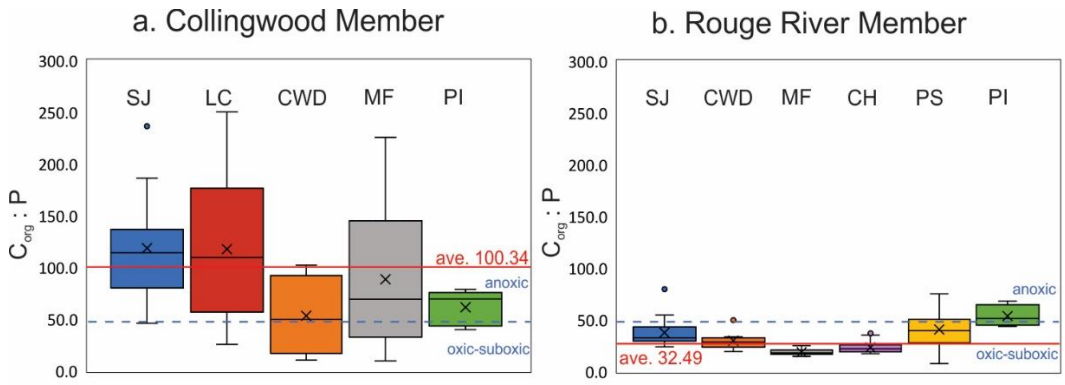

Figure 3.18 Boxplots of C_{org} : P of samples from each drill core for the Collingwood Member (a) and Rouge River Member (b). Horizontal line and cross mark the median and average of the core, respectively. Red lines are the overall average C_{org} : P values of that unit. Blue dashed line is the threshold for oxic-suboxic and anoxic conditions in Algeo and Ingall (2007).

3.5.1.2.2 The Rouge River Member

Similar approaches (i.e., RSTM EF vs TOC/S, RSTM EF covariations, Fe speciation, and C_{org} : P ratios) are applied to infer bottom water redox conditions during Rouge River Member deposition. Trace metal enrichments are generally minimal when TOC is below 2.5% (the CH, PI, SJ, MF, and CWD cores), suggesting predominantly oxic-suboxic bottom water conditions (Fig. 3.14; Tribovillard et al., 2006). The Mo, U, and Re EFs are only slightly elevated with higher TOC contents (> 2.5%), particularly for samples from the PS core, suggesting locally more reducing bottom water conditions (Fig. 3.14). The majority of Rouge River Member samples contain S contents of < 3%, except for four samples. A positive

correlation between Mo EF and S is observed for the Rouge River Member from the PS core, whereas no obvious correlations between trace metal EF and S are observed for the samples from the other cores. This suggests relatively more reducing bottom water conditions for the Rouge River Member from the PS core than the other cores. Compared with the Collingwood Member, relatively less reducing bottom waters are inferred for the Rouge River Member during deposition (Fig. 3.15).

Generally less reducing bottom water redox conditions for the Rouge River Member are further supported by Mo-U EF and Mo-Re EF covariations. The Mo-U EF covariation pattern suggests the operation of a particulate Fe-Mn shuttle (Fig. 3.16; Algeo and Tribovillard, 2009). The Mo/U EF ratios of Rouge River Member are across 0.3× and 1× Mo/U_{SW}, suggesting predominantly oxic-suboxic conditions (Algeo and Tribovillard, 2009). Some Rouge River Member samples, especially from the PS core, contain Mo/U EF ratios above the Mo/U_{SW}, but the Mo and U EFs are not as high as those of the Collingwood Member deposited in the deeper waters (e.g., LC and SJ cores), suggesting generally less reducing bottom waters than during Collingwood Member deposition (Fig. 3.16; Algeo and Tribovillard, 2009). A positive correlation is observed between Mo and Re EFs (Fig. 3.16). Notably, samples from the PI core have consistently lower average Re EF (~0.9) and TOC (~0.9%) compared with other cores (Re EF > 1.3, TOC > 1.5%). This might be associated with either locally more oxidizing environment or thermal maturation after deposition that caused the loss of TOC and Re.

The Fe speciation data suggest the Rouge River Member was predominantly deposited under oxic-suboxic conditions (Fe_{HR}/Fe_T = 0.07–0.29; Fig. 3.17). The Fe_{py}/Fe_{HR} ratios of Rouge River Member are generally below 0.7, except for two samples from the PI core containing higher Fe_{py}/Fe_{HR} ratios of 0.84 and 0.85. Although high Fe_{py}/Fe_{HR} ratios are a feature of euxinic bottom waters, the two samples have consistently low Fe_{HR}/Fe_T ratios (< 0.3) and low Mo EF (< 5.5), both of which are against the interpretation of locally euxinic conditions. This interpretation is further supported by the C_{org} : P ratios. The average C_{org} : P ratio of the

Rouge River Member is 32.49, which is suggestive of oxic-suboxic conditions during deposition (Fig. 3.18).

Collectively, multiple trace metals (Mo, U, Re) and sedimentary Fe speciation data reveal the spatiotemporal bottom water redox variations during Late Ordovician ORS deposition in southern Ontario. More O_2-deficient bottom waters (typically anoxic and ferruginous rather than euxinic) are inferred for the Collingwood Member deposited in the deeper waters of the Michigan Basin and Appalachian Basin, whereas predominantly oxic to suboxic bottom waters are inferred for those deposited in the shallower waters of the basins near the Algonquin Arch. The Rouge River Member was deposited under oxic-suboxic conditions and there were no significant spatial bottom water redox variations. The particulate Fe-Mn shuttle operated during the deposition of both units because Mo accumulation occurred much faster than U.

3.5.2 Constraining global ocean redox conditions by uranium isotope compositions

3.5.2.1 Diagenetic influences on the $\delta^{238}U$ of the Collingwood Member

Diagenesis that could potentially alter the chemical composition of sedimentary rocks should be assessed before making any interpretations. The analyzed Rouge River Member samples are siliciclastic shales and do not show any obvious petrographic evidence for post-depositional disturbance (e.g., quartz veins), thus the RSTM data are least likely to be affected by such processes. By contrast, the Collingwood Member is carbonate-rich and is more susceptible to diagenetic alteration. The influence of diagenesis on the carbonate fractions of the Collingwood Member should be carefully evaluated. Although no specific proxies are developed to assess if carbonate $\delta^{238}U$ were affected by diagenesis, traditional diagenetic proxies (e.g., $\delta^{18}O$, Mn/Sr ratios) are used to assess the post-depositional alterations of carbonates (e.g., Veizer, 1983; Banner and Hanson, 1990; Jacobsen and Kaufman, 1999; Zhang et al., 2020a). Correlations between carbonate $\delta^{238}U$ and diagenetic proxies are evaluated by R^2 (coefficient of determination) and *p* values. We define R^2 values < 0.25, 0.25–

0.64, > 0.64 as showing weak, moderate, and strong correlations and use *p* value to assess its significance/robustness (i.e., $p < 0.05$)

Post-depositional diagenetic effects on samples with $\delta^{238}U_{carb}$ can be evaluated by $\delta^{18}O$ (e.g., Zhang et al., 2020a). The compiled $\delta^{18}O$ of well-preserved Katian bulk carbonate are generally between −7‰ and −4‰ and diagenetic alterations could cause lower $\delta^{18}O$ values (Veizer, 1983; Shield et al., 2003; Goldberg et al., 2021). The $\delta^{18}O$ of samples from the MF and CWD cores are from −8.9‰ to −6.0‰ and from −9.0‰ to −7.6‰, respectively. The lower $\delta^{18}O$ of samples from the MF and CWD cores relative to coeval bulk rocks could suggest diagenetic alteration of O isotope compositions (Brookfield and Hannigan, 2021; Goldberg et al., 2021). However, diagenetic modification of $\delta^{238}U$ was not likely to be significant because 1) previous studies used fluid-rock interaction modeling to show that $\delta^{238}U_{carb}$ is more resistant to diagenesis than $\delta^{18}O$ (Lau et al., 2017; Chen et al., 2018b), and 2) no robust linear correlations are found between $\delta^{238}U_{carb}$ and $\delta^{18}O$ ($R^2 = 0.11$, $p = 0.25$; Fig. 3.19; Table 3.4).

Table 3.4 Statistical linear regression test of the influences of diagenesis on $\delta^{238}U$ of the Collingwood Member

	$\delta^{238}U_{carb}$		$\delta^{238}U_{non\text{-}detrital}$	
	R^2	*p* value	R^2	*p* value
$\delta^{238}U$ vs $\delta^{13}C$	0.14	0.19	0.05	0.44
$\delta^{238}U$ vs $\delta^{18}O$	0.11	0.25	0.10	0.27
$\delta^{238}U$ vs Mn	0.19	0.12	0.28	0.05
$\delta^{238}U$ vs Sr	0.02	0.61	0.02	0.64
$\delta^{238}U$ vs Mn/Sr	0.19	0.12	0.23	0.09
$\delta^{238}U$ vs Mg/Ca	0.20	0.10	0.20	0.11
$\delta^{238}U$ vs Sr/Ca	< 0.01	0.99	0.13	0.20
$\delta^{238}U$ vs TOC	0.04	0.49	0.33	0.03
$\delta^{238}U$ vs Al	0.07	0.38	0.55	< 0.01
$\delta^{238}U$ vs Mo/Al	0.14	0.20	0.59	0.01
$\delta^{238}U$ vs Mo/U	0.27	0.07	0.01	0.69
$\delta^{238}U$ vs U/Al	0.36	0.02	0.82	< 0.01

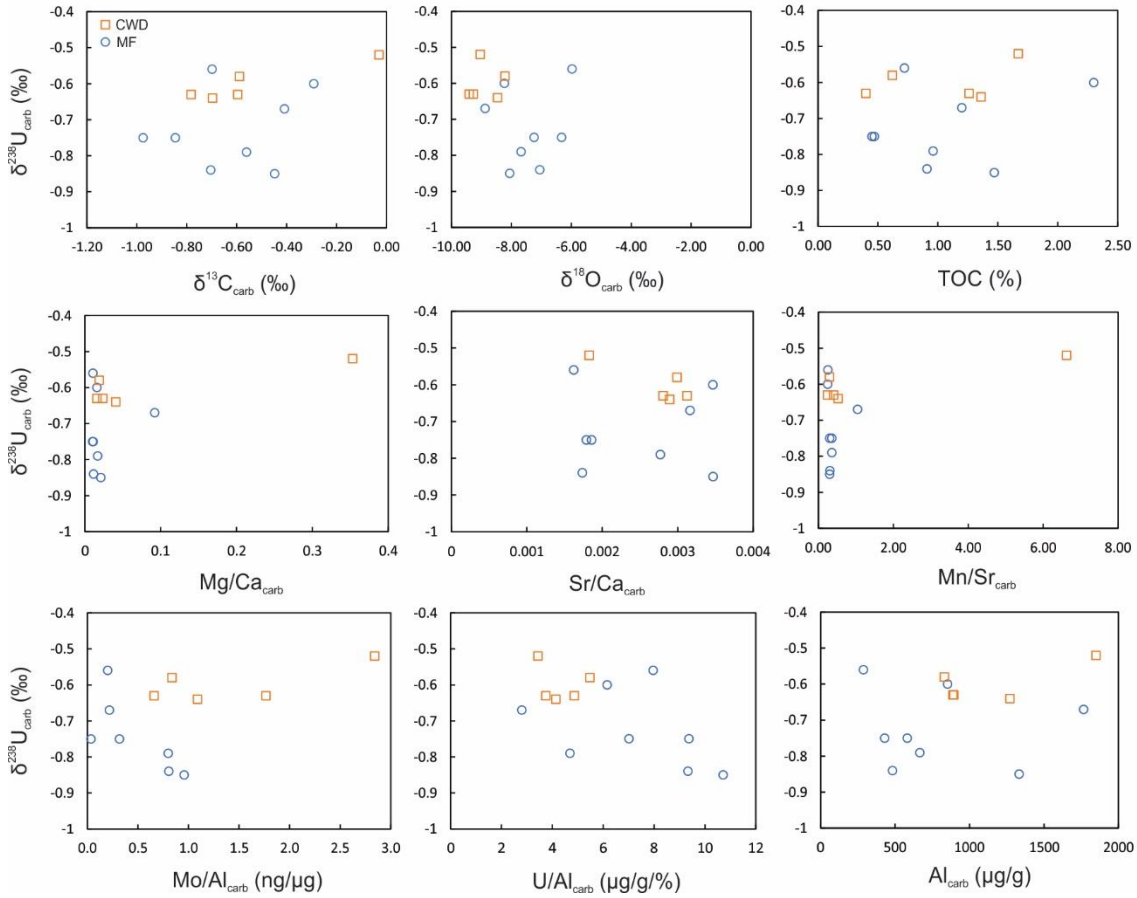

Figure 3.19 Covariations between carbonate $\delta^{238}U$ and diagenetic proxies for samples from the CWD and MF cores. All elemental ratios are weight ratios.

Besides $\delta^{18}O$, post-depositional diageneses can be evaluated by Mn/Sr ratios (e.g., Banner and Hanson, 1990). Lower Mn/Sr ratios are commonly found for carbonates with no clear diagenetic overprints (Banner and Hanson, 1990; Jacobsen and Kaufman, 1999; Lau et al., 2017). Except for sample CWD21 (Mn/Sr = 6.62), the other samples analyzed for $\delta^{238}U_{carb}$ have Mn/Sr ratios lower than 2 and thus are compatible with the interpretation that the carbonate fractions were less likely to be affected by diagenesis. No correlation between $\delta^{238}U_{carb}$ and Mn/Sr is observed for all these samples ($R^2 = 0.19$, $p = 0.12$; Fig. 3.19; Table 3.4).

Although sample CWD21 has a high Mn/Sr ratio that suggests relatively more severe carbonate diagenesis, the $\delta^{238}U_{carb}$ may not have been significantly altered because its $\delta^{238}U_{carb}$ value (−0.52 ± 0.08‰) is indistinguishable from stratigraphically adjacent samples (~−0.60‰) that have Mn/Sr ratios < 1. In support of this interpretation, we note that identical $\delta^{238}U_{carb}$ stratigraphic trends have been reported for the Neoproterozoic carbonates with variable Mn/Sr ratios (0.27–8.16) from the Jiulongwan section (south China) and the co-deposited well-preserved carbonates with low Mn/Sr ratios (< 1) from the Bol'shoy Patom section (Siberia), which suggest $\delta^{238}U_{carb}$ is more resistant to diagenesis than carbonate Mn/Sr ratios (Zhang et al., 2019).

Dolomitization and lithology changes (from aragonite to calcite) are not considered to significantly alter the $\delta^{238}U_{carb}$ of samples from the MF and CWD cores. Except for sample CWD21 with a Mg/Ca ratio of 0.35, all the other samples from the two cores have Mg/Ca lower than 0.1. The $\delta^{238}U_{carb}$ of CWD21 does not seem to be significantly altered by dolomitization because: 1) the $\delta^{238}U_{carb}$ of the sample is indistinguishable from that of stratigraphically adjacent samples; 2) dolomitization does not cause a systematic difference in $\delta^{238}U$ from the investigations of calcites and dolomites in the modern Bahamas carbonate platform (Chen et al., 2018b; Tissot et al., 2018); and 3) the Neoproterozoic and Late Permian dolomites yield similar trends in $\delta^{238}U$ compared with the coevally deposited carbonates elsewhere (e.g., Lau et al., 2016; Elrick et al., 2017; Zhang et al., 2018a, 2018b, 2019, 2020b; Cao et al., 2020). Low Sr/Ca ratios (< 0.005) are observed for all these Collingwood Member samples. Moreover, no correlations are observed between $\delta^{238}U_{carb}$ and Mg/Ca ratios (R^2 = 0.20, p = 0.10) and between $\delta^{238}U_{carb}$ and Sr/Ca ratio (R^2 < 0.01, p = 0.99), suggesting minimal alteration of $\delta^{238}U_{carb}$ due to dolomitization and aragonite-calcite transformation, respectively (Fig. 3.19; Table 3.4).

Detrital contaminations to the $\delta^{238}U_{carb}$ of samples from the MF and CWD cores are not likely to be significant. It is because 1) 1N HCl dissolves carbonate minerals rather than detrital minerals, and 2) leached samples have higher U/Al values (> 3 μg/g/%) than the U/Al background (0.42 μg/g/%). Moreover, no correlation between $\delta^{238}U_{carb}$ and Al content is

observed for the Collingwood Member samples, suggesting minimal influences from detrital components (R^2 = 0.07, p = 0.38; Fig. 3.19; Table 3.4).

Enrichment of U(IV) in sediments during early diagenesis has been proposed to influence $\delta^{238}U_{carb}$ (Romaniello et al., 2013; Chen et al., 2018b; Tissot et al., 2018). Modern Bahamas carbonates deposited under oxygenated waters and sulfidic porewaters have $\delta^{238}U_{carb}$ that are 0.27 ± 0.14‰ (1SD) higher than modern seawater, which is associated with authigenic enrichment of U(IV) (Romaniello et al., 2013; Chen et al., 2018b; Tissot et al., 2018). Local water redox conditions are inferred to be oxic-suboxic for the Collingwood Member from the MF and CWD cores (see Section 3.5.1.2.1). In addition, low Mo concentrations (< 0.6 μg/g) in carbonate fractions are observed for all these samples, implying no euxinic sulfidic porewaters. Although a moderate correlation between $\delta^{238}U_{carb}$ and U/Al ratios is observed for all these Collingwood Member samples (R^2 = 0.36, p = 0.02), no correlations exist if calculating samples from the MF (R^2 = 0.17, p = 0.31) and CWD (R^2 = 0.07, p = 0.60) cores separately. In addition, no correlations are observed between $\delta^{238}U_{carb}$ and Mo/Al ratios (and Mo/U ratios), suggesting local redox conditions did not significantly influence the $\delta^{238}U_{carb}$ values. Because of locally oxic-suboxic waters and non-sulfidic porewaters for these samples compared with the Bahamas sediments under oxic waters and sulfidic porewaters (average $\delta^{238}U$ offset of 0.27 ± 0.14‰; Chen et al., 2018b), a smaller U isotope offset (≤ 0.27‰) is considered as a possible influence when interpreting the $\delta^{238}U_{carb}$ data from the CWD and MF cores.

Similarly, $\delta^{238}U_{non\text{-}detrital}$ data for the Collingwood Member were evaluated for diagenetic alterations of the carbonate fractions using trace metal concentrations ($\delta^{238}U_{carb}$ data from 1N HCl leaches are not obtained because no significant difference is found between $\delta^{238}U_{carb}$ and $\delta^{238}U_{non\text{-}detrital}$ in the experimental comparison test; Fig. 3.12; Table B5) and $\delta^{18}O$ data (Fig. 3.20, Table B4 and B6). The $\delta^{18}O$ of the Collingwood Member from the SJ, LC and CWD cores are lower than coeval bulk rock $\delta^{18}O$ (Goldberg et al., 2021), suggesting the carbonate fractions were influenced by diagenesis. Most samples contain low Mn/Sr ratios (< 2) and Mg/Ca ratios (< 0.1), except for SJ30 and LC3. The Sr/Ca ratios are all below 0.01. No

significant correlations are observed between $\delta^{238}U_{non\text{-}detrital}$ and these diagenetic proxies, suggesting no systematic alteration of $\delta^{238}U_{non\text{-}detrital}$ by post-depositional diagenesis ($p > 0.05$; Fig. 3.20; Table 3.4). Local water redox conditions for these samples are inferred from oxic-suboxic to ferruginous (see Section 3.5.1.2.1). The Mo concentrations of these samples (up to 2 μg/g) approach that of the shallow water Bahamas carbonates (Romaniello et al., 2016), suggesting the appearance of sulfidic porewaters during deposition. Moderate to strong correlations between $\delta^{238}U_{non\text{-}detrital}$ and redox proxies (i.e., U/Al and Mo/Al ratios; $R^2 = 0.59–0.82$, $p < 0.02$) suggest that the $\delta^{238}U_{non\text{-}detrital}$ data were influenced by variable enrichment of U(IV) due to changes in local water and porewater redox conditions (Fig. 3.20; Table 3.4). A moderate negative correlation between $\delta^{238}U_{non\text{-}detrital}$ and Al content ($R^2 = 0.55$, $p < 0.01$) possibly reflects a pattern that deeper water samples (from LC and SJ cores) with high $\delta^{238}U_{non\text{-}detrital}$ and low Al were deposited under more reducing conditions with less influences from terrestrial materials, whereas shallower water samples (from the CWD core) with low $\delta^{238}U_{non\text{-}detrital}$ and high Al were deposited under more oxidizing conditions with more influences from terrestrial materials. This is consistent with geological background and the interpretation of spatiotemporal local redox conditions.

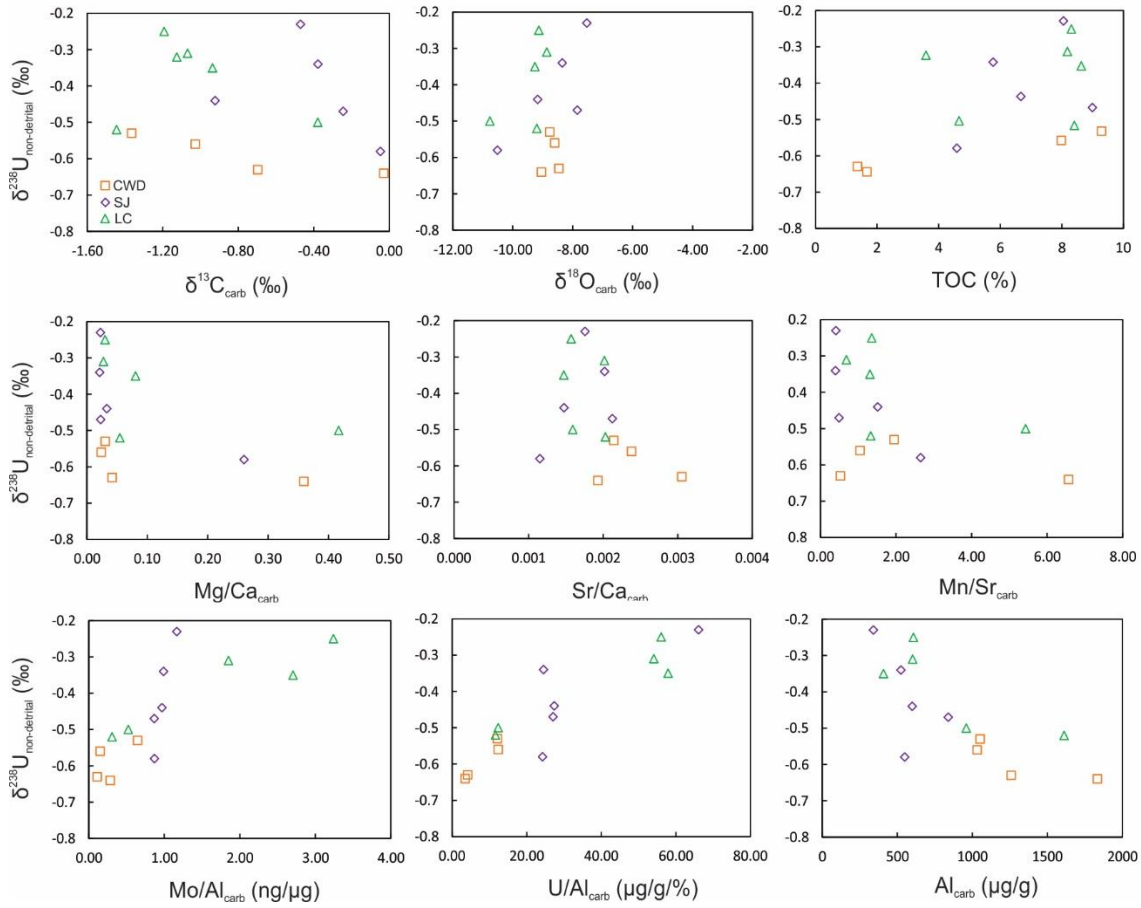

Figure 3.20 Covariations between $\delta^{238}U_{non\text{-}detrital}$ (corrected from the bulk $\delta^{238}U$) and diagenetic proxies (leached with 1N HCl) for samples from the CWD, LC, and SJ cores. All elemental ratios are weight ratios.

In summary, the carbonate fractions of the Collingwood Member experienced some diagenesis, as evidenced by relatively lower $\delta^{18}O$ values for all samples and higher Mn/Sr ratios for a few samples. However, there is no compelling evidence for significant alteration of $\delta^{238}U$. Variations in local redox conditions caused the positive correlation between $\delta^{238}U_{non\text{-}detrital}$ and Mo/Al ratios for the Collingwood Member. A similar correlation was not observed

for carbonates from the MF and CWD cores, but early diagenesis could still have influenced these $\delta^{238}U_{carb}$ data, resulting in a small $\delta^{238}U$ offset (< 0.27‰) from coeval seawater.

3.5.2.2 Global ocean redox dynamics revealed by U isotope data

The coeval global ocean redox conditions are inferred from both the $\delta^{238}U_{carb}$ and $\delta^{238}U_{non\text{-}detrital}$ data for the Collingwood Member and $\delta^{238}U_{non\text{-}detrital}$ data for the Rouge River Member.

The $\delta^{238}U_{carb}$ of Collingwood Member from the MF and CWD cores do not show any obvious stratigraphic trends. However, the $\delta^{238}U_{carb}$ data from the MF core vary significantly between −0.85‰ and −0.56‰ (average = −0.73 ± 0.11‰, 1SD, n = 8; Fig. 3.6) whereas the $\delta^{238}U_{carb}$ from the CWD core vary slightly between −0.64‰ and −0.52‰ (average = −0.60 ± 0.05‰, n = 5; Fig. 3.5). As it is unlikely that global ocean redox conditions could dramatically change over a short period, it seems that $\delta^{238}U_{carb}$ data from the CWD core possibly represent global ocean redox conditions whereas those from the MF core reflect local redox signals superimposed on the global ocean redox signals.

Large variations in the $\delta^{238}U_{carb}$ data from the MF core could be associated with 1) episodic deposition of TOC-rich and TOC-poor layers, 2) the operation of a particulate Fe-Mn shuttle that delivers isotopically light $\delta^{238}U$ into sediments, and 3) enrichment of U(IV) that lead to higher $\delta^{238}U$ of sediments (e.g., Chen et al., 2018b, 2022). First, alternating TOC-rich and -poor layers are observed for the MF core, but not the CWD core, raising the possibility that episodic organic matter buildup influenced $\delta^{238}U_{carb}$. However, no correlation between $\delta^{238}U_{carb}$ and TOC exists for samples from the MF core ($R^2 = 0.06$, $p = 0.57$; Fig. 3.19). Second, samples from both cores were affected by a particulate Fe-Mn shuttle, based on the covariation patterns of Mo-U EF (Fig. 3.16). Carbonate U mainly comes from incorporation of oxidized U(VI) during carbonate precipitation (with seawater-like $\delta^{238}U$) and addition of U during early diagenesis (e.g., isotopically heavy U(IV) due to reducing porewaters, isotopically light U(VI) released from the dissolution of Mn oxides) and $\delta^{238}U_{carb}$ could be more susceptible to be modified when carbonate U concentration is low (Chen et al., 2022). Compared with those

from the MF core, samples from the CWD core contain higher Mo/U ratios, higher Mo/Al ratios, and lower U/Al ratios (average Mo/U: 0.32 vs. 0.07; average Mo/Al: 0.13 ng/μg vs. 0.05 ng/μg; average U/Al: 4.38 μg/g/% vs. 7.25 μg/g/%), suggesting more efficient operation of the Fe-Mn shuttle process that could possibly deliver more isotopically light U and thus result in lower $\delta^{238}U_{carb}$ values. However, these samples have relatively invariant $\delta^{238}U_{carb}$ values and it is the samples from the MF core that show large $\delta^{238}U_{carb}$ variations. Third, $\delta^{238}U_{carb}$ variations in the MF core could be associated with enrichment of U(IV) during early diagenesis. Because the CWD samples contain lower U/Al and higher Mo/Al ratios, addition of a small amount of heavy ^{238}U in those samples could possibly result in higher $\delta^{238}U_{carb}$ values that are similar to the upper limit of $\delta^{238}U_{carb}$ data from the MF core, although no correlations exist between $\delta^{238}U_{carb}$ and Mo/Al (and U/Al) for the CWD core. Large $\delta^{238}U_{carb}$ variations in the MF core possibly reflect a case that enrichment of heavy ^{238}U in samples from the MF core have variable impact on $\delta^{238}U_{carb}$ values due to its relatively higher U/Al ratios, although no correlations exist between $\delta^{238}U$and Mo/Al (and U/Al). Therefore, lower $\delta^{238}U_{carb}$ values in the MF core are suggestive of less impact from heavy ^{238}U enrichment and thus are close to the $\delta^{238}U$ of seawater.

The $\delta^{238}U_{carb}$ of the Collingwood Member from the CWD core is used to infer the $\delta^{238}U$ of global seawater. The invariant $\delta^{238}U_{carb}$ data from the CWD core imply relatively stable local and global ocean redox conditions during Collingwood Member deposition. Given locally oxic-suboxic waters and non-sulfidic porewater conditions for these samples, we tentatively assume a $\delta^{238}U$ offset of 0–0.27‰ between carbonate and seawaters. The assumed $\delta^{238}U$ offset is lower than that from shallow Bahamas carbonate (0.27 ± 0.14‰) due to comparatively less reducing porewater conditions (Romaniello et al., 2013; Chen et al., 2018b; Tissot et al., 2018). Applying the $\delta^{238}U$ offset of 0–0.27‰ to the average $\delta^{238}U_{carb}$ from the CWD core (−0.60 ± 0.05‰), the coeval seawater $\delta^{238}U$ is estimated from −0.87 ± 0.05‰ to −0.60 ± 0.05‰. The lower endmember of seawater $\delta^{238}U$ estimation is consistent with the lowest $\delta^{238}U$ value from the MF core (−0.85‰) that potentially records the seawater $\delta^{238}U$ with minimal isotope offsets.

Besides the $\delta^{238}U_{carb}$ data, the $\delta^{238}U_{non\text{-}detrital}$ of the Collingwood Member provide another opportunity to constrain coeval global seawater $\delta^{238}U$. There are no obvious stratigraphic trends in $\delta^{238}U_{non\text{-}detrital}$ from different cores (Fig. 3.5, 3.7–3.8). Positive correlations are observed between $\delta^{238}U_{non\text{-}detrital}$ and bulk U EF ($R^2 = 0.52$, $p < 0.01$; and other redox proxies such as Mo EF [$R^2 = 0.57$, $p < 0.01$] and C_{org} : P [$R^2 = 0.59$, $p < 0.01$]; Fig. 3.21). The observed correlations suggest a dominant control of local redox gradients on the magnitude of U isotope offsets between the seawater and sediments. It is reported that sediments from modern ferruginous lakes have variable $\delta^{238}U$ values and show no correlations between $\delta^{238}U$ and RSTMs (Cole et al., 2020). The U removal rate under oxic-suboxic waters and sulfidic porewaters has been correlated with sulfate reduction rates (Barnes and Cochran, 1993). As local bottom water redox conditions of these samples are from oxic-suboxic to ferruginous (see Section 3.5.2.2), it is possible that the Collingwood Member samples with higher U EF and $\delta^{238}U$ values were deposited under ferruginous bottom waters with sulfidic porewaters. The operation of a particulate Fe-Mn shuttle for the Collingwood Member does not seem to significantly influence the $\delta^{238}U$ record because a negative correlation between $\delta^{238}U_{non\text{-}detrital}$ and U EF is expected rather than a positive correlation. Due to the observation of a positive correlation between $\delta^{238}U_{non\text{-}detrital}$ and U EF, the lowest $\delta^{238}U_{non\text{-}detrital}$ value ($-0.64 \pm 0.08‰$) is considered as the maximum estimate of coeval seawater $\delta^{238}U$ as it represents the smallest U isotope offset from seawater. This is consistent with the deduced seawater $\delta^{238}U$ ($-0.87 \pm 0.05‰$ to $-0.60 \pm 0.05‰$) based on the $\delta^{238}U_{carb}$ data from the CWD core. The lower estimated seawater $\delta^{238}U$ during the Collingwood Member deposition ($-0.87 \pm 0.05‰$ to $-0.64 \pm 0.08‰$) compared to modern seawater ($-0.39 \pm 0.04‰$; e.g., Weyer et al., 2008) suggests globally more widespread ocean euxinia.

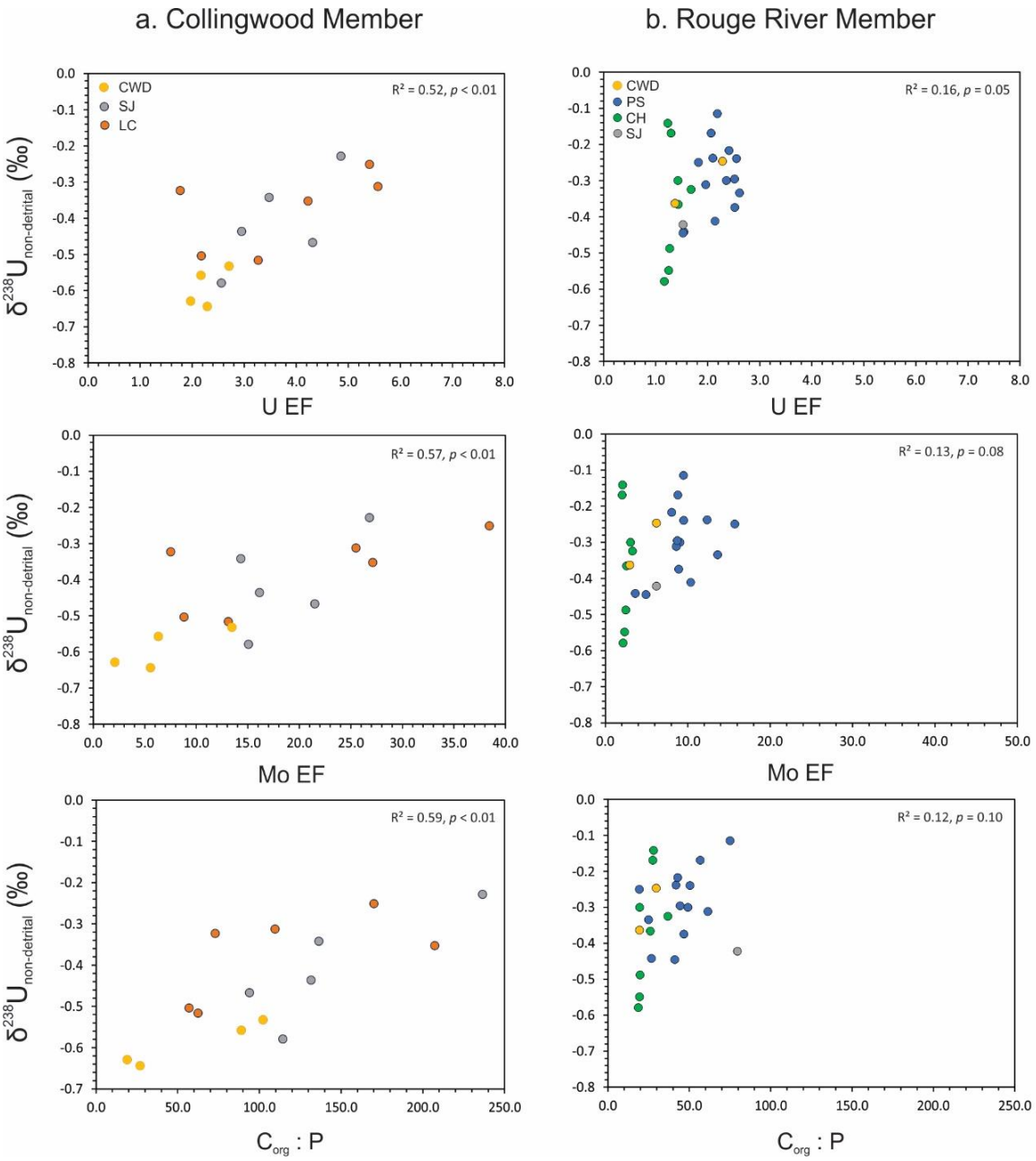

Figure 3.21 Correlations between $\delta^{238}U_{non\text{-}detrital}$ and several redox proxies (U EF, Mo EF, and C_{org} : P) are presented for a) Collingwood Member and b) Rouge River Member.

The $\delta^{238}U_{non\text{-}detrital}$ of the Rouge River Member yields an estimate for the $\delta^{238}U$ of coeval seawater that is different from the Collingwood Member. Weak to no correlations are observed between $\delta^{238}U_{non\text{-}detrital}$ and redox proxies ($R^2 < 0.20$, $p \geq 0.05$), suggesting no significant local redox gradient control on $\delta^{238}U$ (Fig. 3.21). As there are no specific stratigraphic trends in $\delta^{238}U_{non\text{-}detrital}$ from each drill core and the range of $\delta^{238}U_{non\text{-}detrital}$ values is not large (average = −0.32 ± 0.12‰, n = 25), variations in coeval seawater $\delta^{238}U$ may have been limited during deposition of the Rouge River Member. Given the oxic-suboxic local bottom water conditions for the Rouge River Member and a small $\delta^{238}U$ offset under such conditions in the modern environment (~0.1–0.3‰; Weyer et al., 2008; Andersen et al., 2016; Cole et al., 2020; Abshire et al., 2020; He et al., 2021; Bruggmann et al., 2022), the contemporaneous global seawater $\delta^{238}U$ is estimated between −0.62 ± 0.12‰ and −0.42 ± 0.12‰. To our knowledge, this is the first attempt to use $\delta^{238}U$ from suboxic shales to reconstruct the $\delta^{238}U$ of contemporaneous global seawater. The estimated seawater $\delta^{238}U$ during the Rouge River Member deposition is relatively higher and thus reflects less extensive global ocean euxinia than that during the Collingwood Member deposition.

3.5.3 Quantitative constraints on the areal extent of global euxinic seafloor during the Katian

A three-sink U isotope mass balance model can be used to infer the areal extent of euxinic seafloor based on the estimated ancient seawater $\delta^{238}U$. The modeling approach follows Stockey et al. (2020) and is briefly introduced here. Seawater U concentrations and $\delta^{238}U$ can be described as follows (Goto et al., 2014; Wang et al., 2016):

$$d[U]_{SW}/dt = F_{river} - F_{eux} - F_{red} - F_{oxic} \qquad \text{(I)}$$

$$d[U]_{SW}\delta^{238}U_{SW}/dt = F_{river}\delta^{238}U_{river} - F_{eux}(\delta^{238}U_{SW} + \Delta_{eux}) - F_{red}(\delta^{238}U_{SW} + \Delta_{red}) - F_{oxic}(\delta^{238}U_{SW} + \Delta_{oxic}) \qquad \text{(II)}$$

where F is the U flux and Δ_i is the $\delta^{238}U$ offset between each U sink and seawater ($\Delta_i = \delta^{238}U_i - \delta^{238}U_{SW}$) (Table 3.5). The three U sinks are euxinic (eux), reducing (red, including suboxic and ferruginous), and oxic (oxic). Assuming there is a first order relationship between U

removal flux into each sink and seawater U concentration (Partin et al., 2013; Reinhard et al., 2013; Wang et al., 2016), then:

$$F_i = b_i A f_i \alpha_i ([U]_{SW}/[U]_{M.SW}) \qquad \text{(III)}$$

where b_i is the burial flux per area for each sink, A is the total seafloor area, f_i is the fraction of seafloor that was covered by each U sink, α_i is a pseudospatial scaling coefficient that relates burial rate to the area of the sink (Reinhard et al., 2013), $[U]_{SW}$ is the average modeled U concentration in the seawater, and $[U]_{M.SW}$ is the average U concentration in the modern seawater (Table 3.5).

Table 3.5 Parameters used for U isotope mass balance model.

Parameters	Unit	Minimum value	Maximum value	References
$F_{riv}(U)$	*mol/yr*	2.75×10^7	5.65×10^7	1
$b_{U.eux}$	*mol/(m^2 × yr)*	5.4×10^{-6}	4.62×10^{-5}	1
$b_{U.red}$	*mol/(m^2 × yr)*	9.2×10^{-7}	4.37×10^{-6}	1
$b_{U.ox}$	*mol/(m^2 × yr)*	2.72×10^{-8}	6.75×10^{-8}	1
$\delta^{238}U_{riv}$	*‰*	–0.34	–0.24	2-3
$\Delta^{238}U_{eux}$	*‰*	0.4	0.8	2-8
$\Delta^{238}U_{red}$	*‰*	0	0.4	2, 4, 9, 10, 18-20
$\Delta^{238}U_{oxic}$	*‰*	–0.05	0.01	4, 11-14, 20
$f_{ox.lim}$	*%*	83.89	100	15
f_{red}	*%*	0	100-f_{eux}	/
A	m^2	3.6×10^{14}	(fixed value)	15
M	*kg*	1.41×10^{21}	(fixed value)	12
$[U]_{U.sw}$	*mol/kg*	14×10^9	(fixed value)	16
$\delta^{238}U_{M.sw}$	*‰*	–0.39	(fixed value)	17

References: 1, Dunk et al., (2002); 2, Andersen et al., (2016); 3, Noordmann et al., (2016); 4, Weyer et al., (2008); 5, Andersen et al., (2014); 6, Holmden et al., (2015); 7, Bura-Nakić et al., (2018); 8, Brüske et al., (2020); 9, Abshire et al., (2020); 10, Cole et al., (2020); 11, Goto et al., (2014); 12, Lau et al., (2017); 13, Wei et al., (2018); 14, Zhang et al., (2018b); 15, Reinhard et al., (2013); 16, Morford and Emerson, (1999); 17, Tissot and Dauphas (2015); 18, He et al., (2021); 19, Bruggmann et al., (2022); 20, Gilleaudeau et al., (2019)

The burial scaling coefficient (α) is used in the model such that U burial rates in the euxinic and reducing settings are scaled to organic carbon remineralization (Reinhard et al., 2013), as described by the following equations:

$$\alpha_{eux} = \frac{\sum_{min(z_{eux})}^{max(z_{eux})} 1.58\text{-}0.16ln(z_{eux})}{N(z_{eux})\{1.58\text{-}0.16ln(min(z_{eux}))\}} \qquad \text{(V)}$$

$$\alpha_{red} = \frac{\sum_{min(z_{red})}^{max(z_{red})} 1.58 - 0.16ln(z_{red} + maxln(z_{eux}))}{N(z_{red})\{1.58\text{-}0.16ln(min(z_{eux}))\}} \qquad \text{(VI)}$$

where z_i (eux or red) is the modeled water depth of euxinic or reducing environment from a LOESS model to fit the modern global seafloor bathymetric data (Menard and Smith, 1966), N_i is the number of modeled water depths of euxinic or reducing environment. Burial rate in the oxic sink is assumed to scale independent of organic carbon remineralization ($\alpha_{oxic} = 1$).

The euxinic seafloor area (f_{eux}) is modeled in 31 logarithmically scaled spaces with Monte Carlo simulations for given seawater $\delta^{238}U$ values (Fig. 3.22). For the modern seawater $\delta^{238}U$ of −0.39 ± 0.04‰ (e.g., Weyer et al., 2008; Tissot and Dauphas, 2015), the model estimates 0.2–0.3% (32^{th}–68^{th} percentile; median = 0.3%) euxinic seafloor area in the modern ocean, which is generally consistent with estimates of 0.1–0.3% from other studies (Reinhard et al., 2013; Tissot and Dauphas, 2015). For the estimated seawater $\delta^{238}U$ of −0.87 ± 0.05‰ (lower endmember) and −0.64 ± 0.08‰ (higher endmember) during the deposition of Collingwood Member, the model estimates 6.3–31.6% (32^{th}–68^{th} percentile; median = 14.2%) and 0.5–2.0% (32^{th}–68^{th} percentile; median = 1.0%) euxinic seafloor area, respectively. For the estimated seawater $\delta^{238}U$ of −0.62 ± 0.12‰ and −0.42 ± 0.12‰ during the deposition of Rouge River Member, the model estimates 0.4–2.0% (32^{th}–68^{th} percentile; median = 1.0%) and 0.2–0.4% (32^{th}–68^{th} percentile; median = 0.3%) euxinic seafloor area, respectively. In comparison, euxinic seafloor area during the Hirnantian ocean anoxic event is estimated as 4–30% (30^{th}–70^{th} percentile; Bartlett et al., 2018; Stockey et al., 2020). Nonetheless, based on the estimated coeval seawater $\delta^{238}U$ value, this model cannot distinguish between if it was an expansion of oxia or suboxia-anoxia that was accompanied with the contraction of ocean euxinia during deposition of the Rouge River Member.

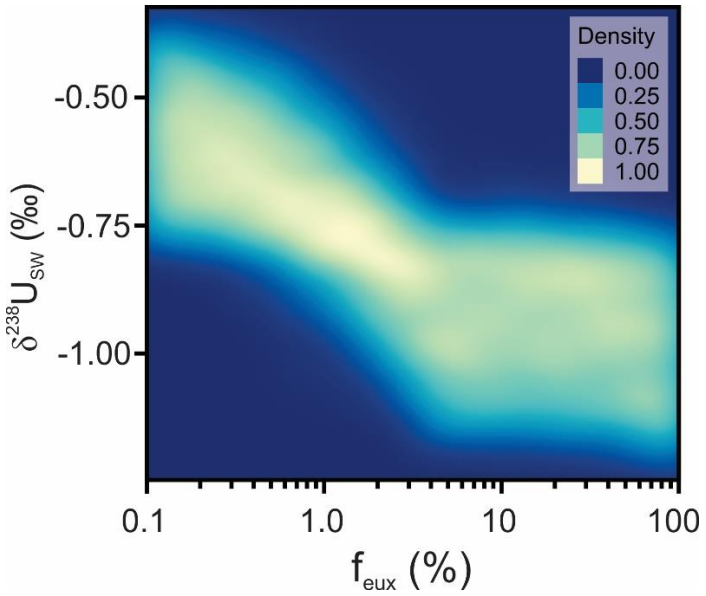

Figure 3.22 Uranium isotope mass balance model output that shows the frequency distribution of modeled seawater U isotope compositions ($\delta^{238}U_{SW}$) as a function of global ocean euxinic seafloor area (f_{eux}).

3.5.4 Implications for the global ocean redox change during the Taconic Orogeny and the Katian ocean redox dynamics

Expansion of global ocean euxinia could be the result of increased nutrient supply, which has been proposed as a main mechanism for the Phanerozoic ocean anoxic events (OAE; e.g., Meyer and Kump, 2008; Monteiro et al., 2012). Relatively lower estimated seawater $\delta^{238}U$ values (−0.87‰ to −0.64‰) during deposition of the Collingwood Member suggests expanded ocean euxinia, which could be caused by increased nutrient supply during the Taconic Orogeny. Contemporaneously low global seawater $^{87}Sr/^{86}Sr$ ratios from carbonates (Young et al., 2009; Saltzman et al., 2014; Edwards et al., 2015) and high εNd values from shales and carbonates (Swanson-Hysell and MacDonald, 2017; Conwell et al., 2022) have been proposed to reflect intensified weathering of mafic/ultramafic rocks during the Taconic Orogeny, which

could effectively consume CO_2 and cause a cooling period (Jagoutz et al., 2016; MacDonald et al., 2018). In addition, intensified weathering of mafic/ultramafic rocks could increase nutrient availability and promote primary productivity, which could increase organic carbon burial and increase O_2 release to the atmosphere (Lenton et al., 2012; 2016). The cooling climate could increase the O_2 solubility in the water columns. On the other hand, high primary productivity increased oxygen demand because more oxygen would be consumed when organic carbon sinks through the water column, thus ultimately resulting in expanded anoxia/euxinia (e.g., Meyer and Kump, 2008; Monteiro et al., 2012).

In comparison, higher estimated seawater $\delta^{238}U$ values (−0.62‰ to −0.42‰) during deposition of the Rouge River Member suggest a smaller extent of global ocean euxinia, which could be due to decreased nutrient input. During a period of decreased nutrient supply (thus lower productivity and less oxygen demand in the water column) and climate cooling (higher O_2 solubility), relatively higher estimated seawater $\delta^{238}U$ values during the Rouge River Member deposition could be interpreted as either a deeper water oxygenation event or an expansion of ocean suboxia-anoxia (e.g., replacing seafloor that was previously euxinic during deposition of the Collingwood Member). The latter interpretation is possible because the deposition of both Collingwood Member and Rouge River Member is coeval with the positive Fairview CIE, which is related to a period of expanded ocean suboxia-anoxia (Bergström et al., 2010; 2020b; Brookfield and Hannigan, 2021). However, it should be noted that the Fairview CIE is only found in North America and has not been globally correlated (e.g., Bergström et al., 2020b). Currently, it is difficult to rule out either possibility solely based on the $\delta^{238}U$ data (e.g., Gilleaudeau et al., 2019; Cole et al., 2020).

Current available non-traditional metal isotope data (e.g., $\delta^{98}Mo$, $\delta^{238}U$) suggest dynamic Katian ocean redox conditions prior to the LOME (Zhou et al., 2012, 2015; Lu et al., 2017, 2020; Dahl et al., 2021; Liu et al., 2022; and this study). The Katian is subdivided into four stage slices (Ka1 to Ka4; Bergström et al., 2009). Currently, there are no published studies utilizing metal isotopes to study the global ocean redox conditions during the Ka1. In this study, the Collingwood Member and Rouge River Member deposition is coeval with the

Fairview CIE, which is correlated with BC9 (Baltoscandian carbon isotope zone) and corresponds to the Ka2 (Ainsaar et al., 2010; Bergström et al., 2009; 2015, 2020b). The lower and higher estimated seawater $\delta^{238}U$ during the deposition of Collingwood Member and Rouge River Member, respectively, represent an expansion and a contraction of global ocean euxinia, respectively. The deposition of Fjäcka Shale in the Siljan area (Sweden) is coeval with the BC11 (corresponding to the Ka3; Ainsaar et al., 2010; Bergström et al., 2009; 2015, 2020b; Ebbestad et al., 2014) and was analyzed for both $\delta^{98}Mo$ and $\delta^{238}U$ (Lu et al., 2017). A positive correlation between $\delta^{98}Mo$ and $\delta^{238}U$ from the euxinic Fjäcka Shale provides compelling evidence of a transient global ocean oxygenation event during the middle stage of shale deposition (Lu et al., 2020). Widespread ocean anoxia could have been prevailed during the latest Katian (Ka4; prior to the Hirnantian) as evidenced by relatively low $\delta^{98}Mo$ from shales (Zhou et al., 2012, 2015; Dahl et al., 2021) and low $\delta^{238}U$ from carbonates (Liu et al., 2022). Collectively, fluctuated ocean redox conditions are inferred during the Katian.

3.5.5 Implications for the link between Late Ordovician ocean redox conditions and metazoan evolutions

Fluctuated Katian ocean redox conditions inferred from this study are accompanied with a decrease in biodiversity after the GOBE. However, dynamic ocean redox conditions are hypothesized to promote rather than hinder metazoan diversification (e.g., G. Wei et al., 2018, 2020; Wood and Erwin, 2018). If the hypothesis is correct, other factors must have played important roles in the decline of metazoans during the Katian, such as volcanism and climate change (e.g., Huff et al., 2010; Brookfield and Hannigan, 2021; Du et al., 2021; Goldberg et al., 2021; Metzger et al., 2021). Nevertheless, more studies are needed to understand the role of ocean redox dynamics on metazoan evolutions.

Widespread ocean anoxia has been widely accepted as a trigger for the second phase of LOME (LOME2; e.g., Sheehan, 2001; Algeo et al., 2016; Dahl et al., 2021; Kozik et al., 2022; Liu et al., 2022). However, expanded ocean anoxia alone cannot fully explain the extinction (e.g., Melchin et al., 2013; Longman et al., 2021; Pohl et al., 2021). An abrupt

decrease in carbonate $\delta^{238}U$ (~0.3‰) from the Anticosti Island (Canada), which is suggestive of an expanded ocean anoxia/euxinia, is observed during the LOME2 before peak Hirnantian glaciation (Ghienne et al., 2014; Bartlett et al., 2018). The average $\delta^{238}U_{carb}$ of carbonate during LOME2 is −0.45‰ (Bartlett et al., 2018). Assuming the $\delta^{238}U$ offset between carbonate and seawater is similar to the observations of modern Bahamas sediments (0.27 ± 0.14‰; Romaniello et al., 2013; Chen et al., 2018b; Tissot et al., 2018), the coeval seawater $\delta^{238}U$ could be −0.72 ± 0.14‰ for LOME2 (Bartlett et al., 2018). This estimate overlaps with the deduced seawater $\delta^{238}U$ values during deposition of the Collingwood Member (−0.87 ± 0.05‰ to −0.64 ± 0.08‰, Ka2; this study) and early and late stage of the Fjäcka Shale (−0.80‰ to −0.54‰, Ka3; Lu et al., 2020), both of which suggest episodic occurrence of expanded ocean anoxia/euxinia prior to the Hirnantian. However, LOME2-like mass extinction events have been not reported during the Katian, implying that expanded ocean anoxia/euxinia alone could not trigger the LOME2. In addition, carbonate I/Ca ratios from the Anticosti Island (Canada) and Tartu (Estonia) suggest oxygenated surface seawaters during the LOME2, in spite of expanded deep water anoxia (Pohl et al., 2021; Kozik et al., 2022). This suggests that the shallow continental shelf remained oxygenated for many taxa, which were wiped out during the LOME2. Therefore, other factors such as the cooling associated with the glaciation and changes in nutrient cycling could have played important roles in the LOME2 (e.g., Melchin et al., 2013; Longman et al., 2021; Pohl et al., 2021).

3.5.6 Implications for using geochemical data from multiple locations to reconstruct local and global ocean redox conditions

Our study demonstrates the significance of using geochemical data from several localities to reveal local and global ocean redox conditions. Benefited from examining samples from several drillcores, local detrital background (i.e., trace metal/Al ratios and detrital $\delta^{238}U$ value) can be evaluated and used, rather than using universal reference materials (e.g., PAAS, AUCC; e.g., Cole et al., 2017). This allows for better data normalization, thus benefiting the following interpretations. In addition, using multiple ocean redox proxies (e.g., Gilleaudeau et

al., 2021), spatiotemporal bottom water redox conditions are inferred for the Collingwood Member, whereas no significant local redox variations are suggested for the Rouge River Member. If the geochemical data were only examined for samples from one drill core, local detrital background could not be effectively examined and the redox condition could be inferred for only one locality (e.g., Li et al., 2018). Moreover, generating $\delta^{238}U$ data from several localities can greatly help constrain the global ocean redox conditions. If $\delta^{238}U$ data were only measured for one drillcore, it would be difficult to deduce coeval seawater U isotope compositions because local signals (e.g., redox conditions) could be superimposed on the global ocean redox signals. Therefore, generating geochemical data from multiple locations is necessary to better reconstruct local and global ocean redox conditions.

3.6 Conclusions

The Collingwood Member and Rouge River Member that were deposited during the concurrent Taconic Orogeny are the Katian organic-rich sedimentary rocks in southern Ontario, Canada. Paleosalinity proxies (Sr/Ba and S/TOC) consistently point to brackish/marine environments for both ORS units, suggesting some water exchange between the basin and open ocean during deposition that is consistent with previous studies. Redox sensitive trace metals, sedimentary Fe speciation and C_{org} : P ratios suggest that the Collingwood Member from the deeper waters of the Michigan and Appalachian basins were mostly deposited under anoxic and ferruginous conditions whereas those deposited in the shallower waters (near the Algonquin Arch) were under pervasive oxic-suboxic conditions. By contrast, predominantly oxic-suboxic conditions are inferred for the Rouge River Member. Particulate Fe-Mn oxide shuttles operated during the deposition of both units.

Global ocean redox dynamics during the Katian (Late Ordovician) are revealed by U isotope compositions. Carbonate $\delta^{238}U$ of the Collingwood Member from the MF cores shows large variations and likely reflect variations in local redox conditions. By contrast, the $\delta^{238}U_{carb}$ from the CWD core vary slightly and possibly record open ocean $\delta^{238}U$ signals. The $\delta^{238}U_{non\text{-}detrital}$ of the Collingwood Member are positively correlated with several redox proxies,

suggesting a local redox control rather than a particulate Fe-Mn shuttle influenced $\delta^{238}U$ offsets between the sediments and seawater. By comparison, no correlations between $\delta^{238}U_{non\text{-}detrital}$ and redox proxies are observed for the Rouge River Member. Considering the $\delta^{238}U$ offsets in sediments from different settings, the estimated seawater $\delta^{238}U$ values during deposition of the Collingwood Member (-0.87 ± 0.05‰ to -0.64 ± 0.08‰) and Rouge River Member (-0.62 ± 0.12‰ to -0.42 ± 0.12‰) suggest an expansion and a contraction of global ocean euxinia, respectively. A three-sink U isotope mass balance model suggests a global euxinic seafloor area of 0.5–31.6% and 0.2–2.0% during the deposition of Collingwood Member and Rouge River Member, respectively. Current available global ocean redox proxies ($\delta^{98}Mo$, $\delta^{238}U$) suggested fluctuating Katian ocean redox conditions during a decrease in biodiversity prior to the LOME. Episodic ocean anoxia during the Katian did not trigger the LOME2-like mass extinctions, suggesting that other factors (e.g., cooling and nutrient cycling) could have significantly influenced the living habitat of metazoan and resulted in the LOME2. This study further highlights the significance of examining samples from multiple locations to better reveal spatiotemporal variations in local redox conditions and reconstruct global ocean redox states.

Chapter 4 No evidence for expansion of global ocean euxinia during the base Stairsian mass extinction event (Tremadocian, Early Ordovician)

Submitted to Geochimica et Cosmochimica Acta.

Citation: Lu, X., Edwards, C. T., and Kendall, B. submitted. No evidence for expansion of global ocean euxinia during the base Stairsian mass extinction event (Tremadocian, Early Ordovician). Geochimica et Cosmochimica Acta. (Now under review)

4.1 Introduction

The Late Cambrian to Early Ordovician is an important transition interval in terms of biotic events, occurring between the decline of the Cambrian Explosion and the initial stage of the Great Ordovician Biodiversification Event (GOBE; Stigall et al., 2019). This transition period is characterized by a greenhouse environment, high eustatic level, and a plateau of metazoan diversification (e.g., Haq and Schutter, 2008; Munnecke et al., 2010; Saltzman et al., 2015; Algeo et al., 2016; Goldberg et al., 2021). Several mass extinction events repeatedly occurred during this transition period and have been referred to as "biomere" (extinction-bounded and trilobite-based biostratigraphic unit) boundaries in North America (e.g., Stitt, 1983; Palmer, 1984; Bambach et al., 2004; Taylor, 2006; Adrain et al., 2009, 2014). However, the trigger and recovery processes at "biomere" boundaries are not well understood (Fig. 4.1; Ji and Barnes, 1983; Bambach et al., 2004; Adrain et al., 2009, 2014; Taylor et al., 2012; Saltzman et al., 2015).

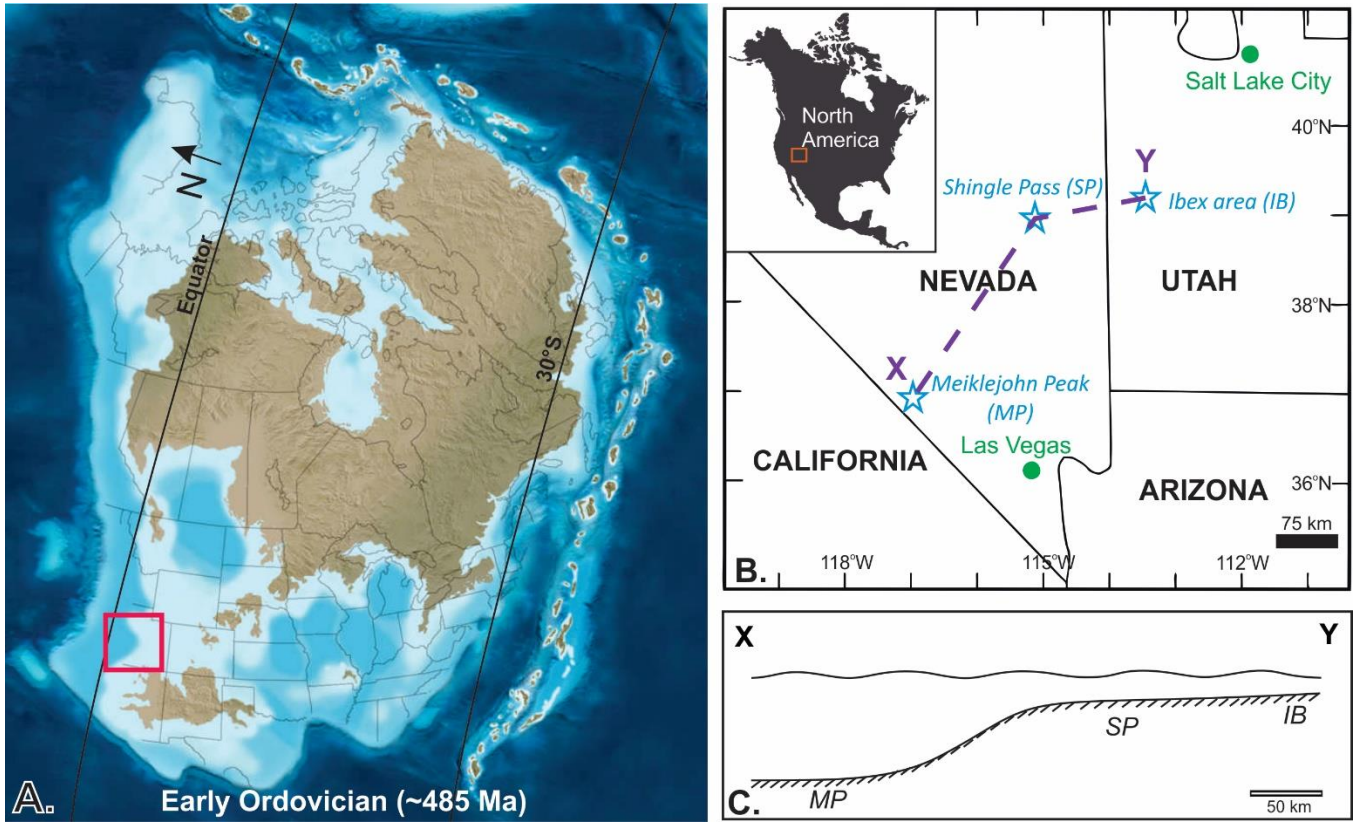

Figure 4.1 A) Paleogeographic map showing the location of Laurentia during the Early Ordovician (~485 Ma, modified from Blakey, 2011), B) map of the three sampling locations in the Great Basin, the United States (marked in blue; modified from Edwards et al., 2018), and C) A schematic view of the cross-section (X–Y shown in B) among the Meiklejohn Peak (MP), Shingle Pass (SP), and Ibex (IB) sections (modified from Edwards et al., 2018).

A trilobite extinction event at the base Stairsian "biomere" boundary is recorded in the Ibex area, western Utah, USA (Stitt, 1983; Palmer, 1984; Adrain et al., 2014). Notably, brachiopod and conodont species went extinct following the trilobite turnover in the same area (Ethington and Clark, 1981; Miller et al., 2003; Holmer et al., 2005). Although limited trilobite data/records prevent further recognition of this trilobite extinction event in other localities of the world, abrupt coeval conodont extinctions have been reported in several countries (e.g., Canada, China, Kazakhstan, Russia, Sweden, the United States; e.g., Moskalenko, 1967; An, 1981; Ethington and Clark, 1981; Ji and Barnes, 1983; Popov and Tolmacheva, 1995; Barnes et al., 1996; Löfgren, 1997; Landing et al., 2003; Wu et al., 2010) and thus could be a global biotic crisis. The magnitude of the base Stairsian mass extinction event (BSME) is not comparable to the "big five" mass extinctions (Sepkoski, 1981) and has not yet been described on a global scale (which may be partly due to a sparse record). In the Ibex area, the BSME represents a ~30% loss of standing genetic biodiversity (including trilobites, brachiopods, and conodonts; Hintze 1951, 1952; Ethington and Clark, 1981; Holmer et al., 2005; Adrain et al., 2009, 2014; Edwards et al., 2018). Coincidently, the BSME is accompanied by a locally well-defined positive carbon isotope excursion (CIE; $\delta^{13}C_{carb}$ increases by ~2‰; Edwards and Saltzman, 2014, 2016; Saltzman et al., 2015) that is correlated with many other localities worldwide, suggesting a primary global seawater signature (Zhang et al., 1999; Buggisch et al., 2003; Bergström et al., 2009; Hong et al., 2011; Thompson and Kah, 2012; Edwards and Saltzman, 2014, 2016; Saltzman et al., 2015; Wu et al., 2020; Strauss et al., 2020). The expansion of anoxic seawaters into shallow shelf environments (Saltzman et al., 2015) and ecological stress associated with sea level drops (Westrop and Ludvigsen, 1987; Miller et al., 2003) are proposed to result in the BSME.

Geochemical data have been reported for carbonate successions from the Ibex (most proximal), Shingle Pass, and Meiklejohn Peak (most distal) sections of the Great Basin (western USA) and it has been suggested that expanded local and global ocean anoxia occurred during the BSME (Edwards et al., 2018). Edwards et al. (2018) interpret near-zero I/Ca ratios

from the distal Shingle Pass and Meiklejohn Peak sections as evidence for local water anoxia during the BSME. In contrast, relatively low I/Ca ratios from the proximal Ibex area occur *before* the BSME and are interpreted to record localized coastal hypoxia (Edwards et al., 2018), yet variable I/Ca ratios during the BSME are not well understood. Concurrent positive carbon ($\delta^{13}C_{carb}$) and carbonate-associated sulfur ($\delta^{34}S_{CAS}$) isotope excursions are related to increased organic carbon and pyrite burial, respectively, which collectively imply that expanded global ocean anoxia coincided with the BSME (Edwards et al., 2018). However, the extent of global ocean anoxia associated with the BSME has not been quantitatively estimated, much less whether euxinic conditions existed. More generally, Early Ordovician ocean redox conditions are poorly understood from the perspective of novel non-traditional metal isotope systems. In this study, we analyzed elemental concentrations and uranium isotope compositions of previously studied samples (Edwards et al., 2018) from the three sections in the Great Basin to quantitatively constrain the role of global ocean euxinia associated with the BSME.

4.2 Background

4.2.1 Geological background

During the Late Cambrian and Early Ordovician, a carbonate ramp developed on Laurentia, which was in the equatorial area (Fig. 4.1; Derby et al., 2012 and references therein). Carbonates that deposited along this ramp are up to a few kilometers thick and cover a wide area in the United States and Mexico (Fig. 4.1; Derby et al., 2012; Morgan, 2012). Lower Ordovician marine strata in the Great Basin belong to the lower Pogonip Group (Ross et al., 1989; Miller et al., 2003; Derby et al., 2012). To study the BSME, we collected carbonate samples from three Great Basin sections. From proximal to distal locations, the stratigraphic units examined in this study are the House Limestone and overlying Fillmore Formation at the Ibex area (Utah), the House Limestone and overlying Parker Spring Formation at the Shingle Pass section (Nevada), and the Goodwin Formation at the Meiklejohn Peak section (Nevada) (Ross et al., 1989; Miller et al., 2003, 2012; Derby et al., 2012; Edwards and Saltzman, 2016).

Fine-grained lime mudstone and wackestone, sometimes interbedded with siltstone, are the most common lithologies in all three sections (Miller et al., 2003, 2012; Edwards and Saltzman, 2014, 2016; Saltzman et al., 2015; Edwards et al., 2018). Coarse-grained lithologies occasionally occur, including packstone, grainstone, and flat pebble conglomerate (Adrain et al., 2014; Saltzman et al., 2015; Edwards et al., 2018). [See Miller et al. (2003) or Adrain et al. (2014) for a more detailed review of lithologies of these sections]. Because most samples are lime mudstone with some clay laminae and lack wave-generated sedimentary structures, it suggests a low energy environment at or below fair-weather wave base (Miller et al., 2003). The presence of flat pebble conglomerates (Adrain et al., 2014; Saltzman et al., 2015) suggests an intermittent high-energy environment that indicates deposition above storm wave base (Miller et al., 2003). Nonetheless, no extensive disconformities are reported for the studied interval from all three sections (Hintze, 1951, 1952; Sweet and Tolbert, 1997; Miller et al., 2003; Edwards et al., 2018).

Temporal correlations among the three sections are based on paleontological data (Hintze, 1951, 1952; Ethington and Clark, 1981; Sweet and Tolbert, 1997) and geochemical proxies (i.e., δ13Ccarb from all three sections; Edwards and Saltzman, 2014; Saltzman et al., 2015; Edwards et al., 2018). Specifically, correlations between the Ibex and Shingle Pass sections are based on the conodont biostratigraphy (i.e., the conodont *Rossodus manitouensis* zone and *Low Diversity Interval*; Ethington and Clark, 1981; Sweet and Tolbert, 1997) and a positive $\delta^{13}C_{carb}$ excursion (Edwards and Saltzman, 2014; Saltzman et al., 2015). Though conodont biostratigraphic control at the Meiklejohn Peak section is unconstrained, trilobite data of the Goodwin Formation (e.g., *Parabolinella*, but no trilobite biostratigraphy is available; Ross, 1970) are consistent with trilobites reported from the Skullrockian-Stairsian interval of the Ibex and Shingle Pass sections (Hintze, 1951, 1952). Therefore, correlations between the Meiklejohn Peak and Ibex/Shingle Pass sections are mainly based on the positive $\delta^{13}C_{carb}$ excursion (Edwards and Saltzman, 2014; Edwards et al., 2018; Figs. 4.2–4.4).

The proximal Ibex area has been more intensely studied compared with the distal Shingle Pass and Meiklejohn Peak sections in the Great Basin due to its more extensive

paleontological record. Regionally, the Ibex area is between the House Range embayment and Wah Wah Arch, both of which are important regional tectonic elements (along with the Tooele Arch) that are thought to have originated from the rifting event that formed the Laurentian margin during the Neoproterozoic (Miller et al., 2003; Sears and Price, 2003). Stratigraphic thickness variations are observed from several sections across the three tectonic elements and have been explained by influences from both the active local tectonics and relative sea level changes (Miller et al., 2003, 2012). In addition, sequence boundaries are identified in the Ibex area based on changes in carbonate facies (e.g., occurrence of karst, microkarst, or planar truncation surfaces) and/or large increase of siliciclastic materials (mostly fine quartz sand) in carbonates (Miller et al., 2003, 2012). For the stratigraphic units of interest for this study, the upper House Limestone and overlying lower Fillmore Formation, corresponding to sequence 13 and part of sequence 14, were deposited during a relative sea level lowstand, which has been recognized as the Tule Valley Lowstand (Miller et al., 2003; Edwards and Saltzman, 2014; Saltzman et al., 2015). This overall sea level fall could be an eustatic event as it is also correlated with the *Ceratopyge* Regressive Event (Erdtmann, 1986; Löfgren et al., 1999; Miller et al., 2003; Holmer et al., 2005).

The base Stairsian mass extinction event occurs within the conodont *Rossodus manitouensis* Zone and trilobite *Paraplethopeltis helli* Zone, roughly corresponding to the boundary between House Limestone and Fillmore Formation at the Ibex area (Hintze, 1951, 1952; Ethington and Clark, 1981; Adrain et al., 2003, 2014; Miller et al., 2003). Specifically, the trilobite extinction occurred at the lower boundary of sequence 13, prior to the conodont extinction at the upper boundary of sequence 13 (Miller et al., 2003). Brachiopod turnover is in between the trilobite and conodont extinctions (Holmer et al., 2005). The extinction event likely lasted for < 0.5 Myr based on conodont zonation compared to the 2020 Geologic Time Scale (Edwards et al., 2018; Goldman et al., 2020). After the extinction of conodont species that are characteristic of the *R. manitouensis* Zone, they are replaced by a low-diversity fauna (i.e., nondescript coniform taxa with uncertain taxonomic placement) in the lower Fillmore Formation (named as "*Low Diversity Interval*"), followed by a radiation that is characterized

by species such as *Glyptoconus bolites* and *Macerodus dianae* in the lower-middle Fillmore Formation (Ethington and Clark, 1981; Barnes et al., 1996). The latter radiation reflects the generation of many new nektobenthic taxa and a reduced population of the coniform taxa (Barnes et al., 1996 and references therein).

4.2.2 Uranium isotopes as a global ocean redox proxy

Uranium isotope compositions ($\delta^{238}U$) of sedimentary rocks have been used to infer global ocean redox conditions, taking advantage of the long oceanic residence time of U (~400–500 kyr in the modern ocean; see recent reviews in Andersen et al. 2017 and Zhang et al. 2020a). Modern seawater has a uniform $\delta^{238}U$ value of -0.39 ± 0.04‰ (2SD; Stirling et al., 2007; Weyer et al., 2008; Tissot and Dauphas, 2015; Andersen et al., 2016; Noordmann et al., 2016). The $\delta^{238}U$ of modern seawater reflects the relative extent of non-euxinic and euxinic settings because each redox setting corresponds to different U isotopic offsets between sediment and its overlying seawater (e.g., Weyer et al., 2008; Goto et al., 2014; Tissot and Dauphas, 2015; Andersen et al., 2016; Stylo et al., 2017; Cole et al., 2020). Rivers are the major source of oceanic U, which mainly exists as Ca/Mg-UO_2-CO_3 complexes in oxygenated waters (Dunk et al., 2002; Endrizzi et al., 2016). Groundwater could also be a source of oceanic U, but the fluxes are poorly understood. The largest U isotope offsets from the open ocean seawater are observed in euxinic settings (~0.6 ± 0.2‰), whereas smaller U isotope offsets are reported in the other redox settings (e.g., oxic, suboxic, ferruginous; Weyer et al., 2008; Andersen et al., 2014, 2016; Tissot and Dauphas, 2015; Holmden et al., 2015; Noordmann et al., 2016; Bura-Nakić et al., 2018; Brüske et al., 2020; Abshire et al., 2020; Cole et al., 2020; He et al., 2021; Bruggmann et al., 2022; Zhao et al., 2022). These observations suggest that the global seawater $\delta^{238}U$ value is more sensitive to the extent of ocean euxinia than to general ocean anoxia. For instance, at a time of expanded ocean euxinia, more ^{238}U will be preferentially removed to sediments, thus driving seawater $\delta^{238}U$ to lower values.

Carbonate $\delta^{238}U$ values can faithfully record seawater $\delta^{238}U$ with small U isotope offsets (Romaniello et al., 2013; Chen et al., 2018b; Tissot et al., 2018) and have been applied

to reconstruct global paleo-ocean redox conditions (see a review in Zhang et al. 2020a). Incorporation of aqueous U species into primary biogenic carbonates results in non-resolvable U isotope offsets from the modern seawater (i.e., less than the analytical uncertainty; Chen et al., 2018a; Livermore et al., 2020). By contrast, an average U isotopic offset of 0.27 ± 0.14‰ is observed between shallow-water platform carbonates of the modern Bahamas bank and seawater, which is associated with the authigenic enrichment of reduced U(IV) in sulfidic porewaters and preferential incorporation of charged isotopically heavy aqueous U(VI) species (Romaniello et al., 2013; Chen et al., 2016, 2017, 2018b; Tissot et al., 2018). Congruent negative carbonate $\delta^{238}U$ excursions from different sections worldwide during some geologic intervals, such as the Late Devonian (Song et al., 2017; White et al., 2018), Late Permian (e.g., Brennecka et al., 2011a; Lau et al., 2016; Zhang et al., 2018a, 2020b), and the Cretaceous Oceanic Anoxic Event 2 (OAE2; Clarkson et al., 2018), reflect changes to global seawater $\delta^{238}U$ caused by expanded ocean euxinia. This highlights the use of carbonate $\delta^{238}U$ to reconstruct ancient global ocean redox conditions during mass extinctions and major perturbations to the carbon cycle.

4.3 Materials and methods

A total of 66 fine-grained limestone samples were obtained from the Ibex (n = 35), Shingle Pass (n = 20), and Meiklejohn Peak (n = 11) sections of the Great Basin, which have previously been characterized for signs of alteration by transmitted light and cathodoluminescence microscopy (CL) and analyzed for some geochemical data ($\delta^{13}C_{carb}$, $\delta^{18}O_{carb}$, $\delta^{34}S_{CAS}$, $\delta^{34}S_{pyrite}$, I/Ca ratios) by Edwards et al. (2018).

Total organic carbon (TOC) data were measured at the Environmental Isotope Laboratory, University of Waterloo for selected samples or were obtained from the literature (Edwards and Saltzman, 2016). Samples were treated with an excess amount of 1N hydrochloric acid (HCl) to remove inorganic carbon, washed with ultrapure water, and then dried on a hotplate. Approximately 8–40 mg of the residual material was analyzed by a Costech 4010 Elemental Analyzer coupled to a Thermo-Finnigan Delta Plus XL continuous flow

isotope ratio mass spectrometer. The SBC-1 (Brush Creek Shale) rock standard from the United States Geological Survey (USGS) served as a secondary standard and yielded TOC content within 90% of the certified value.

Wet chemistry and analysis of elemental concentrations and U isotope compositions were carried out at the Metal Isotope Geochemistry Laboratory, Department of Earth and Environmental Sciences, University of Waterloo. Before leaching all the carbonate samples, three leaching agents (0.8N acetic acid, 0.5N HCl, and 1N HCl) were used to dissolve a few carbonate samples and examine the effects of different leaching acids on carbonate U isotope compositions ($\delta^{238}U_{carb}$). Among the studies that utilize $\delta^{238}U_{carb}$ to reconstruct paleo-ocean redox conditions, several have reported leaching tests (Hood et al., 2016; Lau et al., 2016; Dahl et al., 2017; Tissot et al., 2018; Zhang et al., 2018a; Clarkson et al., 2020). Although no significant difference in $\delta^{238}U_{carb}$ was found with various leaching acids in these earlier studies, complete carbonate digestion should be done and a comparison test is recommended (Clarkson et al., 2020; Zhang et al., 2020a). Consistent with findings from previous studies, the $\delta^{238}U_{carb}$ values of the same sample are identical for the three leaching acids tested in this study (see Table C1 in Appendix C). Therefore, 1N HCl was used for the rest of the carbonate samples.

Carbonate powders (~3g) were dissolved using an excess amount of 1N HCl at room temperature for 24 hours to ensure the complete dissolution of carbonate fractions. Samples were then centrifuged to separate the supernatant from residue. A split of supernatant from each sample was dried, redissolved in 2% nitric acid (HNO_3), and measured for elemental concentrations on an Agilent 8800 triple quadrupole inductively coupled plasma mass spectrometer (QQQ-ICP-MS). Four water standards (T207, T211, T225, T231) from the USGS were used as secondary standards to ensure instrument accuracy. Except for an 85% recovery rate for Mo, the recovery rates for the other elements are better than 92% and the precisions are typically within 10%. The reported elemental concentrations were corrected using the recovery rates of each element (compared with certified values) to ensure data accuracy.

Prior to the purification of U by ion exchange chromatography, a weighed amount of ^{236}U-^{233}U double spike (IRMM-3636) was added to each sample (200–500 ng U, leached by

1N HCl) to achieve a U_{spike} : U_{sample} ratio of ~0.03. Eichrom® UTEVA resin was used to purify U from sample-spike solutions following the protocols in Weyer et al. (2008) and Kendall et al. (2020). After column chemistry, samples were treated with both concentrated HNO_3 and 30% H_2O_2 (hydrogen peroxide) twice to break down any residual organic matter from the resin. A small aliquot of each sample after column chemistry was measured on the Agilent 8800 QQQ-ICP-MS to ensure the adequate removal of matrix elements. Samples were diluted to ~100 ng/g U in 2% HNO_3 and measured on a Nu Plasma II multi-collector ICP-MS. The U isotope compositions are reported relative to CRM145:

$$\delta^{238}U\ (‰) = [(^{238}U/^{235}U)_{sample} / (^{238}U/^{235}U)_{CRM145} - 1] \times 1000$$

The CRM145 and CRM129a standards were measured during the study and have average $\delta^{238}U$ values of 0.00 ± 0.09‰ (2SD, n = 170) and −1.42 ± 0.09‰ (2SD, n = 46), respectively. Because different $\delta^{238}U$ values have been reported for CRM129a from various laboratories (Andersen et al., 2017), the CRM129a can be only used as an internal $\delta^{238}U$ standard to monitor long-term instrument reproducibility. Fully digested SBC-1, SDO-1 (Devonian Ohio Shale), and SGR-1b (Green River Shale) (using HF-HNO_3-HCl; see methods in Kendall et al., 2020) rock standards (USGS) that have undergone column chemistry were measured along with other samples in this study to ensure the accuracy of the measurements. The average $\delta^{238}U$ of the measured SBC-1, SDO-1, and SGR-1b are −0.29 ± 0.11‰ (2SD, n = 6), −0.12 ± 0.06‰ (2SD, n = 4), and −0.21 ± 0.08‰ (2SD, n = 5), respectively. These data are identical to respective $\delta^{238}U$ values for these rock standards reported from several laboratories worldwide (Tissot and Dauphas, 2015; Kendall et al., 2015, 2020; Rolison et al., 2017; Lu et al., 2017, 2020; Yang et al., 2017; Brüske et al., 2020; Clarkson et al., 2021). Moreover, five carbonate samples chosen for full procedural duplicate analysis yielded reproducible $\delta^{238}U$ values given 2SD uncertainties in all cases.

4.4 Results

4.4.1 Elemental data

Measured geochemical data are shown in Table C2 (see Appendix C). Combined with published TOC data (Edwards and Saltzman, 2016), exceptionally low TOC contents (< 0.06%) are observed for samples from all three sections (Ibex area: 0.005–0.047%, n = 18; Shingle Pass: 0.013–0.031%, n = 12; Meiklejohn Peak: 0.012–0.051%, n = 8; Figs. 4.2–4.4, Table C2). Most samples contain U concentrations < 1 µg/g, with only four exceptions (Table C2). Similarly, low Mo concentrations (< 250 ng/g) are observed for samples from all three sections. Mo/U ratios are all < 0.6, except for one outlier (1.37 for LDN7391; Table C2). A wide range of Mn concentrations is observed from < 100 µg/g to ~1800 µg/g (Table C2).

There are several noteworthy observations with respect to the stratigraphic trends of the elemental data. Similar stratigraphic trends between U concentrations and U/Ca ratios and between Mo concentrations and Mo/Ca ratios suggest that both U and Mo concentration data were not significantly affected by carbonate dilution or sedimentation rate (Fig. 4.2–4.4). The U and Mo concentration data could be influenced by siliciclastic detrital input and are thus normalized to Al to reflect authigenic enrichments. The U/Al ratios in the Ibex area are elevated (> 4 ng/µg) and fluctuated prior to and during the CIE and remained at low values (< 3 ng/µg) after the CIE (Fig. 4.2). A similar stratigraphic U/Al trend is observed at the Shingle Pass section (Fig. 4.3). At the Meiklejohn Peak section, U/Al ratios are relatively low (< 2 ng/µg) prior to the CIE and slightly elevated (> 4 ng/µg) during and after the CIE (Fig. 4.4). The Mo/Al ratios in the Ibex area are slightly elevated (> 1 ng/µg) and fluctuate prior to and during the first half of the CIE. However, Mo/Al ratios sharply decrease to < 0.4 ng/µg at the peak of the CIE and remain low thereafter (Fig. 4.2). Conversely, Mo/Al ratios are slightly elevated and fluctuate during the CIE at the Shingle Pass section (Fig. 4.3). A similar stratigraphic Mo/Al trend might exist at the Meiklejohn Peak section (< 0.6 ng/µg; Fig. 4.4) but not as obvious as at the Shingle Pass section. A significant increase in Mn concentrations (up to ~1800 µg/g) during the first half of the CIE is observed for the Ibex and Shingle Pass sections

(Figs. 4.2–4.3), whereas the Mn peak at the Meiklejohn Peak section (as only represented by a single point) is more muted (up to ~400 μg/g; Fig. 4.4). The stratigraphic trend of Mn/Sr is identical to that of Mn concentrations, suggesting a dominant control of Mn concentrations on Mn/Sr ratios.

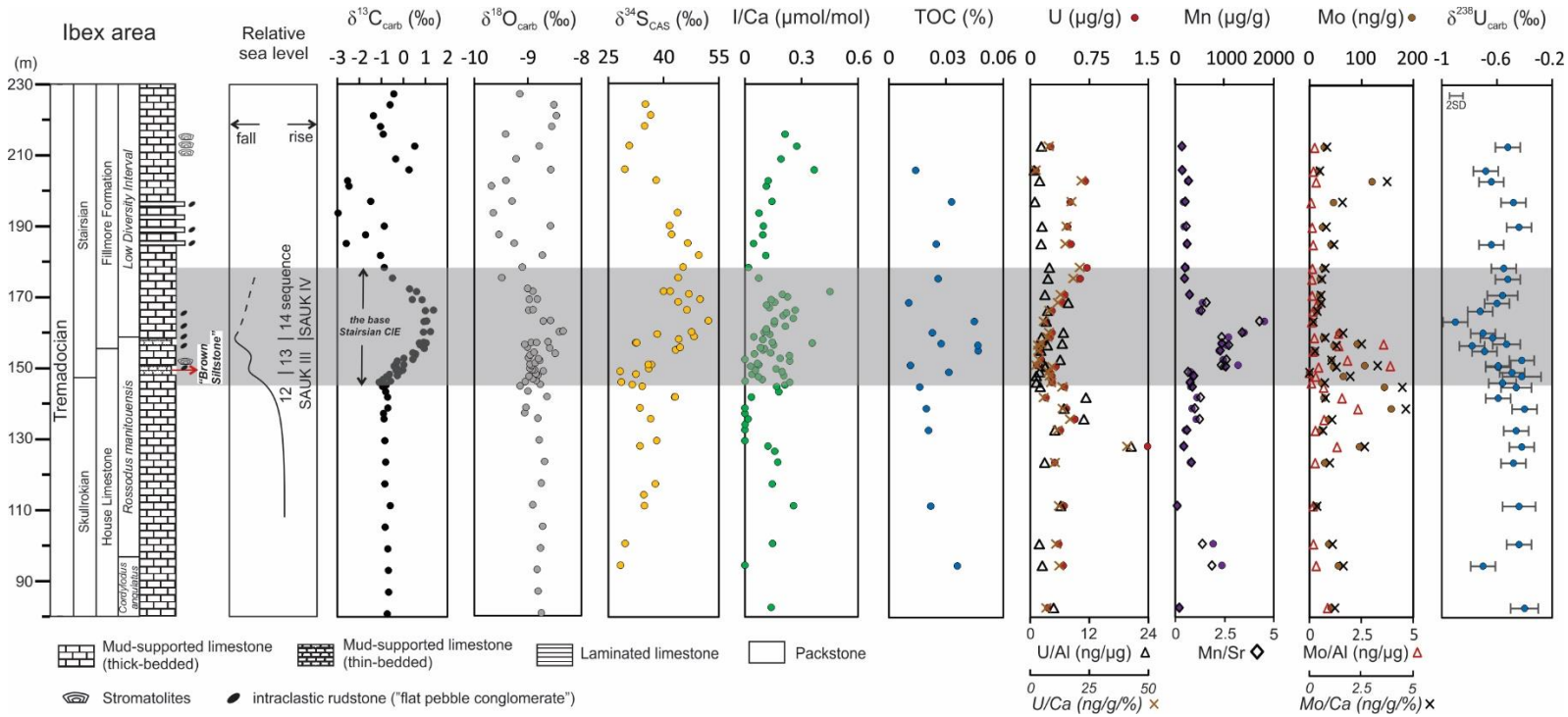

Figure 4.2 Geochemical profile for the Ibex area section, Utah. Carbon, oxygen, and sulfur isotopic data, and I/Ca ratios are from Edwards et al. (2018). Conodont zones are from Ethington and Clark (1981). Grey box shows the onset of base Stairsian carbon isotope excursion. "Brown Siltstone" marked in the stratigraphic column is from Saltzman et al. (2015), which represents the lowstand system tract. Relative sea level changes and sequences in the Ibex area are from Miller et al. (2003, 2012). Long-term analytical reproducibility for $\delta^{238}U$ is shown by the error bar in the top left of the U isotope profile.

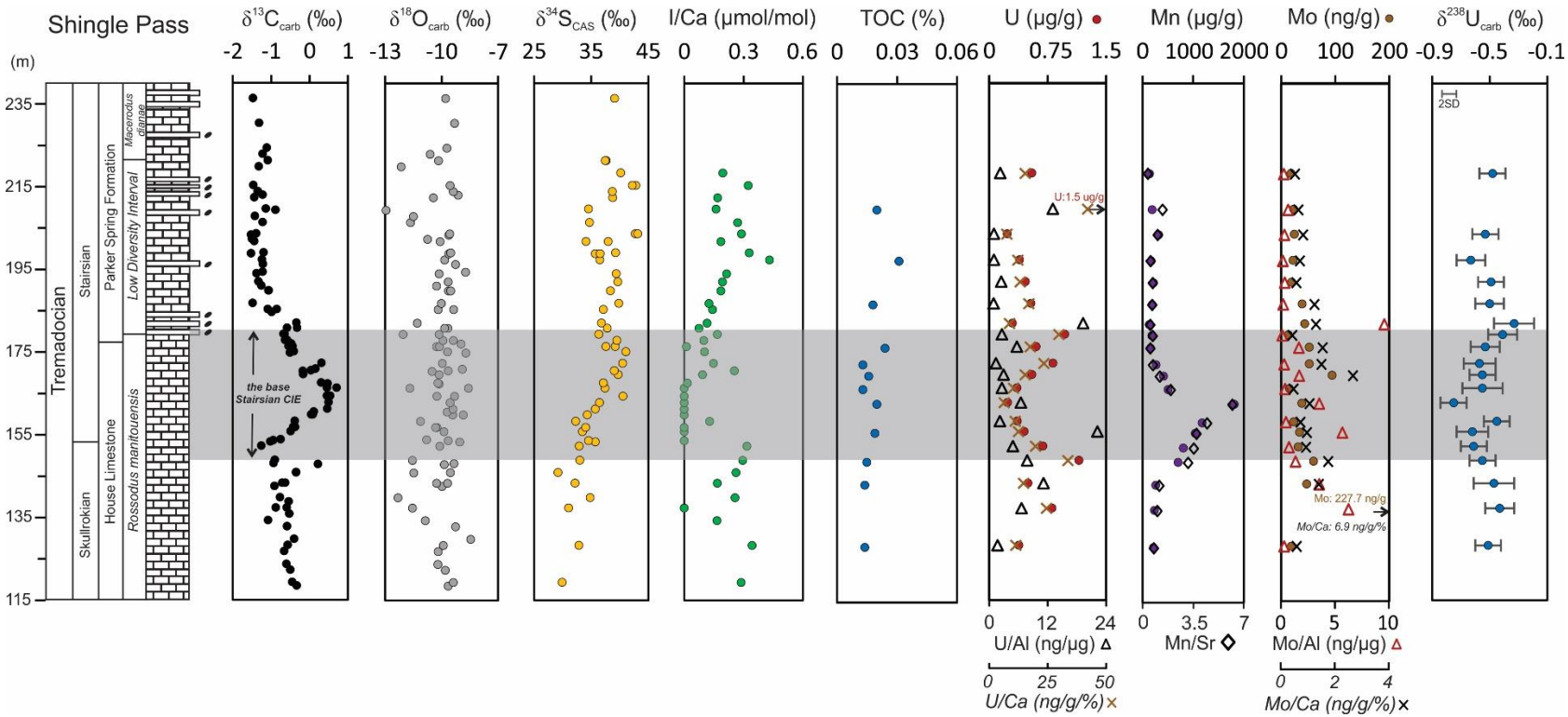

Figure 4.3 Geochemical profile for the Shingle Pass section, Nevada. Conodont zones are from Sweet and Tolbert (1997). Legends and data source are the same as in Figure 4.2.

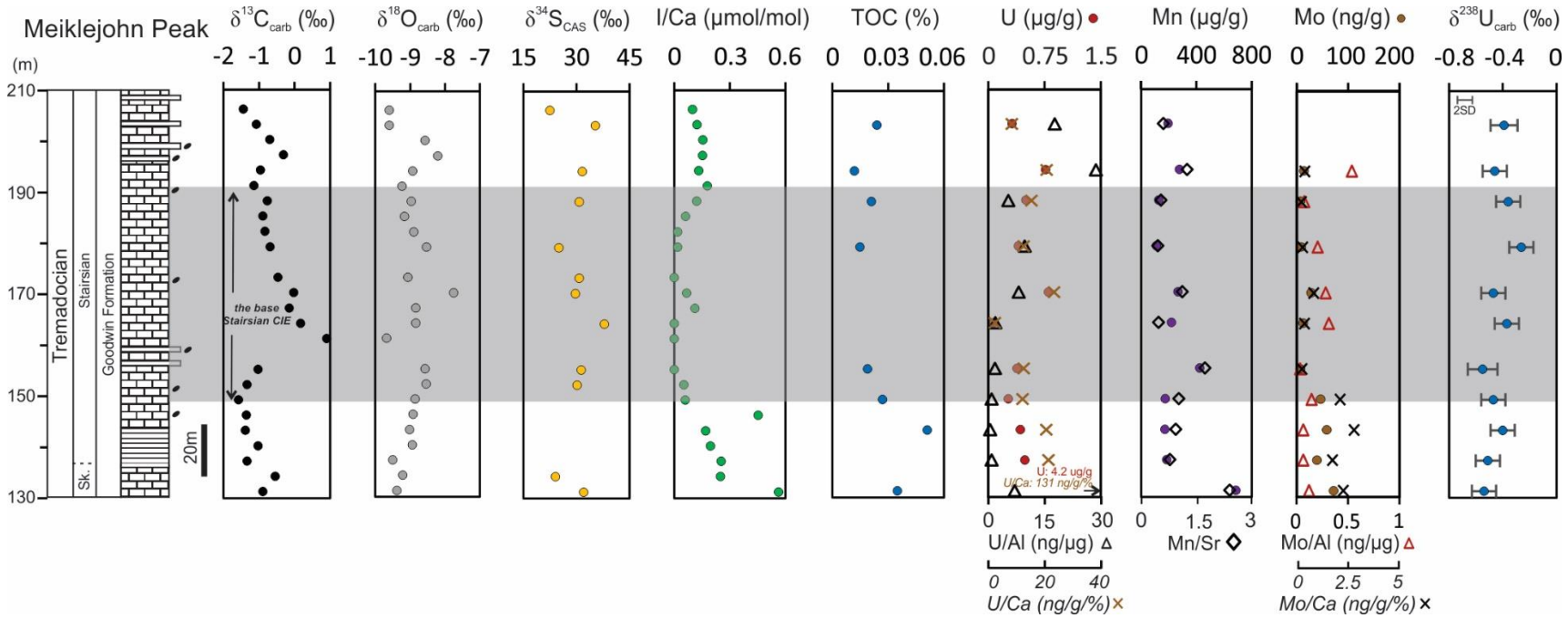

Figure 4.4 Geochemical profile for the Meiklejohn Peak section, Nevada. Legends and data source are the same as in Figure 4.2. Sk. = Skullrockian.

4.4.2 Uranium isotope compositions from carbonates

Carbonate $\delta^{238}U$ values of the Ibex, Shingle Pass, and Meiklejohn Peak sections range from −0.90‰ to −0.40‰ (n = 35), −0.75‰ to −0.33‰ (n = 19), and −0.55‰ to −0.26‰ (n = 11), respectively (Table C2). Different $\delta^{238}U$ trends are exhibited among the three carbonate sections. The proximal shallow water Ibex section has a negative $\delta^{238}U$ excursion (mostly from ~−0.50‰ to ~−0.70‰, the lowest value down to −0.90‰) that occurs within the middle of the positive $\delta^{13}C_{carb}$ excursion (Fig. 4.2), whereas the distal deep water Meiklejohn Peak section shows no clear trend during the CIE (Fig. 4.4). The shallow water Shingle Pass section, located between the other two sections, does not show an obvious trend (considering analytical uncertainties), except for a single point with a lower $\delta^{238}U$ of −0.75‰ (SP5388; Fig. 4.3).

4.5 Discussion

4.5.1 Evaluation of diagenetic factors and local depositional influences on carbonate $\delta^{238}U$ and U concentrations

Before making any meaningful interpretations for global ocean redox conditions, the influence of diagenesis and local depositional conditions on the carbonate $\delta^{238}U$ data should be carefully assessed in the study units. Edwards et al. (2018) suggested that carbonate phases experienced late burial diagenesis based on petrographic analysis using CL, but seawater geochemical signals were still preserved based on $\delta^{13}C$ correlations to sections around the globe. Diagenetic alteration could have impacted some geochemical data, for example: some anomalously low $\delta^{18}O_{carb}$ values at Shingle Pass, three low $\delta^{34}S_{CAS}$ values at Meiklejohn Peak, and variable $\delta^{34}S_{py}$ values from all three sections (Edwards et al., 2018). Nevertheless, there is no compelling evidence that the observed trends in geochemical data were solely controlled by diagenetic alteration (Edwards et al., 2018).

As it is possible that alteration can affect some geochemical trends, here we assess whether our new U data reflect seawater trends or have been overprinted by diagenetic processes. Correlations between carbonate $\delta^{238}U$ and diagenetic proxies (e.g., $\delta^{13}C$, $\delta^{18}O$,

Mn/Sr, Mg/Ca, Sr/Ca) are evaluated by R^2 and p values. We define $R^2 < 0.25$, 0.25–0.64, and > 0.64 as showing weak, moderate, and strong correlations and use *p* values to assess the significance/robustness of correlations (i.e., < 0.05 means a significant/robust correlation). Only when the correlation is significant/robust will it be described as weak, moderate, or strong.

4.5.1.1 Evaluation of detrital contamination

Detrital contamination could potentially influence the U concentrations and isotope compositions. In this study, samples were leached using 1N HCl to dissolve the carbonates and minimize the dissolution of detrital materials. The average U/Al ratio of the upper continental crust is 0.33 µg/g/% (Rudnick and Gao, 2014), which is assumed to be the U detrital background signature for the Great Basin. The U/Al ratios of the carbonate samples are 1–3 orders of magnitude higher than the upper crust, suggesting minimal effects by detrital material on the $\delta^{238}U$ of the 1N HCl leaches. This interpretation is also compatible with the absence of significant correlations between $\delta^{238}U$ and Al ($p > 0.05$; Fig. 4.5; Table 4.1) and between U and Al concentrations ($p > 0.05$).

Table 4.1 Statistical linear regression test of the influences of diagenesis on $\delta^{238}U$ record.

	Ibex		Ibex*		Shingle Pass		Shingle Pass^		Meiklejohn Peak	
	R^2	*p* value	R^2	*p* value	R^2	*p* value	R^2	*p* value	R^2	*p* value
$\delta^{238}U$ vs $\delta^{13}C$	0.16	0.06	0.08	0.19	0.05	0.67	0.00	0.83	0.08	0.40
$\delta^{238}U$ vs $\delta^{18}O$	0.03	0.40	0.00	0.87	0.28	0.02	0.26	0.04	0.01	0.77
$\delta^{238}U$ vs Mn	0.36	< 0.01	0.21	0.01	0.37	< 0.01	0.11	0.17	0.48	0.02
$\delta^{238}U$ vs Sr	0.04	0.27	0.03	0.33	0.04	0.43	0.05	0.39	0.04	0.57
$\delta^{238}U$ vs Mn/Sr	0.37	< 0.01	0.22	0.01	0.32	0.01	0.09	0.22	0.62	< 0.01
$\delta^{238}U$ vs Mg/Ca	0.01	0.51	0.01	0.50	0.00	0.85	0.00	0.96	0.02	0.69
$\delta^{238}U$ vs Sr/Ca	0.00	0.68	0.01	0.60	0.01	0.69	0.03	0.47	0.00	0.90
$\delta^{238}U$ vs U	0.10	0.07	0.09	0.09	0.03	0.53	0.00	0.91	0.19	0.18
$\delta^{238}U$ vs Al	0.02	0.37	0.02	0.49	< 0.01	0.99	0.03	0.46	0.15	0.24
$\delta^{238}U$ vs TOC	0.23	0.04	0.11	0.18	0.18	0.20	0.27	0.12	0.02	0.71
$\delta^{238}U$ vs Mo/Al	0.01	0.60	0.00	0.81	0.07	0.27	0.20	0.06	0.03	0.64
$\delta^{238}U$ vs Mo/U	0.00	0.94	0.01	0.66	0.00	0.78	0.09	0.22	0.01	0.79
$\delta^{238}U$ vs U/Al	0.04	0.24	0.05	0.23	0.01	0.66	0.03	0.51	0.02	0.71

* calculation does not include sample B-TOP7420 with a low $\delta^{238}U$ of −0.90‰ (susceptible to diagenesis due to a high Mn/Sr ratio of 4.3)

^ calculation does not include sample 5388 with a low $\delta^{238}U$ of −0.75‰ (susceptible to diagenesis due to a high Mn/Sr ratio of 6.3)

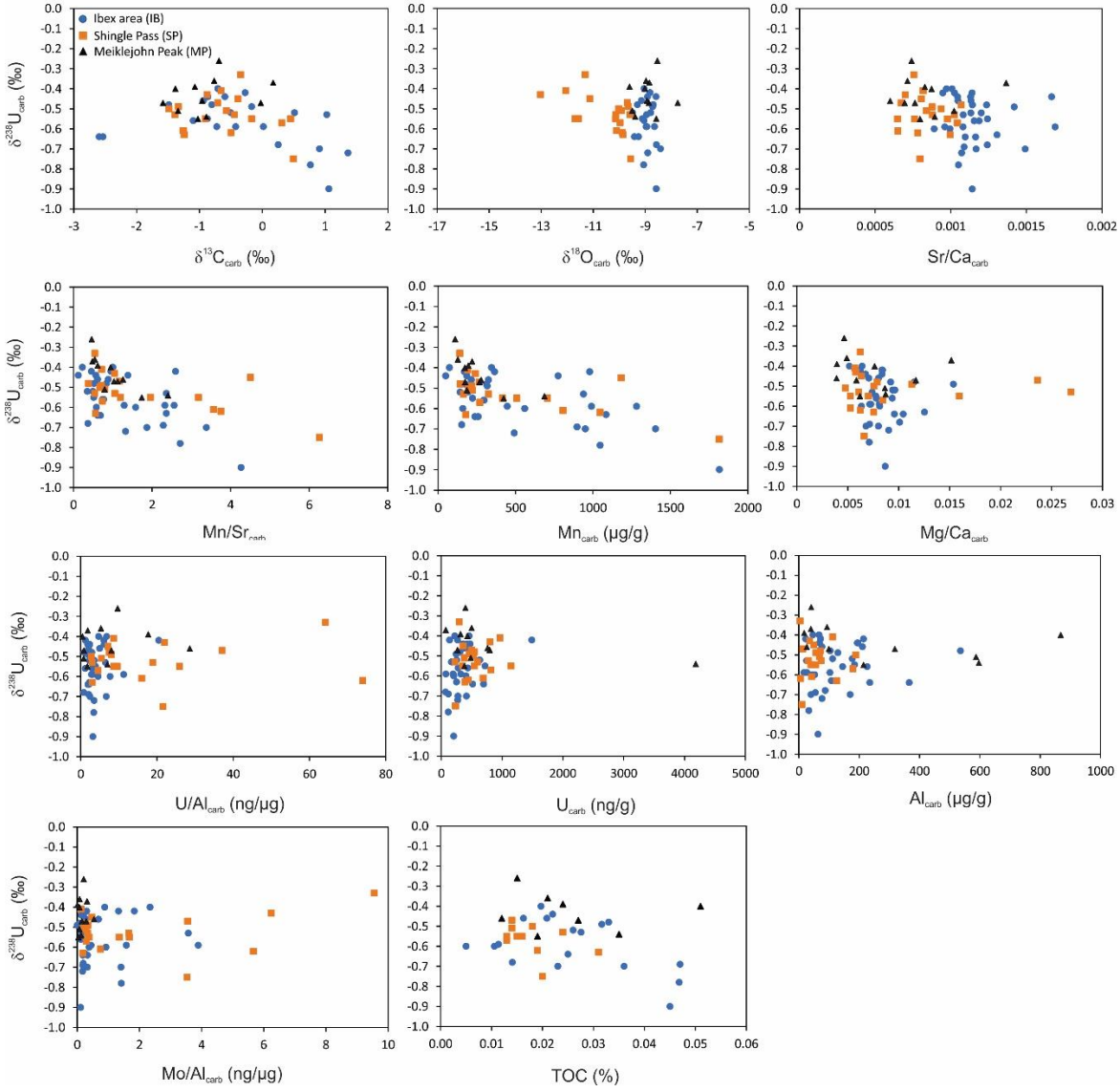

Figure 4.5 Cross plots between $\delta^{238}U$ values and geochemical indicators used to assess diagenesis from the three studied sections. All elemental ratios are weight ratios.

4.5.1.2 Evaluation of post-depositional diagenesis

Post-depositional diagenesis of carbonates and its impact on U isotope compositions are commonly evaluated via diagenetic proxies, such as cross plots with oxygen isotope compositions ($\delta^{18}O$), manganese/strontium (Mn/Sr) ratios (e.g., Veizer, 1983; Banner and Hanson, 1990; Jacobsen and Kaufman, 1999; Zhang et al., 2020a), and petrographic examination using transmitted and CL microscopy (e.g., Edwards et al., 2018). The $\delta^{18}O$ values of most samples from these studied sections are somewhat lower than the range of bulk rock $\delta^{18}O$ values from Newfoundland during the Tremadocian (between −9‰ and −6‰; Goldberg et al., 2021). Exchange with meteoric waters and/or precipitation of secondary calcite at elevated temperatures could result in lower $\delta^{18}O$ values (e.g., Veizer, 1983), and thus the $\delta^{18}O$ values of most samples were altered to some degree due to diagenesis. This was confirmed with petrographic analysis of a range of facies (Edwards et al., 2018). Although a moderate correlation between $\delta^{238}U$ and $\delta^{18}O$ for samples from the Shingle Pass section ($R^2 = 0.28$, $p = 0.02$; Table 4.1) could suggest greater diagenetic alterations on $\delta^{238}U$ values, samples from this section with obviously lower $\delta^{18}O$ values (such as −12.1‰ for SP5399 and −13.0‰ for SP5376) do not have $\delta^{238}U$ values that are statistically different from the stratigraphically adjacent samples. This observation is consistent with previous findings that $\delta^{238}U$ values are more resistant against diagenetic alteration than $\delta^{18}O$ values (Lau et al., 2017; Chen et al., 2018b). In addition, there are no robust correlations between $\delta^{238}U$ and $\delta^{18}O$ for the Ibex and Meiklejohn Peak sections ($p \geqslant 0.40$), suggesting less impact of diagenetic alterations on $\delta^{238}U$ records (Fig. 4.5; Table 4.1).

Carbonates minimally affected by meteoric diagenesis are typically characterized by low Mn/Sr ratios (Banner and Hanson, 1990). Elevated Mn/Sr ratios are observed particularly for the shallow water Ibex area (up to 4.3) and Shingle Pass section (up to 6.3) during the middle CIE, but are lower at the deeper water Meiklejohn Peak section (only up to 1.7; Figure 4.2–4.4, Table C2). Specifically, samples with the highest Mn/Sr ratios from the Ibex and Shingle Pass sections have notably low $\delta^{238}U$ of −0.90‰ and −0.75‰, respectively, which

raises the possibility that the $\delta^{238}U$ of these two samples were altered. Therefore, correlations between $\delta^{238}U$ values and Mn/Sr ratios (and also other diagenetic proxies) with and without the sample with the highest Mn/Sr ratio from both sections were calculated in Table 4.1, to determine whether the correlations are mainly caused by one sample. Moderate correlations between $\delta^{238}U$ and Mn/Sr ratios are observed for all sections (R^2 = 0.32–0.62, $p < 0.02$; Fig. 4.5). Excluding the sample with the highest Mn/Sr ratio from the Ibex and Shingle Pass sections (which might have altered $\delta^{238}U$ values), a weak correlation is observed for the Ibex section (R^2 = 0.22, p = 0.01) whereas no robust correlation is observed for the Shingle Pass section (R^2 = 0.09, p = 0.22; Table 4.1). Although the correlation between $\delta^{238}U$ and Mn/Sr ratio at the Ibex area is not strong, relatively lower $\delta^{238}U$ values coincide with elevated Mn/Sr ratios during the middle CIE, which is consistent with the interpretation that there is some degree of diagenetic overprints on $\delta^{238}U$ values. At the Shingle Pass section, only one sample with the highest Mn/Sr ratio has an anomalously low $\delta^{238}U$ value. For the rest of samples in this section, diagenetic alterations could have less impact on $\delta^{238}U$ values, which is compatible with the absence of a robust correlation between $\delta^{238}U$ and Mn/Sr ratios (p = 0.22; Table 4.1). Despite the moderate correlation between $\delta^{238}U$ and Mn/Sr ratios for the Meiklejohn Peak section, the Mn/Sr ratios are generally low (mostly less than 2) in this section, suggesting a lower extent of diagenetic alteration. This interpretation is consistent with the lack of a negative $\delta^{238}U$ excursion in the Meiklejohn Peak section.

Dolomitization and mineralogical transformations (aragonite to calcite) are not likely to have significantly affected carbonate $\delta^{238}U$ values in this study. This is evidenced by relatively low Mg/Ca (< 0.03) and Sr/Ca (< 0.01) ratios, both of which show no significant correlations with $\delta^{238}U$ ($p > 0.05$; Fig. 4.5; Table 4.1).

4.5.1.3 Evaluation of early diagenetic U(VI) reduction and local water redox conditions

Early diagenetic alteration caused by reducing pore waters has been suggested to result in slightly higher $\delta^{238}U$ in carbonates compared to the seawater they precipitated from (Romaniello et al., 2013; Chen et al., 2018b; Tissot et al., 2018). Modern Bahamas carbonates

deposited under oxygenated bottom waters have $\delta^{238}U$ values that are on average 0.27 ± 0.14‰ higher than the modern seawater, which is likely related to the addition of reduced, isotopically heavy U(IV) from anoxic/sulfidic porewaters and preferential incorporation of isotopically heavy aqueous U(VI) species (Romaniello et al., 2013; Chen et al., 2016, 2018b; Tissot et al., 2018). This effect is not likely to significantly affect carbonate $\delta^{238}U$ at greater burial depths because most porewater U has already been reduced to less soluble U(IV) at shallower depths (Romaniello et al., 2013; Chen et al., 2018b; Tissot et al., 2018). To evaluate the magnitude of the isotopic offset between carbonate and seawater $\delta^{238}U$, it is essential to evaluate the influence of early diagenetic porewater redox conditions as well as local water column redox conditions on the carbonate $\delta^{238}U$ values.

Local water redox conditions can be assessed by comparing the new U data with previously published I/Ca ratios (Edwards et al., 2018), as well as with elemental data (i.e., TOC, C_{org} : P ratios; Mo and U concentrations, Mo/Al ratios, U/Al ratios, and Mo/U ratios; e.g., Algeo and Ingall, 2007; Algeo and Tribovillard, 2009; Lu et al., 2010; Algeo and Liu, 2020; Kendall, 2021). I/Ca ratios have been used as an effective local redox proxy for carbonates because the reduction potential of iodine (iodate [IO_3^-] / iodide [I^-]) is close to that of O_2/H_2O and only oxidized IO_3^- is thought to incorporate into carbonate mineral lattices, whereas the reduced I^- remains in the aqueous phase (e.g., Lu et al., 2010). As iodate can be reduced to iodide in the water column with $O_2 < 20–70$ µM (Rue et al., 1997; Farrenkopf and Luther, 2002; Lu et al., 2016), near-zero I/Ca ratios could suggest low O_2 water columns (dysoxic/suboxic). Edwards et al. (2018) did not find strong evidence to indicate I/Ca ratios from these three Great Basin sections were a result of diagenetic alteration and thus interpreted this data as reflecting the local seawater chemistry. These authors found near-zero I/Ca ratios occur during the CIE for the Shingle Pass and Meiklejohn Peak sections. However, at Ibex the near-zero I/Ca ratios occurred prior to the CIE with fluctuating I/Ca ratios during the CIE, which are not well understood (Edwards et al., 2018). Nonetheless, deoxygenation in the water column could be generally consistent with elevated Mn concentrations during the first half of

the CIE, which show a larger magnitude for the shallow water Ibex and Shingle Pass sections than the deeper water Meiklejohn Peak section (Figs. 4.2–4.4).

Local water redox conditions can be assessed by other proxies, such as TOC and C_{org} : P ratios in the sediment (e.g., Algeo and Ingall, 2007; Algeo and Liu, 2020). TOC values are consistently low among three sections (< 0.06%, there are low C_{org} : P ratios [< 18] as well; Table C2). Average TOC contents at the Ibex, Shingle Pass, and Meiklejohn Peak sections are 0.026%, 0.018%, and 0.026%, respectively (Table C2). In comparison, the Bahamas carbonates deposited from an oxic water column and anoxic/sulfidic porewaters have an average TOC content of 0.26% (0.02–0.81%, n = 44; Tissot et al., 2018). Low TOC content for the Great Basin carbonates could be related to the decomposition of organic matter under an oxic water column, generally low productivity in the surface water, or a fast sedimentation rate (e.g., Tyson, 2005). As the sedimentation rate and productivity are poorly constrained for these carbonates, it is difficult to imply local water redox conditions solely based on TOC content.

Local water redox conditions can be evaluated by redox-sensitive trace metal data. Low Mo concentrations (< 250 ng/g) and generally low Mo/U ratios (< 0.6) are observed for the carbonate samples from all three sections, suggesting non-euxinic water column conditions during carbonate accumulation (Algeo and Tribovillard, 2009). Low Mo concentrations may also indicate no sulfidic porewaters because Bahamas carbonates deposited under oxic water columns and anoxic/sulfidic porewaters are generally characterized by high Mo concentrations of > 2 – 3 μg/g (Romaniello et al., 2016). This interpretation is consistent with generally low U concentrations in our carbonate samples (mostly < 1 μg/g), in comparison to higher U concentrations in Bahamas carbonates/calcite (⩾ 2 μg/g; Chen et al., 2018b). Slightly elevated and fluctuating U/Al ratios during the CIE are observed at all three sections, suggesting briefly more reducing conditions within the sediment. The Mo/Al ratios are observed to be slightly elevated (> 1 ng/μg) and fluctuated prior to and during the first half of the CIE at the Ibex area, suggesting relatively more reducing conditions within the sediment (e.g., Tribovillard et al.,

2006). However, Mo/Al ratios at this section rapidly return to < 0.4 ng/μg at the peak of CIE and remained at such low levels thereafter, which could reflect more oxic conditions. Rapid decrease of Mo/Al to lower values during the CIE at the Ibex area is not observed for the Shingle Pass and Meiklejohn Peak sections (Figs. 4.2–4.4, Table C2). Elevated Mo/Al ratios in all three sections during the CIE are generally consistent with other proxies (e.g., I/Ca ratios, Mn concentrations, U/Al ratios) that are suggestive of an episode of deoxygenation. The deoxygenation event at the Ibex area started prior to the CIE compared with the other distal sections, which could be a local phenomenon. Considering the discussion above, local water redox conditions are inferred to be generally dysoxic/suboxic to oxic with an episode of deoxygenation in the water column and non-sulfidic conditions in the porewater.

Local water redox conditions do not seem to greatly influence carbonate $\delta^{238}U$ values. Although there are a few U-enriched samples (U > 1 μg/g), their $\delta^{238}U$ values do not show significant deviations from the samples above or below, suggesting no significant enrichment of isotopically heavy U in those samples compared with the others. Correlations between $\delta^{238}U$ and TOC are weak for the Ibex area ($R^2 = 0.23$, $p = 0.04$) and not significant for the other two sections ($R^2 = 0.02–0.18$, $p = 0.20–0.71$; Table 4.1). However, if the sample with the lowest $\delta^{238}U$ value from the Ibex area is excluded, no robust correlation exists ($R^2 = 0.11$, $p = 0.18$; Table 4.1). These observations suggest limited influence of organic matter on carbonate $\delta^{238}U$ values. Further, no significant correlations are observed between $\delta^{238}U$ and Mo/U ratios (and Mo/Al or U/Al) ($p > 0.05$; Figs. 4.5, Table 4.1), which is most compatible with the interpretation that carbonate $\delta^{238}U$ values are not significantly controlled by local water redox variations.

Based on the discussion above, some geochemical signals of the studied carbonates were diagenetically altered, as evidenced by relatively low $\delta^{18}O$ values (for all three sections and particularly for the Shingle Pass section), elevated Mn/Sr ratios (particularly during the CIE for the Ibex and Shingle Pass sections), as well as petrographic evidence (dully luminescent; Edwards et al., 2018). Relatively lower $\delta^{238}U$ values of samples from the Ibex area during the middle CIE and of a sample from the Shingle Pass section were likely

influenced by diagenesis (as evidenced by elevated Mn/Sr ratios). Having said that, distinctive geochemical differences (e.g., Mo/Al) exist between the Ibex and Shingle Pass sections that suggests other factor(s) beside diagenetic alteration may further contribute to the negative $\delta^{238}U$ excursion at the Ibex section. This is described in the next section.

4.5.2 Factors that could potentially cause the negative $\delta^{238}U$ excursion at the Ibex area

The brief negative $\delta^{238}U$ excursion during the middle CIE at the Ibex area could be due to diagenetic overprints as evidenced by coincidently elevated Mn/Sr ratios. Because the lighter U isotope (^{235}U) is preferentially adsorbed onto the surface of Mn oxides (Weyer et al., 2008; Brennecka et al., 2011b; Goto et al., 2014; Dang et al., 2016; Jemison et al., 2016; Wang et al., 2016), it would be possible that the dissolution of Mn oxides released isotopically light U within the sediment, which was then incorporated into carbonate during recrystallization or cementation. This seems to be the simplest and direct explanation for the brief negative $\delta^{238}U$ excursion at the Ibex area. In contrast to the negative $\delta^{238}U$ excursion at the shallow Ibex area, however, samples from the shallow Shingle Pass section, which are also characterized by similarly elevated Mn/Sr ratios, have no obvious stratigraphic $\delta^{238}U$ trend during the middle CIE, except for a single sample with low $\delta^{238}U$ (Fig. 4.6). This raises a question about whether the negative $\delta^{238}U$ excursion at the Ibex area is solely associated with Mn oxides and diagenetic alteration. Here, we discuss two other possibilities that could potentially influence carbonate $\delta^{238}U$ in the Ibex area: 1) sea level changes and 2) expanded euxinic settings elsewhere in a restricted basin.

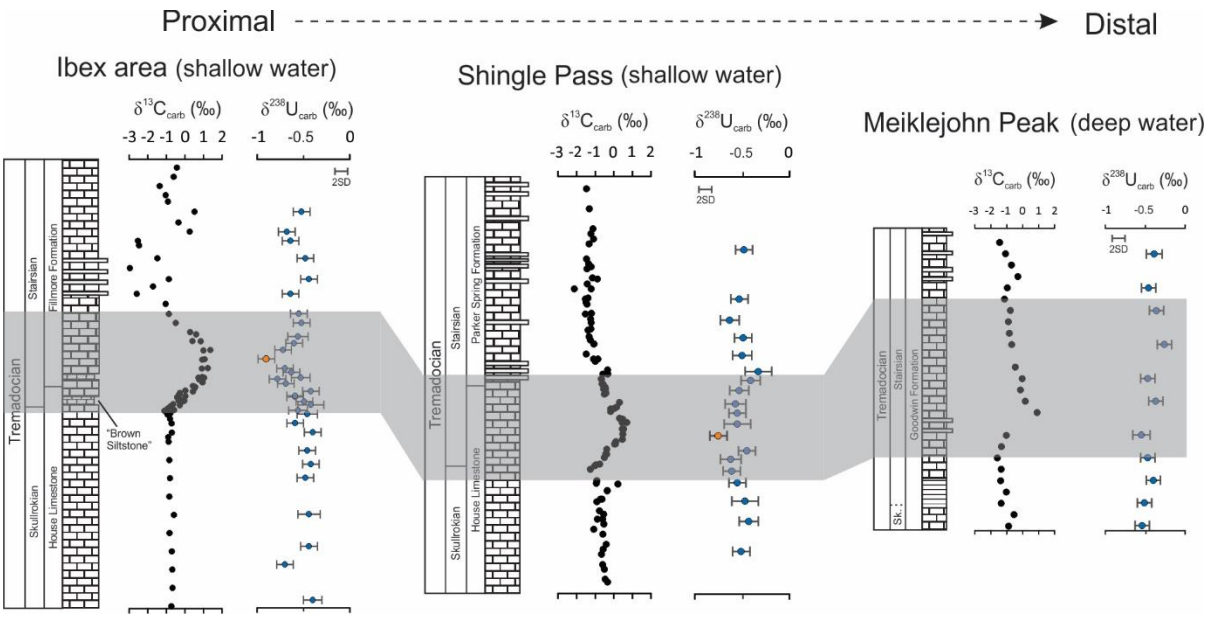

Figure 4.6 Comparison of $\delta^{13}C_{carb}$ and $\delta^{238}U$ values among the Ibex area, Shingle Pass, and Meiklejohn Peak sections in the Great Basin. Grey box shows the correlation of the base Stairsian carbon isotope excursion in the three sections. Samples with the lowest $\delta^{238}U$ values (and also the highest Mn/Sr ratios) from the Ibex and Shingle Pass sections are marked in orange.

(1) Sea level changes have been proposed to influence the seawater $\delta^{238}U$ signals recorded in ancient carbonate platforms (Tissot et al., 2018; del Rey et al., 2020). However, this hypothesis is not supported by other $\delta^{238}U$ studies which did not find a close relationship between carbonate $\delta^{238}U$ and sea level change (e.g., Lau et al., 2016; Bartlett et al., 2018; Wei et al., 2018; Zhang et al., 2018a, 2020b; Dahl et al., 2019). Based on the different $\delta^{238}U$ trends from the brachiopod calcite and surrounding carbonate matrix during the late Silurian Lau CIE (del Rey et al., 2020) and a coincident sea level fall (Eriksson and Calner, 2008), del Rey et al. (2020) hypothesized that carbonates formed during sea level lowstands would have heavier $\delta^{238}U$ values relative to seawater due to higher diagenetic fluid flow rates and/or higher organic

carbon fluxes, whereas carbonates deposited at times of high sea level would have seawater-like $\delta^{238}U$ values due to lower diagenetic fluid flow rates and/or lower organic carbon fluxes. Our studied carbonate intervals were deposited during a sea level lowstand (e.g., Erdtmann, 1986; Miller et al., 2003, 2012), which should show a positive $\delta^{238}U$ excursion according to del Rey et al. (2020). This, however, is the opposite of the trends presented in the Ibex area (and also not consistent with the invariant $\delta^{238}U$ trends in other two distal sections) and suggests sea level change does not have a strong influence on the stratigraphic trend in carbonate $\delta^{238}U$.

(2) The negative $\delta^{238}U$ excursion during the CIE in the Ibex area could be associated with the preferential removal of isotopically heavy U into euxinic settings elsewhere in an episodically restricted basin that included the Ibex section (but no euxinic conditions at the Ibex section itself as evidenced by low Mo concentrations). The notion of episodic local basin restriction is reasonable based on the basin's geologic background. The depositional basin at the Ibex area has been interpreted as periodically restricted during the Middle Ordovician based on anomalous stratigraphic $\delta^{13}C$ and Th/U trends of the Kanosh Shale (Edwards and Saltzman, 2014; Marenco et al., 2013, 2016), although similar interpretations have not yet been extended down to the House and Fillmore formations. Several sponge-microbial reefs have been found in the lower Fillmore Formation at the Ibex area (and also in other places of the North America; Dattilo, 1993; Hinze, 1973; Carrera and Rigby, 1999; Miller et al., 2003, 2012) that could provide seafloor relief and fringing reef-like restrictions during a sea level lowstand. The negative $\delta^{238}U$ excursion (and the CIE) from the Ibex area occurs during a relative sea level lowstand (recognized as the Tule Valley Lowstand), which is evidenced by the deposition of "brown siltstone" at the beginning of the CIE (Fig. 4.2; Miller et al., 2003; 2012; Saltzman et al., 2015). Therefore, a sea level drop could potentially result in some degree of local basin restriction for the most proximal shallow water Ibex area.

The proposed concept of an expanded euxinic setting elsewhere in an episodically restricted basin that includes the Ibex area (non-euxinic at the Ibex itself) could help explain some of the geochemical data. First, compared to the near-zero I/Ca ratios preserved during

the CIE in the other two distal sections (Edwards et al., 2018), the fluctuating I/Ca record during the CIE in the Ibex area could be explained by episodic expansion of relatively low-O_2 waters from the open ocean into shallow oxic surface waters of a locally restricted basin. The near-zero I/Ca ratios at the Ibex area occur prior to the CIE and are poorly understood. Second, the expansion of bottom water euxinia elsewhere in a locally restricted basin near the Ibex area (non-euxinic conditions at the Ibex locality itself) could explain the sudden decrease in Mo/Al at the peak of CIE (and remained at low values thereafter) because Mo would be preferentially removed to euxinic sediment and thus lead to a smaller local seawater Mo reservoir (and thus low Mo/Al in sediment). In comparison, such a Mo/Al pattern is not observed in the other two distal sections (Figs. 4.2–4.4). Third, expanded euxinic settings in a locally restricted basin could lead to a larger extent of pyrite burial and thus result in a greater $\delta^{34}S_{CAS}$ excursion (~20‰) in the Ibex area, compared to smaller $\delta^{34}S_{CAS}$ excursions (~5–7‰) in the other two distal sections (Edwards et al., 2018). Fourth, this proposed mechanism could help explain the distinct stratigraphic $\delta^{238}U$ trend in the Ibex area. Heavy ^{238}U was preferentially removed to euxinic settings elsewhere in the restricted basin and led to a low $\delta^{238}U$ in the basinal water mass, which is the signature that preserved in the Ibex carbonates.

This hypothesis (i.e., expanded euxinic settings elsewhere in a restricted basin) requires further testing because there is no other evidence for basin restriction and an expanded euxinic setting during the CIE. In addition, this restricted basin must be relatively small such that water column euxinia caused shallow basinal water $\delta^{238}U$ values to be slightly altered but global seawater $\delta^{238}U$ values were not significantly influenced. This hypothesis potentially explains some other geochemical data (e.g., Mo/Al ratio, $\delta^{34}S_{CAS}$) besides the negative $\delta^{238}U$ excursion. Basin restriction at the Ibex area but not at the Shingle Pass section may also potentially explain why samples from the Shingle Pass section that have similarly high Mn/Sr ratios do not show a similar negative $\delta^{238}U$ excursion defined by multiple samples as observed in the Ibex area. Alternatively, the discrepancy of stratigraphic $\delta^{238}U$ trend between the two sections may represent a case that samples with lower $\delta^{238}U$ contain a relatively larger proportion of isotopically light U that is released from the dissolution of Mn oxides whereas the other

samples are not. This explanation is simple and directly links low $\delta^{238}U$ values with elevated Mn/Sr ratios, although it cannot explain the other distinct geochemical trends between the Ibex and Shingle Pass sections. Independent of these hypotheses, we still recognize that the most negative $\delta^{238}U$ from the Ibex and Shingle Pass sections are associated with the highest Mn/Sr ratios, which probably reflects diagenetic alteration of these specific samples.

4.5.3 Constraints on ocean redox conditions during the BSME using carbonate $\delta^{238}U$ from the distal Shingle Pass and Meiklejohn Peak sections

Carbonates from the two distal Shingle Pass and Meiklejohn Peak sections likely record global ocean $\delta^{238}U$ signals. Relatively invariant carbonate $\delta^{238}U$ values in the two distal sections suggest minimal changes in global ocean euxinic seafloor area during the Tremadocian (avg. $\delta^{238}U = -0.48 \pm 0.09$‰, excluding sample SP5388 that has a high Mn/Sr of 6.3 and low $\delta^{238}U$ of −0.75‰). This interpretation is compatible with a small $\delta^{34}S_{CAS}$ excursion (~5–7‰) during the CIE from both distal sections (Edwards et al., 2018) because $\delta^{238}U$ is more sensitive to ocean euxinia than $\delta^{34}S_{CAS}$ and small $\delta^{34}S_{CAS}$ excursions do not necessarily fingerprint a small expansion of global ocean euxinia (Dahl et al., 2014). For example, an increase in pyrite burial could occur in sediment underlying ferruginous water masses if there was expansion of ocean anoxia without a significant change in the extent of ocean euxinia (e.g., Dahl et al., 2014). Therefore, $\delta^{34}S_{CAS}$ data do not contradict our interpretation of carbonate $\delta^{238}U$.

The carbonate $\delta^{238}U$ from the two distal sections are used to reconstruct global ocean redox conditions during the studied interval (Tremadocian). Considering the local dysoxic/suboxic to oxic water conditions and non-sulfidic porewaters, we tentatively assume that carbonate $\delta^{238}U$ from the two distal sections record the $\delta^{238}U$ of coeval global seawater with a small U isotope offset (0–0.27‰). The assumed range of U isotope offset between carbonates and seawater is between 0‰ and the average $\delta^{238}U$ offset of 0.27 ± 0.14‰ between Bahamas carbonate sediment and modern seawater because of non-sulfidic porewater conditions (e.g., lower Mo and U concentrations) for the Great Basin carbonates compared to

the Bahamas carbonates (sulfidic porewaters; Romaniello et al., 2013; Chen et al., 2018b; Tissot et al., 2018). Therefore, the estimated $\delta^{238}U$ of coeval seawater is from −0.75 ± 0.09‰ to −0.48 ± 0.09‰, which is lower than that of modern well-oxygenated seawater (−0.39 ± 0.04‰; Stirling et al., 2007; Weyer et al., 2008; Tissot and Dauphas, 2015; Andersen et al., 2016; Noordmann et al., 2016). The lower seawater $\delta^{238}U$ suggests more widespread ocean euxinia during the studied Tremadocian interval than today. This interpretation is consistent with many other studies that suggest widespread ocean anoxia/euxinia continued until the Devonian (e.g., Dahl et al., 2010; Kendall et al., 2015; Elrick et al., 2022; Qin et al., 2022).

4.5.4 Quantitative estimation of Tremadocian ocean euxinia from carbonate $\delta^{238}U$

Numerical modeling of carbonate $\delta^{238}U$ values can be used to quantitatively constrain the global seafloor area that was covered by euxinic seawaters (e.g., Wang et al., 2016; Lau et al., 2016, 2017; Zhang et al., 2018a, 2018b, 2020b; Gilleaudeau et al., 2019; Stockey et al., 2020). The numerical approach follows the model developed by Stockey et al. (2020) and is briefly described here. The global seawater U concentration and $\delta^{238}U$ value can be expressed as the difference between riverine input and output to the seafloor (Wang et al., 2016; Stockey et al., 2020), formulated as equations (I) and (II), respectively:

$$dU_{SW}/dt = F_r - \sum F_i \quad \text{(I)}$$

$$dU_{SW}\delta_{SW}/dt = F_r\delta_r - \sum F_i\,(\delta_{SW} + \Delta_i) \quad \text{(II)}$$

where U_{SW} is the seawater U mass, F_r represents riverine U input, F_i is the U output flux to the euxinic (eux), reducing (red; e.g., ferruginous sink, suboxic sink), and oxic (oxic; e.g., Fe-Mn oxides, biogenic carbonates) U sinks in the ocean, and Δ_i is the U isotopic offset between seawater and each redox sink (eux, red, and oxic) (Table 4.2). Fluxes for each U redox sink are defined as below (Reinhard et al., 2013; Stockey et al., 2020):

$$F_i = Af_ib_i\alpha_i([U]_{SW}/[U]_{M.SW}) \quad \text{(III)}$$

where A is the total seafloor area, f_i is the fraction of the global seafloor area that is covered by each sink, b_i is the burial flux of each sink, α_i is the pseudospatial scaling coefficient that scales the U burial rate to the effects of organic carbon remineralization (e.g., more organic matter

could reach sediment on the shallow water continental shelf to promote U removal than deep water abyssal seafloor) for euxinic and reducing sinks (Menard and Smith, 1966; Middelburg et al., 1996; see details in Reinhard et al. 2013 and Stockey et al. 2020), $[U]_{SW}$ is the average modeled U concentration of ancient seawater, and $[U]_{M.SW}$ is the average U concentration of modern seawater (Table 4.2).

Table 4.2 Parameters used for U isotope mass balance model.

Parameters	Unit	Minimum value	Maximum value	References
$F_{riv}(U)$	*mol/yr*	2.75×10^{7}	5.65×10^{7}	1
$b_{U.eux}$	*mol/(m² × yr)*	5.4×10^{-6}	4.62×10^{-5}	1
$b_{U.red}$	*mol/(m² × yr)*	9.2×10^{-7}	4.37×10^{-6}	1
$b_{U.ox}$	*mol/(m² × yr)*	2.72×10^{-8}	6.75×10^{-8}	1
$\delta^{238}U_{riv}$	*‰*	–0.34	–0.24	2-3
$\Delta^{238}U_{eux}$	*‰*	0.4	0.8	2-8
$\Delta^{238}U_{red}$	*‰*	0	0.4	2, 4, 9, 10, 18-20
$\Delta^{238}U_{oxic}$	*‰*	–0.05	0.01	4, 11-14, 20
$f_{ox.lim}$	*%*	83.89	100	15
f_{red}	*%*	0	100-f_{eux}	/
A	*m²*	3.6×10^{14}	(fixed value)	15
M	*kg*	1.41×10^{21}	(fixed value)	12
$[U]_{U.sw}$	*mol/kg*	14×10^{9}	(fixed value)	16
$\delta^{238}U_{M.sw}$	*‰*	–0.39	(fixed value)	17

References: 1, Dunk et al., (2002); 2, Andersen et al., (2016); 3, Noordmann et al., (2016); 4, Weyer et al., (2008); 5, Andersen et al., (2014); 6, Holmden et al., (2015); 7, Bura-Nakić et al., (2018); 8, Brüske et al., (2020); 9, Abshire et al., (2020); 10, Cole et al., (2020); 11, Goto et al., (2014); 12, Lau et al., (2017); 13, Wei et al., (2018); 14, Zhang et al., (2018b); 15, Reinhard et al., (2013); 16, Morford and Emerson, (1999); 17, Tissot and Dauphas (2015); 18, He et al., (2021); 19, Bruggmann et al., (2022); 20, Gilleaudeau et al., (2019)

This approach couples ocean U concentrations and isotopic compositions to provide a robust estimation of the areal extent of euxinic seafloor by considering a range of several parameters (Table 4.2; Stockey et al., 2020). The model is functioned to run dynamically for 10 Myr to ensure steady state conditions are reached and 1000 Monte Carlo simulations are performed for each of 31 logarithmically scaled scenarios of global ocean euxinia (Fig. 4.7; following Stockey et al., 2020). Using a modern seawater $\delta^{238}U$ value of −0.39 ± 0.04‰ (e.g., Weyer et al., 2008; Tissot and Dauphas, 2015), the model estimates the modern ocean euxinic seafloor area to be 0.2–0.3% (32^{th}–68^{th} percentile; median = 0.2%), which generally fits with previous estimates of modern euxinic seafloor area (0.1–0.3%; Reinhard et al., 2013; Tissot and Dauphas, 2015). Therefore, using estimated Tremadocian seawater $\delta^{238}U$ values of −0.75‰ ± 0.09‰ (lower endmember) and −0.48‰ ± 0.09‰ (higher endmember), the global euxinic seafloor area is estimated to be 2.5–15.8% (32^{th}–68^{th} percentile; median = 6.3%) and 0.2–0.5% (32^{th}–68^{th} percentile; median = 0.3%), respectively. This estimate (0.2–15.8%) overlaps with the lower end of the global euxinic seafloor area estimate for the Hirnantian OAE (~4–30%, 30^{th}–70^{th} percentile; Bartlett et al., 2018; Stockey et al., 2020).

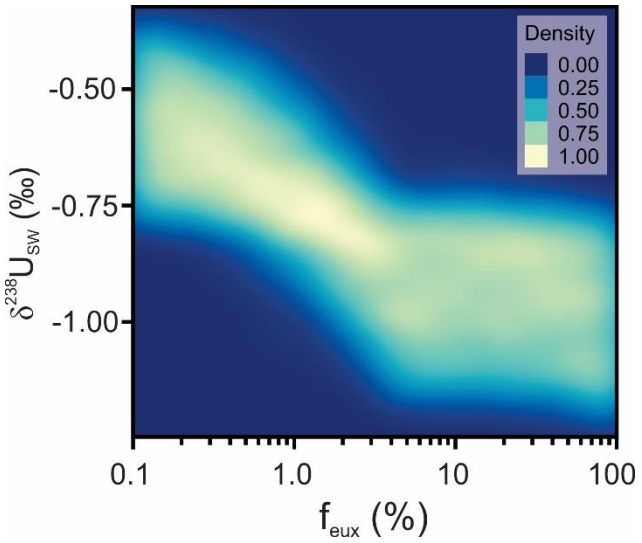

Figure 4.7 Uranium isotope mass balance model output that shows the frequency distribution of modeled seawater U isotope compositions ($\delta^{238}U_{SW}$) as a function of global ocean euxinic seafloor area (f_{eux}).

4.5.5 Implications for the causes of the base Stairsian mass extinction event and the other Late Cambrian-Early Ordovician "biomere" events

During the base Stairsian mass extinction event, a range of niches were affected in the Ibex area, from benthic trilobites, sessile brachiopods, to pelagic and nektic conodonts (e.g., Ethington and Clark, 1981; Adrain et al., 2014). Among these species, benthic deposit-feeding trilobites were more severely affected (Edwards et al., 2018). Different mechanisms have been proposed to be associated with this extinction event, such as ecological stress caused by a sea level drop (Westrop and Ludvigsen, 1987; Miller et al., 2003) and environmental stress related to ocean redox conditions (Saltzman et al., 2015; Edwards et al., 2018).

Our study expands on the hypothesis that anoxia caused the BSME (Saltzman et al., 2015; Edwards et al., 2018). Geochemical data ($\delta^{13}C$, $\delta^{34}S$, and $\delta^{238}U$) measured from the distal Shingle Pass and Meiklejohn Peak sections are interpreted to reflect the global seawater isotopic signals. Invariant carbonate $\delta^{238}U$ from these two distal sections suggest limited changes in the extent of global ocean euxinia (Fig. 4.8; Andersen et al., 2017; Cole et al., 2020).

Paired $\delta^{13}C$ and $\delta^{34}S$ excursions at the base Stairsian from the two distal sections could be associated with globally increased organic carbon and pyrite burial, respectively, suggesting an expansion of suboxic to anoxic (low or no O_2 in the water column and anoxic porewaters within sediment; e.g., Kump and Arthur, 1999; Saltzman et al., 2015; Edwards et al., 2018). Combined with an invariant stratigraphic $\delta^{238}U$ trend, the possibility that $\delta^{238}U$ data do not respond to this magnitude of expanded suboxic-ferruginous conditions, and similarly small sediment-seawater $\delta^{238}U$ offsets for suboxic and ferruginous settings (e.g., Andersen et al., 2016; Cole et al., 2020), we suggest that expanded suboxic-ferruginous seawaters accompanied the BSME. A relatively small expansion of suboxic-ferruginous seawaters without expansion of euxinia may have caused a smaller biotic crisis compared with the dramatic "Big Five" Phanerozoic mass extinctions that occurred during significant expansion of euxinic seawaters (e.g., Diaz and Rosenberg, 1995; Meyer and Kump, 2008; Brennecka et al., 2011a; Lau et al., 2016; Song et al., 2017; Bartlett et al., 2018; White et al., 2018; Zhang et al., 2018a, 2020b).

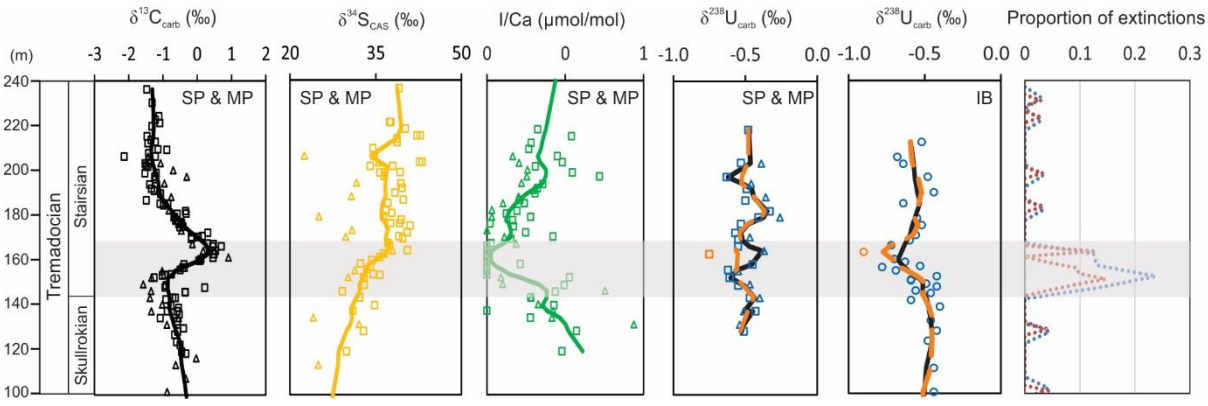

Figure 4.8 Correlations between geochemical data from both Shingle Pass (SP; squares) and Meiklejohn Peak (MP; triangles) sections, Ibex section (IB; circles), and the base Stairsian mass extinctions recorded in the Ibex area using conodont biostratigraphic zonations. Correlation among sections is based on composite meters from Edwards et al. (2018). Lowess curves are shown for each proxy with α = 0.2. The Shingle Pass sample (SP5388, $\delta^{238}U$ = −0.75‰) with a low $\delta^{238}U$ value (−0.75‰) is marked in orange and the $\delta^{238}U$ lowess curves calculated with (dashed orange line) and without this sample (solid black line) are present (see main text for details). The orange dashed $\delta^{238}U$ lowess curve for the Ibex area includes all samples whereas solid black curve does not include one Ibex sample (B-TOP7420, $\delta^{238}U$ = −0.90‰). $\delta^{13}C$, $\delta^{34}S_{CAS}$, and I/Ca ratios are from Edwards et al. (2018). The proportions of extinctions are calculated from Table S4 in Edwards et al. (2018). Blue and red dotted lines are calculated using stratigraphic frequency intervals of 5m and 2.5m, respectively.

Our study further sheds light on the causes of the other Late Cambrian and Early Ordovician "biomere" events (i.e., trilobite extinctions). The base Steptoean "biomere" occurred during the first half of the SPICE (Steptoean Positive Carbon Isotope Excursion), which is characterized by the largest magnitude of positive $\delta^{13}C$ and $\delta^{34}S$ excursions (≥ 4‰ and ≥ 20‰, respectively) during the Late Cambrian (e.g., Gill et al., 2011; Dahl et al., 2014). Carbonate $\delta^{238}U$ data show a small negative excursion (0.18‰) during the first half of the

SPICE, suggesting a causal relationship between expanded ocean euxinia and the base Steptoean trilobite extinction event (Dahl et al., 2014). In this study, the BSME is characterized by smaller positive $\delta^{13}C$ and $\delta^{34}S$ excursions ($\leq$ 2‰ and $\leq$ 7‰, respectively) with the magnitude of $\delta^{13}C$ excursion being the largest following the SPICE event (e.g., Bergström et al., 2009; Edwards and Saltzman, 2014; Saltzman et al., 2015). Invariant carbonate $\delta^{238}U$ from the two distal sections in this study suggest limited changes in global ocean euxinia during the base Stairsian CIE. For the other "biomere" events that are not reported with paired $\delta^{13}C$ and $\delta^{34}S$ excursions (i.e., the base Sunwaptan, the base Skullrockian, and the base Tulean; Adrain et al., 2009) and given the BSME as a case study, we hypothesize that those extinction events were not associated with expanded global ocean euxinia, but rather expanded ocean suboxic and ferruginous conditions to a lesser degree (that might not be detected by $\delta^{13}C$ or $\delta^{34}S$) and/or some other ecological stress (e.g., sea level changes).

4.5.6 Implications for the post-SPICE Cambrian and Early Ordovician global ocean redox conditions

Our current understanding of global ocean redox patterns during the post-SPICE Cambrian and Early Ordovician is mostly inferred from studies utilizing traditional stable isotope systems (e.g., $\delta^{13}C$, $\delta^{18}O$, $\delta^{34}S$; e.g., Buggisch et al., 2003; Bergström et al., 2009; Thompson and Kah, 2012; Edwards and Saltzman, 2014; Saltzman et al., 2015; Kah et al., 2016). The post-SPICE Cambrian and Early Ordovician is thought to have experienced a warmer climate, as inferred from the $\delta^{18}O$ values of bulk carbonates and fossils (Trotter et al., 2008; Bergmann et al., 2018; Albanesi et al., 2020; Goldberg et al., 2021; Edwards et al., 2022). A warm climate was likely not favorable for metazoan diversification because it could lead to sluggish ocean circulation and ventilation (e.g., Goldberg et al., 2021). Smaller seawater $\delta^{13}C$ perturbations (excursions $\leq$ 2‰) are observed at the time, compared with large perturbations (> 2‰) of the Late Cambrian (SPICE; e.g., Saltzman et al., 2000; Gill et al., 2011) and Late Ordovician (Hirnantian CIE; e.g., Bergström et al., 2009). Based on $\delta^{13}C$ and $\delta^{34}S$ trends, the post-SPICE Cambrian and Early Ordovician oceans are generally thought to have been anoxic

and stratified under a greenhouse environment (e.g., Thompson and Kah, 2012; Saltzman et al., 2015).

Only a few studies so far have utilized non-traditional metal isotope systems to investigate the global ocean redox conditions during the post-SPICE Cambrian and Early Ordovician (e.g., δ^{98}Mo, δ^{53}Cr, δ^{238}U; Dahl et al., 2010; Azmy et al., 2015; D'Arcy et al., 2017; Lu et al., 2020; Li et al., 2022) with varying levels of success due to influences from the local depositional environment or limited data. For example, it was suggested that the repeated occurrence of black shale in the carbonate succussions at the Cambrian-Ordovician boundary (Green Point Formation, western Newfoundland, Canada) influenced the carbonate δ^{238}U record (Azmy et al., 2015; Li et al., 2022). A small positive carbonate δ^{53}Cr excursion occurred during the Early Ordovician (La Silla Formation, Cerro La Silla section, Argentina) and was proposed to be influenced by a reducing sink that developed elsewhere in the basin, thus representing a local phenomenon (D'Arcy et al., 2017). Based on the coupled δ^{98}Mo-δ^{238}U data of Lower Ordovician euxinic black shales (Alum Shale Formation, Scania, Sweden), coeval global seawater δ^{98}Mo and δ^{238}U values are estimated to range from 1.37‰ to 2.27‰ and from −0.78‰ to −0.34‰, respectively (Dahl et al., 2010; Lu et al., 2020). However, there are large uncertainties for these estimates due to a small number of samples (n = 4).

Our study provides a high-resolution investigation of global ocean redox conditions during the Early Ordovician using U isotope data from carbonates. Invariant carbonate δ^{238}U values from the two distal sections imply no significant changes of global ocean euxinia during the base Stairsian CIE (Tremadocian). Because the base Stairsian CIE is the largest CIE during the post-SPICE Cambrian and Early Ordovician (Bergström et al., 2009; Edwards and Saltzman, 2014; Saltzman et al., 2015), we propose that the post-SPICE Cambrian and Early Ordovician ocean had only limited changes in global ocean euxinia, with a few episodes of expanded suboxic-ferruginous seawaters during the small carbon isotope perturbations. In addition, small variations in δ^{34}S during the Early Ordovician were not necessarily caused by expansion/contraction of ocean euxinia (Thompson and Kah, 2012), but rather due to different degrees of pyrite burial in response to expansion and contraction of suboxic and ferruginous

water masses where microbial sulfate reduction was restricted to the sediment (Dahl et al., 2014, this study).

4.6 Conclusions

Elemental concentrations and $\delta^{238}U$ values have been measured from three carbonate sections in the Great Basin region to infer the global ocean redox dynamics during the base Stairsian (Tremadocian, Early Ordovician) mass extinction event and enhance our understanding of basin dynamics and previously reported geochemical data. Regarding stratigraphic carbonate $\delta^{238}U$ trends, the proximal Ibex section shows a negative δ238U excursion defined by multiple samples, whereas the distal Shingle Pass section has one sample with unusually low $\delta^{238}U$ and the Meiklejohn Peak section does not have any samples with unusually low $\delta^{238}U$. The lowest $\delta^{238}U$ value from each of the Ibex and Shingle Pass sections are associated with the highest Mn/Sr ratios in those sections, suggesting diagenetic alteration. Invariant carbonate $\delta^{238}U$ data from the two distal sections suggest no significant changes in the extent of global ocean euxinia during the CIE. A three-sink U isotope mass balance model estimated a global euxinic seafloor area of 0.2–15.8% in the Tremadocian ocean. Coupled with the paired $\delta^{13}C$ and $\delta^{34}S$ excursions, an expansion of suboxic-ferruginous seawaters developed during the BSME. In contrast to significant $\delta^{238}U$ excursions that are commonly accompanied by large carbon isotope perturbations and significant biotic turnover (i.e., the "Big Five" Phanerozoic mass extinctions), our study finds no carbonate $\delta^{238}U$ excursion during the small globally correlated base Stairsian CIE (the largest during the post-SPICE Cambrian and Early Ordovician) and a smaller extent of biotic crisis (i.e., the BSME). We propose that there were limited changes in global ocean euxinia during the post-SPICE Cambrian and Early Ordovician and that the "biomere" events within this period were probably related to expanded suboxic-ferruginous oceans and/or other ecological stresses.

Chapter 5 Conclusions

5.1 Summary of the thesis

This thesis has focused on using the U isotope system from sedimentary rocks to provide a better understanding of global ocean redox conditions in the Early Paleozoic, especially the Ordovician. Uranium isotope compositions were measured from different geologic materials, specifically fine-grained siliciclastic sedimentary rocks (i.e., shales, mudstones) deposited under various redox conditions (euxinic [Chapter 2], ferruginous and suboxic [Chapter 3]) and carbonates precipitating beneath an oxygenated water column (Chapter 4). Conclusions from each project are summarized below.

This thesis first presents the coupled use of δ^{98}Mo-δ^{238}U from the same euxinic organic-rich mudrocks to reconstruct coeval ocean redox conditions (Chapter 2; Lu et al., 2020). Coupled δ^{98}Mo-δ^{238}U data from the same euxinic ORM units are compiled from this and previous studies (Dahl et al., 2010; Asael et al., 2013; Kendall et al., 2015, 2020; Lu et al., 2017b; Stockey et al., 2020) and overall do not show any correlations. However, individual euxinic ORM units are found to exhibit different patterns between δ^{98}Mo and δ^{238}U data. A negative correlation between δ^{98}Mo and δ^{238}U from the Upper Devonian Kettle Point Formation (Kendall et al., 2020) is similar to the observations from modern euxinic basins, suggesting a predominant control of local depositional environment and a generally stable global ocean redox condition. A positive δ^{98}Mo-δ^{238}U correlation from the Upper Ordovician Fjäcka Shale (Lu et al., 2017b) is best explained by changes in global ocean redox conditions that shift both isotopic values in the same direction. No correlations between δ^{98}Mo and δ^{238}U could be associated with different mechanisms, such as relatively stable local and global redox conditions (the Lower Silurian Tanezzuft Formation; Stockey et al., 2020), changes in local depositional environment (the middle Paleoproterozoic Zaonega Formation; Aseal et al., 2013), a combination of both local environment and global ocean redox states (Member IV of the upper Ediacaran Doushantuo Formation; Kendall et al., 2015), and a limited set of data. Although using a limited set of data is difficult to precisely reconstruct coeval marine redox conditions, both high δ^{98}Mo and δ^{238}U values from the Upper Devonian Chattanooga Shale

and New Albany Shale (similar to euxinic sediments in modern euxinic basins) are compelling evidence of widespread ocean oxygenation at that time. This study provides a general framework of using coupled δ^{98}Mo-δ^{238}U data from the same euxinic ORM unit to disentangle local depositional factors and global marine redox conditions.

The local depositional environment and global ocean redox states during the Katian Collingwood Member and Rouge River Member deposition (Late Ordovician) in southern Ontario (Canada) are evaluated by elemental data and uranium isotope compositions, respectively (Chapter 3). Paleosalinity proxies suggest brackish-marine conditions for both ORS units, suggesting some water exchange between the basin and open ocean during deposition. Spatiotemporal variations in local bottom water redox conditions are revealed for both units across southern Ontario. For the Collingwood Member, local bottom water redox conditions are generally more reducing (ferruginous at maximum) in the deeper waters of the Michigan and Appalachian basins and mostly oxic/suboxic near the Algonquin Arch. The Rouge River Member was predominantly deposited under oxic/suboxic conditions with sporadic bottom water anoxia. Considering the local depositional environment, lower estimated coeval seawater δ^{238}U values during Collingwood Member deposition suggest an expansion of global ocean euxinia, whereas higher estimated seawater δ^{238}U values during Rouge River deposition suggest a contraction of global ocean euxinia. Combined with previous studies (Zhou et al., 2012, 2015; Lu et al., 2017b; Dahl et al., 2021; Liu et al., 2022), dynamic global ocean redox conditions are revealed during the Katian. Episodic expansion of ocean euxinia occurred prior to the Late Ordovician mass extinction event but do not coincidently have similar level of mass extinctions, suggesting that expanded ocean anoxia is not the only mechanism that result in the second largest Phanerozoic mass extinction event.

Marine redox changes during the base Stairsian mass extinction event (Early Ordovician) are assessed by uranium isotope compositions of carbonates from three sections (from proximal to distal section: Ibex area, Shingle Pass, and Meiklejohn Peak) in the Great Basin (western USA) (Chapter 4). The proximal Ibex section shows a negative δ^{238}U excursion during the CIE, whereas the distal Shingle Pass section has only one sample with unusually

low $\delta^{238}U$ during the CIE and the Meiklejohn Peak section does not has any samples with unusually low $\delta^{238}U$. The lowest $\delta^{238}U$ from each of the Ibex and Shingle Pass sections are associated with the highest Mn/Sr ratios in those sections, suggesting diagenetic alteration. Invariant carbonate $\delta^{238}U$ data from the distal Shingle Pass and Meiklejohn Peak sections better reflect open ocean signals and suggest no significant changes in the extent of global ocean euxinia during the BSME. Although there is no expansion of euxinia, there is evidence of expanded ocean suboxia-anoxia based on the concurrent positive carbon and sulfur isotope excursions. Limited changes in global ocean euxinia are further proposed during the post-SPICE Cambrian and Early Ordovician because other carbon isotope perturbations during this time are smaller than that associated with the BSME. The "biomere" events within this period (including the BSME) were probably associated with an expansion of ocean suboxia-anoxia and/or some ecological stresses.

5.2 Early Paleozoic ocean redox dynamics inferred by U isotopes from sedimentary rocks

A growing number of studies suggest transient oxygenation events occurred during the Ediacaran and Cambrian and the near-modern level of widespread ocean oxygenation is not reached until the Devonian based on different geochemical proxies (e.g., Ce anomaly, $\delta^{98}Mo$; e.g., Dahl et al., 2010; Chen et al., 2015; Kendall et al., 2015; Sperling et al., 2015; Wallace et al., 2017; Qin et al., 2022; Reinhard and Planavsky, 2022). Uranium isotopes from sedimentary rocks have also provided important insights on the evolution of marine redox conditions during the Early Paleozoic (Cambrian, Ordovician, Silurian; Dahl et al., 2014, 2017, 2019; Azmy et al., 2015; Lu et al., 2017b; Bartlett et al., 2018; G. Wei et al., 2018, 2020; Zhang et al., 2018b; Cheng et al., 2020; del Rey et al., 2020; Stockey et al., 2020). Therefore, Early Paleozoic ocean redox conditions inferred from sedimentary $\delta^{238}U$ records are summarized below (Fig. 5.1).

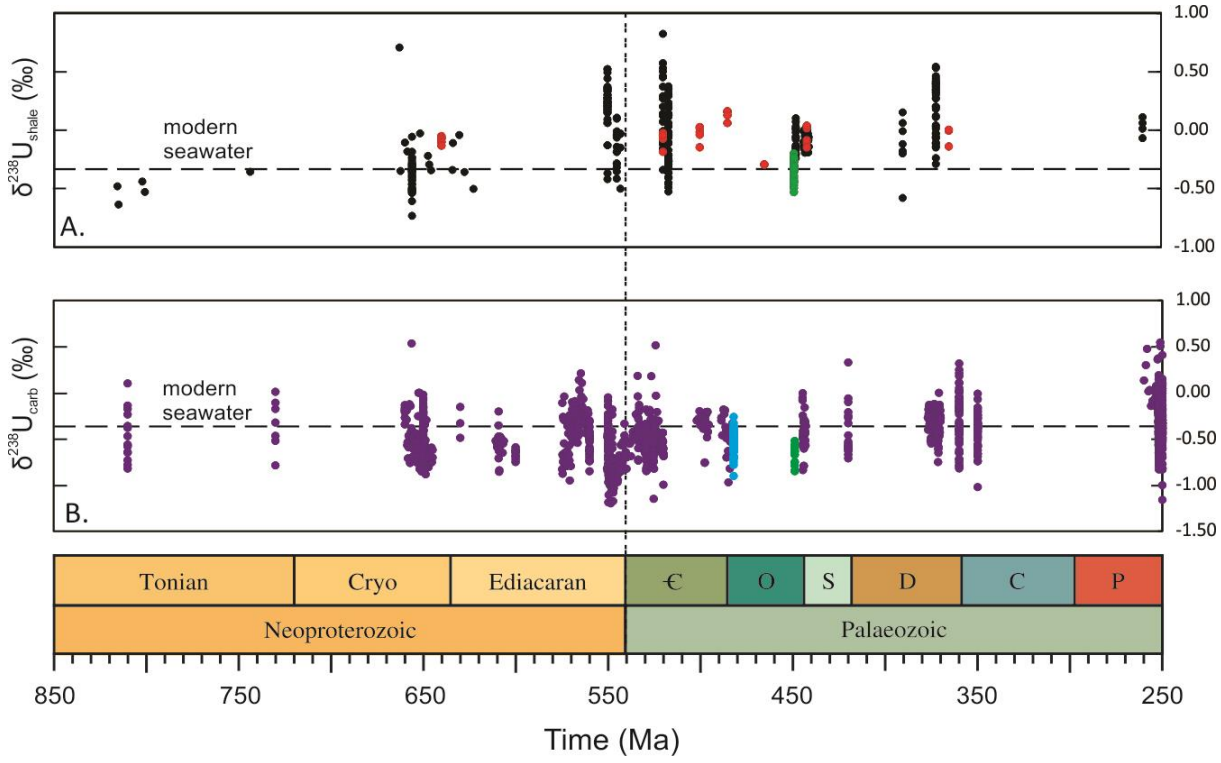

Figure 5.1 Compilations of $\delta^{238}U$ data from shales (A; Dang et al., 2018 and references therein) and carbonates (B; Liu et al., 2022; X. Chen et al., 2021 and references therein). $\delta^{238}U$ data from Chapter 2 (red), 3 (green), and 4 (blue) are included in this compilation.

Among the three geologic periods of the Early Paleozoic, the Cambrian has been intensively studied with a high resolution of sedimentary $\delta^{238}U$ records (particularly from carbonates for the Early Cambrian), which suggest highly dynamic ocean redox conditions (see a review by Wei et al., 2021; Dahl et al., 2014, 2017, 2018; Azmy et al., 2015; G. Wei et al., 2018, 2020; Zhang et al., 2018b; Cheng et al., 2020). Estimated seawater $\delta^{238}U$ values during the Early Cambrian (ca. 541–510 Ma) mostly vary between −0.60‰ and −0.40‰ (Dahl et al., 2017, 2019; G. Wei et al., 2018, 2020), approaching that of modern seawater (~−0.39‰; e.g., Weyer et al., 2008; Tissot and Dauphas, 2015). Two ocean anoxic events (OAE) have been identified with negative $\delta^{238}U$ excursions (seawater $\delta^{238}U$ values likely down to

~−0.90‰) from both carbonates and shales during the late Fortunian (ca. 529 Ma) and middle Stage 2 (ca. 526 Ma) (G. Wei et al., 2018, 2020; Dahl et al., 2019). An episode of widespread ocean oxygenation occurred at the Stage 2–Stage 3 boundary (ca. 521 Ma; Dahl et al., 2017; G. Wei et al., 2018, 2020; Cheng et al., 2020). However, an extensive ocean anoxia followed afterwards (ca. 517 Ma) with the estimated seawater value as low as ~−1.20‰ (Wei et al., 2020), which is similar to that of the terminal Ediacaran (Zhang et al., 2018b; Tostevin et al., 2019). Available $\delta^{238}U$ data are rather sparse for the Late Cambrian (ca. 510–485 Ma). Two negative $\delta^{238}U$ isotope excursions are observed during the Steptoean CIE (ca. 500–496 Ma), suggesting two episodes of expanded ocean anoxia (Dahl et al., 2014). Widespread ocean anoxia generally remained during the latest Cambrian, with an estimated seawater $\delta^{238}U$ value of −0.54 ± 0.14‰ (assuming a carbonate $\delta^{238}U$ offset of −0.27 ± 0.14‰; Azmy et al., 2015).

Sedimentary $\delta^{238}U$ data are only available for the Early and Late Ordovician and there is a large knowledge gap in between (Azmy et al., 2015; Lu et al., 2017b; Bartlett et al., 2018; Liu et al., 2022; this dissertation). The earliest Ordovician seawater is characterized by widespread ocean anoxia, with a low estimated seawater $\delta^{238}U$ value of ~−0.85‰ (Azmy et al., 2015; Li et al., 2022). However, large variations are found in carbonate $\delta^{238}U$ data (between −0.97‰ and −0.33‰), which could be influenced by repeated occurrence of black shales within carbonates (Azmy et al., 2015; Li et al., 2022). Chapter 4 of this dissertation presents a high-resolution investigation of $\delta^{238}U$ record in carbonates during the base Stairsian mass extinction event (ca. 482 Ma) and suggests an expansion of suboxic to ferruginous seawater during the base Stairsian CIE with an estimated seawater $\delta^{238}U$ value of −0.75‰ to −0.48‰. With respect to the Late Ordovician, fluctuating ocean redox conditions are revealed during the Katian (Ka2, ca. 449 Ma, Chapter 3 of this dissertation; and Ka3, ca. 448 Ma, Lu et al., 2017b, Chapter 2 of this dissertation). During the Ka2, lower estimated seawater $\delta^{238}U$ values (−0.87‰ to −0.64‰) during the deposition of Collingwood Member suggest an expansion of ocean euxinia. In comparison, relatively higher estimated seawater $\delta^{238}U$ values (−0.62‰ to −0.42‰) during the deposition of overlying Rouge River Member represents a contraction of global ocean euxinia. During the Fjäcka Shale deposition (Ka3), the deduced seawater $\delta^{238}U$

changed from ~−0.80/−0.54‰, to ~−0.69/−0.34‰, and back to ~−0.80/−0.54‰ (Chapter 2). Widespread ocean anoxia is inferred during the latest Katian (Ka4) and earliest Hirnantian based on carbonate $\delta^{238}U$, with an estimated seawater $\delta^{238}U$ value of ~−0.77‰ (Liu et al., 2022). A potentially transient ocean oxygenation event could have been occurred between the LOME1 and LOME2 based on a positive carbonate $\delta^{238}U$ excursion (with estimated seawater $\delta^{238}U$ of ~−0.40‰ to ~−0.30‰; Liu et al., 2022). An abrupt negative shift in carbonate $\delta^{238}U$ values (~0.3‰) during the LOME2 of the Hirnantian coincided with the LOME2, with an estimated seawater $\delta^{238}U$ of ~−0.72‰ (Bartlett et al., 2018; Liu et al., 2022).

Silurian ocean redox conditions are not well understood by $\delta^{238}U$ as only a few studies available (Bartlett et al., 2018; del Rey et al., 2020; Stockey et al., 2020). The early Silurian (Rhuddanian; ca. 444–441 Ma) is characterized by widespread ocean anoxia (following the Hirnantian OAE) based on both carbonate and shale $\delta^{238}U$ records, with an estimated seawater $\delta^{238}U$ value of ~−0.72‰ (Bartlett et al., 2018; Stockey et al., 2020; Liu et al., 2022). The global ocean redox conditions remained anoxic during the Lau CIE (ca. 424 Ma) based on $\delta^{238}U$ from brachiopod calcite, with an estimated seawater $\delta^{238}U$ value of ~−0.58‰ (del Rey et al., 2020).

5.3 The role of marine redox conditions on the metazoan evolutions

Marine oxygenation (and deoxygenation) events have been long associated with the flourishing (and demise) of metazoans (e.g., Nursall, 1959; see opposite views in Butterfield, 2009 and Mills and Canfield, 2014). With the application of new geochemical redox proxies (e.g., $\delta^{98}Mo$, $\delta^{238}U$, I/Ca ratios), environmental changes in the deep time are better understood, providing new insights on the evolution of metazoans (e.g., Dahl et al., 2010; Kendall et al., 2015; Lu et al., 2018; Wood and Ervin, 2018; Dahl et al., 2019; Wei et al., 2021).

Earth' surface oxygenations are traditionally hypothesized to be linked with metazoan diversifications (e.g., Nursall, 1959). Low oxygen content could suppress the proportions of carnivorous taxa and lead to severe ecological constraints (e.g., Sperling et al., 2013; Planavsky et al., 2014). On the other hand, more oxygenated environments could provide sufficient energy to support higher respiratory oxygen demand of carnivores and promote ecological

"arm races" among animals, thus stimulate the metazoan diversifications (e.g., Catling et al., 2005; Sperling et al., 2013). Episodically more oxygenated conditions in some geologic periods as revealed by various geochemical redox proxies (e.g., δ^{98}Mo, Ce anomaly) have been correlated with the concurrent metazoan diversifications, for instance, the notable "Cambrian Explosion" during the Early Cambrian (e.g., Chen et al., 2015; Wen et al., 2015; Wallace et al., 2017; He et al., 2019; Cheng et al., 2020; Qin et al., 2022) and the radiation of large predatory fish during the Devonian (e.g., Dahl et al., 2010; Wallace et al., 2017).

An alternative hypothesis is that dynamic ocean redox conditions could promote, rather than hinder, metazoan evolutions (e.g., Boyle and Lenton, 2006; Reinhard et al., 2016; Wood and Erwin, 2018). Fluctuating redox conditions are proposed to cause ecological restructuring and stimulate evolutionary novelties, thus promoting metazoan diversifications (Boyle and Lenton, 2006; Reinhard et al., 2016; Wood and Erwin, 2018). This hypothesis is favored by some recent studies to explain the "Cambrian Explosion" (Wood et al., 2019), especially δ^{238}U studies that suggest highly dynamic ocean redox conditions at the time (e.g., G. Wei et al., 2018, 2020). Nevertheless, more studies are needed to better constrain the co-evolutionary relationship between marine redox conditions and metazoan evolutions.

5.4 Future work

With the development and application of δ^{238}U on sedimentary rocks, marine redox conditions during the Early Paleozoic are better reconstructed and provide new insights on the evolution of metazoans. However, there are still many unknowns of ocean redox conditions during the Early Paleozoic, particularly the Early-Middle Ordovician (during the GOBE) and Silurian. To portray a detailed redox landscape during the Early Paleozoic, future investigations are needed and two general aspects are proposed.

First, to better use δ^{238}U as a redox proxy, uranium isotope system in ferruginous environment and carbonates should be better studied and understood. Current understanding of δ^{238}U offsets in ferruginous settings is only based on Cole et al. (2020) that studied two modern ferruginous lakes. With respect to δ^{238}U in carbonates, current studies are solely based

on sediments from the Bahamas bank (Romaniello et al., 2013; Chen et al., 2018b; Tissot et al., 2018). Studies on carbonate sediments from other depositional settings with different diagenetic history could improve the understanding of diagenetic alterations on $\delta^{238}U$ and the use of $\delta^{238}U$ from carbonates to reconstruct marine redox conditions.

Second, combined use of different non-traditional isotope systems could help to depict a more complete redox landscape of the Early Paleozoic (and also other geologic time; e.g. Kendall, 2021). As introduced earlier, both $\delta^{98}Mo$ and $\delta^{238}U$ systems are sensitive to the extent of global ocean euxinia (e.g., Andersen et al., 2017; Kendall et al., 2017). Thallium isotope system has been an emerging proxy to track ocean oxygenation, providing another perspective of ocean redox conditions from the extent of Mn oxides burial (e.g., Owens et al., 2017). Further, though under development, V and Re isotope systems are potential novel proxies to fingerprint the extent of ocean anoxia and suboxia-anoxia, respectively, because V and Re could be effectively removed to sediments under anoxic and suboxic-anoxic conditions, respectively (e.g., Morford et al., 2005; Algeo and Liu, 2020). If correct and combined with the use of $\delta^{98}Mo$ and/or $\delta^{238}U$, the extent of suboxic and ferruginous seafloor area would be revealed to improve the understanding of ocean redox evolutions through time. Therefore, collective use of these robust geochemical proxies could portray a more detailed ocean redox landscape (oxygenated vs suboxic vs ferruginous vs euxinic) in the geologic deep time and thus improve the understanding of metazoan evolutions.

References

Abe, M., Suzuki, T., Fujii, Y., Hada, M. and Hirao, K. (2008) An ab initio molecular orbital study of the nuclear volume effects in uranium isotope fractionations. *J. Chem. Phys.* **129,** 164309.

Abshire, M. L., Romaniello, S. J., Kuzminov, A. M., Cofrancesco, J., Severmann, S. and Riedinger, N. (2020) Uranium isotopes as a proxy for primary depositional redox conditions in organic-rich marine systems. *Earth Planet. Sci. Lett.* ***529,*** 115878.

Adrain, J. M., McAdams, N. E. B. and Westrop, S. R. (2009) Trilobite biostratigraphy and revised bases of the Tulean and Blackhillsian Stages of the Ibexian Series, Lower Ordovician, western United States. *Mem. Assoc. Australas. Palaeontol.* **37,** 541–610.

Adrain, J. M., Westrop, S. R., Karim, T. S. and Landing, E. (2014) Trilobite biostratigraphy of the Stairsian Stage (upper Tremadocian) of the Ibexian Series, Lower Ordovician, western United States. *Mem. Assoc. Australas. Palaeontol.* **45,** 167–214.

Ainsaar, L., Kaljo, D., Martma, T., Meidla, T., Männik, P., Nõlvak, J. and Tinn, O. (2010) Middle and Upper Ordovician carbon isotope chemostratigraphy in Baltoscandia: A correlation standard and clues to environmental history. *Palaeogeogr. Palaeoclimatol. Palaeoecol.* **294(3-4),** 189–201.

Albanesi, G. L., Barnes, C. R., Trotter, J. A., Williams, I. S. and Bergström, S. M. (2020) Comparative Lower-Middle Ordovician conodont oxygen isotope palaeothermometry of the Argentine Precordillera and Laurentian margins. *Palaeogeogr. Palaeoclimatol. Palaeoecol.* **549,** 109115.

Algeo, T. J. (2004) Can marine anoxic events draw down the trace element inventory of seawater? *Geology* **32,** 1057–1060.

Algeo, T. J. and Ingall, E. (2007) Sedimentary C_{org}:P ratios, paleocean ventilation, and Phanerozoic atmospheric pO_2. *Palaeogeogr. Palaeoclimatol. Palaeoecol.* **256(3-4),** 130–155.

Algeo, T. J. and Li, C. (2020) Redox classification and calibration of redox thresholds in sedimentary systems. *Geochim. Cosmochim. Acta* **287,** 8–26.

Algeo, T. J. and Liu, J. (2020) A re-assessment of elemental proxies for paleoredox analysis. *Chem. Geol.* **540,** 119549.

Algeo, T. J. and Lyons, T. W. (2006) Mo-total organic carbon covariation in modern anoxic marine environments: Implications for analysis of paleoredox and paleohydrographic conditions. *Paleoceanography* **21,** PA1016.

Algeo, T. J., Marenco, P. J. and Saltzman, M. R. (2016) Co-evolution of oceans, climate, and the biosphere during the 'Ordovician Revolution': A review. *Palaeogeogr. Palaeoclimatol. Palaeoecol.* **458,** 1–11.

Algeo, T. J. and Maynard, J. B. (2004) Trace-element behavior and redox facies in core shales of Upper Pennsylvanian Kansas-type cyclothems. *Chem. Geol.* **206,** 289–318.

Algeo, T. J. and Tribovillard, N. (2009) Environmental analysis of paleoceanographic systems based on molybdenum–uranium covariation. *Chem. Geol.* **268,** 211–225.

An, T. X. (1981) Recent progress in Cambrian and Ordovician conodont biostratigraphy of China. *Geol. Soc. Am. Spec. Pap.* **187,** 209–226.

Anbar, A. D., Knab, K. A. and Barling, J. (2001) Precise determination of mass-dependent variations in the isotopic composition of molybdenum using MC-ICPMS. *Anal. Chem.* **73,** 1425–1431.

Andersen, M. B., Elliott, T., Freymuth, H., Sims, K. W., Niu, Y. and Kelley, K. A. (2015) The terrestrial uranium isotope cycle. *Nature* **517,** 356–359.

Andersen, M. B., Matthews, A., Bar-Matthews, M. and Vance, D. (2020) Rapid onset of ocean anoxia shown by high U and low Mo isotope compositions of sapropel S1. *Geochem. Perspect. Lett.* **15,** 10–14.

Andersen, M. B., Matthews, A., Vance, D., Bar-Matthews, M., Archer, C. and de Souza, G. F. (2018) A 10-fold decline in the deep Eastern Mediterranean thermohaline overturning circulation during the last interglacial period. *Earth Planet. Sci. Lett.* **503,** 58–67.

Andersen, M. B., Romaniello, S., Vance, D., Little, S. H., Herdman, R. and Lyons, T. W. (2014) A modern framework for the interpretation of $^{238}U/^{235}U$ in studies of ancient ocean redox. *Earth Planet. Sci. Lett.* **400,** 184–194.

Andersen, M. B., Stirling, C. H. and Weyer, S. (2017) Uranium Isotope Fractionation. *Rev. Mineral. Geochem.* **82,** 799–850.

Andersen, M. B., Vance, D., Morford, J. L., Bura-Nakić, E., Breitenbach, S. F. M. and Och, L. (2016) Closing in on the marine $^{238}U/^{235}U$ budget. *Chem. Geol.* **420,** 11–22.

Anderson, R. F., Fleisher, M. Q. and Lehuray, A. P. (1989) Concentration, oxidation state, and particulate flux of uranium in the Black Sea. *Geochim. Cosmochim. Acta* **53,** 2215–2224.

Archer, C. and Vance, D. (2008) The isotopic signature of the global riverine molybdenum flux and anoxia in the ancient oceans. *Nat. Geosci.* **1,** 597–600.

Ardakani, O. H., Chappaz, A., Sanei, H. and Mayer, B. (2016) Effect of thermal maturity on remobilization of molybdenum in black shales. *Earth Planet. Sci. Lett.* **449,** 311–320.

Armstrong, D. K. and Carter, T. R. (2010) The subsurface Paleozoic stratigraphy of southern Ontario. *Ont. Geol. Surv.* **7,** 301p.

Arnold, G. L., Anbar, A. D., Barling, J. and Lyons, T. W. (2004) Molybdenum isotope evidence for widespread anoxia in mid-Proterozoic oceans. *Science* **304,** 87–90.

Arnold, G. L., Lyons, T. W., Gordon, G. W. and Anbar, A. D. (2012) Extreme change in sulfide concentrations in the Black Sea during the Little Ice Age reconstructed using molybdenum isotopes. *Geology* **40,** 595–598.

Asael, D., Rouxel, O., Poulton, S. W., Lyons, T. W. and Bekker, A. (2018) Molybdenum record from black shales indicates oscillating atmospheric oxygen levels in the early Paleoproterozoic. *Am. J. Sci.* **318,** 275–299.

Asael, D., Tissot, F. L. H., Reinhard, C. T., Rouxel, O., Dauphas, N., Lyons, T. W., Ponzevera, E., Liorzou, C. and Chéron, S. (2013) Coupled molybdenum, iron and uranium stable isotopes as oceanic paleoredox proxies during the Paleoproterozoic Shunga Event. *Chem. Geol.* **362,** 193–210.

Azmy, K., Kendall, B., Brand, U., Stouge, S. and Gordon, G. W. (2015) Redox conditions across the Cambrian–Ordovician boundary: Elemental and isotopic signatures retained in the GSSP carbonates. *Palaeogeogr. Palaeoclimatol. Palaeoecol.* **440,** 440–454.

Bambach, R. K., Knoll, A. H. and Wang, S. C. (2004) Origination, extinction, and mass depletions of marine diversity. *Paleobiology* **30,** 522–542.

Banner, J. L. and Hanson, G. N. (1990) Calculation of simultaneous isotopic and trace element variations during water-rock interaction with applications to carbonate diagenesis. *Geochim. Cosmochim. Acta* **54,** 3123–3137.

Barling, J. and Anbar, A. D. (2004) Molybdenum isotope fractionation during adsorption by manganese oxides. *Earth Planet. Sci. Lett.* **217,** 315–329.

Barling, J., Arnold, G. L. and Anbar, A. D. (2001) Natural mass-dependent variations in the isotopic composition of molybdenum. *Earth Planet. Sci. Lett.* **193,** 447–457.

Barnes, C. E. and Cochran, J. K. (1990) Uranium removal in oceanic sediments and the oceanic U balance. *Earth Planet. Sci. Lett.* **97,** 94–101.

Barnes, C. E. and Cochran, J. K. (1993) Uranium geochemistry in estuarine sediments: Controls on removal and release processes. *Geochim. Cosmochim. Acta* **57,** 555–569.

Barnes, C., Hallam, A., Kaljo, D., Kauffman, E. G. and Walliser, O.H. (1996) Global event stratigraphy. In O. H. Walliser, (ed.), Global Events and Event Stratigraphy in the Phanerozoic. Springer, Berlin, pp. 321–333.

Bartlett, R., Elrick, M., Wheeley, J. R., Polyak, V., Desrochers, A. and Asmerom, Y. (2018) Abrupt global-ocean anoxia during the Late Ordovician-early Silurian detected using uranium isotopes of marine carbonates. *Proc. Natl. Acad. Sci. U.S.A.* **115,** 5896–5901.

Basu, A., Sanford, R. A., Johnson, T. M., Lundstrom, C. C. and Löffler, F. E. (2014) Uranium isotopic fractionation factors during U(VI) reduction by bacterial isolates. *Geochim. Cosmochim. Acta* **136,** 100–113.

Bau, M. and Koschinsky, A. (2009) Oxidative scavenging of cerium on hydrous Fe oxide: evidence from the distribution of rare earth elements and yttrium between Fe oxides and Mn oxides in hydrogenetic ferromanganese crusts. *Geochem. J.* **43,** 37–47

Béland-Otis, C. (2015) Upper Ordovician organic-rich mudstones of southern Ontario: Drilling project results. *Ont. Geol. Surv.* Open File Report 6312, 59p.

Bekker, A. and Holland, H. D. (2012) Oxygen overshoot and recovery during the early Paleoproterozoic. *Earth Planet. Sci. Lett.* **317-318,** 295–304.

Bennett, W. W. and Canfield, D. E. (2020) Redox-sensitive trace metals as paleoredox proxies: A review and analysis of data from modern sediments. *Earth Sci. Rev.* **204,** 103175.

Bergmann, K. D., Finnegan, S., Creel, R., Eiler, J. M., Hughes, N. C., Popov, L. E. and Fischer, W. W. (2018) A paired apatite and calcite clumped isotope thermometry approach to estimating Cambro-Ordovician seawater temperatures and isotopic composition. *Geochim. Cosmochim. Acta* **224,** 18–41.

Bergström, S. M., Chen, X., Gutiérrez-Marco, J. C. and Dronov, A. (2009) The new chronostratigraphic classification of the Ordovician System and its relations to major regional series and stages and to $\delta^{13}C$ chemostratigraphy. *Lethaia* **42(1),** 97–107.

Bergström, S. M., Eriksson, M. N. E. and Ahlberg, P. (2020a) Ordovician $\delta^{13}C$ chemostratigraphy: a global review of major excursions and their ties to graptolite and conodont biostratigraphy. *Stratigraphy & Timescales* **5,** 319–351.

Bergström, S. M., Kleffner, M. and Eriksson, M. E. (2020b) Upper Katian (Upper Ordovician) trans-Atlantic $\delta^{13}C$ chemostratigraphy: the geochronological equivalence of the ELKHORN and PAROVEJA excursions and its implications. *Lethaia* **53(2),** 199–216.

Bergström, S. M., Saltzman, M. R., Leslie, S. A., Ferretti, A. and Young, S. A. (2015) Trans-Atlantic application of the Baltic Middle and Upper Ordovician carbon isotope zonation. *Est. J. Earth Sci.* **64(1),** 8–12.

Bergström, S. M., Young, S. and Schmitz, B. (2010) Katian (Upper Ordovician) $\delta^{13}C$ chemostratigraphy and sequence stratigraphy in the United States and Baltoscandia: A regional comparison. *Palaeogeogr. Palaeoclimatol. Palaeoecol.* **296(3-4),** 217–234.

Berner, R. A. (1984) Sedimentary pyrite formation: An update*. *Geochim. Cosmochim. Acta* **48,** 605–615.

Berner, R. A. and Raiswell, R. (1984) C/S method for distinguishing freshwater from marine sedimentary rocks. *Geology* **12(6),** 365–368.

Bertine, K. K. and Turekian, K. K. (1973) MoIybdenum in marine deposits. *Geochim. Cosmochim. Acta* **37,** 1415–1434.

Bigeleisen, J. (1996) Nuclear Size and Shape Effects in Chemical Reactions. Isotope Chemistry of the Heavy Elements. *J. Am. Chem. Soc.* **118,** 3676–3680.

Bingham-Koslowski, N., Tsujita, C., Jin, J., Azmy, K. and Melchin, M. (2016) Widespread Late Devonian marine anoxia in eastern North America: a case study of the Kettle Point Formation black shale, southwestern Ontario. *Can. J. Earth Sci.* **53,** 837–855.

Blakey, R. C. and Ranney, W. D. (2018) Ancient Landscapes of Western North America: A Geologic History with Paleogeographic Maps: Springer.

Bond, D. P. G. and Grasby, S. E. (2020) Late Ordovician mass extinction caused by volcanism, warming, and anoxia, not cooling and glaciation. *Geology* **48(8),** 777–781.

Boyle, R. A. and Lenton, T. M. (2006) Fluctuation in the physical environment as a mechanism for reinforcing evolutionary transitions. *J. Theor. Biol.* **242(4),** 832–843.

Bradley, D. C. and Kidd, W. S. F. (1991) Flexural extension of the upper continental crust in collisional foredeeps. *Geol. Soc. Am. Bull.* **103,** 1416–1438.

Brennecka, G. A., Herrmann, A. D., Algeo, T. J. and Anbar, A. D. (2011a) Rapid expansion of oceanic anoxia immediately before the end-Permian mass extinction. *Proc. Natl. Acad. Sci. U.S.A* **108,** 17631–17634.

Brennecka, G. A., Wasylenki, L. E., Bargar, J. R., Weyer, S. and Anbar, A. D. (2011b) Uranium isotope fractionation during adsorption to Mn-oxyhydroxides. *Environ. Sci. Technol.* **45,** 1370–1375.

Brett, C. E., Allison, P. A., Tsujita, C. J., Soldani, D. and Moffat, H. A. (2006) Sedimentology, taphonomy, and paleoecology of meter-scale cycles from the Upper Ordovician of Ontario. *Palaios* **21,** 530–547.

Brett, C. E., Aucoin, C. D., Dattilo, B. F., Freeman, R. L., Hartshorn, K. R., McLaughlin, P. I. and Schwalbach, C. E. (2020) Revised sequence stratigraphy of the upper Katian Stage (Cincinnatian) strata in the Cincinnati Arch reference area: Geological and paleontological implications. *Palaeogeogr. Palaeoclimatol. Palaeoecol.* **540,** 109483.

Brookfield, M. E. and Hannigan, R. E. (2021) Carbon and oxygen isotope variations in shell beds from the Upper Ordovician (mid-Cincinnatian: Maysvillian to early Richmondian) of Ontario: Evaluation of the Warm Saline Deep Ocean hypothesis, paleoceanographic changes, and Milankovitch orbital cycles in the transition to the Hirnantian glaciation. *Palaeogeogr. Palaeoclimatol. Palaeoecol.* **577,** 110528.

Brown, S. T., Basu, A., Ding, X., Christensen, J. N. and DePaolo, D. J. (2018) Uranium isotope fractionation by abiotic reductive precipitation. *Proc. Natl. Acad. Sci. U.S.A.* **115,** 8688–8693.

Bruggmann, S., Gilleaudeau, G. J., Romaniello, S. J., Severmann, S., Canfield, D. E., Anbar, A. D., Scholz, F. and Frei, R. (2022) Uranium isotope cycling on the highly productive Peruvian margin. *Chem. Geol.* **590,** 120705.

Brüske, A., Weyer, S., Zhao, M.-Y., Planavsky, N. J., Wegwerth, A., Neubert, N., Dellwig, O., Lau, K. V. and Lyons, T. W. (2020) Correlated molybdenum and uranium isotope signatures in modern anoxic sediments: implications for their use as paleo-redox proxy. *Geochim. Cosmochim. Acta* **270,** 449–474.

Buggisch, W., Keller, M. and Lehnert, O. (2003) Carbon isotope record of Late Cambrian to Early Ordovician carbonates of the Argentine Precordillera. *Palaeogeogr. Palaeoclimatol. Palaeoecol.* **195,** 357–373.

Bura-Nakić, E., Andersen, M. B., Archer, C., de Souza, G. F., Marguš, M. and Vance, D. (2018) Coupled Mo-U abundances and isotopes in a small marine euxinic basin: Constraints on processes in euxinic basins. *Geochim. Cosmochim. Acta* **222,** 212–229.

Butterfield, N. J. (2009) Oxygen, animals and oceanic ventilation: an alternative view. *Geobiology*, **7,** 1-7.

Canfield, D. E., Poulton, S. W. and Narbonne, G. M. (2007) Late-Neoproterozoic deep-ocean oxygenation and the rise of animal life. *Science* **315,** 92–95.

Canfield, D. E., Raiswell, R., Westrich, J. T., Reaves, C. M. and Berner, R. A. (1986) The use of chromium reduction in the analysis of reduced inorganic sulfur in sediments and shales. *Chem. Geol.* **54,** 149–155.

Cao, M., Daines, S. J., Lenton, T. M., Cui, H., Algeo, T. J., Dahl, T. W., Shi, W., Chen, Z. Q., Anbar, A. and Zhou, Y. Q. (2020) Comparison of Ediacaran platform and slope $\delta^{238}U$ records in South China: Implications for global-ocean oxygenation and the origin of the Shuram Excursion. *Geochim. Cosmochim. Acta* **287,** 111–124.

Carrera, M. G. and Rigby, J. K. (1999) Biogeography of Ordovician sponges. *J. Paleontol.* **73,** 26–37.

Catling, D. C., Glein, C. R., Zahnle, K. J. and Mckay, C. P. (2005) Why O_2 Is required by complex life on habitable planets and the concept of planetary "oxygenation time". *Astrobiology* **5,** 415–438.

Chen, X., Ling, H. F., Vance, D., Shields-Zhou, G. A., Zhu, M., Poulton, S. W., Och, L. M., Jiang, S. Y., Li, D., Cremonese, L. and Archer, C. (2015) Rise to modern levels of ocean oxygenation coincided with the Cambrian radiation of animals. *Nat. Commun.* **6,** 7142.

Chen, X., Robinson, S. A., Romaniello, S. J. and Anbar, A. D. (2022) $^{238}U/^{235}U$ in calcite is more susceptible to carbonate diagenesis. *Geochim. Cosmochim. Acta* **326,** 273–287.

Chen, X., Romaniello, S. J. and Anbar, A. D. (2017) Uranium isotope fractionation induced by aqueous speciation: Implications for U isotopes in marine $CaCO_3$ as a paleoredox proxy. *Geochim. Cosmochim. Acta* **215,** 162–172.

Chen, X., Romaniello, S. J., Herrmann, A. D., Hardisty, D., Gill, B. C. and Anbar, A. D. (2018a) Diagenetic effects on uranium isotope fractionation in carbonate sediments from the Bahamas. *Geochim. Cosmochim. Acta* **237,** 294–311.

Chen, X., Romaniello, S. J., Herrmann, A. D., Samankassou, E. and Anbar, A. D. (2018b) Biological effects on uranium isotope fractionation ($^{238}U/^{235}U$) in primary biogenic carbonates. *Geochim. Cosmochim. Acta* **240,** 1–10.

Chen, X., Romaniello, S. J., Herrmann, A. D., Wasylenki, L. E. and Anbar, A. D. (2016) Uranium isotope fractionation during coprecipitation with aragonite and calcite. *Geochim. Cosmochim. Acta* **188,** 189–207.

Chen, X., Tissot, F. L. H., Jansen, M. F., Bekker, A., Liu, C. X., Nie, N. X., Halverson, G. P., Veizer, J. and Dauphas, N. (2021) The uranium isotopic record of shales and carbonates through geologic time. *Geochim. Cosmochim. Acta* **300,** 164–191.

Chen, Z., Hannigan, P., Carter, T., Liu, X., Crowe, R. and Obermajer, M. (2021) A petroleum Resource Assessment of the Huron domain area, southern Ontario. *Geol. Surv. Can.* Open File 8784, 59p.

Chen, X., Zheng, W. and Anbar, A. D. (2020) Uranium Isotope Fractionation ($^{238}U/^{235}U$) during U(VI) Uptake by Freshwater Plankton. *Environ. Sci. Technol.* **54,** 2744–2752.

Cheng, M., Li, C., Jin, C., Wang, H., Algeo, T. J., Lyons, T. W., Zhang, F. and Anbar, A. (2020) Evidence for high organic carbon export to the early Cambrian seafloor. *Geochim. Cosmochim. Acta* **287,** 125–140.

Churcher, P. L., Johnson, M. D., Telford, R. G. and Barker, J. F. (1991) Stratigraphy and Oil Shale Resource Potential of the Upper Ordovician Collingwood Member, Lindsay Formation, Southwestern Ontario. *Ont. Geol. Surv.* Open File Report 5817, 98p.

Cisne, J. L., Karig, D. E., Rabe, B. D. and Hay, B. J. (1982) Topography and tectonics of the Taconic outer trench slope as revealed through gradient analysis of fossil assemblages. *Lethaia* **15,** 229–246.

Clark, S. K. and Johnson, T. M. (2008) Effective isotopic fractionation factors for solute removal by reactive sediments: A laboratory microcosm and slurry study. *Environ. Sci. Technol.* **42,** 7850–7855.

Clarkson, M. O., Hennekam, R., Sweere, T. C., Andersen, M. B., Reichart, G.-J. and Vance, D. (2021) Carbonate associated uranium isotopes as a novel local redox indicator in oxidatively disturbed reducing sediments. *Geochim. Cosmochim. Acta* **311,** 12–28.

Clarkson, M. O., Müsing, K., Andersen, M. B. and Vance, D. (2020) Examining pelagic carbonate-rich sediments as an archive for authigenic uranium and molybdenum isotopes using reductive cleaning and leaching experiments. *Chem. Geol.* **539,** 119412.

Clarkson, M. O., Poulton, S. W., Guilbaud, R. and Wood, R. A. (2014) Assessing the utility of Fe/Al and Fe-speciation to record water column redox conditions in carbonate-rich sediments. *Chem. Geol.* **382,** 111–122.

Clarkson, M. O., Stirling, C. H., Jenkyns, H. C., Dickson, A. J., Porcelli, D., Moy, C. M., Pogge von Strandmann, P. A., Cooke, I. R. and Lenton, T. M. (2018) Uranium isotope evidence for two episodes of deoxygenation during Oceanic Anoxic Event 2. *Proc. Natl. Acad. Sci. U.S.A* **115,** 2918–2923.

Cocks, L. R. M. and Torsvik, T. H. (2005) Baltica from the late Precambrian to mid-Palaeozoic times: The gain and loss of a terrane's identity. *Earth-Sci. Rev.* **72,** 39–66.

Cocks, L. R. M. and Torsvik, T. H. (2021) Ordovician palaeogeography and climate change. *Gondwana Res.* **100,** 53–72.

Cole, D. B., Planavsky, N. J., Longley, M., Böning, P., Wilkes, D., Wang, X., Swanner, E. D., Wittkop, C., Loydell, D., Busigny, V., Knudsen, A., and Sperling, E. A. (2020) Uranium isotope fractionation in non-sulfidic anoxic settings and the global uranium isotope mass balance. *Global Biogeochem. Cycles* **34,** e2020GB006649.

Cole, D. B., Zhang, S. and Planavsky, N. J. (2017) A new estimate of detrital redox-sensitive metal concentrations and variability in fluxes to marine sediments. *Geochim. Cosmochim. Acta* **215,** 337–353.

Conwell, C. T., Saltzman, M. R., Edwards, C. T., Griffith, E. M. and Adiatma, Y. D. (2022) Nd isotopic evidence for enhanced mafic weathering leading to Ordovician cooling. *Geology* **50,** 886–890.

Crusius, J., Calvert, S., Pedersen, T. and Sage, D. (1996) Rhenium and molybdenum enrichments in sediments as indicators of oxic, suboxic and sulfidic conditions of deposition. *Earth Planet. Sci. Lett.* **145,** 65–78.

D'Arcy, J., Gilleaudeau, G. J., Peralta, S., Gaucher, C. and Frei, R. (2017) Redox fluctuations in the Early Ordovician oceans: An insight from chromium stable isotopes. *Chem. Geol.* **448,** 1–12.

Dahl, T. W., Boyle, R. A., Canfield, D. E., Connelly, J. N., Gill, B. C., Lenton, T. M. and Bizzarro, M. (2014) Uranium isotopes distinguish two geochemically distinct stages during the later Cambrian SPICE event. *Earth Planet. Sci. Lett.* **401,** 313–326.

Dahl, T. W., Canfield, D. E., Rosing, M. T., Frei, R. E., Gordon, G. W., Knoll, A. H. and Anbar, A. D. (2011) Molybdenum evidence for expansive sulfidic water masses in ~750Ma oceans. *Earth Planet. Sci. Lett.* **311,** 264–274.

Dahl, T. W., Chappaz, A., Fitts, J. P. and Lyons, T. W. (2013) Molybdenum reduction in a sulfidic lake: Evidence from X-ray absorption fine-structure spectroscopy and implications for the Mo paleoproxy. *Geochim. Cosmochim. Acta* **103,** 213–231.

Dahl, T. W., Chappaz, A., Hoek, J., McKenzie, C. J., Svane, S. and Canfield, D. E. (2017a) Evidence of molybdenum association with particulate organic matter under sulfidic conditions. *Geobiology* **15,** 311–323.

Dahl, T. W., Connelly, J. N., Kouchinsky, A., Gill, B. C., Månsson, S. F. and Bizzarro, M. (2017b) Reorganisation of Earth's biogeochemical cycles briefly oxygenated the oceans 520 Myr ago. *Geochem. Perspect. Lett.* **3,** 210–220.

Dahl, T. W., Connelly, J. N., Li, D., Kouchinsky, A., Gill, B. C., Porter, S., Maloof, A. C. and Bizzarro, M. (2019) Atmosphere-ocean oxygen and productivity dynamics during early animal radiations. *Proc. Natl. Acad. Sci. U. S. A.* **116,** 19352–19361.

Dahl, T. W. and Hammarlund, E. U. (2011) "Do large predatory fish track ocean oxygenation?" *Commun. Integr. Biol.* **4,** 92–94.

Dahl, T. W., Hammarlund, E. U., Anbar, A. D., Bond, D. P. G., Gill, B. C., Gordon, G. W., Knoll, A. H., Nielsen, A. T., Schovsbo, N. H. and Canfield, D. E. (2010) Devonian rise in atmospheric oxygen correlated to the radiations of terrestrial plants and large predatory fish. *Proc. Natl. Acad. Sci. U.S.A.* **107,** 17911–17915.

Dahl, T. W., Hammarlund, E. U., Rasmussen, C. M. Ø., Bond, D. P. G. and Canfield, D. E. (2021) Sulfidic anoxia in the oceans during the Late Ordovician mass extinctions – insights from molybdenum and uranium isotopic global redox proxies. *Earth Sci. Rev.* **220,** 103748.

Dattilo, B. F. (1993) The Lower Ordovician Fillmore Formation of western Utah: Storm-dominated sedimentation on a passive margin. *Brigham Young Univ. Geol. Stud.* **39,** 71–100.

Dang, D. H., Novotnik, B., Wang, W., Georg, R. B. and Evans, R. D. (2016) Uranium isotope fractionation during adsorption, (co)precipitation, and biotic reduction. *Environ. Sci. Technol.* **50,** 12695–12704.

Davidson, L., Beswetherick, S., Craig, J., Eales, M., Fisher, A., Himmali, A., Jho, J., Mejrab, B., Smart, J., 2000. The structure, stratigraphy and petroleum geology of the Murzuq Basin, southwest Libya. In M. A. Sola and D. Worsley (Eds.) *Geological Exploration in the Murzuq Basin* (pp. 295–320): Elsevier.

del Rey, Á., Havsteen, J. C., Bizzarro, M. and Dahl, T. W. (2020) Untangling the diagenetic history of uranium isotopes in marine carbonates: A case study tracing the $\delta^{238}U$ composition of late Silurian oceans using calcitic brachiopod shells. *Geochim. Cosmochim. Acta* **287,** 93–110.

Dellwig, O., Leipe, T., März, C., Glockzin, M., Pollehne, F., Schnetger, B., Yakushev, E. V., Böttcher, M. E. and Brumsack, H.-J. (2010) A new particulate Mn–Fe–P-shuttle at the redoxcline of anoxic basins. *Geochim. Cosmochim. Acta* **74,** 7100–7115.

Dellwig, O., Schnetger, B., Brumsack, H.-J., Grossart, H.-P. and Umlauf, L. (2012). Dissolved reactive manganese at pelagic redoxclines (part II): Hydrodynamic conditions for accumulation. *J. Mar. Sys.* **90,** 31–41.

Derby, J. R., Raine, R. J., Runkel, A. C. and Smith, P. M. (2012) Paleogeography of the Great American Carbonate Bank of Laurentia in the Earliest Ordovician (Early Tremadocian): The Stonehenge Transgression. In J. R. Derby, R. D. Fritz, S. A. Longacre, W. A. Morgan, & C. A. Sternbach (Eds.), *The Great American Carbonate Bank: The Geology and Economic Resources of the Cambrian-Ordovician Sauk Megasequence of Laurentia* (Vol. 98, pp. 5–13): Association of American Petroleum Geologists Memoir.

Desio, A. (1936) Riassunto sulla presenza del Silurico fossilifero nel Fezzan. *Bollettino. Soc. Geol. Ital.* **55,** 319–356.

Diamond, C. W., Planavsky, N. J., Wang, C., & Lyons, T. W. (2018). What the ~1.4 Ga Xiamaling Formation can and cannot tell us about the mid-Proterozoic ocean. *Geobiology* **16,** 219–236.

Diaz, R. and Rosenberg, R. (1995) Marine benthic hypoxia: A review of its ecological effects and the behavioural response of benthic macrofauna. *Oceanogr. Mar. Biol. Ann. Rev.* **33,** 245–303.

Dickson, A. J., Idiz, E., Porcelli, D. and van den Boorn, S. H. J. M. (2020). The influence of thermal maturity on the stable isotope compositions and concentrations of molybdenum, zinc and cadmium in organic-rich marine mudrocks. *Geochim. Cosmochim. Acta* **287,** 205–220.

Du, X., Jia, J., Zhao, K., Shi, J., Shu, Y., Liu, Z. and Duan, D. (2021) Was the volcanism during the Ordovician-Silurian transition in South China actually global in extent? Evidence from the distribution of volcanic ash beds in black shales. *Mar. Petrol. Geol.* **123,** 104721.

Dunk, R. M., Mills, R. A. and Jenkins, W. J. (2002) A reevaluation of the oceanic uranium budget for the Holocene. *Chem. Geol.* **190,** 45–67.

Ebbestad, J. O. R., Högström, A. E. S., Frisk, Å. M., Martma, T., Kaljo, D., Kröger, B. and Pärnaste, H. (2014) Terminal Ordovician stratigraphy of the Siljan district, Sweden. *Gff* **137,** 36–56.

Edwards, C. T. (2019) Links between early Paleozoic oxygenation and the Great Ordovician Biodiversification Event (GOBE): A review. *Palaeoworld* **28(1-2),** 37–50.

Edwards, C. T., Fike, D. A., Saltzman, M. R., Lu, W. and Lu, Z. (2018) Evidence for local and global redox conditions at an Early Ordovician (Tremadocian) mass extinction. *Earth Planet. Sci. Lett.* **481,** 125–135.

Edwards, C. T., Jones, C. M., Quinton, P. C. and Fike, D. A. (2022) Oxygen isotope ($\delta^{18}O$) trends measured from Ordovician conodont apatite using secondary ion mass

spectrometry (SIMS): Implications for paleo-thermometry studies. *Geol. Soc. Am. Bull.* **134,** 261–274.

Edwards, C.T. and Saltzman, M. R. (2014) Carbon isotope ($\delta^{13}C_{carb}$) stratigraphy of the Lower–Middle Ordovician (Tremadocian–Darriwilian) in the Great Basin, western United States: Implications for global correlation. *Palaeogeogr. Palaeoclimatol. Palaeoecol.* **399,** 1–20.

Edwards, C. T. and Saltzman, M. R. (2016) Paired carbon isotopic analysis of Ordovician bulk carbonate ($\delta^{13}C_{carb}$) and organic matter ($\delta^{13}C_{org}$) spanning the Great Ordovician Biodiversification Event. *Palaeogeogr. Palaeoclimatol. Palaeoecol.* **458,** 102–117.

Edwards, C. T., Saltzman, M. R., Leslie, S. A., Bergström, S. M., Sedlacek, A. R. C., Howard, A., Bauer, J. A., Sweet, W. C. and Young, S. A. (2015) Strontium isotope ($^{87}Sr/^{86}Sr$) stratigraphy of Ordovician bulk carbonate: Implications for preservation of primary seawater values. *Geol. Soc. Am. Bull.* **127(9-10),** 1275–1289.

Edwards, C. T., Saltzman, M. R., Royer, D. L. and Fike, D. A. (2017) Oxygenation as a driver of the Great Ordovician Biodiversification Event. *Nat. Geosci.* **10(12),** 925–929.

Elrick, M., Gilleaudeau, G. J., Romaniello, S. J., Algeo, T. J., Morford, J. L., Sabbatino, M., Goepfert, T. J., Cleal, C., Cascales-Miñana, B. and Chernyavskiy, P. (2022) Major Early-Middle Devonian oceanic oxygenation linked to early land plant evolution detected using high-resolution U isotopes of marine limestones. *Earth Planet. Sci. Lett.* **581,** 117410.

Elrick, M., Polyak, V., Algeo, T. J., Romaniello, S., Asmerom, Y., Herrmann, A. D., Anbar, A. D., Zhao, L. and Chen, Z. (2017) Global-ocean redox variation during the middle-late Permian through Early Triassic based on uranium isotope and Th/U trends of marine carbonates. *Geology* **45(2),** 163–166.

Emerson, S. R. and Huested, S. S. (1991) Ocean anoxia and the concentrations of molybdenum and vanadium in seawater. *Mar. Chem.* **34,** 177–196.

Endrizzi, F., Leggett, C. J. and Rao, L. (2016) Scientific Basis for Efficient Extraction of Uranium from Seawater. I: Understanding the Chemical Speciation of Uranium under Seawater Conditions. *Ind. Eng. Chem. Res.* **55,** 4249–4256.

Erdtmann, B. D. (1986) Early Ordovician eustatic cycles and their bearing on punctuations in early nematophorid (planktic) graptolite evolution. *Lect. Notes Earth Sci.* **8,** 139–152.

Erickson, B. E. and Helz, G. R. (2000) Molybdenum(VI) speciation in sulfidic waters: Stability and lability of thiomolybdates. *Geochim. Cosmochim. Acta* **64,** 1149–1158.

Eriksson, M. J. and Calner, M. (2008) A sequence stratigraphical model for the Late Ludfordian (Silurian) of Gotland, Sweden: Implications for timing between changes in sea level, palaeoecology, and the global carbon cycle. *Facies* **54,** 253–276.

Eroglu, S., Scholz, F., Frank, M. and Siebert, C. (2020) Influence of particulate versus diffusive molybdenum supply mechanisms on the molybdenum isotope composition of continental margin sediments. *Geochim. Cosmochim. Acta.* **273,** 51–69.

Erwin, D. H., Laflamme, M., Tweedt, S. M., Sperling, E. A., Pisani, D. and Peterson, K. J. (2011) The Cambrian conundrum: early divergence and later ecological success in the early history of animals. *Science* **334(6059),** 1091–1097.

Ethington, R. L. and Clark, D. L. (1981) Lower and Middle Ordovician conodonts from the Ibex area, western Millard County, Utah. *Brigham Young Univ. Geol. Stud.* **28,** 1–155.

Fan, J., Shen, S., Erwin, D. H., Sadler, P. M., MacLeod, N., Cheng, Q., Hou, X., Yang, J., Wang, X., Wang, Y., Zhang, H., Chen, X., Li, G., Zhang, Y., Shi, Y., Yuan, D., Chen, Q., Zhang, L., Li, C. and Zhao, Y. (2020) A high-resolution summary of Cambrian to Early Triassic marine invertebrate biodiversity. *Science* **367,** 272–277.

Farquhar, J., Bao, H. and Thiemens, M. (2000) Atmospheric influence of Earth's earliest sulfur cycle. *Science* **289,** 756–758.

Farrenkopf, A. M. and Luther, G. W. (2002) Iodine chemistry reflects productivity and denitrification in the Arabian Sea: evidence for flux of dissolved species from sediments of western India into the OMZ. *Deep Sea Res. II* **49,** 2303–2318.

Finnegan, S., Bergmann, K., Eiler, J. M., Jones, D. S., Fike, D. A., Eisenman, I., Hughes, N. C., Tripati, A. K. and Fischer, W. W. (2011) The Magnitude and Duration of Late Ordovician - Early Silurian Glaciation. *Science* **331,** 903–906.

Finnegan, S., Heim, N. A., Peters, S. E. and Fischer, W. W. (2012) Climate change and the selective signature of the Late Ordovician mass extinction. *Proc. Natl. Acad. Sci. U.S.A.* **109,** 6829–6834.

Ghienne, J. F., Desrochers, A., Vandenbroucke, T. R., Achab, A., Asselin, E., Dabard, M. P., Farley, C., Loi, A., Paris, F., Wickson, S. and Veizer, J. (2014) A Cenozoic-style scenario for the end-Ordovician glaciation. *Nat. Commun.* **5,** 4485.

Gill, B. C., Lyons, T. W., Young, S. A., Kump, L. R., Knoll, A. H. and Saltzman, M. R. (2011) Geochemical evidence for widespread euxinia in the later Cambrian ocean. *Nature* **469,** 80–83.

Gilleaudeau, G. J., Algeo, T. J., Lyons, T. W., Bates, S. and Anbar, A. D. (2021) Novel watermass reconstruction in the Early Mississippian Appalachian Seaway based on integrated proxy records of redox and salinity. *Earth Planet. Sci. Lett.* **558,** 116746.

Gilleaudeau, G. J., Romaniello, S. J., Luo, G., Kaufman, A. J., Zhang, F., Klaebe, R. M., Kah, L. C., Azmy, K., Bartley, J. K., Zheng, W., Knoll, A. H. and Anbar, A. D. (2019). Uranium isotope evidence for limited euxinia in mid-Proterozoic oceans. *Earth Planet. Sci. Lett.* **521,** 150–157.

Goldberg, S. L., Present, T. M., Finnegan, S. and Bergmann, K. D. (2021) A high-resolution record of early Paleozoic climate. *Proc. Natl. Acad. Sci. U.S.A.* **118(6),** e2013083118.

Goldberg, T., Archer, C., Vance, D. and Poulton, S. W. (2009) Mo isotope fractionation during adsorption to Fe (oxyhydr)oxides. *Geochim. Cosmochim. Acta* **73,** 6502–6516.

Goldberg, T., Archer, C., Vance, D., Thamdrup, B., McAnena, A. and Poulton, S. W. (2012) Controls on Mo isotope fractionations in a Mn-rich anoxic marine sediment, Gullmar Fjord, Sweden. *Chem. Geol.* **296-297,** 73–82.

Goldberg, T., Poulton, S. W., Wagner, T., Kolonic, S. F. and Rehkämper, M. (2016) Molybdenum drawdown during Cretaceous Oceanic Anoxic Event 2. *Earth Planet. Sci. Lett.* **440,** 81–91.

Goldman, D. and Bergström, S. M. (1997) Late Ordovician graptolites from the North American Midcontinent. *Palaeontology* **40,** 965–1010.

Gordon, G. W., Lyons, T. W., Arnold, G. L., Roe, J., Sageman, B. B. and Anbar, A. D. (2009) When do black shales tell molybdenum isotope tales? *Geology* **37,** 535–538.

Goto, K. T., Anbar, A. D., Gordon, G. W., Romaniello, S. J., Shimoda, G., Takaya, Y., Tokumaru, A., Nozaki, T., Suzuki, K., Machida, S., Hanyu, T. and Usui, A. (2014) Uranium isotope systematics of ferromanganese crusts in the Pacific Ocean: Implications for the marine $^{238}U/^{235}U$ isotope system. *Geochim. Cosmochim. Acta* **146,** 43–58.

Gromet, L. P., Dymek, R. F., Haskin, L. A. and Korotev, R. L. (1984) The "North American shale composite": Its compilation, major and trace element characteristics. *Geochim. Cosmochim. Acta* **48,** 2469–2482.

Hamblin, A. P. (2010) Detailed outcrop and core measured sections of the Kettle Point formation, southwestern Ontario, with reference to shale gas potential. *Geological Survey of Canada*, Open File 6579, 26p.

Hamblin, A. P. (2018) Stratigraphic architecture, sedimentology and resource potential of the Upper Ordovician Nottawasaga Group of southwestern Ontario, surface and subsurface: tectonics and sequence stratigraphy in the distal Appalachian Foreland. *Geol. Surv. Can.* Open File 8153, 86p.

Hammarlund, E. U., Dahl, T. W., Harper, D. A. T., Bond, D. P. G., Nielsen, A. T., Bjerrum, C. J., Schovsbo, N. H., Schönlaub, H. P., Zalasiewicz, J. A. and Canfield, D. E. (2012) A sulfidic driver for the end-Ordovician mass extinction. *Earth Planet. Sci. Lett.* **331-332,** 128–139.

Hannah, J. L., Stein, H. J., Zimmerman, A., Yang, G., Melezhik, V. A., Filippov, M. M., Turgeon S. C. and Creaser, R. A. (2008) Re-Os geochronology of shungite: a 2.05 Ga fossil oil field in Karelia. *Geochimica et Cosmochimica Acta* **72,** A351.

Hannigan, R., Brookfield, M. E. and Basu, A. R. (2010) A detailed $^{87}Sr/^{86}Sr$ isotopic curve for the mid-Cincinnatian (Upper Katian–Lower Hirnantian, Upper Ordovician), NE North American Shelf (Ontario, Canada) transition to the Hirnantian glaciation. *Chem. Geol.* **277(3-4),** 336–344.

Haq, B. U. and Schutter, S. R. (2008) A Chronology of Paleozoic Sea-Level Changes. *Science* **322,** 64–68.

Hardisty, D. S., Lu, Z., Bekker, A., Diamond, C. W., Gill, B. C., Jiang, G., Kah, L. C., Knoll, A. H., Loyd, S. J., Osburn, M. R., Planavsky, N. J., Wang, C., Zhou, X. and Lyons, T. W. (2017) Perspectives on Proterozoic surface ocean redox from iodine contents in ancient and recent carbonate. *Earth Planet. Sci. Lett.* **463,** 159–170.

Harper, D. A. T., Hammarlund, E. U. and Rasmussen, C. M. Ø. (2014) End Ordovician extinctions: A coincidence of causes. *Gondwana Res.* **25(4),** 1294–1307.

Harper, D. A. T., Zhan, R. B. and Jin, J. (2015) The Great Ordovician Biodiversification Event: Reviewing two decades of research on diversity's big bang illustrated by mainly brachiopod data. *Palaeoworld* **24(1-2),** 75–85.

He, T., Zhu, M., Mills, B. J. W., Wynn, P. M., Zhuravlev, A. Y., Tostevin, R., Pogge von Strandmann, P. A. E., Yang, A., Poulton, S. W. and Shields, G. A. (2019) Possible links between extreme oxygen perturbations and the Cambrian radiation of animals. *Nat. Geosci.* **12(6),** 468–474.

He, Z., Clarkson, M. O., Andersen, M. B., Archer, C., Sweere, T. C., Kraal, P., Guthauser, A., Huang, F. and Vance, D. (2021) Temporally and spatially dynamic redox conditions on an upwelling margin: The impact on coupled sedimentary Mo and U isotope systematics, and implications for the Mo-U paleoredox proxy. *Geochim. Cosmochim. Acta* **309,** 251–271.

Helz, G. R., Bura-Nakić, E., Mikac, N. and Ciglenečki, I. (2011) New model for molybdenum behavior in euxinic waters. *Chem. Geol.* **284,** 323–332.

Helz, G. R., Miller, C. V., Charnock, J. M., Mosselmans, J. F. W., Pattrick, R. A. D., Garner, C. D. and Vaughan, D. J. (1996) Mechanism of molybdenum removal from the sea and its concentration in black shales: EXAFS evidence. *Geochim. Cosmochim. Acta* **60,** 3631–3642.

Hintze, L. F. (1951) Lower Ordoviclan detalled stratigraphic sections for western Utah. *Bull. Utah Geol. Mineral. Surv.* **39,** 99p.

Hintze, L. F. (1952) Lower Ordovician trilobites from western Utah and eastern Nevada. *Bull. Utah Geol. Mlneral. Surv.* **48,** 249p.

Hintze, L. F. (1973) Lower and Middle Ordovician stratigraphic sections in the Ibex area, Millard County, Utah. *Brigham Young Univ. Geol. Stud.* **20,** 3–36.

Holland, H. D. (2006). The oxygenation of the atmosphere and oceans. *Philos. Trans. R. Soc. Lond. B. Biol. Sci.* **361,** 903–915.

Holland, S. M and Patzkowsky, M. E. (1996) Sequence stratigraphy and longterm paleooceanographic change in the Middle and Upper Ordovician of the eastern United States. *Geol. Soc. Am. Spec. Pap.* **306,** 117–129.

Holmer, L. E., Popov, L. E., Streng, M. and Miller, J. F. (2005) Lower Ordovician (Tremadocian) ligulate brachiopods from the House and Fillmore Formations, Ibex area, western Utah, USA. *J. Paleont.* **79,** 884–906.

Holmden, C., Amini, M. and Francois, R. (2015) Uranium isotope fractionation in Saanich Inlet: A modern analog study of a paleoredox tracer. *Geochim. Cosmochim. Acta* **153,** 202–215.

Hong, S. K., Lee, Y. I. and Jeong, S. Y. (2011) Carbon isotope composition of Upper Cambrian to Lower Ordovician carbonate in Korea, and its bearing on the Cambrian–Ordovician boundary and Lower Ordovician paleoceanography. *J. Asian Earth Sci.* **40,** 252–260.

Hood, A. v. S., Planavsky, N. J., Wallace, M. W., Wang, X., Bellefroid, E. J., Gueguen, B. and Cole, D. B. (2016) Integrated geochemical-petrographic insights from component-selective $\delta^{238}U$ of Cryogenian marine carbonates. *Geology* **44,** 935–938.

Howell, P. D. and van der Pluijm, B. A. (1990) Early history of the Michigan basin: Subsidence and Appalachian tectonics. *Geology* **18,** 1195–1198.

Howell, P. D. and van der Pluijm, B. A. (1999) Structural sequences and styles of subsidence in the Michigan basin. *Geol. Soc. Am. Bull.* **111,** 974–991.

Hu, D., Li, M., Zhang, X., Turchyn, A. V., Gong, Y. and Shen, Y. (2020) Large mass-independent sulphur isotope anomalies link stratospheric volcanism to the Late Ordovician mass extinction. *Nat. Commun.* **11(1),** 2297.

Huckriede, H. and Meischner, D. (1996) Origin and environment of manganese-rich sediments within black-shale basins. *Geochim. Cosmochim. Acta* **60,** 1399–1413.

Huff, W. D., Bergström, S. M. and Kolata, D. R. (2010) Ordovician explosive volcanism. *Geol. Soc. Am. Spec. Pap.* **466,** 13–28.

Jacobsen, S. B. and Kaufman, A. J. (1999) The Sr, C and O isotopic evolution of Neoproterozoic seawater. *Chem. Geol.* **161,** 37–57.

Jagoutz, O., Macdonald, F. A. and Royden, L. (2016) Low-latitude arc-continent collision as a driver for global cooling. *Proc. Natl. Acad. Sci. U.S.A.* **113(18),** 4935–4940.

Jemison, N. E., Johnson, T. M., Shiel, A. E., & Lundstrom, C. C. (2016). Uranium Isotopic Fractionation Induced by U(VI) Adsorption onto Common Aquifer Minerals. *Environ. Sci. Technol.* **50(22),** 12232–12240.

Ji, Z. and Barnes, C. R. (1983) A major conodont extinction event during the early Ordovician within the Midcontinent realm. *Palaeogeogr. Palaeoclimatol. Palaeoecol.* **104,** 37–47.

Jiang, G., Shi, X., Zhang, S., Wang, Y. and Xiao, S. (2011) Stratigraphy and paleogeography of the Ediacaran Doushantuo Formation (ca. 635–551Ma) in South China. *Gondwana Res.* **19,** 831–849.

Jiang G., Sohl L. E. and Christie-Blick N. (2003) Neoproterozoic stratigraphic comparison of the Lesser Himalaya (India) and Yangtze block (South China): Paleogeographic implications. *Geology* **31,** 917–920.

Jing, X., Stouge, S., Tian, Y., Wang, X. and Zhou, H. (2019) Katian (Upper Ordovician) carbon isotope chemostratigraphy in the Neixiang area, central China: implications for intercontinental correlation. *Geol. Mag.* **156(12),** 2053–2066.

Johnson, M. D., Armstrong, D. K., Sanford, B. V., Telford, P. G. and Rutka, M. A. (1992) Paleozoic and Mesozoic geology of Ontario. In P. C. Thurston, H. R. Williams, R. H. Sutcliffe, and G. M. Stott (eds.): Geology of Ontario. *Ont. Geol. Surv.* **4(2),** 907–1008.

Johnson, M. D., Russell, D. J. and Telford, P. G. (1983) Oil shale assessment project, Volume 1 Shallow drilling results 1981/82. *Ont. Geol. Surv.* Open File Report 5458, 36p.

Jones, D. S., Martini, A. M., Fike, D. A. and Kaiho, K. (2017) A volcanic trigger for the Late Ordovician mass extinction? Mercury data from south China and Laurentia. *Geology* **45,** 631–634.

Jost, A. B., Bachan, A., van de Schootbrugge, B., Lau, K. V., Weaver, K. L., Maher, K. and Payne, J. L. (2017) Uranium isotope evidence for an expansion of marine anoxia during the end-Triassic extinction. *Geochem. Geophys. Geosyst.* **18(8),** 3093–3108.

Kah, L. C., Thompson, C. K., Henderson, M. A. and Zhan, R. (2016) Behavior of marine sulfur in the Ordovician. *Palaeogeogr. Palaeoclimatol. Palaeoecol.* **458,** 133–153.

Kelemen, P. B., McQueen, N., Wilcox, J., Renforth, P., Dipple, G. and Vankeuren, A. P. (2020) Engineered carbon mineralization in ultramafic rocks for CO_2 removal from air: Review and new insights. *Chem. Geol.* **550,** 119628.

Kendall, B. (2021) Recent advances in geochemical paleo-oxybarometers. *Annu. Rev. Earth Planet. Sci.* **49,** 399–433.

Kendall, B., Creaser, R. A., Gordon, G. W. and Anbar, A. D. (2009) Re–Os and Mo isotope systematics of black shales from the Middle Proterozoic Velkerri and Wollogorang Formations, McArthur Basin, northern Australia. *Geochim. Cosmochim. Acta* **73,** 2534-2558.

Kendall, B., Dahl, T. W. and Anbar, A. D. (2017) The stable isotope geochemistry of molybdenum. *Rev. Mineral. Geochem.* **82,** 683–732.

Kendall, B., Komiya, T., Lyons, T. W., Bates, S. M., Gordon, G. W., Romaniello, S. J., Jiang, G., Creaser, R. A., Xiao, S., McFadden, K., Sawaki, Y., Tahata, M., Shu, D., Han, J., Li, Y., Chu, X. and Anbar, A. D. (2015) Uranium and molybdenum isotope evidence for an episode of widespread ocean oxygenation during the late Ediacaran Period. *Geochim. Cosmochim. Acta* **156,** 173–193.

Kendall, B., Reinhard, C. T., Lyons, T. W., Kaufman, A. J., Poulton, S. W. and Anbar, A. D. (2010) Pervasive oxygenation along late Archaean ocean margins. *Nat. Geosci.* **3,** 647–652.

Kendall, B., Wang, J., Zheng, W., Romaniello, S. J., Jeffrey Over, D., Bennett, Y., Xing, L., Kunert, A., Boyes, C. and Liu, J. (2020) Inverse correlation between the molybdenum and uranium isotope compositions of Upper Devonian black shales caused by changes in local depositional conditions rather than global ocean redox variations. *Geochim. Cosmochim. Acta* **287,** 141–164.

Kendall, B. S., Creaser, R. A., Ross, G. M. and Selby, D. (2004) Constraints on the timing of Marinoan "Snowball Earth" glaciation by ^{187}Re–^{187}Os dating of a Neoproterozoic, post-glacial black shale in Western Canada. *Earth Planet. Sci. Lett.* **222,** 729–740.

King, E. K. and Pett-Ridge, J. C. (2018) Reassessing the dissolved molybdenum isotopic composition of ocean inputs: The effect of chemical weathering and groundwater. *Geology* **46,** 955–958.

King, E. K., Thompson, A., Chadwick, O. A. and Pett-Ridge, J. C. (2016) Molybdenum sources and isotopic composition during early stages of pedogenesis along a basaltic climate transect. *Chem. Geol.* **445,** 54–67.

Klinkhammer, G. R. and Palmer, M. R. (1991) Uranium in the oceans: Where it goes and why. *Geochim. Cosmochim. Acta* **55,** 1799–1806.

Krause, A. J., Mills, B. J. W., Zhang, S., Planavsky, N. J., Lenton, T. M. and Poulton, S. W. (2018) Stepwise oxygenation of the Paleozoic atmosphere. *Nat. Commun.* **9(1),** 4081.

Kozik, N. P., Gill, B. C., Owens, J. D., Lyons, T. W. and Young, S. A. (2022) Geochemical records reveal protracted and differential marine redox change associated with Late Ordovician climate and mass extinctions. *AGU Adv.* **3(1),** e2021AV000563.

Kröger, B. (2017) Changes in the latitudinal diversity gradient during the Great Ordovician Biodiversification Event. *Geology* **46,** 127–130.

Ku, T. L., Knauss, K. G. and Mathieu, G. G. (1977) Uranium in open ocean: concentration and isotopic composition*. *Deep-sea Res.* **24,** 1005–1017.

Kump, L. R. and Arthur, M. A. (1999) Interpreting carbon-isotope excursions: carbonates and organic matter. *Chem. Geol.* **161,** 181–198.

Landing, E., Westrop, S. R. and Van Aller Hernick, L. (2003) Uppermost Cambrian-Lower Ordovician faunas and Laurentian platform sequence stratigraphy, eastern New York and Vermont. *J. Paleontol.* **77,** 78–98.

Langmuir, D. (1978) Uranium solution-mineral equilibria at low temperatures with applications to sedimentary ore deposits. *Geochim. Cosmochim. Acta* **42,** 547–569.

Lau, K. V., Hancock, L. G., Severmann, S., Kuzminov, A., Cole, D. B., Behl, R. J., Planavsky, N. J. and Lyons, T. W. (2022) Variable local basin hydrography and productivity control the uranium isotope paleoredox proxy in anoxic black shales. *Geochim. Cosmochim. Acta* **317,** 433–456.

Lau, K. V., Lyons, T. W. and Maher, K. (2020) Uranium reduction and isotopic fractionation in reducing sediments: Insights from reactive transport modeling. *Geochim. Cosmochim. Acta* **287,** 65–92.

Lau, K. V., Macdonald, F. A., Maher, K. and Payne, J. L. (2017) Uranium isotope evidence for temporary ocean oxygenation in the aftermath of the Sturtian Snowball Earth. *Earth Planet. Sci. Lett.* **458,** 282–292.

Lau, K. V., Maher, K., Altiner, D., Kelley, B. M., Kump, L. R., Lehrmann, D. J., Silva-Tamayo, J. C. and Payne, J. L. (2016) Marine anoxia and delayed Earth system recovery after the end-Permian extinction. *Proc. Natl. Acad. Sci. U.S.A.* **113,** 2360–2365.

Lavoie, D., Hamblin, A. P., Thériault, R., Beaulieu, J. and Kirkwood, D. (2008) The Upper Ordovician Utica Shales and Lorraine Group Flysch in southern Québec: Tectonostratigraphic setting and significance for unconventional gas. *Geol. Surv. Can.* Open File 5900, 5954p.

Lehmann, D., Brett, C. E., Cole, R. and Baird, G. (1995) Distal sedimentation in a peripheral foreland basin: Ordovician black shales and associated flysch of the western Taconic foreland, New York State and Ontario. *Geol. Soc. Am. Bull.* **107,** 708–724.

Lenton, T. M., Crouch, M., Johnson, M., Pires, N. and Dolan, L. (2012) First plants cooled the Ordovician. *Nat. Geosci.* **5(2),** 86–89.

Lenton, T. M., Dahl, T. W., Daines, S. J., Mills, B. J., Ozaki, K., Saltzman, M. R. and Porada, P. (2016) Earliest land plants created modern levels of atmospheric oxygen. *Proc. Natl. Acad. Sci. U.S.A.* **113(35),** 9704–9709.

Li, J., Azmy, K. and Kendall, B. (2022) The Mo- and U-isotope signatures in alternating shales and carbonate beds of rhythmites: A comparison and implications for redox conditions across the Cambrian-Ordovician boundary. *Chem. Geol.* **602,** 120882.

Li, J. and Yin, L. (2019) Rhenium–osmium isotope measurements in marine shale reference material SBC-1: Implications for method validation and quality control. *Geostand. Geoanal. Res.* **43(3),** 497–507.

Li, M., Chen, J., Wang, T., Zhong, N. and Shi, S. (2018) Nitrogen isotope and trace element composition characteristics of the Lower Cambrian Niutitang Formation shale in the upper -middle Yangtze region, South China. *Palaeogeogr. Palaeoclimatol. Palaeoecol.* **501,** 1–12.

Liberty, B. A. (1969) Paleozoic geology of the Lake Simcoe area, Ontario. *Geol. Surv. Can.* **335,** 201p.

Liu, M., Chen, D., Jiang, L., Stockey, R. G., Aseal, D., Zhang, B., Liu, K., Yang, X., Yan, D. and Planavsky, N. J. (2022) Oceanic anoxia and extinction in the latest Ordovician. *Earth Planet. Sci. Lett.* **588,** 117553.

Liu, X. M., Kah, L. C., Knoll, A. H., Cui, H., Wang, C., Bekker, A. and Hazen, R. M. (2021) A persistently low level of atmospheric oxygen in Earth's middle age. *Nat. Commun.* **12(1),** 351.

Livermore, B. D., Dahl, T. W., Bizzarro, M. and Connelly, J. N. (2020) Uranium isotope compositions of biogenic carbonates – Implications for U uptake in shells and the application of the paleo-ocean oxygenation proxy. *Geochim. Cosmochim. Acta* **287,** 50–64.

Löfgren, A. (1997) Conodont faunas from the upper Tremadoc at Brattefors, south-central Sweden, and reconstruction of the Paltodus apparatus. *Gff* **119,** 257–266.

Löfgren, A., Repetski, J. E., and Ethington, R. L. (1999) Some trans-Iapetus conodont faunal connections in the Tremadocian. *Boll. Soc. Paleontol. Ital.* **37,** 159–173.

Longman, J., Mills, B. J. W., Manners, H. R., Gernon, T. M. and Palmer, M. R. (2021) Late Ordovician climate change and extinctions driven by elevated volcanic nutrient supply. *Nat. Geosci.* **14(12),** 924–929.

Lowenstein, T. K., Kendall, B. and Anbar, A. D. (2014) The Geologic History of Seawater. *Treatise on Geochemistry, 2nd Edition*, 569–622.

Lu, W., Ridgwell, A., Thomas, E., Hardisty, D. S., Luo, G., Algeo, T. J., Saltzman, M. R., Gill, B. C., Shen, Y., Ling, H., Edwards, C. T., Whalen, M. T., Zhou, X., Gutchess, K. M., Jin, L., Rickaby, R. E. M., Jenkyns, H. C., Lyons, T. W., Lenton, T. M., Kump, L. R. and Lu, Z. (2018) Late inception of a resiliently oxygenated upper ocean. *Science* **361,** 174–177.

Lu, W., Wörndle, S., Halverson, G. P., Zhou, X., Bekker, A., Rainbird, R. H., Hardisty, D. S., Lyons, T. W.and Lu, Z. (2017) Iodine proxy evidence for increased ocean oxygenation during the Bitter Springs Anomaly. *Geochem. Perspect. Lett.* **5,** 53–57.

Lu, X., Dahl, T. W., Zheng, W., Wang, S. and Kendall, B. (2020) Estimating ancient seawater isotope compositions and global ocean redox conditions by coupling the molybdenum and uranium isotope systems of euxinic organic-rich mudrocks. *Geochim. Cosmochim. Acta* **290,** 76–103.

Lu, X., Kendall, B., Stein, H. J. and Hannah, J. L. (2017a) Temporal record of osmium concentrations and $^{187}Os/^{188}Os$ in organic-rich mudrocks: Implications for the osmium geochemical cycle and the use of osmium as a paleoceanographic tracer. *Geochim. Cosmochim. Acta* **216,** 221–241.

Lu, X., Kendall, B., Stein, H. J., Li, C., Hannah, J. L., Gordon, G. W. and Ebbestad, J. O. R. (2017b) Marine redox conditions during deposition of Late Ordovician and Early Silurian organic-rich mudrocks in the Siljan ring district, central Sweden. *Chem. Geol.* **457,** 75–94.

Lu, Z., Hoogakker, B. A. A., Hillenbrand, C., Zhou, X., Thomas, E., Gutchess, K. M., Lu, W., Jones, L. and Rickaby, R. E. M. (2016) Oxygen depletion recorded in upper waters of the glacial Southern Ocean. *Nat. Commun.* **7,** 11146.

Lu, Z., Jenkyns, H. C. and Rickaby, R. E. M. (2010) Iodine to calcium ratios in marine carbonate as a paleo-redox proxy during oceanic anoxic events. *Geology* **38,** 1107–1110.

Lüning, S., Craig, J., Loydell, D. K., Štorch, P. and Fitches, B. (2000) Lower Silurian 'hot shales' in North Africa and Arabia: regional distribution and depositional model. *Earth Sci. Rev.* **49,** 121–200.

Lowenstein, T. K., Kendall, B. and Anbar, A. D. (2014) The Geologic History of Seawater. *Treatise on Geochemistry, 2nd Edition,* 569–622.

Lyons, T. W., Reinhard, C. T. and Planavsky, N. J. (2014) The rise of oxygen in Earth's early ocean and atmosphere. *Nature* **506,** 307–315.

Macauley, G. and Snowdon, L. R. (1984) A rock-eval appraisal of the Ordovician collingwood shales, southern Ontario. *Geol. Surv. Can.* Open File 1092, 12p.

Macdonald, F. A., Swanson-Hysell, N. L., Park, Y., Lisiecki, L. and Jagoutz, O. (2019) Arc-continent collisions in the tropics set Earth's climate state. *Science* **364,** 181–184.

Mänd, K., Lalonde, S. V., Robbins, L. J., Thoby, M., Paiste, K., Kreitsmann, T., Paiste, P., Reinhard, C. T., Romashkin, A. E., Planavsky, N. J., Kirsimäe, K., Lepland, A. and

Konhauser, K. O. (2020) Palaeoproterozoic oxygenated oceans following the Lomagundi–Jatuli Event. *Nat. Geosci.* **13**, 302–306.

Marenco, P. J., Marenco, K. N., Lubitz, R. L. and Niu, D. (2013) Contrasting long-term global and short-term local redox proxies during the Great Ordovician Biodiversification Event: A case study from Fossil Mountain, Utah, USA. *Palaeogeogr. Palaeoclimatol. Palaeoecol.* **377,** 45–51.

Marenco, P. J., Martin, K. R., Marenco, K. N. and Barber, D. C. (2016) Increasing global ocean oxygenation and the Ordovician Radiation: Insights from Th/U of carbonates from the Ordovician of western Utah. *Palaeogeogr. Palaeoclimatol. Palaeoecol.* **458,** 77–84.

März, C., Poulton, S. W., Beckmann, B., Küster, K., Wagner, T. and Kasten, S. (2008) Redox sensitivity of P cycling during marine black shale formation: Dynamics of sulfidic and anoxic, non-sulfidic bottom waters. *Geochim. Cosmochim. Acta* **72(15),** 3703–3717.

McLennan, S. M. (2001) Relationships between the trace element composition of sedimentary rocks and upper continental crust. *Geochem. Geophys. Geosyst.* **2,** e2000GC000109.

McManus, J., Berelson, W. M., Severmann, S., Poulson, R. L., Hammond, D. E., Klinkhammer, G. P. and Holm, C. (2006) Molybdenum and uranium geochemistry in continental margin sediments: Paleoproxy potential. *Geochim. Cosmochim. Acta* **70,** 4643–4662.

McManus, J., Nägler, T. F., Siebert, C., Wheat, C. G. and Hammond, D. E. (2002) Oceanic molybdenum isotope fractionation: Diagenesis and hydrothermal ridge-flank alteration. *Geochem. Geophys. Geosyst.* **3,** 1078.

Melchin, M. J., Mitchell, C. E., Holmden, C. and Storch, P. (2013) Environmental changes in the Late Ordovician-early Silurian: Review and new insights from black shales and nitrogen isotopes. *Geol. Soc. Am. Bull.* **125,** 1635–1670.

Melezhik, V. A., Fallick, A. E., Brasier, A. T. and Lepland, A. (2015) Carbonate deposition in the Palaeoproterozoic Onega basin from Fennoscandia: a spotlight on the transition from the Lomagundi-Jatuli to Shunga events. *Earth-Sci. Rev.* **147,** 65–98.

Melezhik, V. A., Fallick, A. E., Filippov, M. M. and Larsen, O. (1999) Karelian shungite-an indication of 2.0-Ga-old metamorphosed oil-shale and generation of petroleum: geology, lithology and geochemistry. *Earth-Sci. Rev.* **47,** 1–40.

Menard, H. W. and Smith, S. M. (1966) Hypsometry of ocean basin provinces. *J. Geophys. Res.* **71(18),** 4305–4325.

Metzger, J. G., Ramezani, J., Bowring, S. A. and Fike, D. A. (2021) New age constraints on the duration and origin of the Late Ordovician Guttenberg δ^{13}Ccarb excursion from high-precision U-Pb geochronology of K-bentonites. *Geol. Soc. Am. Bull.* **133(3-4),** 580–590.

Meyer, K. M. and Kump, L. R. (2008) Oceanic Euxinia in Earth History: Causes and Consequences. *Annu. Rev. Earth Planet. Sci.* **36,** 251–288.

Middelburg, J. J., Soetaert, K., Herman, P. M. J. and Heip, C. H. R. (1996) Denitrification in marine sediments: a model study. *Global Biogeochem. Cycles* **10,** 661–673.

Miller, J. F., Evans, K. E., Loch, J. D., Ethington, R. L., Stitt, J. H., Holmer, L. E. and Popov, L. E., (2003) Stratigraphy of the Sauk III interval (Cambrian–Ordovician) in the Ibex area, western Millard County, Utah. *Brigham Young Univ. Geol. Stud.* **47,** 23–118.

Miller, J. F., Evans, K. R. and Dattilo, B. F. (2012) The Great American Carbonate Bank in the miogeocline of western central Utah: Tectonic influences on sedimentation. In J. R. Derby, R. D. Fritz, S. A. Longacre, W. A. Morgan, & C. A. Sternbach (Eds.), *The Great American Carbonate Bank: The Geology and Economic Resources of the Cambrian-Ordovician Sauk Megasequence of Laurentia* (Vol. 98, pp. 769–854): Association of American Petroleum Geologists Memoir.

Miller, C. A., Peucker-Ehrenbrink, B., Walker, B. D. and Marcantonio, F. (2011) Re-assessing the surface cycling of molybdenum and rhenium. *Geochim. Cosmochim. Acta* **75,** 7146–7179.

Mills, D. B. and D. E. Canfield (2014) Oxygen and animal evolution: did a rise of atmospheric oxygen "trigger" the origin of animals? *Bioessays* **36,** 1145–1155.

Monteiro, F. M., Pancost, R. D., Ridgwell, A. and Donnadieu, Y. (2012) Nutrients as the dominant control on the spread of anoxia and euxinia across the Cenomanian-Turonian oceanic anoxic event (OAE2): Model-data comparison. *Paleoceanography* **27,** PA4209.

Montoya-Pino, C. (2011). *Molybdenum and Uranium Isotope Signatures of Mesozoic Black Shales: Implications on the Spatial Dimension of Oceanic Anoxic Events.*

Montoya-Pino, C., Weyer, S., Anbar, A. D., Pross, J., Oschmann, W., van de Schootbrugge, B. and Arz, H. W. (2010) Global enhancement of ocean anoxia during Oceanic Anoxic Event 2: A quantitative approach using U isotopes. *Geology* **38,** 315–318.

Moore, W.S. (1996) Large groundwater inputs to coastal waters revealed by ^{226}Ra enrichments. *Nature* **380,** 612–614.

Morford, J. L. and Emerson, S. (1999) The geochemistry of redox sensitive trace metals in sediments. *Geochim. Cosmochim. Acta* **63,** 1735–1750.

Morford, J. L., Emerson, S. R., Breckel, E. J. and Kim, S. H. (2005) Diagenesis of oxyanions (V, U, Re, and Mo) in pore waters and sediments from a continental margin. *Geochim. Cosmochim. Acta* **69(21),** 5021–5032.

Morgan, W. A. (2012) Sequence stratigraphy of the Great American Carbonate Bank. In J. R. Derby, R. D. Fritz, S. A. Longacre, W. A. Morgan, & C. A. Sternbach (Eds.), *The Great American Carbonate Bank: The Geology and Economic Resources of the Cambrian-Ordovician Sauk Megasequence of Laurentia* (Vol. 98, pp. 37–82): Association of American Petroleum Geologists Memoir.

Moskalenko, T. A. (1967) Conodonts from the Chunsky Stage (Lower Ordovician) of the rivers Moiero and Podkamennaya Tunguska. In A. B. Ivanovskii, & B. S. Sokolov (Eds.), *New data on the biostratigraphy of the lower Paleozoic deposits of the Siberian platform* (pp. 98–116): Akademiya Nauk SSSR, Sibirskoye Otdeleniye, Instituta Geologii i Geofiziki.

Mukherjee, I. and Large, R. R. (2016) Pyrite trace element chemistry of the Velkerri Formation, Roper Group, McArthur Basin: Evidence for atmospheric oxygenation during the Boring Billion. *Precambrian Res.* **281,** 13–26.

Munnecke, A., Calner, M., Harper, D. A. T. and Servais, T. (2010) Ordovician and Silurian sea–water chemistry, sea level, and climate: A synopsis. *Palaeogeogr. Palaeoclimatol. Palaeoecol.* **296,** 389–413.

Nägler, T. F., Anbar, A. D., Archer, C., Goldberg, T., Gordon, G. W., Greber, N. D., Siebert, C., Sohrin, Y. and Vance, D. (2014) Proposal for an International Molybdenum Isotope Measurement Standard and Data Representation. *Geostand. Geoanal. Res.* **38,** 149–151.

Nägler, T. F., Neubert, N., Böttcher, M. E., Dellwig, O. and Schnetger, B. (2011) Molybdenum isotope fractionation in pelagic euxinia: Evidence from the modern Black and Baltic Seas. *Chem. Geol.* **289,** 1–11.

Nakagawa, Y., Takano, S., Firdaus, M. L., Norsuye, K., Hirata, T., Vance, D. and Sohrin, Y. (2012) The molybdenum isotopic composition of the modern ocean. *Geochim. Cosmochim. Acta* **46,** 131–141.

Narbonne, G. M. (2005) THE EDIACARA BIOTA: Neoproterozoic Origin of Animals and Their Ecosystems. *Annu. Rev. Earth Planet. Sci.* **33(1),** 421–442.

Neely, R. A., Gislason, S. R., Ólafsson, M., McCoy-West, A. J., Pearce, C. R. and Burton, K. W. (2018) Molybdenum isotope behaviour in groundwaters and terrestrial hydrothermal systems, Iceland. *Earth Planet. Sci. Lett.* **486,** 108–118.

Neubert, N., Nägler, T. F. and Böttcher, M. E. (2008) Sulfidity controls molybdenum isotope fractionation into euxinic sediments: Evidence from the modern Black Sea. *Geology* **36,** 775–778.

Niocaill, C. M., Van der Pluijm, B. A. and Van der Voo, R. (1997) Ordovician paleogeography and the evolution of the Iapetus ocean. *Geology* **25,** 159–162.

Noordmann, J., Weyer, S., Georg, R. B., Jons, S. and Sharma, M. (2016) $^{238}U/^{235}U$ isotope ratios of crustal material, rivers and products of hydrothermal alteration: new insights on the oceanic U isotope mass balance. *Isot. Environ. Health Stud.* **52,** 141–163.

Noordmann, J., Weyer, S., Montoya-Pino, C., Dellwig, O., Neubert, N., Eckert, S., Paetzel, M. and Böttcher, M. E. (2015) Uranium and molybdenum isotope systematics in modern euxinic basins: Case studies from the central Baltic Sea and the Kyllaren fjord (Norway). *Chem. Geol.* **396,** 182–195.

Nursall, J. R. (1959) Oxygen as a prerequiste of the origin of the metazoa. *Nature* **183,** 1170–1172.

Obermajer, M., Fowler, M. G. and Snowdon, L. R. (1999) Depositional environment and oil generation in Ordovician source rocks from southwestern Ontario, Canada: Organic geochemical and petrological approach. *Am. Assoc. Petrol. Geol. Bull.* **83,** 1426–1453.

Och, L. M. and Shields-Zhou, G. A. (2012) The Neoproterozoic oxygenation event: Environmental perturbations and biogeochemical cycling. *Earth Sci. Rev.* **110(1-4),** 26–57.

Ogg, J. G., Ogg, G. M. and Gradstein, F. M. (2016) *A Concise Geologic Time Scale.* Amsterdam, Netherlands: Elsevier.

Ostrander, C. M., Sahoo, S. K., Kendall, B., Jiang, G., Planavsky, N. J., Lyons, T. W., Nielsen, S. G., Owens, J. D., Gordon, G. W., Romaniello, S. J. and Anbar, A. D. (2019a) Multiple negative molybdenum isotope excursions in the Doushantuo Formation (South China) fingerprint complex redox-related processes in the Ediacaran Nanhua Basin. *Geochim. Cosmochim. Acta* **261,** 191–209.

Ostrander, C. M., Nielsen, S. G., Owens, J. D., Kendall, B., Gordon, G. W., Romaniello, S. J. and Anbar, A. D. (2019b) Fully oxygenated water columns over continental shelves before the Great Oxidation Event. *Nat. Geosci.* **12,** 186–191.

Owens, J. D., Nielsen, S. G., Horner, T. J., Ostrander, C. M. and Peterson, L. C. (2017) Thallium-isotopic compositions of euxinic sediments as a proxy for global manganese-oxide burial. *Geochim. Cosmochim. Acta* **213,** 291–307.

Paiste, K., Lepland, A., Zerkle, A. L., Kirsimäe, K., Izon, G., Patel, N. K., McLean, F., Kreitsmann, T., Mänd, K., Bui, T. H., Romashkin, A. E., Rychanchik, D. V. and Prave, A. R. (2018) Multiple sulphur isotope records tracking basinal and global processes in the 1.98 Ga Zaonega Formation, NW Russia. *Chem. Geol.* **499,** 151–164.

Palmer, A. R. (1984). The biomere problem: Evolution of an idea. *J. Paleontol.* **58,** 599–611.

Partin, C. A., Bekker, A., Planavsky, N. J., Scott, C. T., Gill, B. C., Li, C., Podkovyrov, V., Maslov, A., Konhauser, K. O., Lalonde, S. V., Love, G. D., Poulton, S. W. and Lyons, T. W. (2013) Large-scale fluctuations in Precambrian atmospheric and oceanic oxygen levels from the record of U in shales. *Earth Planet. Sci. Lett.* **369-370,** 284–293.

Pasquier, V., Fike, D. A., Révillon, S. and Halevy, I. (2022) A global reassessment of the controls on iron speciation in modern sediments and sedimentary rocks: A dominant role for diagenesis. *Geochim. Cosmochim. Acta* **335,** 211–230.

Pavlov, A. A. and Kasting, J. F. (2002) Mass-independent fractionation of sulfur isotopes in Archean sediments: strong evidence for an anoxic Archean atmosphere. *Astrobiology* **2,** 27–41.

Payne, J. L., McClain, C. R., Boyer, A. G., Brown, J. H., Finnegan, S., Kowalewski, M., Krause, R. A. Jr., Lyons, S. K., McShea, D. W., Novack-Gottshall, P. M., Smith, F. A., Spaeth, P., Stempien, J. A. and Wang, S. C. (2011) The evolutionary consequences of oxygenic photosynthesis: a body size perspective. *Photosynth. Res.* **107,** 37–57.

Planavsky, N. J., McGoldrick, P., Scott, C. T., Li, C., Reinhard, C. T., Kelly, A. E., Chu, X., Bekker, A., Love, G. D. and Lyons, T. W. (2011) Widespread iron-rich conditions in the mid-Proterozoic ocean. *Nature* **477,** 448–451.

Planavsky, N. J., Reinhard, C. T., Wang, X., Thomson, D., McGoldrick, P., Rainbird, R. H., Johnson, T., Fischer, W. W., and Lyons, T. W. (2014) Low Mid-Proterozoic atmospheric oxygen levels and the delayed rise of animals. *Science* **346,** 635–638.

Pohl, A., Harper, D. A. T., Donnadieu, Y., Le Hir, G., Nardin, E. and Servais, T. (2018) Possible patterns of marine primary productivity during the Great Ordovician Biodiversification Event. *Lethaia* **51,** 187–197.

Pohl, A., Lu, Z., Lu, W., Stockey, R. G., Elrick, M., Li, M., Desrochers, A., Shen, Y., He, R., Finnegan, S. and Ridgwell, A. (2021) Vertical decoupling in Late Ordovician anoxia due to reorganization of ocean circulation. *Nat. Geosci.* **14(11),** 868–873.

Popov, L. E., and Tolmacheva, T. (1995) Conodont distribution in a deep-water Cambrian Ordovician boundary sequence from south-central Kazakhstan. In J. D. Cooper, M. L. Droser, & S. C. Finney (Eds.), *Ordovician Odyssey: Short Papers, 7th International Symposium on the Ordovician System* (Vol. 77, pp. 121–124): Society for Sedimentary Geology.

Poulson Brucker, R. L., McManus, J., Severmann, S. and Berelson, W. M. (2009) Molybdenum behavior during early diagenesis. *Geochem. Geophys. Geosyst.* **10,** Q06010.

Poulson, R. L., Siebert, C., McManus, J. and Berelson, W. M. (2006) Authigenic molybdenum isotope signatures in marine sediments. *Geology* **34,** 617–620.

Poulton, S. W. and Canfield, D. E. (2005) Development of a sequential extraction procedure for iron: implications for iron partitioning in continentally derived particulates. *Chem. Geol.* **214,** 209–221.

Poulton, S. W. and Canfield, D. E. (2011) Ferruginous Conditions: A Dominant Feature of the Ocean through Earth's History. *Elements* **7,** 107–112.

Poulton, S. W. and Raiswell, R. (2002) The low-temperature geochemical cycle of iron: From continental fluxes to marine sediment deposition. *Am. J. Sci.* **302,** 774–805.

Qin, Z., Xu, D., Kendall, B., Zhang, X., Ou, Q., Wang, X., Li, J. and Liu, J. (2022) Molybdenum isotope-based redox deviation driven by continental margin euxinia during the early Cambrian. *Geochim. Cosmochim. Acta* **325,** 152–169.

Qu, Y., Crne, A. E., Lepland, A. and van Zuilen, M. A. (2012) Methanotrophy in a Paleoproterozoic oil field ecosystem, Zaonega Formation, Karelia, Russia. *Geobiology* **10,** 467–478.

Quinlan, G. M. and Beaumont, C. (1984) Appalachian thrusting, lithospheric flexure, and the Paleozoic stratigraphy of the Eastern Interior of North America. *Can. J. Earth Sci.* **21,** 973–996.

Raiswell, R., Hardisty, D. S., Lyons, T. W., Canfield, D. E., Owens, J. D., Planavsky, N. J., Poulton, S. W. and Reinhard, C. T. (2018) The iron paleoredox proxies: A guide to the pitfalls, problems and proper practice. *Am. J. Sci.* **318,** 491–526.

Rancourt, C. C. (2009) "Collingwood" strata in south-central Ontario - A petrophysical chemostratigraphic approach to comparison and correlation using geophysical borehole logs. *M.Sc thesis, University of Toronto,* 65p.

Rasmussen, C. M. O., Kröger, B., Nielsen, M. L. and Colmenar, J. (2019) Cascading trend of Early Paleozoic marine radiations paused by Late Ordovician extinctions. *Proc. Natl. Acad. Sci. U.S.A.* **116(15),** 7207–7213.

Reinhard, C. T. and Planavsky, N. J. (2022) The History of Ocean Oxygenation. *Annu. Rev. Mar. Sci.* **14,** 331–353.

Reinhard, C. T., Planavsky, N. J., Olson, S. L., Lyons, T. W. and Erwin, D. H. (2016) Earth's oxygen cycle and the evolution of animal life. *Proc. Natl. Acad. Sci. U.S.A.* **113,** 8933–8938.

Reinhard, C. T., Planavsky, N. J., Robbins, L. J., Partin, C. A., Gill, B. C., Lalonde, S. V., Bekker, A., Konhauser, K. O. and Lyons, T. W. (2013) Proterozoic ocean redox and biogeochemical stasis. *Proc. Natl. Acad. Sci. U.S.A.* **110,** 5357–5362.

Remírez, M. N. and Algeo, T. J. (2020) Paleosalinity determination in ancient epicontinental seas: A case study of the T-OAE in the Cleveland Basin (UK). *Earth Sci. Rev.* **201,** 103072.

Riva, J. (1974) A revision of some Ordovician graptolites of Eastern North America. *Palaeontology* **17,** 1–40.

Rhoads, D. C. and Morse, J. W. (1971) Evolutionary and ecologic significance of oxygen-deficient marine basins. *Lethaia* **4,** 413–428.

Rolison, J. M., Stirling, C. H., Middag, R. and Rijkenberg, M. J. A. (2017) Uranium stable isotope fractionation in the Black Sea: Modern calibration of the $^{238}U/^{235}U$ paleo-redox proxy. *Geochim. Cosmochim. Acta* **203,** 69–88.

Romaniello, S. J., Herrmann, A. D. and Anbar, A. D. (2013) Uranium concentrations and $^{238}U/^{235}U$ isotope ratios in modern carbonates from the Bahamas: Assessing a novel paleoredox proxy. *Chem. Geol.* **362,** 305–316.

Romaniello, S. J., Herrmann, A. D. and Anbar, A. D. (2016) Syndepositional diagenetic control of molybdenum isotope variations in carbonate sediments from the Bahamas. *Chem. Geol.* **438,** 84–90.

Rooney, A. D., Cantine, M. D., Bergmann, K. D., Gomez-Perez, I., Al Baloushi, B., Boag, T. H., Busch, J. F., Sperling, E. A. and Strauss, J. V. (2020) Calibrating the coevolution of Ediacaran life and environment. *Proc. Natl. Acad. Sci. U.S.A.* **117(29),** 16824–16830.

Rooney, A. D., Chew, D. M., & Selby, D. (2011). Re–Os geochronology of the Neoproterozoic–Cambrian Dalradian Supergroup of Scotland and Ireland: Implications for Neoproterozoic stratigraphy, glaciations and Re–Os systematics. *Precambrian Res.* **185,** 202–214.

Ross Jr., R. J. (1970) Ordovician brachiopods, trilobites, and stratigraphy in eastern central Nevada. *U.S. Geol. Surv. Prof. Pap.* 639, 103p.

Ross Jr., R. J., James, N. P., Hintze, L. F. and Poole, F. G. (1989) Architecture and evolution of a Whiterockian (Early Middle Ordovician) carbonate platform, Basin Ranges of western U.S.A. In P. D. Crevello, J. L. Wilson, J. F. Sarg, & J. F. Read (Eds.), *Controls on Carbonate Platform and Basin Development* (Vol. 44, pp. 167–185): Society of Economic Paleontologists and Mineralogists Special Publication.

Rue, E. L., Smith, G. J., Cutter, G. A. and Bruland, K. W. (1997) The response of trace element redox couples to suboxic conditions in the water column. *Deep-Sea Research, Part I,* **44,** 113–134.

Rudnick, R. L. and Gao, S. (2014) Composition of the Continental Crust. In H. D. Holland & K. K. Turekian (Eds.), *Treatise on Geochemistry (2nd ed.)* (Vol. 4, pp. 1–51): Elsevier.

Russell, D. J. and Telford, P. G. (1983) Revisions to the stratigraphy of the Upper Ordovician Collingwood beds of Ontario - a potential oil shale. *Can. J. Earth Sci.* **20,** 1780–1790.

Sageman, B. B. and Lyons, T. W. (2003). Geochemistry of fine-grained sediments and sedimentary rocks. *Treatise on geochemistry*, 115–158.

Sahoo, S. K., Planavsky, N. J., Jiang, G., Kendall, B., Owens, J. D., Wang, X., Shi, X., Anbar, A. D. and Lyons, T. W. (2016) Oceanic oxygenation events in the anoxic Ediacaran ocean. *Geobiology* **14(5),** 457–468.

Sahoo, S. K., Planavsky, N. J., Kendall, B., Wang, X., Shi, X., Scott, C., Anbar, A. D., Lyons, T. W. and Jiang, G. (2012) Ocean oxygenation in the wake of the Marinoan glaciation. *Nature* **489,** 546–549.

Saltzman, M. R. and Edwards, C. T. (2017) Gradients in the carbon isotopic composition of Ordovician shallow water carbonates: A potential pitfall in estimates of ancient CO_2 and O_2. *Earth Planet. Sci. Lett.* **464,** 46–54.

Saltzman, M. R., Edwards, C. T., Adrain, J. M. and Westrop, S. R. (2015) Persistent oceanic anoxia and elevated extinction rates separate the Cambrian and Ordovician radiations. *Geology* **43,** 807–810.

Saltzman, M. R., Edwards, C. T., Leslie, S. A., Dwyer, G. S., Bauer, J. A., Repetski, J. E., Harris, A. G. and Bergström, S. M. (2014) Calibration of a conodont apatite-based Ordovician 87Sr/86Sr curve to biostratigraphy and geochronology: Implications for stratigraphic resolution. *Geol. Soc. Am. Bull.* **126(11-12),** 1551–1568.

Saltzman, M. R., Ripperdan, R. L., Brasier, M. D., Lohmann, K. C., Robison, R. A., Chang, W. T., Peng, S., Ergaliev, E. K. and Runnegar, B. (2000) A global carbon isotope excursion (SPICE) during the Late Cambrian: relation to trilobite extinctions, organic-matter burial and sea level. *Palaeogeogr. Palaeoclimatol. Palaeoecol.* **162,** 211–223.

Schauble, E. A. (2007) Role of nuclear volume in driving equilibrium stable isotope fractionation of mercury, thallium, and other very heavy elements. *Geochim. Cosmochim. Acta* **71,** 2170–2189.

Scholz, F., Baum, M., Siebert, C., Eroglu, S., Dale, A. W., Naumann, M. and Sommer, S. (2018) Sedimentary molybdenum cycling in the aftermath of seawater inflow to the intermittently euxinic Gotland Deep, Central Baltic Sea. *Chem. Geol.* **491,** 27–38.

Scholz, F., McManus, J. and Sommer, S. (2013) The manganese and iron shuttle in a modern euxinic basin and implications for molybdenum cycling at euxinic ocean margins. *Chem. Geol.* **355,** 56–68.

Scott, C., Lyons, T. W., Bekker, A., Shen, Y., Poulton, S. W., Chu, X. and Anbar, A. D. (2008) Tracing the stepwise oxygenation of the Proterozoic ocean. *Nature* **452,** 456–459.

Scott, C., Wing, B. A., Bekker, A., Planavsky, N. J., Medvedev, P., Bates, S. M., Yun, M. and Lyons, T. W. (2014) Pyrite multiple-sulfur isotope evidence for rapid expansion and contraction of the early Paleoproterozoic seawater sulfate reservoir. *Earth Planet. Sci. Lett.* **389,** 95–104.

Sears, J. W. and Price, R. A. (2003) Tightening the Siberian connection to western Laurentia. *Geol. Soc. Am. Bull.* **115,** 943–953.

Selby, D. and Creaser, R. A. (2005) Direct radiometric dating of the Devonian-Mississippian time-scale boundary using the Re-Os black shale geochronometer. *Geology* **33(7),** 545–548.

Sepkoski, J. J., Jr. (1981) A factor analytic description of the Phanerozoic marine fossil record. *Paleobiology* **7,** 36–53.

Servais, T. and Harper, D. A. T. (2018) The Great Ordovician Biodiversification Event (GOBE): definition, concept and duration. *Lethaia* **51(2),** 151–164.

Sharma, S., Dix, G. R. and Riva, J. F. V. (2003) Late Ordovician platform foundering, its paleoceanography and burial, as preserved in separate (eastern Michigan Basin, Ottawa Embayment) basins, southern Ontario. *Can. J. Earth Sci.* **40,** 135–148.

Sharma, S., Dix, G. R. and Villeneuve, M. (2005) Petrology and potential tectonic significance of a K-bentonite in a Taconian shale basin (eastern Ontario, Canada), northern Appalachians. *Geol. Mag.* **142(2),** 145–158.

Sheehan, P. M. (2001) The late Ordovician mass extinction. *Annu. Rev. Earth Planet. Sci.* **29,** 331–364.

Sheen, A. I., Kendall, B., Reinhard, C. T., Creaser, R. A., Lyons, T. W., Bekker, A., Poulton, S. W. and Anbar, A. D. (2018) A model for the oceanic mass balance of rhenium and implications for the extent of Proterozoic ocean anoxia. *Geochim. Cosmochim. Acta* **227,** 75–95.

Shields, G. A., Carden, G. A. F., Veizer, J., Meidla, T., Rong, J. and Li, R. (2003) Sr, C, and O isotope geochemistry of Ordovician brachiopods: a major isotopic event around the Middle-Late Ordovician transition. *Geochim. Cosmochim. Acta* **67(11),** 2005–2025.

Siebert, C., McManus, J., Bice, A., Poulson, R. L. and Berelson, W. M. (2006) Molybdenum isotope signatures in continental margin marine sediments. *Earth Planet. Sci. Lett.* **241,** 723–733.

Siebert, C., Nägler, T. F. and Kramers, J. D. (2001) Determination of Molybdenum isotope fractionation by double-spike multicollector inductively coupled plasma mass spectrometry. *Geochem. Geophys. Geosyst.* **2,** 2000GC000124.

Siebert, C., Nägler, T. F., von Blanckenburg, F. and Kramers, J. D. (2003) Molybdenum isotope records as a potential new proxy for paleoceanography. *Earth Planet. Sci. Lett.* **211,** 159–171.

Song, H., Song, H., Algeo, T. J., Tong, J., Romaniello, S. J., Zhu, Y., Chu, D., Gong, Y. and Anbar, A. D. (2017) Uranium and carbon isotopes document global-ocean redox-productivity relationships linked to cooling during the Frasnian-Famennian mass extinction. *Geology* **45,** 887–890.

Sperling, E. A., Frieder, C. A., Raman, A. V., Girguis, P. R., Levin, L. A. and Knoll, A. H. (2013) Oxygen, ecology, and the Cambrian radiation of animals. *Proc. Natl. Acad. Sci. U.S.A.* **110,** 13446–13451.

Sperling, E. A., Melchin, M. J., Fraser, T., Stockey, R. G., Farrell, U. C., Bhajan, L., Brunoir, T. N., Cole, D. B., Gill, B. C., Lenz, A., Loydell, D. K., Malinowski, J., Miller, A. J., Plaza-Torres, S., Bock, B., Rooney, A. D., Tecklenburg, S. A., Vogel, J. M., Planavsky, N. J. and Strauss, J. V. (2021) A long-term record of early to mid-Paleozoic marine redox change. *Sci. Adv.* **7,** eabf4382.

Sperling, E. A., Wolock, C. J., Morgan, A. S., Gill, B. C., Kunzmann, M., Halverson, G. P., Macdonald, F. A., Knoll, A. H. and Johnston, D. T. (2015) Statistical analysis of iron geochemical data suggests limited late Proterozoic oxygenation. *Nature* **523,** 451–454.

Stanley, S. M. and Hardie, L. A. (1999) Hypercalcification: Paleontology links plate tectonics and geochemistry to sedimentology. *GSA Today* **9,** 1–7.

Stigall, A. L., Edwards, C. T., Freeman, R. L. and Rasmussen, C. M. Ø. (2019) Coordinated biotic and abiotic change during the Great Ordovician Biodiversification Event: Darriwilian assembly of early Paleozoic building blocks. *Palaeogeogr. Palaeoclimatol. Palaeoecol.* **530,** 249–270.

Stirling, C. H., Andersen, M. B., Potter, E. and Halliday, A. N. (2007) Low-temperature isotopic fractionation of uranium. *Earth Planet. Sci. Lett.* **264,** 208–225.

Stirling, C. H., Andersen, M. B., Warthmann, R. and Halliday, A. N. (2015) Isotope fractionation of ^{238}U and ^{235}U during biologically-mediated uranium reduction. *Geochim. Cosmochim. Acta* **163,** 200–218.

Stitt, J. H. (1983). Trilobite biostratigraphy and lithostratigraphy of the McKenzie Hill Limestone (Lower Ordovician), Wichita and Arbuckle Mountains, Oklahoma. *Oklahoma Geol. Surv. Bull.* **134,** 54p.

Stockey, R. G., Cole, D. B., Planavsky, N. J., Loydell, D. K., Fryda, J. and Sperling, E. A. (2020) Persistent global marine euxinia in the early Silurian. *Nat. Commun.* **11,** 1804.

Strauss, J. V., Fraser, T., Melchin, M. J., Allen, T. J., Malinowski, J., Feng, X., Taylor, J. F., Day, J., Gill, B. C. and Sperling, E. A. (2020) The Road River Group of northern Yukon, Canada: early Paleozoic deep-water sedimentation within the Great American Carbonate Bank. *Can. J. Earth Sci.* **57,** 1193–1219.

Stylo, M., Neubert, N., Wang, Y., Monga, N., Romaniello, S. J., Weyer, S. and Bernier-Latmani, R. (2015) Uranium isotopes fingerprint biotic reduction. *Proc. Natl. Acad. Sci. U.S.A.* **112,** 5619–5624.

Swanson-Hysell, N. L. and Macdonald, F. A. (2017) Tropical weathering of the Taconic orogeny as a driver for Ordovician cooling. *Geology* **45,** 719–722.

Sweet, W. C. and Tolbert, C. M. (1997) An Ibexian (Lower Ordovician) reference section in the Southern Egan Range, Nevada, for a conodont-based chronstratigraphy. In M. E. Taylor, (Eds.), *Early Paleozoic Biochronology of the Great Basin, Western United States* (1579, pp. 51–84): United States Geological Survey Professional Paper.

Taylor, J. F. (2006) History and status of the biomere concept. *Mem. Assoc. Australas. Paleontol.* **32,** 247–265.

Taylor, J. F., Repetski, J. E., Loch, J. D. and Lesile, S. A. (2012) Biostratigraphy and chronostratigraphy of the Cambrian-Ordovician great American carbonate bank. In J. R. Derby, R. D. Fritz, S. A. Longacre, W. A. Morgan, & C. A. Sternbach (Eds.), *The great American carbonate bank: The geology and economic resources of the Cambrian-Ordovician Sauk megasequence of Laurentia* (Vol. 98, pp. 15–35): American Association of Petroleum Geologists Memoir.

Taylor, S. R. and McLennan, S. M. (1985) The continental crust: Its composition and evolution, 312p.

Telus, M., Dauphas, N., Moynier, F., Tissot, F. L. H., Teng, F., Nabelek, P. I., Craddock, P. R. and Groat, L. A. (2012) Iron, zinc, magnesium and uranium isotopic fractionation during continental crust differentiation: The tale from migmatites, granitoids, and pegmatites. *Geochim. Cosmochim. Acta* **97,** 247–265.

Thompson, C. K. and Kah, L. C. (2012) Sulfur isotope evidence for widespread euxinia and a fluctuating oxycline in Early to Middle Ordovician greenhouse oceans. *Palaeogeogr. Palaeoclimatol. Palaeoecol.* **313-314,** 189–214.

Tissot, F. L. H., Chen, C., Go, B. M., Naziemiec, M., Healy, G., Bekker, A., Swart, P. K. and Dauphas, N. (2018) Controls of eustasy and diagenesis on the $^{238}U/^{235}U$ of carbonates

and evolution of the seawater ($^{234}U/^{238}U$) during the last 1.4 Myr. *Geochim. Cosmochim. Acta* **242,** 233–265.

Tissot, F. L. H. and Dauphas, N. (2015) Uranium isotopic compositions of the crust and ocean: Age corrections, U budget and global extent of modern anoxia. *Geochim. Cosmochim. Acta* **167,** 113–143.

Tostevin, R., Clarkson, M. O., Gangl, S., Shields, G. A., Wood, R. A., Bowyer, F., Penny, A. M., Stirling, C. H. and Stirling, C. H. (2019) Uranium isotope evidence for an expansion of anoxia in terminal Ediacaran oceans. *Earth Planet. Sci. Lett.* **506,** 104–112.

Tribovillard, N., Algeo, T. J., Lyons, T. W. and Riboulleau, A. (2006) Trace metals as paleoredox and paleoproductivity proxies: An update. *Chem. Geol.* **232(1-2),** 12–32.

Trotter, J. A., Williams, I. S., Barnes, C. R., Lécuyer, C. and Nicoll, R. S. (2008) Did Cooling Oceans Trigger Ordovician Biodiversification? Evidence from Conodont Thermometry. *Science* **321,** 550–554.

Tyson, R. V. (2005) The "productivity versus preservation" controversy: Cause, flaws, and resolution. *SEPM Spec. Publ.* **82,** 17–33.

Van der Weijden, C. H. (2002) Pitfalls of normalization of marine geochemical data using a common divisor. *Mar. Geol.* **184,** 167–187.

Van Staal, C. R. and Barr S. M. (2012) Lithospheric architecture and tectonic evolution of the Canadian Appalachians and associated Atlantic margin. *Geol. Assoc. Can.* **49,** 41–95.

Veizer, J. (1983) Chemical diagenesis of carbonates: theory and application of trace element technique. In M. A. Arthur, T. F. Anderson, I. R. Kaplan, J. Veizer, & L. S. Land (Eds.), Stable Isotopes in Sedimentary Geology (10, pp. 1–100): Society of Economic Paleontologists and Mineralogists.

Voegelin, A. R., Pettke, T., Greber, N. D., von Niederhäusern, B. and Nägler, T. F. (2014) Magma differentiation fractionates Mo isotope ratios: Evidence from the Kos Plateau Tuff (Aegean Arc). *Lithos* **190-191,** 440–448.

Wallace, M. W., Hood, A. v. S., Shuster, A., Greig, A., Planavsky, N. J. and Reed, C. P. (2017) Oxygenation history of the Neoproterozoic to early Phanerozoic and the rise of land plants. *Earth Planet. Sci. Lett.* **466,** 12–19.

Wang, H., Zhang, Z., Li, C., Algeo, T. J., Cheng, M. and Wang, W. (2020) Spatiotemporal redox heterogeneity and transient marine shelf oxygenation in the Mesoproterozoic ocean. *Geochim. Cosmochim. Acta* **270,** 201–217.

Wang, X., Planavsky, N. J., Hofmann, A., Saupe, E. E., De Corte, B. P., Philippot, P., LaLonde, S. V., Jemison, N. E., Zou, H., Ossa, F. O., Rybacki, K., Alfimova, N., Larson, M. J., Tsikos, H., Fralick, P. W., Johnson, T. M., Knuden, A. C., Reinhard, C. T. and Konhauser, K. O. (2018) A Mesoarchean shift in uranium isotope systematics. *Geochim. Cosmochim. Acta* **238,** 438–452.

Wang, X., Planavsky, N. J., Reinhard, C. T., Hein, J. R. and Johnson, T. M. (2016) A Cenozoic seawater redox record derived from $^{238}U/^{235}U$ in ferromanganese crusts. *Am. J. Sci.* **316,** 64–83.

Wang J. and Li Z.-X. (2003) History of Neoproterozoic rift basins in South China: implications for Rodinia breakup. *Precambrian Res.* **261,** 303–320.

Wasylenki, L. E., Rolfe, B. A., Weeks, C. L., Spiro, T. G. and Anbar, A. D. (2008) Experimental investigation of the effects of temperature and ionic strength on Mo isotope fractionation during adsorption to manganese oxides. *Geochim. Cosmochim. Acta* **72,** 5997–6005.

Webby, B. D., Paris, F., Droser, M. L. and Percival, I. G. (2004) *The Great Ordovician Biodiversification Event*: Columbia University Press, New York. 484 pp.

Wedepohl, K. H. (1971) Environmental influences on the chemical composition of shales and clays. *Phys. Chem. Earth* **8,** 307–333.

Wedepohl, K. H. (2004) The Composition of Earth's Upper Crust, Natural Cycles of Elements, Natural Resources. In E. Merian, M. Anke, M. Ihnat, & M. Stoeppler (eds.): *Elements and Their Compounds in the Environment, Second Edition*. pp. 2–16.

Wei, G. Y., Planavsky, N. J., Tarhan, L. G., Chen, X., Wei, W., Li, D. and Ling, H.-F. (2018) Marine redox fluctuation as a potential trigger for the Cambrian explosion. *Geology* **46,** 587–590.

Wei, G. Y., Planavsky, N. J., Tarhan, L. G., He, T., Wang, D., Shields, G. A., Wei, W. and Ling, H.-F. (2020) Highly dynamic marine redox state through the Cambrian explosion highlighted by authigenic $\delta^{238}U$ records. *Earth Planet. Sci. Lett.* **544,** 116361.

Wei, W. and Algeo, T. J. (2020) Elemental proxies for paleosalinity analysis of ancient shales and mudrocks. *Geochim. Cosmochim. Acta* **287,** 341–366.

Wei, W., Algeo, T. J., Lu, Y., Lu, Y., Liu, H., Zhang, S., Peng, L., Zhang, J. and Chen, L. (2018) Identifying marine incursions into the Paleogene Bohai Bay Basin lake system in northeastern China. *Int. J. Coal Geol.* **200,** 1–17.

Wen, H., Fan, H., Zhang, Y., Cloquet, C. and Carignan, J. (2015) Reconstruction of early Cambrian ocean chemistry from Mo isotopes. *Geochim. Cosmochim. Acta* **164,** 1–16.

Westrop, S. R. and Ludvigsen, R. (1987) Biogeographical control of trilobite mass extinction at an Upper Cambrian "biomere" boundary. *Paleobiology* **13,** 84–99.

Weyer, S., Anbar, A. D., Gerdes, A., Gordon, G. W., Algeo, T. J. and Boyle, E. A. (2008) Natural fractionation of $^{238}U/^{235}U$. *Geochim. Cosmochim. Acta* **72,** 345–359.

White, D. A., Elrick, M., Romaniello, S. and Zhang, F. (2018) Global seawater redox trends during the Late Devonian massextinction detected using U isotopes of marine limestones. *Earth Planet. Sci. Lett.* **503,** 58–67.

Willbold, M. and Elliott, T. (2017) Molybdenum isotope variations in magmatic rocks. *Chem. Geol.* **449,** 253–268.

Williams, D. A. (1991) Paleozoic Geology of the Ottawa-St. Lawrence Lowland, southern Ontario. *Ont. Geol. Surv.* Open File Report 5770, 5292p.

Wood, R. and Erwin, D. H. (2018) Innovation not recovery: dynamic redox promotes metazoan radiations. *Biol. Rev. Camb. Philos. Soc.* **93(2),** 863–873.

Wood, R., Liu, A. G., Bowyer, F., Wilby, P. R., Dunn, F. S., Kenchington, C. G., Cuthill, J. F. H., Mitchell, E. G. and Penny, A. (2019) Integrated records of environmental change and evolution challenge the Cambrian Explosion. *Nat. Ecol. Evol.* **3(4),** 528–538.

Wright, D. F. and Stigall, A. L. (2013) Geologic drivers of late ordovician faunal change in laurentia: investigating links between tectonics, speciation, and biotic invasions. *PLoS One* **8(7),** e68353.

Wu, R., Liu, J., Calner, M., Gong, F., Lehnert, O., Luan, X., Li, L. and Zhan, R. (2020) High-resolution carbon isotope stratigraphy of the Lower and Middle Ordovician succession of the Yangtze Platform, China: Implications for global correlation. *J. Geol. Soc.* **177,** 537–549.

Wu, R., Stouge, S., Li, Z. and Wang, Z. (2010) Lower and Middle Ordovician conodont diversity of the Yichang Region, Hubei Province, Central China. *Bull. Geosci.* **85,** 631–644.

Xiao, S. and Laflamme, M. (2009) On the eve of animal radiation: phylogeny, ecology and evolution of the Ediacara biota. *Trends Ecol. Evol.* **24(1),** 31–40.

Yang, C., Rooney, A. D., Condon, D. J., Li, X., Grazhdankin, D. V., Bowyer, F. T., Hu, C., Macdonald, F. A. and Zhu, M. (2021) The tempo of Ediacaran evolution. *Sci. Adv.* **7,** eabi9643.

Yang, S., Kendall, B., Lu, X., Zhang, F. and Zheng, W. (2017) Uranium isotope compositions of mid-Proterozoic black shales: Evidence for an episode of increased ocean oxygenation at 1.36 Ga and evaluation of the effect of post-depositional hydrothermal fluid flow. *Precambr. Res.* **298,** 187–201.

Ye, Y., Zhang, S., Wang, H., Wang, X., Tan, C., Li, M., Wu, C. and Canfield, D. E. (2021) Black shale Mo isotope record reveals dynamic ocean redox during the Mesoproterozoic Era. *Geochem. Perspect. Lett.* **18,** 16–21.

Yin, L., Li, J., Liu, J., Li, C., Sun, S., Liang, H. and Xu, J. (2017) Precise and accurate Re–Os isotope dating of organic-rich sedimentary rocks by thermal ionization mass

spectrometry with an improved H2O2-HNO3 digestion procedure. *Int. J. Mass Spectrom.* **421,** 263–270.

Young, S. A., Benayoun, E., Kozik, N. P., Hints, O., Martma, T., Bergström, S. M. and Owens J. D. (2020) Marine redox variability from Baltica during extinction events in the latest Ordovician–early Silurian. *Palaeogeogr. Palaeoclimatol. Palaeoecol.* **554,** 109792.

Young, S. A., Saltzman, M. R., Foland, K. A., Linder, J. S. and Kump, L. R. (2009) A major drop in seawater 87Sr/86Sr during the Middle Ordovician (Darriwilian): Links to volcanism and climate? *Geology* **37(10),** 951–954.

Zhang, S., Wang, X., Wang, H., Bjerrum, C. J., Hammarlund, E. U., Costa, M. M., Connelly, J. N., Zhang, B., Su, J. and Canfield, D. E. (2016) Sufficient oxygen for animal respiration 1,400 million years ago. *Proc. Natl. Acad. Sci. U.S.A.* **113,** 1731–1736.

Zhang, F., Algeo, T. J., Romaniello, S. J., Cui, Y., Zhao, L., Chen, Z.-Q. and Anbar, A. D. (2018a) Congruent Permian-Triassic $\delta^{238}U$ records at Panthalassic and Tethyan sites: Confirmation of global-oceanic anoxia and validation of the U-isotope paleoredox proxy. *Geology* **46(4),** 327–330.

Zhang, F., Lenton, T. M., del Rey, Á., Romaniello, S. J., Chen, X., Planavsky, N. J., Clarkson, M. O., Dahl, T. W., Lau, K. V., Wang, W., Li, Z., Zhao, M., Isson, T., Algeo, T. J. and Anbar, A. D. (2020a) Uranium isotopes in marine carbonates as a global ocean paleoredox proxy: A critical review. *Geochim. Cosmochim. Acta* **287,** 27–49.

Zhang, F., Romaniello, S. J., Algeo, T. J., Lau, K. V., Clapham, M. E., Richoz, S., Herrmann, A. D., Smith, H., Horacek, M. and Anbar, A. D. (2018b) Multiple episodes of extensive marine anoxia linked to global warming and continental weathering following the latest Permian mass extinction. *Sci. Adv.* **4,** e1602921.

Zhang, F., Shen, S.-Z., Cui, Y., Lenton, T. M., Dahl, T. W., Zhang, H., Zheng, Q., Wang, W., Krainer, K. and Anbar, A. D. (2020b) Two distinct episodes of marine anoxia during the Permian-Triassic crisis evidenced by uranium isotopes in marine dolostones. *Geochim. Cosmochim. Acta* **287,** 165–179.

Zhang, F., Xiao, S., Kendall, B., Romaniello, S. J., Cui, H., Meyer, M., Gilleaudeau, G. J., Kaufman, A. J. and Anbar, A. D. (2018c) Extensive marine anoxia during the terminal Ediacaran Period. *Sci. Adv.* **4,** eaan8983.

Zhang, F., Xiao, S., Romaniello, S. J., Hardisty, D., Li, C., Melezhik, V., Pokrovsky, B., Cheng, M., Shi, W., Lenton, T. M. and Anbar, A. D. (2019) Global marine redox changes drove the rise and fall of the Ediacara biota. *Geobiology* **17,** 594–610.

Zhang, J. M., Wang, H. F. and Li, G. X. (1999) Study on sequence stratigraphy and chemostratigraphy of the Upper Cambrian Fengshan Formation–Lower Ordovician Yehli Formation at Dayangcha (Jilin). *J. Stratigr.* **23,** 81–106.

Zhang, S., Tarrant, G. A., Barnes, C. R. and Jin, J. (2011) Upper Ordovician conodont biostratigraphy and the age of the Collingwood Member, southern Ontario. *Can. J. Earth Sci.* **48(11),** 1497–1522.

Zhang, T., Shen, Y., Zhan, R., Shen, S. and Chen, X. (2009) Large perturbations of the carbon and sulfur cycle associated with the Late Ordovician mass extinction in South China. *Geology* **37(4),** 299–302.

Zhao, M., Tarhan, L., Shull, D., Wang, X., Asael, D. and Planavsky, N. (2022) Covariation between molybdenum and uranium isotopes in reducing marine sediments. *Chem. Geol.* **603,** 120921.

Zhou, L., Algeo, T. J., Shen, J., Hu, Z., Gong, H., Xie, S., Huang, J. and Gao, S. (2015) Changes in marine productivity and redox conditions during the Late Ordovician Hirnantian glaciation. *Palaeogeogr. Palaeoclimatol. Palaeoecol.* **420,** 223–234.

Zhou, L., Wignall, P. B., Su, J., Feng, Q., Xie, S., Zhao, L. and Huang, J. (2012) U/Mo ratios and $\delta^{98/95}$Mo as local and global redox proxies during mass extinction events. *Chem. Geol.* **324-325,** 99–107.

Zou, C., Qiu, Z., Poulton, S. W., Dong, D., Wang, H., Chen, D., Lu, B., Shi, Z., and Tao, H. (2018) Ocean euxinia and climate change “double whammy” drove the Late Ordovician mass extinction. *Geology* **46,** 535–538.

Appendices

Appendix A. Supplementary materials for Chapter 2

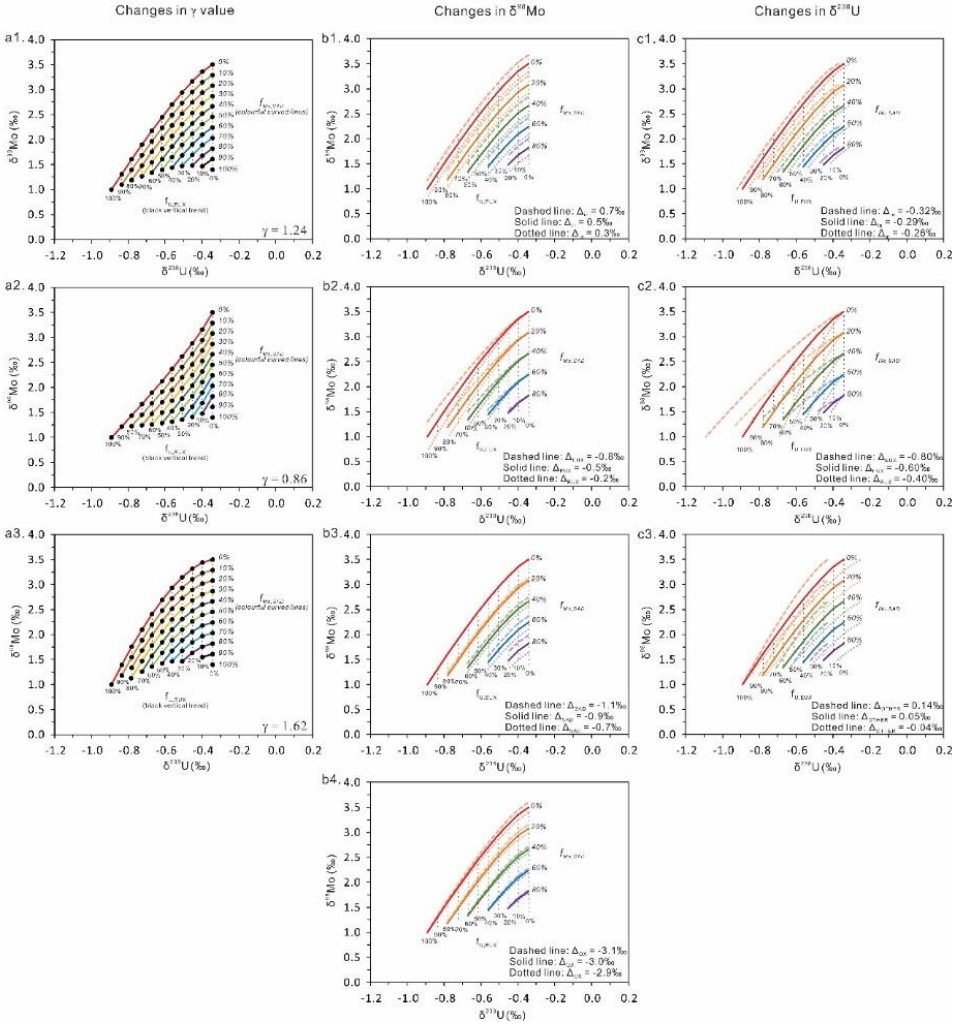

Figure A1. Sensitivity analysis of the coupled Mo-U isotope mass balance model. The left columns represent how the model changes with different γ values. The middle and right columns represent how the model solutions change with different Mo and U isotope compositions (of inputs and sinks) with γ = 1.24, respectively. The curved colorful lines in each figure of the middle and right columns are based on the a1 in the left column. Variations in $\delta^{238}U$ of inputs and sinks have a larger impact on the model solutions compared with variations in $\delta^{98}Mo$ of inputs and sinks.

A2. Geological Background

The 640 Ma Black River Dolomite

The Black River Dolomite was deposited on the Western Tasmania Terrane, which was a part of Antactica continental block during the Neoproterozoic (Direen and Crawford, 2003; Kendall et al., 2009). The depositional setting is a continental margin, and lithologies include dolostones, organic-rich sediments, and diamictite (Calver and Walter, 2000). The organic-rich mudrock interval is at the top of the Black River Dolomite, which has a depositional age of 640.7 ± 4.7 Ma based on Re-Os geochronology (Kendall et al., 2009). Iron speciation data suggest that bottom waters during deposition were anoxic ($Fe_{HR}/Fe_T > 0.79$) and sulfidic ($Fe_{py}/Fe_{HR} > 0.90$), which is also supported by elevated Mo concentrations (14-30 µg/g, Mo EF = 12-33) (Kendall et al., 2015). Molybdenum isotope compositions of the organic-rich shales are variable, ranging from 0.39‰ to 1.15‰ (Kendall et al., 2015).

The 520 Ma Yu'anshan Formation

The core samples of the Yu'anshan Formation are carbonaceous black shales with high TOC and pyrite contents (Dahl et al., 2010). The depositional environment was under debate: isolated from the open ocean (Hagadorn, 2002) vs well-connected to the open ocean (Babcock et al., 2001). Dahl et al. (2010) interpreted the environment to be a semi-restricted basin. The U-Pb dating of detrital zircons from Yu'anshan Shale provided a maximum age of 518.03 ± 0.69 Ma (2σ uncertainty), which is in an agreement with previous paleontological data suggesting a depositional age of 521-517 Ma (Babcock et al., 2001; Zhu et al., 2001; Yang et al., 2018). The Yu'anshan shales are suggested to contain ~2% TOC, Mo concentrations of 8-19 µg/g, and Mo isotope composition of 0.46-1.01‰ (Dahl et al., 2010). The euxinic bottom water conditions are based on iron speciation data (Fe_{HR}/Fe_T = 0.41-0.55, Fe_{py}/Fe_{HR} = 0.83-0.89; Dahl et al., 2010).

The 500 Ma and 485 Ma Alum Shale Formation

The Alum Shale Formation is suggested to be deposited in a shallow epicontinental sea in Baltica from the Middle Cambrian to the Early Ordovician (Schovsbo, 2003; Dahl et al., 2010). Shale samples are extremely enriched in TOC (up to 25%) and have high pyrite content (Schovsbo, 2003). Trilobites and brachiopods are the dominant fossils and are well preserved in the Cambrian Alum shale (Henningsmoen, 1957), whereas graptolites are more common in the Ordovician Alum shale (Tjernvik, 1958). Both Cambrian and Ordovician intervals were deposited under euxinic conditions based on Fe speciation data (Dahl et al., 2010). However, the Cambrian Alum shale (500 Ma) has slightly higher and more uniform Mo isotope compositions (δ^{98}Mo = 0.93-1.29‰) than the Ordovician Alum shale (485 Ma, δ^{98}Mo = 0.20-1.04‰) (Dahl et al., 2010).

The 465 Ma Almelund Shale

The Almelund Shale is carbonaceous dark shale deposited on a continental outer shelf of Baltica (or a foreland basin) during the Middle Ordovician (465-462 Ma), and has a TOC of ~2% (Bergström et al., 2002; Dahl et al., 2010). It contains abundant graptolite and some small brachiopods (Maletz, 1995). Iron speciation suggests euxinic bottom water conditions (Fe_{HR}/Fe_T = 0.36-0.90, Fe_{py}/Fe_{HR} = 0.71-0.73) during deposition. However, Mo concentrations and isotope compositions are only 4.4-5.4 μg/g and 0.58-0.85‰, respectively (Dahl et al., 2010).

The 442 Ma Rastrites Shale

The Rastrites Shale was deposited on the marginal area of Baltica at the Ordovician-Silurian boundary (Koren and Bjerreskov, 1997; Schovsbo, 2003; Dahl et al., 2010). These black shales contain up to 3% TOC and are enriched in graptolites (Koren and Bjerreskov, 1997; Schovsbo, 2003). The bottom water redox conditions during deposition were anoxic (Fe_{HR}/Fe_T = 0.42-0.52) and sulfidic (Fe_{py}/Fe_{HR} = 0.72-0.78) (Dahl et al., 2010). Molybdenum concentrations in the Rastrites Shale (5.6-226.9 μg/g) are higher than that of the Almelund Shale. The Mo isotope compositions range from 0.42‰ to 1.28‰ (Dahl et al., 2010).

The 442 Ma Birkhill Shale

The Birkhill Shale was deposited on a continental margin with minimal restrictions to the open ocean (Scotese and McKerrow, 1990). The depositional age is broadly coeval with the Rastrites Shale (Cocks, 1985; Dahl et al., 2010). The Fe speciation data suggest mostly anoxic bottom water conditions (Fe_{HR}/Fe_T = 0.32-0.91, Fe_{py}/Fe_{HR} = 0.37-0.73; Dahl et al., 2010). The Mo isotope compositions of the Birkhill Shale are between −0.21‰ and 1.44‰ (Dahl et al., 2010).

The 365 Ma New Albany Shale and Chattanooga Shale

The New Albany Shale was deposited in the intracratonic Illinois Basin, whereas the Chattanooga Shale was coevally deposited ~300 km south of the New Albany Shale (Dahl et al., 2010). The conodont biozones of the Chattanooga Shale suggest a depositional age of 359.2-374.5 Ma (Over et al., 2009). Samples were taken from outcrops without weathering surfaces. Iron speciation data and high Mo concentrations support a euxinic depositional environment (Fe_{HR}/Fe_T = 0.66-0.71, Fe_{py}/Fe_{HR} = 0.70-0.80; Mo > 200 μg/g) for both shale intervals (Dahl et al., 2010). The New Albany Shale and the Chattanooga Shale have Mo isotope compositions of 1.65-1.85‰ and 1.37-1.58‰, respectively (Dahl et al., 2010).

Compilations of coupled Mo and U isotope compositions from published euxinic ORM (the Zaonega Formation, the upper Velkerri Formation, the Doushantuo Formation Member IV, the Fjäcka Shale, the Tanezzuft Formation, the Kettle Point Formation) are listed in Table A1.

References

Babcock, L. E., Zhang, W., & Leslie, S. A. (2001). The Chengjiang biota: Record of the Early Cambrian diversification of life and clues to exceptional preservation of fossils. *GSA Today, 11*, 4-9.

Bergström, S. M., Larsson, K., Pålsson, C., & Ahlberg, P. (2002). The Almelund Shale, a replacement name for the Upper Didymograptus Shale and the Lower Dicellograptus Shale in the lithostratigraphical classification of the Ordovician succession in Scania, Southern Sweden. *Bulletin of the Geological Society of Denmark, 49*, 41-47.

Calver, C. R., & Walter, M. R. (2000). The late Neoproterozoic Grassy Group of King Island, Tasmania: correlation and palaeogeographic significanc. *Precambrian Research, 100*, 299-312.

Cocks, L. (1985) The Ordovician-Silurian boundary. *Episodes* 8(2), 98-100.

Dahl, T. W., Hammarlund, E. U., Anbar, A. D., Bond, D. P. G., Gill, B. C., Gordon, G. W., Knoll, A. H., Nielsen, A. T., Schovsbo, N. H., & Canfield, D. E. (2010). Devonian rise in atmospheric oxygen correlated to the radiations of terrestrial plants and large predatory fish. *Proceedings of the National Academy of Sciences, 107*(42), 17911-17915.

Direen, N. G., & Crawford, A. J. (2003). Fossil seaward-dipping reflector sequences preserved in southeastern Australia: a 600 Ma volcanic passive margin in eastern Gondwanaland. *Journal of the Geological Society, London, 160*, 985-990.

Hagadorn, J. W. (2002). *Chengjiang: early record of the Cambrian explosion*. Columbia University Press, pp 35-60.

Henningsmoen, G. (1957). The trilobite family Olenidae: With description of Norwegian material and remarks on the Olenid and Tremadocian Series. *Skrifter Utgitt av det Norske Videnskaps-Akademi I Oslo, I, Matematisk-naturvidenskapelig Klasse*, 1-303.

Kendall, B., Creaser, R. A., Calver, C. R., Raub, T. D., & Evans, D. A. D. (2009). Correlation of Sturtian diamictite successions in southern Australia and northwestern Tasmania by Re–Os black shale geochronology and the ambiguity of "Sturtian"-type diamictite–cap carbonate pairs as chronostratigraphic marker horizons. *Precambrian Research, 172*(3-4), 301-310.

Kendall, B., Komiya, T., Lyons, T. W., Bates, S. M., Gordon, G. W., Romaniello, S. J., Jiang, G., Creaser, R. A., Xiao, S., McFadden, K., Sawaki, Y., Tahata, M., Shu, D., Han, J.,

Li, Y., Chu, X., & Anbar, A. D. (2015). Uranium and molybdenum isotope evidence for an episode of widespread ocean oxygenation during the late Ediacaran Period. *Geochimica et Cosmochimica Acta, 156*, 173-193.

Koren, T., & Bjerreskov, M. (1997). Early Llandovery monograptids from Bornholm and the southern Urals: taxonomy and evolution. *Bulletin of the Geological Society of Denmark, 44*, 1-43.

Maletz, J. (1995). The Middle Ordovician (Llanvirn) graptolite succession of the Albjära core (Scania, Sweden) and its implication for a revised biozonation. *Zeitschrift für Geologische Wissenschaften, 23*, 249-259.

Over, D. J., Lazar, R., Baird, G. C., Schieber, J., & Ettensohn, F. R. (2009). Protosalvinia Dawson and Associated Conodonts of the Upper Trachytera Zone, Famennian, Upper Devonian, in the United States. (Translated from English) *Journal of Paleontology*, 83(1), 70-79.

Schovsbo, N. H. (2003). The geochemistry of Lower Palaeozoic sediments deposited on the margins of Baltica. *Bulletin of the Geological Society of Denmark, 50*, 11-27.

Scotese, C. R., & McKerrow, W. S. (1990). Revised World maps and introduction. In W. S. McKerrow & C. R. Scotese (Eds.), *Paleozoic Paleogeography and Biogeography* (Vol. 12, pp. 1-21): Geological Society London Memoirs.

Tjernvik, T. E. (1958). The Tremadocian Beds at Flagabro in South-Eastern Scania (Sweden). *Geologiska Föreningen i Stockholm Förhandlingar, 80*(3), 259-276.

Yang, C., Li, X.-H., Zhu, M., Condon, D. J., & Chen, J. (2018). Geochronological constraint on the Cambrian Chengjiang biota, South China. *Journal of the Geological Society, 175*(4), 659-666.

Zhu, M., Zhang, J., & Li, G. (2001). Sedimentary environments of the Early Cambrian Chengjiang Biota: Sedimentology of the Yu'anshan Formation in Chengjiang county, eastern Yunnan. *Acta Palaeontologica Sinica, 40 (Sup.)*, 80-105.

Table A1. Compilation of the published Mo and U isotope compositions from the same euxinic organic-rich mudrocks.

Sample	Age (Ma)	Fe_{HR}/Fe_T	Fe_{py}/Fe_{HR}	DOP[e]	TOC (wt.%)	Al (wt.%)	Mo (ppm)	Mo EF[a]	U (ppm)	U EF[a]	$\delta^{98}Mo$[b] (‰)	$\delta^{98}Mo_{auth}$[a] (‰)	2SD	n[d]	$\delta^{238}U$[c] (‰)	$\delta^{238}U_{auth}$[a] (‰)	2SD	n[d]
Kettle Point Formation, Southern Ontario, Canada (Late Devonian); Kendall et al. (2020)	372																	
Unit 4	372																	
KPZ-1	372				12.9	8.2	341.3	416.2	43.1	17.0	0.82	0.82	0.05	3	0.54	0.59	0.07	3
KPZ-2	372				12.5	7.7	438.0	568.8	49.6	20.8	0.98	0.98	0.02	3	0.40	0.44	0.02	3
KPZ-2-rpt	372														0.39		0.01	2
KPZ-3	372				15.6	7.0	450.9	644.1	57.9	26.7	0.95	0.95	0.03	3	0.46	0.49	0.04	3
KPZ-4	372				12.3	6.8	288.3	424.0	46.3	22.0	0.85	0.85	0.03	3	0.40	0.43	0.01	3
KPZ-4-rpt	372										0.90		0.03	3				
KPZ-5	372				10.0	7.7	231.6	300.8	41.1	17.2	0.95	0.95	0.03	3	0.37	0.41	0.1	3
KPZ-6	372				8.8	7.6	55.8	73.4	15.6	6.6	0.76	0.77	0.00	3	0.18	0.27	0.03	3
KPZ-7	372				11.0	6.6	159.8	242.1	31.0	15.2	0.71	0.71	0.04	3	0.53	0.59	0.06	3
KPW6	372				11.0	7.1	96.2	135.5	26.8	12.2	0.68	0.68	0.04	3	0.44	0.51	0.06	3
KPW4	372				8.8	7.2	225.3	312.9	35.6	15.9	0.76	0.76	0.03	3	0.39	0.44	0.04	3
KPW5	372				7.8	7.8	159.1	204.0	32.3	13.4	0.78	0.78	0.05	3	0.41	0.47	0.03	3
KPW5-rpt	372														0.37		0.26	2
KPW3	372				6.9	8.5	113.2	133.2	26.3	10.0	0.69	0.69	0.05	3	0.42	0.50	0.08	3
KPW2	372				4.9	8.7	67.6	77.7	17.5	6.5	0.71	0.72	0.05	3	0.32	0.43	0.07	3
KPW1	372				4.1	9.1	58.2	64.0	13.4	4.8	0.68	0.69	0.03	3	0.30	0.46	0.04	3
KPR2	372				6.4	8.0	97.4	121.8	18.7	7.5	0.55	0.55	0.04	3	0.34	0.44	0.14	3
KPR6	372				7.9	5.9	83.8	142.0	21.2	11.6	0.88	0.88	0.03	3	0.35	0.41	0.07	3
KPR8	372				8.2	6.8	106.1	156.0	24.8	11.8	0.77	0.77	0.03	3	0.34	0.40	0.11	3
KPR11	372				8.5	23.9	407.0	170.3	99.2	13.4	0.79	0.79	0.11	3	0.32	0.37	0.1	3
KPR14	372				7.3	7.0	98.3	140.4	25.9	11.9	0.86	0.86	0.01	3	0.20	0.25	0.06	3
KPR17	372				8.5	7.7	150.9	196.0	37.1	15.5	1.29	1.30	0.02	3	0.12	0.15	0.02	3
KPR-17-rpt	372										1.33		0.04	3				
KPP11	372				7.0	7.5	103.2	137.6	26.9	11.6	1.26	1.27	0.01	3	0.11	0.15	0.11	3
KPP8	372				6.1	8.9	109.5	123.0	25.4	9.2	1.31	1.32	0.03	3				
Unit 3	372																	
KPP4	372				6.4	7.5	88.2	117.6	25.1	10.8	1.06	1.07	0.07	3	0.20	0.25	0.04	3
KPP3	372				3.1	8.9	45.8	51.5	9.4	3.4	0.77	0.78	0.02	3	0.04	0.18	0.04	3
KP21	372				7.3	6.6	81.5	123.5			0.62	0.62	0.02	3				
KP20	372				5.8	7.7	71.4	92.7	18.5	7.8	1.10	1.11	0.06	3	0.03	0.08	0.06	3

Table A1. Continued.

	Sample	Age (Ma)	Fe_{HR}/Fe_T	Fe_{py}/Fe_{HR}	DOP[e]	TOC (wt.%)	Al (wt.%)	Mo (ppm)	Mo EF [a]	U (ppm)	U EF [a]	$\delta^{98}Mo$ [b] (‰)	$\delta^{98}Mo_{auth}$ [a] (‰)	2SD	n [d]	$\delta^{238}U$ [c] (‰)	$\delta^{238}U_{auth}$ [a] (‰)	2SD	n [d]
Unit 2		372																	
	KP18	372				4.5	7.5	62.8	83.7	19.1	8.2	1.17	1.18	0.03	3	-0.06	-0.03	0.08	3
	KP15	372				5.7	6.3	57.3	91.0	17.1	8.8	0.96	0.97	0.05	3	0.01	0.05	0.07	3
	KP10	372				7.7	5.7	115.1	201.9	22.8	12.9	1.60	1.61	0.05	3	-0.06	-0.04	0.05	3
	KP12	372				7.7	5.8	103.2	177.9	22.7	12.6	1.27	1.28	0.09	3	-0.07	-0.05	0.1	3
	KP9	372				5.0	5.1	67.0	131.4	16.0	10.1	1.69	1.70	0.08	3	-0.12	-0.10	0.04	3
	KP8	372				7.1	5.9	79.8	135.3	20.3	11.1	1.45	1.46	0.03	3	-0.14	-0.12	0.11	3
	KP7	372				5.5	4.4	62.4	141.8	14.1	10.3	1.57	1.58	0.07	3	-0.15	-0.13	0.04	3
	KP6	372				9.3	4.5	119.2	264.9	29.8	21.4	1.65	1.66	0.05	3	-0.24	-0.24	0.06	3
Unit 1		372																	
	KP5	372				9.9	5.9	126.6	214.6	26.9	14.7	1.27	1.27	0.02	3	-0.03	-0.01	0.03	2
	KP4	372				12.2	6.2	55.9	90.2	26.6	13.8	2.02	2.04	0.08	3	-0.29	-0.29	0.07	3
	KP3	372				8.2	6.7	127.8	190.7	27.5	13.2	1.22	1.22	0.05	3	-0.03	-0.01	0.08	3
	KP2	372				13.1	6.3	109.4	173.7	25.7	13.2	1.73	1.74	0.01	3	-0.11	-0.09	0.02	2
	KP11	372				7.2	6.9	105.8	153.3	20.5	9.6	2.02	2.03	0.06	3	-0.11	-0.09	0.04	3
	KP1	372				14.4	6.8	144.7	212.8	38.0	18.0	0.97	0.97	0.04	3	0.27	0.30	0.08	3
	KP1-rpt	372										0.99		0.07	3	0.27		0.05	3
Tanezzuft Shale Formation, the Murzuq Basin, Libya (Early Silurian); Stockey et al. (2020)																			
	E1-NC174 core																		
	R16A-01	444	0.62	0.82			9.3	25.5	27.5	16.1	5.6	0.52	0.53	0.06		-0.10	-0.06	0.06	
	R16A-02	444	0.48	0.80		5.0	8.5	29.0	34.3	11.8	4.5								
	R16A-03	444	0.50	0.80		5.4	8.9	38.5	43.3	13.3	4.8	0.80	0.81	0.04		-0.01	0.07	0.04	
	R16A-04	444	0.50	0.79		4.8	9.0	23.8	26.6	12.5	4.5								
	R16A-05	444	0.52	0.80			9.1	22.4	24.7	12.7	4.5								
	R16A-06	444	0.49	0.82		5.3	8.6	41.3	48.2	13.7	5.2								
	R16A-07	444	0.50	0.82			8.9	16.9	19.0	11.3	4.1	0.62	0.64	0.04		-0.13	-0.08	0.11	
	R16A-08	443	0.58	0.89		3.9	8.9	14.1	15.9	8.1	2.9								
	R16A-09	443	0.68	0.90			9.1	20.6	22.8	8.1	2.9	0.62	0.63	0.04		-0.16	-0.08	0.06	
	R16A-10	443	0.48	0.81		5.0	8.9	17.7	19.9	8.8	3.2								

Table A1. Continued.

Sample	Age (Ma)	Fe_{HR}/Fe_T	Fe_{py}/Fe_{HR}	DOP[e]	TOC (wt.%)	Al (wt.%)	Mo (ppm)	Mo EF[a]	U (ppm)	U EF[a]	$\delta^{98}Mo$[b] (‰)	$\delta^{98}Mo_{auth}$[a] (‰)	2SD	n[d]	$\delta^{238}U$[c] (‰)	$\delta^{238}U_{auth}$[a] (‰)	2SD	n[d]
R16A-11	443	0.45	0.81		5.1	9.1	19.9	21.8	10.2	3.6	0.56	0.57	0.06		-0.10	-0.03	0.04	
R16A-12	443	0.57	0.82			8.9	23.3	26.1	9.1	3.3								
R16A-13	443	0.71	0.87		6.0	8.8	24.1	27.4	12.4	4.5	0.66	0.67	0.06		-0.11	-0.06	0.03	
R16A-14	443	0.73	0.86			9.0	27.5	30.6	12.5	4.5								
R16A-15	443	0.68	0.87		5.3	8.5	28.2	33.1	12.4	4.7	0.73	0.74	0.06		-0.12	-0.08	0.05	
R16A-16	443	0.60	0.85			9.3	22.9	24.7	9.5	3.3								
R16A-17	443	0.64	0.84			9.2	38.4	42.0	18.8	6.6	0.74	0.75	0.06		0.00	0.06	0.04	
R16A-18	443	0.71	0.81		6.0	8.9	28.0	31.4	16.9	6.1								
R16A-19	443	0.63	0.78			9.1	31.9	35.1	13.8	4.9								
R16A-20	443	0.59	0.83			8.8	25.0	28.4	13.7	5.0	0.82	0.84	0.06		-0.05	0.01	0.04	
R16A-21	443	0.67	0.81		5.9	9.0	55.5	62.0	17.3	6.2	0.96	0.97	0.06		-0.19	-0.17	0.04	
R16A-22	443	0.65	0.80		6.7	8.4	60.5	72.0	16.0	6.1	0.55	0.55	0.06		-0.11	-0.07	0.05	
R16A-23	443	0.74	0.86		6.3	8.9	64.6	72.3	16.3	5.9								
R16A-24	443	0.71	0.85		8.6	8.8	81.8	93.4	19.6	7.2	0.47	0.47	0.06		-0.03	0.01	0.07	
R16A-25	443	0.70	0.83		6.4	8.4	31.7	37.8	14.5	5.6								
R16A-26	443	0.69	0.81			9.0	39.9	44.2	17.2	6.1	0.70	0.71	0.06		-0.04	0.01	0.07	
R16A-27	443	0.67	0.82		5.6	8.7	30.5	35.3	14.1	5.3								
R16A-28	443	0.59	0.87		5.1	9.3	41.5	44.8	14.9	5.2	0.55	0.56	0.04		-0.10	-0.06	0.04	
R16A-29	443	0.74	0.82			9.4	45.8	48.6	21.3	7.3								
R16A-30	442	0.76	0.89		6.5	9.6	23.3	24.3	19.7	6.6	0.48	0.49	0.04					
R16A-31	442	0.52	0.85			9.1	25.5	28.1	19.7	7.0								
R16A-32	442	0.73	0.84		6.4	9.0	36.2	40.1	17.5	6.3	0.69	0.70	0.06					
R16A-33	442	0.59	0.81		5.7	9.1	34.8	38.1	17.9	6.3								
R16A-34	442	0.75	0.89		9.2	9.0	48.4	53.9	32.0	11.5	0.51	0.51	0.06					
R16A-35	442	0.70	0.88		7.4	9.3	51.9	56.1	25.3	8.8	0.58	0.59	0.06					
R16A-36	442	0.76	0.84		10.5	8.5	98.2	115.3	35.9	13.6								
R16A-37	442	0.95	0.90		10.3	8.4	77.8	93.0	40.1	15.5	0.58	0.58	0.06		-0.06	-0.05	0.06	
R16A-38	442	0.84	0.90		9.4	8.9	58.2	65.7	35.2	12.8								
R16A-39	442	0.65	0.86			8.5	72.3	85.2	38.0	14.4	0.72	0.72	0.06		0.02	0.05	0.04	
R16A-40	442	0.65	0.87		11.4	8.4	81.5	97.0	53.9	20.7								
R16A-41	442	0.73	0.86			8.5	96.8	114.2	49.6	18.9	0.81	0.81	0.06		-0.01	0.01	0.04	
R16A-42	442	0.76	0.80		12.0	8.5	74.8	88.2	53.0	20.2								

Table A1. Continued.

Sample	Age (Ma)	Fe_{HR}/Fe_T	Fe_{py}/Fe_{HR}	DOP[e]	TOC (wt.%)	Al (wt.%)	Mo (ppm)	Mo EF [a]	U (ppm)	U EF [a]	$\delta^{98}Mo$ [b] (‰)	$\delta^{98}Mo_{auth}$ [a] (‰)	2SD	n [d]	$\delta^{238}U$ [c] (‰)	$\delta^{238}U_{auth}$ [a] (‰)	2SD	n [d]
R16A-43	442	0.60	0.85		14.0	8.2	93.2	113.7	59.2	23.3	0.67	0.67	0.04		0.00	0.01	0.05	
R16A-44	442	0.60	0.89		8.3	9.0	122.3	135.7	36.3	13.0								
R16A-45	442	0.72	0.85		9.0	8.8	96.4	109.7	49.3	18.1	0.80	0.80	0.06		-0.03	-0.02	0.04	
R16A-46	441	0.70	0.84		11.5	9.2	72.5	79.2	38.9	13.7								
R16A-47	441	0.71	0.83		9.3	8.8	74.5	84.9	35.6	13.1	0.74	0.75	0.06		-0.03	-0.01	0.06	
R16A-48	441	0.75	0.82			8.8	83.0	93.9	37.0	13.5								
R16A-49	441	0.65	0.84		10.2	9.0	61.5	68.2	32.9	11.8	0.71	0.72	0.06		-0.06	-0.03	0.05	
R16A-50	441	0.71	0.83		9.4	9.2	88.6	95.9	33.6	11.7								
R16A-51	441	0.84	0.87		9.6	8.9	114.0	127.7	35.9	13.0	0.89	0.89	0.06		-0.09	-0.08	0.06	
R16A-52	441	0.68	0.87			9.4	61.9	65.6	31.1	10.6	0.90	0.91	0.06		-0.19	-0.18	0.04	
R16A-53	441	0.66	0.80		4.8	10.9	26.4	24.2	20.3	6.0	0.68	0.70	0.04		-0.09	-0.04	0.04	
R16A-54	441	0.54	0.84		4.6	9.8	26.3	26.9	15.7	5.2								
R16A-55	441	0.70	0.81		4.9	10.1	60.5	60.0	17.8	5.7								
R16A-56	441	0.64	0.80		3.7	10.7	37.8	35.3	15.0	4.5	0.61	0.62	0.06		-0.06	0.01	0.05	
R16A-57	441	0.56	0.76		3.3	10.5	32.6	31.0	13.3	4.1								
R16A-58	441	0.61	0.64		2.8	10.4	28.7	27.5	9.8	3.0	0.70	0.72	0.04		-0.14	-0.07	0.05	
R16A-59	441	0.72	0.74		2.1	10.6	8.8	8.3	8.3	2.5								
Fjäcka Shale, Siljan disrict, central Sweden (Late Ordovician); Lu et al., (2017)	448																	
Solberga #1																		
135.01	448	0.57	0.89		4.3	5.4	89.2	166.8	12.6	7.6	0.81	0.81	0.03	3	-0.13	-0.10	0.07	3
135.01rpt1	448										0.78		0.08	3	-0.14		0.08	3
135.15	448	0.64	0.89		4.6	4.6	45.1	98.1	12.4	8.7	0.66	0.66	0.01	3	-0.15	-0.13	0.04	3
135.49	448	0.42	0.85		8.2	6.5	34.8	53.9	12.5	6.2	0.59	0.60	0.05	3	-0.20	-0.18	0.03	3
135.56	448	0.45	0.85		6.8	6.2	25.2	40.7	14.3	7.5	0.62	0.63	0.01	3	-0.24	-0.23	0.07	3
137.31	448	0.54	0.87		6.8	5.7	17.1	30.2	13.9	7.9	0.42	0.42	0.04	3	-0.15	-0.13	0.02	3
137.35	448	0.54	0.86		4.5	5.3	14.1	26.5	12.7	7.7	0.63	0.64	0.03	3	-0.21	-0.20	0.06	3

Table A1. Continued.

Sample	Age (Ma)	Fe_{HR}/Fe_T	Fe_{py}/Fe_{HR}	DOP[e]	TOC (wt.%)	Al (wt.%)	Mo (ppm)	Mo EF [a]	U (ppm)	U EF [a]	$\delta^{98}Mo$ [b] (‰)	$\delta^{98}Mo_{auth}$ [a] (‰)	2SD	n [d]	$\delta^{238}U$ [c] (‰)	$\delta^{238}U_{auth}$ [a] (‰)	2SD	n [d]
Stumsnäs #1																		
217.55	448	0.47	0.79		4.0	4.5	33.2	74.4	15.7	11.3	0.71	0.72	0.03	3	-0.17	-0.16	0.09	3
217.69	448	0.46	0.83		5.6	5.2	35.3	68.0	15.7	9.8	0.58	0.58	0.04	3	-0.16	-0.14	0.04	3
219.42	448	0.47	0.81		4.3	4.2	69.9	165.1	13.6	10.4	1.09	1.09	0.08	3	0.01	0.04	0.05	3
219.58	448	0.41	0.85		7.7	5.3	102.0	193.9	16.3	10.0	0.92	0.92	0.05	3	0.07	0.11	0.04	3
219.74	448	0.51	0.87		6.8	5.3	204.9	385.8	16.6	10.1	1.24	1.24	0.03	3	0.10	0.14	0.03	3
219.95	448	0.54	0.89		6.1	5.7	226.9	399.9	17.1	9.7	1.28	1.28	0.05	3	0.01	0.05	0.03	3
220.87	448	0.45	0.83		4.6	4.4	50.3	115.3	13.0	9.6	1.00	1.01	0.01	3	-0.06	-0.03	0.06	3
220.87rpt	448				4.6	4.3	50.3	116.4	13.1	9.8	1.28	1.29	0.07	3	-0.02	0.01	0.03	3
220.96	448	0.52	0.87		6.3	5.1	97.6	193.0	13.1	8.4	0.87	0.87	0.03	3	0.03	0.07	0.04	3
221.32	448	0.44	0.84		4.5	5.0	73.9	147.0	12.1	7.8	0.63	0.63	0.01	3	-0.06	-0.02	0.06	3
221.44	448	0.47	0.85		4.5	5.2	58.5	112.3	11.3	7.0	0.63	0.63	0.03	3	-0.08	-0.04	0.11	3
Doushantuo Formation (Member IV), Three Gorges region, China (late Ediacaran); Kendall et al. (2015)	555																	
Jiulongwan Section																		
group3																		
HND 41.4 - 154. 2 m	555	0.75	0.86			5.6	372.1	664.5	89.0	51.3	0.20	0.20	0.01	3	0.20	0.21	0.1	3
HN-23 - 154.0 m	555	0.70	0.83		3.9	5.3	180.7	340.9	97.0	59.0	1.01	1.01	0.08	3	-0.40	-0.40	0.09	3
group2																		
HND 41.0 - 153.8 m	555	0.87	0.90	0.9	6.0	3.5	134.0	382.9	18.0	16.6	1.40	1.40	0.1	5	0.27	0.31	0.02	3
HND 40.5 - 153.3 m	555				4.0	5.2	128.4	247.0	30.0	18.6	2.00	2.01	0.2	3	0.24	0.27	0.03	3
HND 40.5rpt - 153.3 m	555				4.9	5.5	125.4	228.0	29.0	17.0	1.99	2.00	0.06	3	0.24	0.27	0.06	3
HND 40.4 - 153.2 m	555				6.4	3.3	122.6	371.4	23.0	22.5	1.41	1.41	0.13	3	0.22	0.24	0.07	4
group 1																		
HND 40.2 - 153.0 m	555			0.9	5.0	5.2	165.0	317.3	20.0	12.4	0.39	0.39	0.07	5	0.22	0.27	0.04	3
HND 39.6 - 152.4 m	555	0.77	0.91	0.9	7.5	6.4	113.0	176.6	12.0	6.0	-0.42	-0.42	0.13	7	0.27	0.38	0.03	3
HND 39.2 - 152.0 m	555	0.84	0.93		7.6	5.8	118.9	205.0	23.0	12.8	0.10	0.10	0.18	8	0.18	0.22	0.05	3
HND 38.9 - 151.7 m	555	0.75	0.92	0.9	5.6	6.3	172.0	273.0	20.0	10.2	0.18	0.18	0.15	6	0.16	0.21	0.08	7
HND 38.2 - 151.0 m	555	0.79	0.92		5.6	5.7	96.4	169.0	10.0	5.7	0.11	0.11	0.14	7	0.26	0.38	0.04	3

Table A1. Continued.

Sample	Age (Ma)	Fe_{HR}/Fe_T	Fe_{py}/Fe_{HR}	DOP[e]	TOC (wt.%)	Al (wt.%)	Mo (ppm)	Mo EF [a]	U (ppm)	U EF [a]	$\delta^{98}Mo$ [b] (‰)	$\delta^{98}Mo_{auth}$ [a] (‰)	2SD	n [d]	$\delta^{238}U$ [c] (‰)	$\delta^{238}U_{auth}$ [a] (‰)	2SD	n [d]
HND 37.8 - 150.6 m	555	0.74	0.93	0.9	6.3	6.4	110.0	171.9	19.0	9.6	0.01	0.01	0.16	7	0.17	0.22	0.08	3
HND 36.85 - 150.0 m	555	0.79	0.92		6.8	5.5	190.6	346.5	19.0	11.1	-0.39	-0.39	0.13	7	0.36	0.43	0.09	3
HND 36.2 - 149.0 m	555	0.84	0.91	0.9	5.3	4.9	115.0	234.7	12.0	7.9	-0.30	-0.30	0.15	7	0.34	0.43	0.01	3
HND 35.0 - 147.8 m	555	0.82	0.95		4.5	6.2	101.6	163.9	25.0	13.0	-0.35	-0.35	0.13	8	0.35	0.40	0.04	4
HND 34.6 - 147.4 m	555			0.9	4.7	6.4	99.0	154.7	14.0	7.1	-0.37	-0.37	0.12	5	0.36	0.47	0.06	3
HND 33.8 - 146.6 m	555	0.77	0.93	0.9	1.6	6.1	60.0	98.4	20.0	10.6	-0.23	-0.24	0.12	5	0.37	0.44	0.09	3
HND 32.9 - 145.7 m	555	0.79	0.93		5.2	6.8	77.1	113.3	24.0	11.4	-0.09	-0.09	0.19	8	0.33	0.39	0.08	3
HND 30.9 - 143.7 m	555					6.3	66.3	105.3	20.0	10.2	0.01	0.01	0.19	6	0.34	0.41	0.06	3
HND 30.35 - 143.2 m	555				8.9	6.9	663.0	960.8	23.0	10.8	-0.47	-0.47	0.15	7	0.44	0.52	0.08	7
HND 29.5 - 142.3 m	555	0.68	0.93	0.9	1.3	6.7	385.0	574.6	29.0	14.0	-1.12	-1.12	0.13	7	0.50	0.56	0.1	3
HND 28.85 - 141.7 m	555			0.9	8.6	6.8	294.0	432.4	22.0	10.4	-1.27	-1.27	0.17	7	0.52	0.61	0.05	4
Three Gorges section																		
group 3																		
40, 4 of 12 - 212.35 m	555					1.8	48.0	266.8	27.0	48.4	0.61	0.61	0.08	3	-0.13	-0.13	0.07	4
40, 4 of 12-rpt - 212.35 m	555					1.9	48.2	253.6	27.0	45.8	0.69	0.69	0.06	3	-0.13	-0.13	0.09	3
group 2																		
S104012 - 211.72 m	555	0.92	0.87		4.4	3.1	104.0	335.4	19.0	19.8	1.12	1.12	0.07	4	0.15	0.17	0.07	3
S104103 - 211.38 m	555		0.82		3.6		25.1		5.0		1.28	1.28	0.21	7	0.18	0.18	0.1	4
S104106 - 211.03 m	555	1.00	0.74			1.2	27.4	228.2	8.0	21.5	1.33	1.33	0.14	5	0.06	0.08	0.07	4
41, 11 of 14 - 210.55 m	555	0.76	0.83			4.1	94.7	230.9	22.0	17.3	1.66	1.67	0.2	3	0.27	0.30	0.07	4
41, 13 of 14 - 210.44 m	555	0.83	0.82		3.0	5.2	127.4	245.0	33.0	20.5	1.62	1.63	0.17	3	0.06	0.08	0.07	3
group 1																		
S104206-A1 - 208.78 m	555	0.65	0.94		3.1	5.2	71.1	136.8	13.0	8.1	0.24	0.24	0.21	5	0.20	0.27	0.07	3
S104206-A2 - 208.75 m	555	0.81	0.94			5.2	145.1	279.0	14.0	8.7	0.14	0.14	0.13	4	0.25	0.32	0.07	3
42, 6 of 7, 1 - 208.49 m	555	0.82	0.93		2.9	4.9	102.3	208.8	13.0	8.6	0.09	0.09	0.09	3	0.30	0.38	0.1	5
42, 6 of 7, 6 - 208.29 m	555					4.4	260.5	592.1	15.0	11.0	0.00	0.00	0.18	3	0.15	0.20	0.14	7
S104301B - 207.95 m	555	0.66	0.94		3.2	6.2	164.0	264.6	13.0	6.8	-0.26	-0.26	0.16	5	0.24	0.33	0.07	4
S104304 - 207.46 m	555	0.86	0.96		2.7	6.6	58.2	88.2	16.0	7.8	0.21	0.21	0.18	5	0.20	0.27	0.07	3
43, 4 of 6, A-1 - 207.37 m	555					4.8	210.0	437.6	18.0	12.1	-0.50	-0.50	0.11	3	0.30	0.35	0.07	4
S104306 - 207.22 m	555	0.74	0.94			6.7	43.6	65.1	15.0	7.2	0.05	0.05	0.09	4	0.09	0.15	0.07	4
43, 6 of 6 - 207.20 m	555	1.00	0.97			5.9	125.0	211.8	18.0	9.8	-0.34	-0.34	0.11	3	0.23	0.29	0.07	4
S104401 - 207.12 m	555	0.94	0.93			6.1	73.1	119.8	17.0	9.0	-0.11	-0.11	0.17	5	0.21	0.27	0.07	4

Table A1. Continued.

Sample	Age (Ma)	Fe_{HR}/Fe_T	Fe_{py}/Fe_{HR}	DOP[e]	TOC (wt.%)	Al (wt.%)	Mo (ppm)	Mo EF [a]	U (ppm)	U EF [a]	$\delta^{98}Mo$ [b] (‰)	$\delta^{98}Mo_{auth}$ [a] (‰)	2SD	n [d]	$\delta^{238}U$ [c] (‰)	$\delta^{238}U_{auth}$ [a] (‰)	2SD	n [d]
S104402 - 206.95 m	555	0.73	0.94			6.6	93.6	141.8	19.0	9.3	-0.21	-0.21	0.13	4	0.28	0.35	0.1	3
44, 3 of 3 - 206.59 m	555					5.7	76.7	134.5	20.0	11.3	-0.35	-0.35	0.02	3	0.20	0.25	0.07	3
Upper Velkerri Formation, McArthur Basin, Australia (Middle Proterozoic); Kendall et al. (2009); Yang et al., (2017); Sheen et al., (2018)	1360																	
136.98-137.05	1360			0.92	6.9	3.1	112.0	361.3	12.7	13.2	1.05	1.05	0.14	5	0.03	0.06	0.08	3
136.98-137.05(rpt)	1360								14.3								0.03	3
137.19-137.26	1360			0.9	5.7	3.2	110.0	343.8	13.9	14.0	0.86	0.86	0.1	3	0.08	0.11	0.02	3
137.26-137.33	1360			0.92	5.3	2.9	106.0	365.5	14.8	16.5	0.98	0.98	0.06	4	0.10	0.13	0.07	3
137.46-137.52	1360			0.92	6.3	3.8	119.0	313.2	14.8	12.6	0.91	0.91	0.11	4	0.09	0.12	0.03	3
137.75-137.79	1360			0.91	5.7	3.3	105.0	318.2	14.7	14.4	0.98	0.98	0.15	4	0.12	0.15	0.08	3
137.84-137.89	1360			0.9	5.6	3.5	114.0	325.7	16.5	15.2	0.91	0.91	0.09	6	0.04	0.06	0.02	3
137.84-137.89(rpt)	1360								16.5						0.06	0.06	0.08	3
Zaonega Formation, Onega Basin, Russia (Paleoproterozoic); Asael et al. (2013)	2050																	
3109562	2050	0.63	0.60		11.7	5.4	8.1	15.1	4.0	2.4	1.14	1.20	0.09		-0.03	0.17	0.05	
3109566	2050	0.67	0.31		3.2	4.7	6.5	13.8	3.1	2.1	-0.35	-0.40	0.12		0.00	0.27	0.05	
3109640	2050	0.57	0.79		10.7	5.1	46.6	90.7	11.5	7.2	0.67	0.67	0.05		0.39	0.50	0.05	
3109576	2050	0.78	0.78		10.2	6.3	72.3	114.8	10.8	5.5	0.55	0.55	0.05		0.26	0.38	0.06	
3109578	2050	0.68	0.82		11.2	7.1	39.5	55.6	9.6	4.4	0.68	0.69	0.05		0.17	0.31	0.06	
3109580	2050	0.78	0.82		9.1	6.1	23.1	37.7	6.4	3.4	0.63	0.64	0.05		0.21	0.43	0.06	
3109582	2050	0.91	0.91		6.1	6.4	10.7	16.6	3.8	1.9	0.86	0.90	0.09		0.02		0.04	
3109594	2050	0.86	0.88		10.0	6.5	15.5	23.8	4.6	2.3	0.63	0.64	0.08		0.06	0.35	0.04	
3109596	2050	0.55	0.88		6.7	2.4	14.1	57.8	3.8	5.0	0.71	0.72	0.06		0.12	0.22	0.04	
3109598	2050	0.30	0.86		8.5	5.3	23.0	43.6	4.6	2.8	0.66	0.67	0.08		0.23	0.52	0.04	
3109600	2050	0.44	0.9		8.9	6.8	38.9	57.6	7.2	3.4	0.81	0.82	0.06		0.19	0.39	0.04	
3109602	2050	0.39	0.85		10.5	5.5	33.6	61.5	9.9	5.8	0.66	0.67	0.06		0.26	0.38	0.05	

Table A1. Continued.

Sample	Age (Ma)	Fe_{HR}/Fe_T	Fe_{py}/Fe_{HR}	DOP[e]	TOC (wt.%)	Al (wt.%)	Mo (ppm)	Mo EF [a]	U (ppm)	U EF [a]	$\delta^{98}Mo$ [b] (‰)	$\delta^{98}Mo_{auth}$ [a] (‰)	2SD	n [d]	$\delta^{238}U$ [c] (‰)	$\delta^{238}U_{auth}$ [a] (‰)	2SD	n [d]
3109604	2050	0.39	0.77		11.3	6.5	39.5	60.4	9.8	4.8	0.58	0.58	0.05		0.36	0.53	0.05	
3109606	2050				11.1	6.7	33.0	49.2	8.5	4.1	0.38	0.38	0.05		0.33	0.54	0.05	
3109608	2050				11.5	7.4	40.7	55.1	8.4	3.7	0.36	0.36	0.06		0.34	0.58	0.05	
3109612	2050				9.2	5.3	11.2	21.1	4.3	2.6	0.62	0.64	0.1		-0.02	0.15	0.05	
3109614	2050	0.91	0.96		12.1	6.2	12.0	19.3	4.0	2.1	0.66	0.68	0.06		0.08	0.43	0.05	
3109620	2050				7.9	6.0	12.0	20.1	3.3	1.8	0.77	0.79	0.06		0.00		0.05	
3109622	2050	0.91	0.91		4.4	6.0	7.7	12.7	2.8	1.5	1.31	1.40	0.11		-0.05		0.05	
3109628	2050				7.3	5.7	4.1	7.2	3.0	1.7	0.78	0.86	0.11		-0.18		0.05	
3109638	2050	0.43	0.54		4.7	2.4	7.2	29.9	1.1	1.5	0.57	0.58	0.13		-0.09		0.05	
3109658	2050				10.0	5.8	15.2	26.1	3.9	2.1	0.49	0.50	0.06		0.19	0.62	0.05	
3109668	2050	0.69	0.47		9.8	5.7	12.3	21.8	3.8	2.2	0.48	0.49	0.06		0.22	0.66	0.05	
3109674	2050				3.5	6.1	4.1	6.7	1.3	0.7	1.01	1.13	0.12		0.06		0.05	
3109676	2050				6.6	3.1	5.2	16.9	1.7	1.8	0.96	1.00	0.11		0.10		0.05	
3109688	2050	1.00	0.7		5.3	8.0	7.1	8.9	2.2	0.9	0.78	0.84	0.14		-0.05		0.05	
3109748	2050	0.57	0.51		3.2	1.5	2.0	13.7	0.8	1.7	0.96	1.01	0.16		-0.12		0.05	
3109706	2050	0.68	0.45		9.8	7.7	10.3	13.5	4.7	2.0	0.74	0.78	0.07		0.08	0.46	0.05	
3109708	2050	0.84	0.61		7.0	8.5	5.1	6.0	4.0	1.5	0.66	0.73	0.1		-0.01		0.05	
3109712	2050	0.27	0.46		2.0	2.4			0.5	0.6	0.42		0.48		-0.33		0.06	
3109722	2050	0.27	0.49		2.4	2.0			0.7	1.1	0.37		0.32		-0.33		0.06	
3109724	2050	0.21	0.51		1.4	3.8	1.7	4.4	1.7	1.4	0.89	1.06	0.18		-0.33		0.05	
3109726	2050	1.00	0.62		6.5	5.5	5.1	9.3	2.9	1.7	0.72	0.77	0.1		0.02		0.06	
3109732	2050				9.4	7.7	11.9	15.5	6.0	2.5	0.75	0.78	0.06		0.10	0.36	0.06	
3109736	2050				7.1	7.1	5.1	7.1	2.7	1.2	0.86	0.95	0.09		-0.06		0.06	
3109738	2050				8.7	6.3	6.5	10.3	3.2	1.6	0.70	0.74	0.1		-0.08		0.06	
3109740	2050	0.81	0.58		7.7	3.7	7.0	18.9	2.8	2.4	0.64	0.66	0.11		0.02	0.24	0.06	

Table A1. Continued.

Sample	Age (Ma)	Fe_{HR}/Fe_T	Fe_{py}/Fe_{HR}	DOP[e]	TOC (wt.%)	Al (wt.%)	Mo (ppm)	Mo EF[a]	U (ppm)	U EF[a]	$\delta^{98}Mo$[b] (‰)	$\delta^{98}Mo_{auth}$[a] (‰)	2SD	n[d]	$\delta^{238}U$[c] (‰)	$\delta^{238}U_{auth}$[a] (‰)	2SD	n[d]
3109744	2050	0.77	0.64		9.2	4.5	9.7	21.5	5.5	4.0	0.61	0.63	0.1		0.01	0.11	0.06	
3109746	2050				10.8	5.1	10.5	20.6	6.3	4.0	0.63	0.65	0.1		0.12	0.26	0.06	
3109752	2050	0.89	0.61		10.7	5.7	25.5	44.4	8.1	4.6	0.75	0.76	0.05		0.20	0.34	0.06	
3109758	2050				10.8	4.4	17.4	39.4	4.9	3.6	0.53	0.54	0.06		0.24	0.45	0.06	
3109760	2050	0.37	0.55		16.1	3.9	21.6	55.7	4.8	4.0	0.48	0.48	0.05		0.15	0.30	0.06	
3109764	2050				10.0	4.2	15.5	37.3	4.8	3.7	0.29	0.29	0.07		0.24	0.44	0.06	
3109778	2050	1.00	0.57		10.7	6.8	4.6	6.8	1.6	0.8	1.17	1.32	0.12		-0.12		0.06	

[a] See calculation methods in the main text

[b] Mo isotope data reported relative to NIST SRM 3134 = 0.25‰

[c] U isotope data reported relative to CRM 145

[d] Number of replicate analyses of the same sample solution

[e] Degree of pyritization

Samples with Mo EF < 2 or U EF < 2 are not calculated for the authigenic $\delta^{98}Mo$ or $\delta^{238}U$ values.

Note:

In the Kettle Point Formation, samples shaded in gray (upper unit 4) are potentially affected by particulate shuttle.

In the Tanezzurft Shale Formation, sample marked in blue is not used because the $Fe_{HR}/Fe_T > 0.38$ and $Fe_{py}/Fe_{HR} > 0.7$ are used as the cut-off values for euxinic depositional environment.

In the Fjäcka Shale, samples shaded in grey have high Mo and U isotope compositions.

In the Zaonega Formation, euxinic samples are shaded in grey based on Fe speciation data [$Fe_{HR}/Fe_T > 0.38$ and $(Fe_{pyrite} + Fe_{pyrrhotite}) /Fe_{HR} > 0.8$].

Appendix B. Supplementary materials for Chapter 3

Table B1. Elemental abundances of the Upper Ordovician samples from seven drill cores in the southern Ontario, Canada.

Dill core	Formation	Sample	Depth	S[a]	TOC[b]	TIC[c]	$CaCO_3$[d]	Na	Mg	Al	K	Ca	Ti	Cr	Mn	Fe	Sr	Mo	Ba	Th	U	Re
			m	%	%	%	%	%	%	%	%	%	%	μg/g	%	%	μg/g	μg/g	μg/g	μg/g	μg/g	ng/g
OGS 82-2	TB	C42	872.13	1.33	1.53	1.33	11.07	0.26	1.60	8.22	3.77	4.52	0.52	74.71	0.07	4.27	160.78	1.17	341.11	12.01	3.77	1.35
OGS 82-2	RR	C43	873.08	1.46	1.56	1.19	9.95	0.28	1.65	8.48	3.98	4.02	0.57	76.63	0.07	4.56	166.14	0.96	345.16	12.22	3.79	1.49
OGS 82-2	RR	C43r	873.08					0.27	1.60	8.33	3.90	4.07	0.55	77.10	0.07	4.49	158.22	0.98	340.12	11.65	3.72	1.39
OGS 82-2	RR	C39	875.71	1.49	1.38	0.91	7.62	0.28	1.52	8.33	4.00	3.25	0.53	76.56	0.06	4.35	162.36	0.96	366.32	11.94	3.63	1.66
OGS 82-2	RR	C40	876.07	1.45	1.42	1.20	10.03	0.27	1.55	8.22	3.89	4.52	0.53	75.53	0.07	4.30	170.18	1.15	334.99	11.98	3.67	1.30
OGS 82-2	RR	C41	876.84	1.44	1.59	1.39	11.60	0.29	1.56	8.30	3.83	4.97	0.53	75.10	0.07	4.28	181.64	1.08	345.27	12.05	3.79	1.50
OGS 82-2	RR	C35	877.30	1.33	1.74	1.27	10.57	0.28	1.51	8.30	3.86	4.93	0.54	74.41	0.06	4.27	181.12	1.21	355.36	12.12	3.81	1.61
OGS 82-2	RR	C36	877.95	1.33	1.77	1.48	12.31	0.28	1.44	7.80	3.68	5.73	0.52	70.10	0.06	3.98	196.43	1.22	331.08	11.73	3.68	1.38
OGS 82-2	RR	C37	878.56	1.38	1.72	1.23	10.24	0.28	1.31	7.43	3.57	4.56	0.51	67.58	0.05	3.76	172.37	1.19	316.73	11.26	3.58	1.43
OGS 82-2	RR	C38	879.26	1.26	2.25	1.46	12.19	0.31	1.88	7.63	3.66	4.49	0.52	68.97	0.08	4.09	157.65	1.56	352.62	11.72	3.98	1.93
OGS 82-2	RR	C31	879.82	0.76	3.01	3.44	28.63	0.21	3.85	5.35	2.70	9.31	0.37	49.93	0.16	4.62	180.99	1.13	268.30	8.22	2.86	1.49
OGS 82-2	RR	C32	880.47	1.44	1.91	1.02	8.52	0.31	1.37	7.95	3.88	4.03	0.53	73.23	0.05	3.78	171.08	1.17	349.47	12.45	4.08	1.53
OGS 82-2	RR	C33	880.71		2.15	1.09	9.07	0.29	1.34	7.70	3.71	4.30	0.52	71.25	0.05	3.73	169.50	1.25	337.78	11.92	3.93	1.51
OGS 82-2	RR	C34	881.62	1.22	2.05	1.39	11.55	0.31	1.42	7.64	3.71	5.16	0.52	69.12	0.06	3.79	180.87	1.54	334.16	11.67	4.09	1.82
OGS 82-2	RR	C27	882.07	0.93	2.03	1.16	9.66	0.29	1.38	8.02	3.98	4.24	0.51	73.84	0.05	3.77	165.86	1.37	355.40	11.99	4.10	1.81
OGS 82-2	RR	C28	882.73	1.17	2.22	0.57	4.76	0.32	1.36	8.32	4.13	2.94	0.55	76.48	0.04	3.87	147.35	1.74	371.54	12.79	4.30	1.93
OGS 82-2	RR	C29	883.20	1.07	2.21	1.22	10.13	0.31	1.96	7.78	3.90	3.54	0.53	70.46	0.07	3.99	155.05	1.68	365.01	12.24	4.12	1.59
OGS 82-2	RR	C29r	883.20					0.33	1.96	8.13	3.92	3.44	0.53	70.60	0.07	4.05	153.33	1.52	373.13	11.69	4.09	1.55
OGS 82-2	RR	C30	883.98	0.84	2.35	3.90	32.51	0.21	3.91	5.47	2.71	9.36	0.37	50.70	0.16	4.80	191.11	1.00	263.46	8.33	2.81	1.22
OGS 82-2	RR	C23	884.37	1.08	2.04	0.38	3.19	0.34	1.28	8.32	4.24	2.28	0.55	75.92	0.04	3.76	138.89	1.27	374.31	13.30	4.34	1.43
OGS 82-2	RR	C24	885.10	1.07	2.20	0.91	7.58	0.31	1.28	7.73	3.96	3.53	0.38	71.76	0.04	3.64	151.34	1.37	391.89	11.85	4.21	1.78
OGS 82-2	RR	C25	885.25	1.10	2.30	0.95	7.93	0.32	1.43	7.89	4.00	3.94	0.53	73.20	0.05	3.83	154.98	1.50	348.94	12.37	4.26	1.86
OGS 82-2	RR	C26	886.64	1.07	2.39	1.24	10.37	0.32	1.71	7.55	3.82	4.24	0.50	67.69	0.06	3.89	151.06	1.59	337.75	11.69	4.29	2.02
OGS 82-2	RR	C19	887.19	0.88	2.40	1.01	8.39	0.33	1.40	7.68	3.94	3.91	0.52	70.10	0.05	3.70	155.04	1.68	347.59	12.11	4.49	2.01
OGS 82-2	RR	C20	887.86	1.06	2.26	0.90	7.53	0.32	1.44	7.96	4.04	3.25	0.44	73.02	0.05	3.72	141.84	1.41	356.65	12.29	4.30	1.54
OGS 82-2	RR	C21	888.52	1.17	2.11	0.54	4.49	0.35	1.33	8.06	4.18	2.64	0.54	73.28	0.04	3.60	142.20	1.37	365.84	12.75	4.30	1.84
OGS 82-2	RR	C22	889.03	0.84	1.93	2.84	23.64	0.29	2.67	6.82	3.47	6.65	0.45	61.67	0.11	4.41	176.69	1.28	313.69	10.37	3.64	1.65

Table B1. Continued.

Dill core	Formation	Sample	Depth	S[a]	TOC[b]	TIC[c]	$CaCO_3$[d]	Na	Mg	Al	K	Ca	Ti	Cr	Mn	Fe	Sr	Mo	Ba	Th	U	Re
			m	%	%	%	%	%	%	%	%	%	%	µg/g	%	%	µg/g	µg/g	µg/g	µg/g	µg/g	ng/g
OGS 82-2	RR	C16	890.01	1.23	2.49	0.39	3.29	0.36	1.29	8.28	3.95	2.57	0.57	72.13	0.04	3.88	143.89	1.66	380.07	12.33	4.63	2.31
OGS 82-2	RR	C17	890.43	1.35	2.47	0.45	3.79	0.37	1.40	8.07	3.84	2.88	0.56	70.38	0.05	3.99	158.66	2.16	373.58	12.45	4.80	2.56
OGS 82-2	RR	C17r	890.43					0.38	1.39	8.04	3.95	2.72	0.51	68.55	0.05	3.83	149.68	2.01	368.37	11.86	4.76	2.53
OGS 82-2	RR	C18	891.23	0.91	2.47	0.66	5.52	0.33	1.46	8.31	3.93	2.99	0.57	76.24	0.05	3.90	147.80	1.53	363.45	12.36	4.54	1.84
OGS 82-2	RR	C12	891.93	1.41	2.22	0.56	4.67	0.33	1.35	8.43	4.01	2.90	0.54	73.83	0.04	4.16	150.47	1.69	366.78	12.51	4.63	1.86
OGS 82-2	RR	C11	892.00	0.96	2.25	2.19	18.28	0.29	2.33	7.51	3.53	5.55	0.50	65.16	0.09	4.30	151.97	1.64	325.92	10.78	4.06	1.61
OGS 82-2	RR	C13	893.32	1.07	2.63	0.67	5.61	0.33	1.35	8.30	3.89	3.33	0.54	73.47	0.04	3.88	156.92	1.68	363.71	12.16	4.77	1.90
OGS 82-2	RR	C14	893.81	0.68	2.39	3.97	33.07	0.22	3.55	5.76	2.77	9.72	0.38	51.62	0.16	4.80	165.88	0.96	258.08	7.87	3.23	1.76
OGS 82-2	RR	C7	894.51	1.03	2.57	0.99	8.27	0.36	1.38	8.15	3.95	3.71	0.52	72.18	0.05	3.75	165.20	1.83	363.71	11.37	4.87	2.61
OGS 82-2	RR	C8	894.69	1.28	1.94	1.68	14.01	0.33	1.30	7.44	3.72	5.60	0.48	63.11	0.05	3.76	195.41	1.84	305.30	10.93	4.20	2.26
OGS 82-2	RR	C9	895.84	1.23	2.45	0.43	3.54	0.34	1.31	8.39	3.96	2.24	0.56	73.36	0.04	3.86	137.71	2.40	390.72	12.83	4.85	2.11
OGS 82-2	RR	C10	896.15	0.44	1.05	7.18	59.82	0.18	5.50	4.49	2.12	13.89	0.29	39.44	0.20	5.55	305.74	0.84	203.77	5.97	2.18	0.98
OGS 82-2	RR	C3	896.89	1.45	2.30	0.77	6.39	0.34	1.31	8.26	3.92	3.11	0.50	69.30	0.04	4.02	155.48	2.42	362.05	12.32	4.90	3.04
OGS 82-2	RR	C4	897.42	1.22	2.56	1.32	10.97	0.30	1.29	7.55	3.57	4.90	0.47	64.20	0.05	3.70	177.54	2.49	335.58	11.09	5.05	3.48
OGS 82-2	RR	C5	898.15	1.04	2.14	1.03	8.60	0.28	1.33	7.96	3.72	3.63	0.52	68.19	0.04	3.62	157.87	2.03	357.90	11.89	4.79	2.41
OGS 82-2	RR	C6	898.50	1.28	2.01	0.76	6.30	0.28	1.32	8.05	3.77	2.93	0.53	69.84	0.04	3.86	141.68	2.14	344.69	12.07	4.61	2.07
OGS 82-2	RR	C2	898.92	1.21	2.36	0.18	1.47	0.31	1.35	8.89	4.41	1.37	0.56	78.10	0.04	3.95	129.23	2.46	346.45	13.14	5.53	2.46
OGS 82-2	RR	C1	899.40	1.03	3.19	0.71	5.94	0.30	1.30	8.33	3.87	3.22	0.56	72.32	0.04	3.77	149.58	2.40	414.08	12.33	5.83	2.87
OGS 82-2	RR	C1r	899.40					0.32	1.38	8.57	3.99	3.20	0.61	76.39	0.04	3.95	155.31	2.71	357.58	12.48	5.68	2.96
OGS 82-2	CF	C44	900.78	0.39	1.36	9.40	78.36	0.06	1.69	1.84	1.11	33.10	0.12	21.19	0.03	0.92	361.46	0.47	88.51	3.54	1.69	1.74
OGS 82-3	TB	PS1	822.14	1.33	1.03	0.74	6.17	0.44	1.54	8.46	3.63	2.27	0.53	80.90	0.07	4.56	139.88	1.37	321.32	12.50	3.75	1.30
OGS 82-3	RR	PS5	825.09	1.28	1.76	1.11	9.25	0.42	1.39	8.07	3.49	3.42	0.50	77.11	0.07	4.08	156.38	1.70	307.62	11.51	3.91	1.54
OGS 82-3	RR	PS4	825.26	1.30	1.25	0.97	8.08	0.43	1.39	8.09	3.42	3.00	0.53	75.79	0.07	4.23	146.13	1.37	317.11	12.47	3.84	1.29
OGS 82-3	RR	PS3	826.29	1.33	2.13	1.38	11.50	0.38	1.32	7.90	3.36	4.44	0.51	74.97	0.07	4.03	180.45	2.07	314.93	11.83	4.66	1.97
OGS 82-3	RR	PS2	826.53	1.40	2.22	1.36	11.33	0.40	1.31	7.91	3.41	4.34	0.52	75.74	0.06	4.09	174.32	2.51	315.55	11.98	5.09	2.06
OGS 82-3	RR	PS2r	826.53					0.44	1.27	7.77	3.39	4.42	0.56	75.82	0.07	4.37	175.89	2.35	322.20	13.32	5.26	2.27
OGS 82-3	RR	PS9	827.27	1.24	2.52	1.19	9.92	0.41	1.29	8.03	3.41	3.73	0.52	76.91	0.06	3.88	168.68	2.00	322.15	11.83	5.03	2.06
OGS 82-3	RR	PS8	828.12	0.85	2.21	4.34	36.17	0.33	3.21	6.02	2.59	8.21	0.39	58.37	0.16	4.75	188.25	1.59	260.60	8.55	4.01	1.71
OGS 82-3	RR	PS7	828.60	0.85	2.40	4.83	40.25	0.31	3.71	5.64	2.43	9.40	0.38	54.27	0.17	4.91	196.74	1.67	250.68	7.96	4.25	1.75
OGS 82-3	RR	PS6	829.18	1.38	2.35	0.94	7.83	0.45	1.36	8.16	3.51	2.90	0.54	78.33	0.05	3.90	141.71	2.30	349.71	12.13	4.48	2.12
OGS 82-3	RR	PS13	829.56	1.23	2.42	1.20	10.00	0.43	1.36	7.99	3.44	3.72	0.53	76.26	0.06	3.83	157.22	2.11	334.11	11.78	4.63	1.68

Table B1. Continued.

Dill core	Formation	Sample	Depth	S[a]	TOC[b]	TIC[c]	$CaCO_3$[d]	Na	Mg	Al	K	Ca	Ti	Cr	Mn	Fe	Sr	Mo	Ba	Th	U	Re
			m	%	%	%	%	%	%	%	%	%	%	µg/g	%	%	µg/g	µg/g	µg/g	µg/g	µg/g	ng/g
OGS 82-3	RR	PS12	830.34	1.26	2.48	1.13	9.42	0.45	1.34	8.39	3.59	3.61	0.54	78.64	0.05	3.88	158.77	2.39	352.43	11.92	4.63	2.02
OGS 82-3	RR	PS11	831.12	1.30	2.21	1.99	16.58	0.41	1.84	7.66	3.28	4.64	0.50	70.95	0.08	4.27	160.40	2.31	327.75	10.92	4.31	1.89
OGS 82-3	RR	PS10	831.45	1.15	2.29	3.31	27.58	0.37	2.56	6.68	2.90	6.82	0.45	63.48	0.11	4.56	177.94	2.29	298.03	9.64	4.17	2.14
OGS 82-3	RR	PS17	831.91	1.12	3.19	1.54	12.83	0.43	1.96	7.53	3.26	4.73	0.48	70.85	0.08	4.17	158.75	2.31	330.60	10.65	4.41	2.20
OGS 82-3	RR	PS16	832.54	1.60	3.40	0.67	5.58	0.48	1.27	7.93	3.44	2.82	0.49	75.65	0.05	3.97	142.83	3.41	387.13	11.18	5.04	2.70
OGS 82-3	RR	PS16r	832.54					0.49	1.26	7.98	3.62	2.80	0.51	77.46	0.05	3.92	145.88	3.49	376.15	11.21	5.03	3.09
OGS 82-3	RR	PS15	833.33	1.16	2.44	2.76	23.00	0.37	2.20	6.86	3.00	5.86	0.45	63.84	0.10	4.42	170.19	2.75	317.70	9.80	4.33	1.91
OGS 82-3	RR	PS14	833.81	1.53	2.88	1.08	9.00	0.46	1.39	8.07	3.46	2.78	0.54	75.96	0.05	3.95	138.67	3.30	354.65	11.82	5.48	2.22
OGS 82-3	RR	PS20	834.98	1.02	2.08	5.35	44.58	0.29	3.63	5.10	2.30	10.02	0.33	47.28	0.16	5.15	212.24	2.48	242.72	6.99	3.67	2.10
OGS 82-3	RR	PS25	835.57	1.56	3.96	0.95	7.92	0.45	1.25	7.96	3.42	2.69	0.52	73.63	0.05	3.73	137.19	6.28	400.26	11.50	7.83	3.55
OGS 82-3	RR	PS25r	835.57					0.47	1.22	8.13	3.67	2.79	0.49	75.26	0.05	3.93	142.06	5.64	399.43	10.95	7.75	
OGS 82-3	RR	PS19	835.74	1.52	3.76	0.75	6.25	0.29	0.82	5.61	2.68	1.55	0.34	47.90	0.03	2.48	85.92	4.10	267.37	7.88	4.83	2.50
OGS 82-3	RR	PS18	836.48	1.50	3.98	0.60	5.00	0.44	1.25	7.67	3.26	2.98	0.51	71.52	0.05	3.74	137.92	5.70	314.45	11.19	6.68	3.39
OGS 82-3	RR	PS22	836.81	1.61	4.37	0.40	3.33	0.44	1.18	8.00	3.42	2.35	0.50	74.55	0.05	3.78	129.33	7.05	353.57	11.06	7.17	3.86
OGS 82-3	RR	PS24	837.34	1.63	3.66	1.56	13.00	0.44	1.57	7.38	3.28	3.90	0.49	68.76	0.07	4.06	147.44	6.27	335.95	10.49	6.76	3.46
OGS 82-3	RR	PS23	838.39	1.74	3.48	1.56	13.00	0.41	1.66	7.60	3.29	3.63	0.49	69.84	0.07	4.21	139.03	8.19	345.20	10.84	6.65	3.66
OGS 82-3	RR	PS23r	838.39					0.44	1.77	7.89	3.34	3.67	0.51	69.28	0.07	4.28	144.34	8.19	330.03	10.47	6.60	
OGS 82-3	RR	PS29	839.53	1.74	3.90	0.49	4.12	0.42	1.21	8.18	3.47	2.53	0.49	76.23	0.05	3.82	135.94	5.08	329.47	10.98	5.94	2.91
OGS 82-3	RR	PS28	840.13	1.46	3.49	1.19	9.92	0.42	1.26	8.03	3.42	3.56	0.51	74.98	0.05	3.90	158.93	5.64	329.72	11.07	6.10	3.04
OGS 82-3	RR	PS27	840.92	1.47	4.11	1.18	9.83	0.45	1.22	7.90	3.40	3.17	0.48	73.79	0.05	3.70	146.74	5.93	333.92	10.73	6.47	3.78
OGS 82-3	RR	PS27r	840.92					0.45	1.22	7.86	3.32	3.20	0.51	73.48	0.05	3.73	149.67	6.20	316.47	9.23	6.52	3.92
OGS 82-3	RR	PS26	841.19	1.76	3.85	1.01	8.42	0.44	1.26	7.79	3.35	2.89	0.50	72.78	0.05	3.93	138.53	6.62	335.08	10.63	5.97	3.66
OGS 82-3	RR	PS33	841.53	1.39	3.45	3.38	28.14	0.34	2.36	6.73	2.88	6.84	0.43	62.31	0.12	4.69	174.21	4.41	277.56	9.01	4.72	2.29
OGS 82-3	RR	PS32	842.49	1.65	4.17	1.24	10.33	0.40	1.38	7.81	3.37	3.75	0.49	71.36	0.06	3.90	157.57	5.75	324.44	10.84	6.42	3.84
OGS 82-3	RR	PS31	843.00	1.63	4.86	0.71	5.95	0.41	1.40	7.57	3.25	4.11	0.49	70.80	0.07	3.92	162.38	5.04	311.87	10.43	5.79	3.11
OGS 82-3	RR	PS30	843.60	1.74	4.78	0.89	7.43	0.41	1.20	7.90	3.36	3.38	0.50	73.37	0.05	3.77	154.58	6.53	318.54	10.94	7.20	3.72
OGS 82-3	RR	PS30r	843.60					0.45	1.26	8.16	3.47	3.54	0.52	75.53	0.05	4.02	158.58	7.03	324.93	9.20	7.02	
OGS 82-3	RR	PS37	844.53	1.62	3.59	0.80	6.67	0.44	1.28	8.43	3.57	3.14	0.51	74.98	0.05	3.93	153.10	4.93	331.35	11.31	6.11	2.77
OGS 82-3	RR	PS36	844.82	2.13	3.82	0.89	7.39	0.40	1.19	7.68	3.52	3.22	0.47	64.72	0.05	3.73	153.54	5.45	354.69	11.30	6.21	3.86
OGS 82-3	RR	PS35	845.30	2.19	4.36	0.77	6.41	0.46	1.18	7.69	3.25	3.28	0.52	71.16	0.05	4.03	166.91	5.90	363.05	11.00	6.61	4.03
OGS 82-3	RR	PS34	846.24	1.60	4.00	1.01	8.41	0.38	1.31	7.57	3.52	3.19	0.46	64.93	0.05	3.49	141.06	4.60	354.91	11.17	6.65	2.73

Table B1. Continued.

Dill core	Formation	Sample	Depth	S[a]	TOC[b]	TIC[c]	$CaCO_3$[d]	Na	Mg	Al	K	Ca	Ti	Cr	Mn	Fe	Sr	Mo	Ba	Th	U	Re
			m	%	%	%	%	%	%	%	%	%	%	µg/g	%	%	µg/g	µg/g	µg/g	µg/g	µg/g	ng/g
OGS 82-3	RR	PS41	846.63	1.13	4.07	0.99	8.21	0.43	1.27	7.87	3.36	3.54	0.49	71.77	0.05	3.70	153.29	5.20	321.47	10.51	6.62	3.24
OGS 82-3	RR	PS40	847.45	1.27	4.45	1.49	12.45	0.40	1.14	7.15	3.04	4.70	0.47	66.12	0.05	3.50	190.06	5.93	301.31	10.57	7.61	3.99
OGS 82-3	RR	PS40r	847.45					0.40	1.07	7.06	3.15	4.74	0.44	67.74	0.05	3.46	184.70	5.84	328.85	10.16	7.47	
OGS 82-3	RR	PS39	847.67	1.58	3.68	1.14	9.49	0.37	1.12	7.33	3.28	3.86	0.46	62.42	0.04	3.56	171.65	5.88	327.27	10.96	6.75	3.12
OGS 82-3	RR	PS38	848.64	1.30	4.26	1.77	14.74	0.38	1.14	7.10	3.00	6.04	0.48	66.07	0.05	3.57	216.80	5.51	290.52	10.44	7.46	4.12
OGS 82-3	RR	PS45	849.32	1.34	4.15	1.40	11.69	0.39	1.15	7.29	3.08	4.87	0.46	62.71	0.05	3.46	183.90	5.47	321.52	10.54	7.58	4.25
OGS 82-3	RR	PS44	849.69	1.13	4.47	1.72	14.34	0.42	1.22	7.39	3.14	5.83	0.50	68.03	0.05	3.58	212.85	5.63	305.52	10.42	7.75	4.22
OGS 82-3	RR	PS44r	849.69					0.40	1.07	6.92	3.23	5.50	0.42	63.88	0.05	3.36	203.59	4.97	310.14	9.83	7.22	
OGS 82-3	RR	PS43	850.50	1.33	3.74	1.46	12.17	0.41	1.19	7.34	3.09	5.33	0.48	66.32	0.05	3.69	196.35	4.87	302.60	10.03	6.40	2.89
OGS 82-3	RR	PS42	851.17	1.23	3.03	1.23	10.29	0.40	1.21	7.86	3.31	4.03	0.49	71.25	0.05	3.72	175.37	4.08	343.25	10.80	5.96	2.59
OGS 82-3	RR	PS48	852.01	1.18	3.48	1.28	10.63	0.38	1.15	7.28	3.12	4.21	0.46	63.26	0.04	3.44	170.07	4.48	331.33	10.90	6.40	3.12
OGS 82-3	RR	PS47	852.60	1.68	3.99	1.57	13.05	0.41	1.19	7.27	3.09	5.10	0.35	66.53	0.05	3.95	197.62	6.43	399.62	10.50	7.43	3.95
OGS 82-3	RR	PS49	853.00	1.22	3.80	1.38	11.46	0.42	1.18	7.31	3.20	5.08	0.47	67.57	0.05	3.58	195.85	5.14	307.61	10.40	7.35	3.80
OGS 82-3	RR	PS49r	853.00					0.45	1.17	7.64	3.37	5.13	0.44	70.62	0.05	3.73	196.87	4.89	332.50	10.27	7.04	
OGS 82-3	RR	PS46	853.46	1.52	3.81	1.36	11.34	0.43	1.24	7.68	3.28	5.16	0.51	69.52	0.05	4.04	191.45	6.09	305.74	10.68	7.24	3.73
OGS 82-3	RR	PS53	854.04	2.34	3.89	1.35	11.24	0.40	1.14	7.11	3.00	4.72	0.46	61.77	0.04	4.16	195.90	8.46	201.75	10.87	7.75	7.50
OGS 82-3	RR	PS52	854.26	1.42	3.08	1.36	11.33	0.44	1.29	8.03	3.48	4.56	0.53	72.16	0.05	3.98	189.59	4.43	315.39	11.15	6.37	3.51
OGS 82-3	RR	PS51	854.74	3.93	2.73	0.88	7.36	0.44	1.28	7.90	3.29	7.29	0.49	72.79	0.05	5.90	276.07	10.82	133.93	11.08	6.01	7.31
OGS 82-3	RR	PS50	855.63	6.41	2.11	5.55	46.22	0.25	4.33	4.60	1.69	21.44	0.21	44.96	0.18	11.36	544.64	11.92	93.95	5.61	3.73	15.87
OGS 82-3	RR	PS57	856.26	2.03	2.38	1.00	8.37	0.46	1.37	8.40	3.63	5.55	0.54	77.77	0.05	4.33	229.96	2.45	353.43	12.26	5.24	4.20
OGS 82-3	RR	PS56	857.01	1.09	1.00	0.88	7.36	0.45	1.42	8.05	3.44	3.99	0.52	69.88	0.05	3.54	160.40	1.55	347.76	12.01	3.81	1.66
OGS 82-3	RR	PS55	857.81	1.67	2.51	2.34	19.48	0.39	1.32	7.77	3.36	9.65	0.49	72.24	0.06	4.04	308.11	1.42	294.92	10.67	4.10	3.72
OGS 82-3	RR	PS54	858.28	2.84	2.56	1.25	10.42	0.42	1.27	7.71	3.24	5.09	0.48	67.94	0.05	4.68	216.78	4.21	337.64	11.49	5.79	5.19
OGS 83-3	TB	P19	25.99	1.62	2.97	1.05	8.72	0.44	1.48	8.41	3.28	3.65	0.38	75.60	0.07	4.65	196.60	3.17	355.00	11.21	6.11	4.20
OGS 83-3	TB	P20	26.22	1.60	3.07	0.92	7.71	0.46	1.55	8.86	3.46	3.77	0.43	80.41	0.08	4.77	197.97	4.09	362.60	11.40	6.37	4.16
OGS 83-3	TB	P21	27.01	1.82	1.51	0.65	5.42	0.52	1.76	9.40	3.58	2.16	0.54	84.13	0.08	5.28	171.73	4.33	340.97	12.32	5.40	2.45
OGS 83-3	TB	P22	27.91	2.00	0.49	0.29	2.41	0.50	1.87	10.17	3.98	1.03	0.59	89.44	0.09	5.79	153.09	1.12	371.13	14.06	4.88	0.54
OGS 83-3	TB	P23	29.38	0.41	0.53	0.59	4.91	0.66	1.83	9.89	3.75	1.81	0.59	84.21	0.09	4.62	152.24	1.74	352.22	13.20	4.71	0.61
OGS 83-3	TB	P24	30.41	1.40	2.48	0.76	6.30	0.51	1.57	8.84	3.47	2.86	0.52	81.12	0.07	4.66	175.41	4.99	381.62	12.39	7.77	4.31
OGS 83-3	TB	P24r	30.41					0.53	1.66	9.29	3.56	2.85	0.58	84.35	0.07	5.04	182.84	4.81	374.18	12.52	7.83	
OGS 83-3	RR	P25	31.27	6.15	0.41	0.50	4.14	0.51	1.58	8.94	3.56	1.68	0.49	80.37	0.09	7.79	148.32	7.24	289.81	12.09	4.02	0.55

Table B1. Continued.

Dill core	Formation	Sample	Depth	S[a]	TOC[b]	TIC[c]	$CaCO_3$[d]	Na	Mg	Al	K	Ca	Ti	Cr	Mn	Fe	Sr	Mo	Ba	Th	U	Re
			m	%	%	%	%	%	%	%	%	%	%	µg/g	%	%	µg/g	µg/g	µg/g	µg/g	µg/g	ng/g
OGS 83-3	RR	P26	31.86	1.74	2.59	1.27	10.57	0.48	1.56	8.59	3.31	4.49	0.52	78.62	0.08	4.85	235.23	4.98	354.67	11.05	5.87	3.79
OGS 83-3	RR	P27	32.23	1.66	0.59	0.44	3.66	0.62	1.79	9.56	3.63	1.40	0.59	85.90	0.08	5.52	134.35	1.67	354.46	12.75	4.99	0.64
OGS 83-3	RR	P28	33.46	0.23	0.41	1.02	8.48	0.57	1.90	9.03	3.44	2.67	0.40	81.44	0.11	4.47	158.49	0.44	337.97	12.49	3.74	0.43
OGS 83-3	RR	P13	33.73	1.60	0.47	0.34	2.85	0.58	1.71	9.41	3.62	1.16	0.56	85.27	0.08	5.32	132.45	1.09	347.17	13.21	4.28	0.56
OGS 83-3	RR	P14	34.40	2.92	0.46	0.44	3.64	0.54	1.72	9.08	3.46	1.35	0.52	81.57	0.09	6.06	138.15	1.25	337.18	12.91	4.36	0.62
OGS 83-3	RR	P15	35.13	2.35	0.52	0.33	2.76	0.59	1.69	8.90	3.46	1.09	0.54	81.43	0.07	5.55	125.89	1.60	346.11	12.59	4.55	0.72
OGS 83-3	RR	P16	36.47	3.86	0.70	0.46	3.86	0.66	1.75	8.84	3.39	1.59	0.51	80.03	0.09	6.58	147.36	4.46	337.72	12.54	4.72	1.13
OGS 83-3	RR	P16r	36.47					0.66	1.64	8.67	3.37	1.47	0.48	77.68	0.08	6.22	137.64	4.25	382.75	12.32	4.58	1.25
OGS 83-3	RR	P17	36.84	0.43	0.58	0.52	4.34	0.69	1.77	9.07	3.52	1.64	0.55	82.04	0.09	4.45	146.87	1.45	343.68	12.90	4.31	0.66
OGS 83-3	RR	P18	38.10	2.11	0.49	0.43	3.58	0.60	1.80	9.52	3.75	1.28	0.56	85.03	0.09	5.56	141.13	1.41	321.02	12.88	4.69	0.60
OGS 83-3	RR	P7	38.70	0.27	0.46	0.95	7.94	0.56	1.98	9.10	3.60	2.43	0.53	82.13	0.11	4.42	140.19	1.09	327.63	12.68	4.41	0.65
OGS 83-3	RR	P8	39.03	0.31	0.54	0.60	5.00	0.60	1.74	9.17	3.70	1.87	0.53	82.35	0.09	4.19	153.02	1.13	341.44	12.50	4.51	0.68
OGS 83-3	RR	P9	40.02	0.37	0.54	0.52	4.35	0.63	1.77	8.95	3.51	1.52	0.55	81.39	0.09	4.29	142.74	1.21	319.57	13.22	4.10	0.68
OGS 83-3	RR	P10	40.96	0.37	0.57	0.49	4.12	0.61	1.77	9.03	3.58	1.29	0.54	82.12	0.08	4.26	140.20	1.25	317.54	12.99	4.06	0.75
OGS 83-3	RR	P11	41.45	0.37	1.30	1.61	13.40	0.61	1.86	9.45	3.65	1.34	0.57	85.38	0.08	4.43	136.85	0.82	329.17	13.40	4.12	0.70
OGS 83-3	RR	P12	42.54	2.53	2.13	0.18	1.48	0.61	1.74	9.42	3.60	1.04	0.57	83.96	0.08	5.63	126.54	4.42	336.93	12.66	5.27	1.25
OGS 83-3	RR	P12r	42.54					0.61	1.77	9.40	3.55	1.00	0.60	86.46	0.08	5.88	127.99	4.46	346.80	12.59	5.31	
OGS 83-3	RR	P1	43.34	2.76	2.00	0.11	0.95	0.58	1.62	8.86	3.49	1.07	0.50	78.92	0.07	5.22	114.25	4.94	297.24	12.32	6.88	1.16
OGS 83-3	RR	P1r	43.34					0.61	1.56	8.87	3.63	1.05	0.50	80.25	0.06	5.25	109.88	4.37	313.41	12.13	6.67	1.18
OGS 83-3	CM	P2	44.49	3.78	4.62	4.67	38.88	0.33	3.02	5.27	2.05	12.60	0.32	58.21	0.13	5.63	417.37	8.59	214.66	7.27	5.53	14.18
OGS 83-3	CM	P3	45.29	1.58	4.81	5.21	43.38	0.33	1.08	5.00	2.00	16.56	0.31	58.49	0.06	2.79	589.27	1.99	218.91	7.02	4.07	8.23
OGS 83-3	CM	P4	45.78	3.46	5.44	4.73	39.42	0.33	1.01	4.68	1.90	16.05	0.28	57.92	0.05	4.02	563.85	8.81	184.00	6.98	6.45	13.98
OGS 83-3	CM	P4r	45.78					0.33	0.98	4.63	1.86	15.38	0.28	55.46	0.05	3.77	561.61	7.87	190.63	6.96	6.51	12.85
OGS 83-3	CM	P5	46.24	1.59	4.50	6.41	53.45	0.29	1.07	4.09	1.66	20.32	0.24	50.38	0.05	2.48	763.87	3.62	143.27	6.08	4.53	11.70
OGS 83-3	CM	P6	46.24	0.96	4.29	5.92	49.36	0.32	1.24	4.52	1.80	19.15	0.30	54.25	0.04	2.25	804.41	3.07	177.25	6.71	3.94	11.86
OGS 83-5	CM	LC1	105.73	1.34	3.59	2.54	21.17	0.12	2.47	5.68	3.09	4.20	0.35	56.61	0.06	3.19	136.72	3.73	216.37	7.92	4.19	8.51
OGS 83-5	CM	LC2	106.26	1.35	2.86	5.56	46.33	0.10	5.34	4.72	2.56	11.19	0.28	48.71	0.11	4.12	214.13	3.62	208.53	6.83	3.87	8.00
OGS 83-5	CM	LC3	106.81	1.36	4.66	5.34	44.50	0.10	5.18	4.75	2.71	10.93	0.28	53.46	0.11	3.71	197.22	3.65	173.98	6.67	4.31	10.42
OGS 83-5	CM	LC4	107.34	1.93	5.95	5.19	43.25	0.08	4.67	3.82	2.23	11.01	0.25	50.47	0.07	3.56	289.45	4.62	147.12	6.06	4.89	8.08
OGS 83-5	CM	LC5	107.73	1.64	8.41	3.95	32.92	0.09	1.13	3.89	2.45	11.17	0.26	58.57	0.04	2.32	241.69	4.44	161.07	6.09	5.30	11.48
OGS 83-5	CM	LC5r	107.73					0.08	1.09	3.95	2.39	11.18	0.26	56.48	0.04	2.22	235.77	4.33	156.94	6.27	5.27	12.15

Table B1. Continued.

Dill core	Formation	Sample	Depth	S[a]	TOC[b]	TIC[c]	$CaCO_3$[d]	Na	Mg	Al	K	Ca	Ti	Cr	Mn	Fe	Sr	Mo	Ba	Th	U	Re
			m	%	%	%	%	%	%	%	%	%	%	µg/g	%	%	µg/g	µg/g	µg/g	µg/g	µg/g	ng/g
OGS 83-5	CM	LC6	108.01	2.52	8.41	3.05	25.42	0.10	1.49	4.59	3.05	9.02	0.31	67.82	0.04	3.45	227.33	5.38	188.65	7.08	6.63	13.16
OGS 83-5	CM	LC7	108.51	1.30	8.31	5.76	48.00	0.08	1.04	3.35	2.42	19.16	0.21	51.65	0.05	2.03	329.31	11.24	140.65	4.92	7.56	16.26
OGS 83-5	CM	LC8	108.94	0.96	6.46	6.29	52.42	0.06	0.93	2.12	1.67	23.30	0.14	33.07	0.05	1.34	383.54	5.66	90.15	3.17	5.10	8.46
OGS 83-5	CM	LC9	109.43	1.12	8.18	6.44	53.67	0.07	0.84	2.55	1.88	19.45	0.18	41.70	0.03	1.34	432.52	5.68	115.46	4.02	5.93	10.65
OGS 83-5	CM	LC10	110.08	0.52	3.53	8.71	72.58	0.06	1.29	1.95	1.49	29.59	0.13	28.02	0.04	0.98	569.68	2.49	85.32	3.43	3.08	2.99
OGS 83-5	CM	LC11	110.68	0.59	4.75	8.13	67.75	0.05	2.59	2.31	1.79	24.39	0.14	32.94	0.05	1.24	413.97	3.88	93.78	3.55	3.33	6.51
OGS 83-5	CM	LC12	110.86	0.70	5.33	7.40	61.67	0.05	2.62	2.00	1.54	24.75	0.12	29.53	0.05	1.36	420.19	3.62	80.93	3.19	2.97	5.00
OGS 83-5	CM	LC13	111.27	0.57	3.77	8.35	69.58	0.04	1.83	1.62	1.32	26.43	0.10	22.59	0.03	0.97	488.95	1.93	77.02	2.64	2.25	2.74
OGS 83-5	CM	LC14	111.67	0.94	8.63	6.09	50.75	0.06	1.56	2.81	2.15	15.50	0.17	40.32	0.03	1.29	262.69	6.64	116.97	4.39	4.94	8.16
OGS 83-5	CM	LC14r	111.67					0.06	1.64	2.80	2.25	16.22	0.18	41.52	0.04	1.30	271.54	6.43	122.67	4.58	5.32	7.95
OGS 83-5	CM	LC15	112.12	0.74	5.50	7.07	58.92	0.05	3.99	2.53	2.12	14.49	0.16	35.44	0.05	1.54	213.76	3.72	111.00	4.20	3.25	6.23
OGS 83-6	TB	SJ1	134.88	1.22	1.39	2.08	17.33	0.19	3.06	7.04	3.84	4.23	0.43	66.60	0.07	4.24	76.48	2.91	261.61	9.15	3.31	2.42
OGS 83-6	TB	SJ2	135.67	1.44	1.37	0.33	2.77	0.22	1.66	7.15	4.24	0.85	0.49	74.87	0.04	4.32	61.77	2.88	223.74	5.84	3.46	2.49
OGS 83-6	RR	SJ3	136.48	1.20	1.77	0.60	5.03	0.20	1.77	7.02	3.84	1.34	0.42	68.47	0.04	3.75	69.82	2.49	254.99	7.86	3.35	3.65
OGS 83-6	RR	SJ4	138.36	1.11	0.90	1.48	12.33	0.20	2.49	7.13	3.83	3.19	0.44	64.93	0.06	4.01	88.33	0.41	301.50	9.33	2.76	1.18
OGS 83-6	RR	SJ5	139.84	1.29	1.06	1.11	9.25	0.22	2.37	7.94	4.33	2.53	0.48	74.53	0.06	4.51	86.20	0.70	296.56	9.87	3.08	1.61
OGS 83-6	RR	SJ6	142.09	1.43	1.01	0.56	4.68	0.24	2.23	8.93	4.95	1.56	0.57	86.25	0.06	5.19	81.58	1.09	329.60	10.24	3.75	1.60
OGS 83-6	RR	SJ6r	142.09					0.21	1.96	7.57	4.37	1.37	0.50	76.45	0.05	4.52	71.59	1.05	283.68	7.77	3.23	1.73
OGS 83-6	RR	SJ7	143.38	1.23	0.96	0.37	3.07	0.20	1.80	7.60	4.25	0.91	0.47	74.61	0.04	4.17	62.77	0.95	273.45	8.85	3.04	1.38
OGS 83-6	RR	SJ8	144.39	1.33	1.29	0.51	4.27	0.23	2.01	8.56	4.79	1.83	0.53	79.93	0.05	4.65	84.95	1.07	324.19	10.04	3.29	1.70
OGS 83-6	RR	SJ9	145.54	1.24	1.34	0.51	4.21	0.18	1.67	7.08	3.92	1.34	0.41	66.58	0.04	3.82	69.62	1.22	266.25	9.61	2.82	1.99
OGS 83-6	RR	SJ10	146.14	1.40	1.40	0.50	4.16	0.21	1.79	8.73	5.17	1.62	0.47	80.02	0.05	4.80	86.26	2.14	342.18	12.03	3.83	2.80
OGS 83-6	RR	SJ11	148.11	1.33	1.50	0.54	4.48	0.20	1.77	8.16	4.32	1.57	0.48	74.17	0.05	4.27	81.15	1.95	283.33	10.33	3.29	2.17
OGS 83-6	RR	SJ12	150.09	1.13	1.35	0.47	3.88	0.22	1.96	8.68	4.63	1.41	0.48	78.17	0.05	4.32	80.55	2.54	315.12	10.85	3.81	2.20
OGS 83-6	RR	SJ12r	150.09					0.21	1.78	7.77	4.45	1.37	0.49	78.09	0.05	4.35	72.88	2.20	293.82	7.46	3.76	2.31
OGS 83-6	RR	SJ13	150.81	1.29	1.29	0.51	4.23	0.22	1.82	8.91	5.12	1.62	0.48	80.00	0.05	4.72	85.83	2.37	344.49	12.24	4.21	2.35
OGS 83-6	RR	SJ14	152.00	1.22	1.56	0.58	4.86	0.18	1.76	7.79	4.25	1.48	0.46	70.02	0.04	3.87	78.33	2.35	291.04	10.51	3.65	2.62
OGS 83-6	RR	SJ15	153.14	1.27	1.67	0.68	5.69	0.21	1.72	7.68	4.48	1.96	0.53	77.88	0.05	4.32	83.19	2.15	300.09	9.40	3.92	3.48
OGS 83-6	RR	SJ16	154.31	1.42	1.87	0.76	6.36	0.18	1.71	7.24	3.96	1.89	0.45	66.93	0.04	3.81	80.37	1.66	300.79	10.36	3.16	3.57
OGS 83-6	RR	SJ17	155.88	1.31	1.09	1.16	9.67	0.15	1.57	5.32	3.26	1.83	0.39	51.71	0.04	3.17	53.86	1.00	212.67	5.21	2.57	1.93
OGS 83-6	RR	SJ18	157.10	1.20	1.91	1.24	10.33	0.15	1.82	6.04	3.48	2.08	0.39	58.34	0.04	3.27	71.41	2.38	235.68	8.99	3.18	3.91

Table B1. Continued.

Dill core	Formation	Sample	Depth	S[a]	TOC[b]	TIC[c]	$CaCO_3$[d]	Na	Mg	Al	K	Ca	Ti	Cr	Mn	Fe	Sr	Mo	Ba	Th	U	Re
			m	%	%	%	%	%	%	%	%	%	%	µg/g	%	%	µg/g	µg/g	µg/g	µg/g	µg/g	ng/g
OGS 83-6	RR	SJ19	157.98	1.34	4.38	2.80	23.33	0.14	3.02	5.76	3.27	5.19	0.35	60.88	0.07	3.70	95.62	3.11	206.60	7.98	3.67	10.71
OGS 83-6	CM	SJ20	159.02	0.66	5.69	7.19	59.92	0.08	1.08	2.52	1.85	22.48	0.19	41.33	0.05	1.30	371.11	2.53	101.19	3.83	2.90	7.94
OGS 83-6	CM	SJ20r	159.02					0.08	1.01	2.49	1.75	21.10	0.18	38.52	0.05	1.20	348.81	2.28	133.60	3.76	2.65	7.95
OGS 83-6	CM	SJ21	159.18	0.77	6.67	7.15	59.58	0.09	1.04	2.71	1.96	23.10	0.19	44.54	0.06	1.39	360.95	3.81	132.77	4.24	3.33	12.27
OGS 83-6	CM	SJ22	159.98	0.72	5.60	7.41	61.75	0.09	0.74	2.35	1.74	25.36	0.18	40.68	0.03	1.04	472.87	1.41	104.27	3.92	3.45	5.75
OGS 83-6	CM	SJ23	160.78	1.12	8.06	5.91	49.25	0.09	0.75	2.81	2.26	19.15	0.22	51.36	0.03	1.50	427.59	2.54	129.84	4.54	4.06	7.11
OGS 83-6	CM	SJ24	161.95	1.35	8.99	5.79	48.25	0.10	0.78	3.47	2.56	19.20	0.24	52.48	0.03	1.63	405.86	6.50	148.77	5.12	6.23	14.42
OGS 83-6	CM	SJ24r	161.95					0.10	0.81	3.63	2.57	19.18	0.24	53.06	0.03	1.70	405.57	5.98	141.70	5.14	6.08	13.17
OGS 83-6	CM	SJ25	163.78	1.00	8.02	6.44	53.67	0.10	0.68	2.42	2.24	20.91	0.21	48.24	0.02	1.27	501.39	3.34	133.14	4.19	4.55	6.85
OGS 83-6	CM	SJ26	164.28	0.71	5.77	7.65	63.75	0.09	0.76	2.39	1.87	25.83	0.19	35.39	0.02	0.92	500.45	2.99	105.37	3.95	3.47	5.56
OGS 83-6	CM	SJ27	165.08	0.91	4.17	7.73	64.42	0.08	0.90	1.74	1.40	28.21	0.13	27.75	0.03	1.13	470.54	3.04	101.64	2.73	2.16	4.00
OGS 83-6	CM	SJ28	166.13	0.81	8.05	7.66	63.83	0.07	0.68	1.86	1.69	21.38	0.14	32.64	0.02	0.83	411.06	4.35	91.47	3.06	3.76	6.50
OGS 83-6	CM	SJ29	167.31	0.85	6.47	6.77	56.42	0.07	1.34	2.27	2.35	18.64	0.18	40.89	0.03	1.14	358.11	3.89	108.07	3.53	3.41	5.65
OGS 83-6	CM	SJ30	168.24	0.72	4.59	7.30	60.83	0.08	5.29	3.09	2.80	17.07	0.20	42.92	0.06	1.72	219.16	4.06	135.06	4.64	3.29	6.36
OGS-SG11-02	RR	F1	464.09	1.40	1.87	1.33	11.08	0.40	1.67	8.08	3.46	4.27	0.51	74.01	0.08	4.68	170.69	1.45	320.45	11.40	4.05	2.90
OGS-SG11-02	RR	F2	464.83	1.47	1.07	0.85	7.08	0.39	1.68	8.50	3.62	2.75	0.52	77.15	0.07	4.83	144.53	1.21	347.03	12.07	4.05	1.83
OGS-SG11-02	RR	F3	465.87	1.60	1.56	1.11	9.25	0.42	1.63	8.35	3.57	3.63	0.54	76.55	0.07	4.82	170.75	1.52	333.76	12.60	4.19	2.32
OGS-SG11-02	RR	F4	466.77	1.44	1.36	1.09	9.08	0.45	1.66	8.49	3.57	3.59	0.52	75.74	0.07	4.77	167.30	1.04	329.62	12.43	3.92	2.32
OGS-SG11-02	RR	F5	467.75	1.65	1.79	1.45	12.08	0.39	1.55	7.86	3.35	4.98	0.52	73.31	0.08	4.68	207.58	1.39	322.21	11.69	4.14	2.74
OGS-SG11-02	RR	F6	468.65	1.65	1.67	1.35	11.25	0.39	1.54	7.84	3.27	4.26	0.52	71.69	0.07	4.78	178.64	1.28	319.87	11.67	3.94	1.98
OGS-SG11-02	RR	F7	469.14	1.29	1.96	1.33	11.08	0.41	1.54	8.03	3.48	4.73	0.51	76.50	0.07	4.49	196.25	1.21	317.05	11.62	4.11	2.32
OGS-SG11-02	RR	F8	470.34	2.39	1.44	1.31	10.92	0.38	1.54	7.94	3.34	4.31	0.51	73.82	0.07	5.18	196.97	1.20	364.29	11.75	3.80	1.67
OGS-SG11-02	RR	F9	471.38	1.38	1.54	1.64	13.67	0.42	1.64	8.21	3.44	5.54	0.53	76.10	0.08	4.67	229.21	0.95	325.07	12.01	3.95	2.81
OGS-SG11-02	RR	F9r	471.38					0.39	1.58	8.16	3.46	4.38	0.53	74.96	0.07	5.43	201.63	1.23	396.72	11.99	3.88	
OGS-SG11-02	RR	F10	471.82	0.51	0.57	2.02	16.83	0.30	1.71	8.16	3.47	7.12	0.52	71.73	0.09	4.02	265.86	0.92	322.33	11.42	3.23	0.58
OGS-SG11-02	RR	F11	472.22	1.50	2.10	1.44	12.00	0.42	1.52	7.46	3.27	4.76	0.49	68.80	0.07	4.30	197.88	1.29	304.95	10.86	4.02	3.03
OGS-SG11-02	RR	F12	473.20	1.33	1.65	1.20	10.00	0.41	1.71	8.45	3.55	4.38	0.55	78.12	0.07	4.66	185.47	0.97	333.42	12.13	4.22	1.50
OGS-SG11-02	RR	F13	473.88	1.41	1.96	1.41	11.75	0.42	1.57	7.89	3.38	4.79	0.51	72.46	0.06	4.40	209.19	1.27	324.43	11.54	4.10	2.05
OGS-SG11-02	RR	F14	474.84	1.29	1.39	0.79	6.58	0.44	1.57	8.08	3.58	2.61	0.51	73.29	0.05	4.29	144.65	0.96	310.61	11.34	3.44	1.83
OGS-SG11-02	RR	F15	475.96	1.26	2.11	1.84	15.33	0.35	1.71	7.03	2.96	4.58	0.44	63.56	0.07	3.88	178.45	1.61	272.36	9.76	3.45	1.56
OGS-SG11-02	RR	F16	476.57	1.44	0.79	0.45	3.75	0.49	1.74	8.89	3.79	1.50	0.55	82.66	0.06	5.05	125.12	1.94	326.52	12.03	3.86	1.06

Table B1. Continued.

Dill core	Formation	Sample	Depth	S[a]	TOC[b]	TIC[c]	$CaCO_3$[d]	Na	Mg	Al	K	Ca	Ti	Cr	Mn	Fe	Sr	Mo	Ba	Th	U	Re
			m	%	%	%	%	%	%	%	%	%	%	µg/g	%	%	µg/g	µg/g	µg/g	µg/g	µg/g	ng/g
OGS-SG11-02	RR	MF1	476.80	1.25	2.02	2.29	19.08	0.34	2.19	6.47	3.00	5.30	0.42	59.67	0.08	4.22	203.51	1.34	239.99	8.69	3.30	2.38
OGS-SG11-02	CM	MF2	477.36	0.77	7.19	5.62	46.83	0.22	1.00	4.20	2.18	18.82	0.28	63.53	0.06	2.08	630.23	2.03	163.11	6.51	3.56	7.97
OGS-SG11-02	CM	MF2r	477.36					0.20	0.89	3.88	1.87	17.78	0.25	58.66	0.06	1.90	594.54	2.22	145.54	5.06	3.63	7.47
OGS-SG11-02	CM	MF4	478.45	0.21	1.20	6.66	55.50	0.19	2.72	3.84	2.18	19.59	0.29	45.07	0.08	2.21	847.45	0.28	170.82	6.02	2.43	2.73
OGS-SG11-02	CM	MF5	479.18	0.13	2.13	7.42	61.83	0.07	0.94	1.35	0.71	26.75	0.09	15.66	0.04	0.79	898.91	0.05	55.54	2.02	1.00	1.80
OGS-SG11-02	CM	MF6	480.36	0.24	0.96	7.17	59.75	0.09	0.76	1.33	0.67	29.02	0.09	16.11	0.04	0.79	985.31	0.16	53.15	1.39	0.92	1.24
OGS-SG11-02	CM	MF7	480.60	0.51	4.11	5.25	43.75	0.20	1.26	4.11	2.18	15.13	0.28	49.72	0.04	1.77	502.06	1.21	167.56	6.80	3.10	5.56
OGS-SG11-02	CM	MF8	481.65	0.15	2.30	7.51	62.58	0.06	0.69	1.06	0.54	30.81	0.07	13.31	0.03	0.61	1239.99	0.03	49.56	1.31	1.00	0.79
OGS-SG11-02	CM	MF10	482.25	0.18	2.67	6.61	55.08	0.12	1.06	2.79	1.52	24.50	0.21	33.92	0.03	1.13	1006.43	0.42	108.73	4.60	1.93	2.16
OGS-SG11-02	CM	MF11	482.45	0.34	1.47	8.09	67.42	0.11	0.90	2.31	1.33	24.04	0.16	28.13	0.03	1.05	976.40	0.58	85.56	4.93	3.30	4.74
OGS-SG11-02	CM	MF11r	482.45					0.12	0.92	2.69	1.36	26.05	0.17	28.46	0.03	1.10	970.31	0.72	88.62	5.57	3.47	4.60
OGS-SG11-02	CM	MF13	483.07	0.17	3.15	6.42	53.50	0.04	0.51	0.74	0.38	34.07	0.05	10.82	0.02	0.44	797.73	0.21	30.14	0.71	0.87	1.04
OGS-SG11-02	CM	MF14	483.78	0.14	0.72	8.05	67.08	0.03	0.47	0.53	0.25	33.90	0.03	5.60	0.02	0.32	590.10	0.11	22.50	0.84	0.49	0.68
OGS-SG11-02	CM	MF16	484.41	0.16	0.67	7.78	64.83	0.05	0.62	0.78	0.40	35.89	0.05	11.08	0.02	0.50	1244.30	0.17	29.94	1.05	1.98	1.45
OGS-SG11-02	CM	MF17	484.84	0.12	0.91	8.19	68.25	0.03	0.47	0.60	0.29	31.87	0.04	6.64	0.02	0.32	581.11	0.09	31.28	0.60	0.84	1.30
OGS-SG11-02	CM	MF18	485.21		0.45	10.70	89.17	0.03	0.50	0.78	0.40	34.73	0.05	9.17	0.03	0.39	707.09	0.20	27.69	0.86	0.98	1.17
OGS-SG11-02	CM	MF18r	485.21					0.04	0.52	0.85	0.44	36.54	0.05	9.46	0.03	0.42	716.22	0.21	29.18	1.15	1.00	1.16
OGS-SG11-02	CM	MF20	485.69		0.47	8.34	69.50	0.03	0.45	0.74	0.40	26.33	0.05	9.42	0.02	0.34	537.66	0.21	26.63	1.04	0.72	1.21
OGS-SG11-02	CF	MF22	487.32					0.05	0.53	0.90	0.47	29.09	0.06	11.11	0.02	0.42	658.72	0.17	82.66	1.30	0.89	0.87
OGS-SG11-02	CF	MF23	487.73		0.44	10.80	90.00	0.04	0.56	0.68	0.35	35.99	0.04	9.90	0.02	0.40	583.83	0.04	26.70	0.51	0.60	0.61
OGS CLGD No.7A	TB	CW1	43.35	0.98	0.55	0.82	6.84	0.41	1.63	6.81	2.94	2.01	0.49	68.33	0.07	4.47	112.11	0.42	290.97	7.01	3.05	1.27
OGS CLGD No.7A	TB	CW2	44.58	1.45	1.28	0.30	2.52	0.39	1.44	6.84	3.12	0.94	0.56	84.46	0.05	5.27	106.29	1.49	278.14	8.49	3.98	2.83
OGS CLGD No.7A	TB	CW2r	44.58																			2.77
OGS CLGD No.7A	TB	CW3	46.05		0.31	1.23	10.25	0.22	1.22	4.56	2.05	1.98	0.31	44.71	0.06	3.06	78.09	0.14	197.56	5.52	1.95	0.61
OGS CLGD No.7A	TB	CW4	47.81	1.57	1.91	0.99	8.25	0.27	1.68	6.59	2.89	2.14	0.42	63.66	0.08	4.58	102.23	1.38	247.70	8.30	2.99	6.05
OGS CLGD No.7A	TB	CW5	49.18		0.34	0.32	2.64	0.36	1.63	7.86	3.52	1.11	0.53	78.58	0.06	4.92	110.04	0.57	306.28	8.01	3.48	0.58
OGS CLGD No.7A	TB	CW6	51.06	1.78	2.17	0.59	4.91	0.23	1.03	5.09	2.32	1.37	0.33	51.05	0.04	3.39	75.47	2.23	206.14	5.53	3.03	7.36
OGS CLGD No.7A	TB	CW7	52.65	1.35	1.92	0.68	5.67	0.29	1.35	6.95	2.69	1.85	0.42	62.96	0.05	3.91	89.67	2.64	232.15	5.58	3.39	5.68
OGS CLGD No.7A	TB	CW7r	52.65					0.29	1.33	6.39	2.85	1.83	0.40	61.22	0.05	3.90	93.99	2.39	230.99	7.93	3.26	5.32
OGS CLGD No.7A	TB	CW8	54.44	1.15	1.31	0.80	6.67	0.25	1.27	5.86	2.53	1.82	0.36	54.84	0.05	3.32	90.98	2.66	229.60	7.85	2.91	3.24
OGS CLGD No.7A	TB	CW9	55.38		0.38	0.50	4.16	0.32	1.36	6.44	2.85	1.43	0.42	63.72	0.05	4.36	90.43	0.74	249.74	6.74	2.92	0.66

Table B1. Continued.

Dill core	Formation	Sample	Depth	S[a]	TOC[b]	TIC[c]	$CaCO_3$[d]	Na	Mg	Al	K	Ca	Ti	Cr	Mn	Fe	Sr	Mo	Ba	Th	U	Re
			m	%	%	%	%	%	%	%	%	%	%	µg/g	%	%	µg/g	µg/g	µg/g	µg/g	µg/g	ng/g
OGS CLGD No.7A	TB	CW10	57.35	1.20	1.78	0.46	3.81	0.44	1.37	7.11	3.30	1.60	0.56	84.59	0.05	4.97	91.98	3.40	247.27	8.49	5.02	4.02
OGS CLGD No.7A	TB	CW10r	57.35																			4.00
OGS CLGD No.7A	TB	CW11	58.53	1.32	1.62	0.66	5.47	0.27	1.14	5.73	2.57	1.65	0.37	55.33	0.04	3.36	84.63	1.71	227.29	6.58	3.22	3.71
OGS CLGD No.7A	TB	CW12	59.73	1.30	1.87	0.96	8.03	0.33	1.37	6.63	2.88	2.77	0.43	64.28	0.06	4.00	117.18	2.57	268.96	7.41	4.26	4.45
OGS CLGD No.7A	RR	CW13	61.56	1.26	1.38	0.61	5.04	0.30	1.19	6.00	2.77	1.59	0.38	58.23	0.04	3.54	94.59	1.85	226.17	7.02	3.10	3.01
OGS CLGD No.7A	RR	CW14	62.76	1.19	1.59	0.53	4.43	0.31	1.20	5.91	2.67	1.33	0.39	57.79	0.04	3.47	83.61	2.20	225.48	7.15	3.35	3.12
OGS CLGD No.7A	RR	CW15	64.74	1.61	1.44	0.89	7.45	0.29	1.16	5.87	2.60	2.33	0.38	55.87	0.05	3.59	104.65	3.17	233.69	6.54	5.58	3.12
OGS CLGD No.7A	RR	CW16	65.89	1.10	1.98	1.14	9.50	0.45	1.06	6.11	3.03	4.05	0.59	82.77	0.06	4.77	134.20	2.73	236.15	8.36	4.15	2.92
OGS CLGD No.7A	RR	CW16r	65.89					0.44	1.12	6.15	2.99	3.86	0.55	79.14	0.06	4.54	137.21	2.79	290.36	8.98	4.70	3.28
OGS CLGD No.7A	RR	CW17	67.48	2.18	1.18	0.86	7.19	0.30	1.15	5.68	2.44	2.38	0.36	54.25	0.05	3.91	103.15	1.10	215.50	7.31	2.49	2.79
OGS CLGD No.7A	RR	CW18	68.99	1.22	1.75	1.24	10.33	0.46	1.61	8.07	3.51	4.75	0.55	78.78	0.06	4.61	172.60	2.08	363.59	8.56	4.62	3.64
OGS CLGD No.7A	RR	CW19	70.55	1.20	2.26	1.32	11.00	0.29	1.16	5.73	2.45	3.36	0.37	53.78	0.04	3.06	131.50	1.37	231.18	8.14	3.43	3.58
OGS CLGD No.7A	RR	CW20	72.24	1.04	1.49	3.28	27.33	0.22	2.41	4.99	2.15	5.27	0.33	45.72	0.10	3.25	151.06	1.11	203.95	7.39	2.48	1.85
OGS CLGD No.7A	CM	CW21	72.98	1.23	1.67	5.56	46.33	0.17	4.14	4.22	2.13	9.92	0.34	46.05	0.17	4.15	210.86	2.04	153.83	5.80	4.02	2.58
OGS CLGD No.7A	CM	CW21r	72.98																			2.69
OGS CLGD No.7A	CM	CW22	73.13	0.86	9.29	4.97	41.42	0.20	1.05	3.99	1.82	14.58	0.24	56.60	0.07	1.83	364.05	4.68	143.10	5.93	4.51	17.95
OGS CLGD No.7A	CM	CW23	73.68	0.82	7.98	5.43	45.25	0.21	1.05	4.09	1.89	17.88	0.27	60.66	0.06	1.93	479.22	2.26	156.50	6.10	3.70	15.73
OGS CLGD No.7A	CM	CW27	76.11	0.28	0.62	9.58	79.83	0.07	0.66	1.22	0.60	24.73	0.08	15.70	0.03	0.68	781.98	0.18	51.48	1.86	0.93	1.30
OGS CLGD No.7A	CM	CW28	77.16	0.27	1.26	7.96	66.33	0.04	0.47	0.74	0.42	21.59	0.05	11.70	0.02	0.49	736.89	0.36	35.00	1.26	0.62	0.94
OGS CLGD No.7A	CM	CW29	77.95	0.24	1.36	7.60	63.33	0.15	1.39	2.66	1.50	24.15	0.22	33.65	0.05	1.29	744.62	0.50	114.94	5.02	2.25	2.76
OGS CLGD No.7A	CM	CW29r	77.95					0.15	1.38	2.72	1.46	23.67	0.21	33.23	0.04	1.26	739.85	0.50	114.69	3.16	2.23	2.90
OGS CLGD No.7A	CM	CW30	78.79	0.70	0.40	8.51	70.92	0.10	1.00	1.81	0.97	28.90	0.13	23.14	0.04	0.88	911.77	0.19	110.18	3.05	1.42	1.66

TB = Thornbury Member
RR = Rouge River Member
CM = Collingwood Member
CF = Cobourg Formation
[a] S = total sulfur
[b] TOC = total organic carbon
[c] TIC = total inorganic carbon
[d] $CaCO_3$ is calculated as TIC/12 × 100

Table B2. Element/aluminum ratios and elemental enrichment factors of the Upper Ordovician samples from seven drill cores in the southern Ontario, Canada.

Sample	Depth	Mo/Al	U/Al	Re/Al	Fe/Al	Sr/Al	Ba/Al	Sr/Ba^{o}	Sr/Ba^{c}	S/TOC	Mo EF[a]	U EF	Re EF	Fe EF	Sr EF	Ba EF
	m	µg/g/%	µg/g/%	ng/g/%	-	µg/g/%	µg/g/%	-	-	-	-	-	-	-	-	-
C42	872.13	0.14	0.46	0.16	0.52	19.57	41.52	0.47	0.31	0.87	1.63	1.10	1.48	1.18	1.52	1.16
C43	873.08	0.11	0.45	0.18	0.54	19.59	40.70	0.48	0.32	0.94	1.30	1.07	1.57	1.22	1.52	1.13
C43r	873.08	0.12	0.45	0.17	0.54	18.99	40.82	0.47	0.32		1.34	1.07	1.49	1.22	1.47	1.14
C39	875.71	0.12	0.44	0.20	0.52	19.48	43.95	0.44	0.29	1.08	1.32	1.04	1.79	1.19	1.51	1.22
C40	876.07	0.14	0.45	0.16	0.52	20.71	40.77	0.51	0.32	1.02	1.60	1.07	1.42	1.19	1.60	1.14
C41	876.84	0.13	0.46	0.18	0.52	21.88	41.59	0.53	0.31	0.91	1.49	1.10	1.62	1.17	1.69	1.16
C35	877.30	0.15	0.46	0.19	0.51	21.81	42.79	0.51	0.30	0.77	1.67	1.10	1.73	1.17	1.69	1.19
C36	877.95	0.16	0.47	0.18	0.51	25.19	42.47	0.59	0.30	0.75	1.80	1.13	1.59	1.16	1.95	1.18
C37	878.56	0.16	0.48	0.19	0.51	23.19	42.61	0.54	0.30	0.81	1.84	1.15	1.73	1.15	1.80	1.19
C38	879.26	0.20	0.52	0.25	0.54	20.66	46.20	0.45	0.28	0.56	2.35	1.25	2.27	1.22	1.60	1.29
C31	879.82	0.21	0.53	0.28	0.86	33.81	50.11	0.67	0.26	0.25	2.41	1.28	2.50	1.96	2.62	1.40
C32	880.47	0.15	0.51	0.19	0.48	21.52	43.97	0.49	0.29	0.75	1.69	1.23	1.72	1.08	1.67	1.22
C33	880.71	0.16	0.51	0.20	0.48	22.02	43.88	0.50	0.29		1.87	1.22	1.75	1.10	1.71	1.22
C34	881.62	0.20	0.53	0.24	0.50	23.67	43.73	0.54	0.30	0.60	2.31	1.28	2.13	1.13	1.83	1.22
C27	882.07	0.17	0.51	0.23	0.47	20.69	44.34	0.47	0.29	0.46	1.96	1.23	2.02	1.07	1.60	1.24
C28	882.73	0.21	0.52	0.23	0.47	17.72	44.68	0.40	0.29	0.53	2.39	1.24	2.08	1.06	1.37	1.24
C29	883.20	0.22	0.53	0.20	0.51	19.94	46.93	0.42	0.28	0.48	2.48	1.27	1.83	1.16	1.54	1.31
C29r	883.20	0.19	0.50	0.19	0.50	18.86	45.90	0.41	0.28		2.14	1.21	1.71	1.13	1.46	1.28
C30	883.98	0.18	0.51	0.22	0.88	34.93	48.16	0.73	0.27	0.36	2.09	1.23	2.00	1.99	2.71	1.34
C23	884.37	0.15	0.52	0.17	0.45	16.70	45.02	0.37	0.29	0.53	1.75	1.25	1.55	1.03	1.29	1.25
C24	885.10	0.18	0.54	0.23	0.47	19.57	50.67	0.39	0.25	0.49	2.03	1.31	2.07	1.07	1.52	1.41
C25	885.25	0.19	0.54	0.24	0.49	19.64	44.21	0.44	0.29	0.48	2.18	1.30	2.11	1.10	1.52	1.23
C26	886.64	0.21	0.57	0.27	0.52	20.00	44.71	0.45	0.29	0.45	2.42	1.36	2.40	1.17	1.55	1.25
C19	887.19	0.22	0.58	0.26	0.48	20.19	45.27	0.45	0.29	0.37	2.51	1.40	2.35	1.10	1.56	1.26
C20	887.86	0.18	0.54	0.19	0.47	17.83	44.83	0.40	0.29	0.47	2.04	1.30	1.73	1.06	1.38	1.25
C21	888.52	0.17	0.53	0.23	0.45	17.64	45.39	0.39	0.28	0.55	1.95	1.28	2.05	1.02	1.37	1.26
C22	889.03	0.19	0.53	0.24	0.65	25.91	46.00	0.56	0.28	0.43	2.14	1.28	2.17	1.47	2.01	1.28
C15	889.23	0.19	0.50	0.23	0.47	15.51	43.07	0.36	0.30	0.52	2.20	1.21	2.08	1.06	1.20	1.20

Table B2. Continued.

Sample	Depth	Mo/Al	U/Al	Re/Al	Fe/Al	Sr/Al	Ba/Al	Sr/Ba^{o}	Sr/Ba^{c}	S/TOC	Mo EF^{a}	U EF	Re EF	Fe EF	Sr EF	Ba EF
	m	µg/g/%	µg/g/%	ng/g/%	-	µg/g/%	µg/g/%	-	-	-	-	-	-	-	-	-
C16	890.01	0.20	0.56	0.28	0.47	17.39	45.93	0.38	0.28	0.50	2.30	1.34	2.50	1.06	1.35	1.28
C17	890.43	0.27	0.59	0.32	0.50	19.67	46.31	0.42	0.28	0.55	3.07	1.43	2.84	1.13	1.52	1.29
C17r	890.43	0.25	0.59	0.31	0.48	18.63	45.84	0.41	0.28		2.87	1.42	2.82	1.08	1.44	1.28
C18	891.23	0.18	0.55	0.22	0.47	17.78	43.71	0.41	0.30	0.37	2.12	1.31	1.98	1.07	1.38	1.22
C12	891.93	0.20	0.55	0.22	0.49	17.84	43.50	0.41	0.30	0.64	2.30	1.32	1.98	1.12	1.38	1.21
C11	892.00	0.22	0.54	0.21	0.57	20.23	43.37	0.47	0.30	0.43	2.51	1.30	1.91	1.30	1.57	1.21
C13	893.32	0.20	0.57	0.23	0.47	18.90	43.82	0.43	0.29	0.41	2.32	1.38	2.05	1.06	1.46	1.22
C14	893.81	0.17	0.56	0.30	0.83	28.78	44.78	0.64	0.29	0.28	1.90	1.34	2.73	1.89	2.23	1.25
C7	894.51	0.23	0.60	0.32	0.46	20.27	44.64	0.45	0.29	0.40	2.58	1.44	2.87	1.05	1.57	1.24
C8	894.69	0.25	0.56	0.30	0.51	26.25	41.02	0.64	0.31	0.66	2.84	1.36	2.72	1.15	2.03	1.14
C9	895.84	0.29	0.58	0.25	0.46	16.40	46.54	0.35	0.28	0.50	3.27	1.39	2.25	1.05	1.27	1.30
C10	896.15	0.19	0.49	0.22	1.24	68.10	45.39	1.50	0.28	0.42	2.15	1.17	1.97	2.81	5.27	1.26
C3	896.89	0.29	0.59	0.37	0.49	18.82	43.83	0.43	0.29	0.63	3.35	1.42	3.30	1.10	1.46	1.22
C4	897.42	0.33	0.67	0.46	0.49	23.53	44.47	0.53	0.29	0.48	3.78	1.60	4.13	1.11	1.82	1.24
C5	898.15	0.25	0.60	0.30	0.45	19.82	44.94	0.44	0.29	0.49	2.92	1.44	2.71	1.03	1.54	1.25
C6	898.50	0.27	0.57	0.26	0.48	17.59	42.79	0.41	0.30	0.64	3.04	1.37	2.30	1.09	1.36	1.19
C2	898.92	0.28	0.62	0.28	0.44	14.53	38.95	0.37	0.33	0.51	3.17	1.49	2.48	1.01	1.13	1.08
C1	899.40	0.29	0.70	0.34	0.45	17.95	49.69	0.36	0.26	0.32	3.30	1.68	3.09	1.03	1.39	1.38
C1r	899.40	0.32	0.66	0.35	0.46	18.11	41.71	0.43	0.31		3.62	1.59	3.10	1.05	1.40	1.16
C44	900.78	0.26	0.92	0.94	0.50	196.16	48.03	4.08	0.27	0.29	2.95	2.20	8.45	1.13	15.19	1.34
PS1	822.14	0.16	0.44	0.15	0.54	16.53	37.98	0.44	0.34	1.29	1.85	1.06	1.38	1.23	1.28	1.06
PS5	825.09	0.21	0.48	0.19	0.51	19.37	38.10	0.51	0.34	0.73	2.41	1.16	1.71	1.15	1.50	1.06
PS4	825.26	0.17	0.47	0.16	0.52	18.06	39.19	0.46	0.33	1.04	1.94	1.14	1.43	1.19	1.40	1.09
PS3	826.29	0.26	0.59	0.25	0.51	22.84	39.86	0.57	0.32	0.62	3.00	1.41	2.23	1.16	1.77	1.11
PS2	826.53	0.32	0.64	0.26	0.52	22.03	39.88	0.55	0.32	0.63	3.64	1.54	2.34	1.17	1.71	1.11
PS2r	826.53	0.30	0.68	0.29	0.56	22.63	41.45	0.55	0.31		3.46	1.62	2.61	1.28	1.75	1.15
PS9	827.27	0.25	0.63	0.26	0.48	21.01	40.12	0.52	0.32	0.49	2.86	1.50	2.30	1.10	1.63	1.12
PS8	828.12	0.26	0.67	0.28	0.79	31.27	43.29	0.72	0.30	0.38	3.02	1.60	2.55	1.79	2.42	1.21
PS7	828.60	0.30	0.75	0.31	0.87	34.89	44.46	0.78	0.29	0.35	3.39	1.81	2.78	1.98	2.70	1.24
PS6	829.18	0.28	0.55	0.26	0.48	17.36	42.85	0.41	0.30	0.59	3.23	1.32	2.32	1.09	1.34	1.19
PS13	829.56	0.26	0.58	0.21	0.48	19.66	41.79	0.47	0.31	0.51	3.03	1.39	1.88	1.09	1.52	1.16

Table B2. Continued.

Sample	Depth	Mo/Al	U/Al	Re/Al	Fe/Al	Sr/Al	Ba/Al	Sr/Ba^{o}	Sr/Ba^{c}	S/TOC	Mo EF^{a}	U EF	Re EF	Fe EF	Sr EF	Ba EF
	m	µg/g/%	µg/g/%	ng/g/%	-	µg/g/%	µg/g/%	-	-	-	-	-	-	-	-	-
PS12	830.34	0.29	0.55	0.24	0.46	18.93	42.03	0.45	0.31	0.51	3.27	1.32	2.16	1.05	1.47	1.17
PS11	831.12	0.30	0.56	0.25	0.56	20.95	42.80	0.49	0.30	0.59	3.46	1.35	2.21	1.27	1.62	1.19
PS10	831.45	0.34	0.62	0.32	0.68	26.64	44.61	0.60	0.29	0.50	3.93	1.50	2.87	1.55	2.06	1.24
PS17	831.91	0.31	0.59	0.29	0.55	21.09	43.93	0.48	0.29	0.35	3.52	1.41	2.62	1.26	1.63	1.22
PS16	832.54	0.43	0.64	0.34	0.50	18.01	48.82	0.37	0.26	0.47	4.93	1.53	3.05	1.14	1.40	1.36
PS16r	832.54	0.44	0.63	0.39	0.49	18.29	47.16	0.39	0.27		5.01	1.51	3.47	1.12	1.42	1.31
PS15	833.33	0.40	0.63	0.28	0.64	24.83	46.34	0.54	0.28	0.48	4.59	1.52	2.49	1.47	1.92	1.29
PS14	833.81	0.41	0.68	0.28	0.49	17.19	43.95	0.39	0.29	0.53	4.68	1.63	2.47	1.11	1.33	1.22
PS20	834.98	0.49	0.72	0.41	1.01	41.64	47.62	0.87	0.27	0.49	5.57	1.73	3.70	2.30	3.23	1.33
PS25	835.57	0.79	0.98	0.45	0.47	17.23	50.26	0.34	0.26	0.39	9.04	2.36	3.99	1.06	1.33	1.40
PS25r	835.57	0.69	0.95		0.48	17.48	49.13	0.36	0.26		7.96	2.29		1.10	1.35	1.37
PS19	835.74	0.73	0.86	0.44	0.44	15.31	47.64	0.32	0.27	0.40	8.37	2.07	3.98	1.00	1.19	1.33
PS18	836.48	0.74	0.87	0.44	0.49	17.98	41.00	0.44	0.31	0.38	8.52	2.09	3.96	1.11	1.39	1.14
PS22	836.81	0.88	0.90	0.48	0.47	16.17	44.21	0.37	0.29	0.37	10.11	2.15	4.32	1.07	1.25	1.23
PS24	837.34	0.85	0.92	0.47	0.55	19.97	45.51	0.44	0.28	0.45	9.74	2.20	4.19	1.25	1.55	1.27
PS23	838.39	1.08	0.87	0.48	0.55	18.29	45.41	0.40	0.28	0.50	12.35	2.10	4.31	1.26	1.42	1.27
PS23r	838.39	1.04	0.84		0.54	18.30	41.85	0.44	0.31		11.91	2.01		1.23	1.42	1.17
PS29	839.53	0.62	0.73	0.36	0.47	16.61	40.26	0.41	0.32	0.44	7.12	1.74	3.18	1.06	1.29	1.12
PS28	840.13	0.70	0.76	0.38	0.49	19.80	41.08	0.48	0.31	0.42	8.06	1.82	3.40	1.10	1.53	1.14
PS27	840.92	0.75	0.82	0.48	0.47	18.57	42.26	0.44	0.31	0.36	8.61	1.96	4.29	1.06	1.44	1.18
PS27r	840.92	0.79	0.83	0.50	0.47	19.03	40.24	0.47	0.32		9.04	1.99	4.47	1.08	1.47	1.12
PS26	841.19	0.85	0.77	0.47	0.50	17.78	43.01	0.41	0.30	0.46	9.74	1.84	4.21	1.15	1.38	1.20
PS33	841.53	0.65	0.70	0.34	0.70	25.88	41.24	0.63	0.31	0.40	7.50	1.68	3.05	1.58	2.00	1.15
PS32	842.49	0.74	0.82	0.49	0.50	20.18	41.55	0.49	0.31	0.40	8.44	1.97	4.41	1.13	1.56	1.16
PS31	843.00	0.67	0.76	0.41	0.52	21.44	41.18	0.52	0.31	0.33	7.63	1.83	3.68	1.18	1.66	1.15
PS30	843.60	0.83	0.91	0.47	0.48	19.56	40.31	0.49	0.32	0.36	9.48	2.19	4.21	1.08	1.52	1.12
PS30r	843.60	0.86	0.86		0.49	19.45	39.84	0.49	0.32		9.88	2.07		1.12	1.51	1.11
PS37	844.53	0.59	0.72	0.33	0.47	18.15	39.29	0.46	0.33	0.45	6.71	1.74	2.94	1.06	1.41	1.09
PS36	844.82	0.71	0.81	0.50	0.49	20.00	46.20	0.43	0.28	0.56	8.15	1.94	4.51	1.10	1.55	1.29
PS35	845.30	0.77	0.86	0.52	0.52	21.72	47.24	0.46	0.27	0.50	8.80	2.06	4.70	1.19	1.68	1.32
PS34	846.24	0.61	0.88	0.36	0.46	18.62	46.86	0.40	0.28	0.40	6.96	2.11	3.23	1.05	1.44	1.31

Table B2. Continued.

Sample	Depth	Mo/Al	U/Al	Re/Al	Fe/Al	Sr/Al	Ba/Al	Sr/Ba^{o}	Sr/Ba^{c}	S/TOC	Mo EF^{a}	U EF	Re EF	Fe EF	Sr EF	Ba EF
	m	µg/g/%	µg/g/%	ng/g/%	-	µg/g/%	µg/g/%	-	-	-	-	-	-	-	-	-
PS41	846.63	0.66	0.84	0.41	0.47	19.47	40.83	0.48	0.32	0.28	7.57	2.02	3.69	1.07	1.51	1.14
PS40	847.45	0.83	1.06	0.56	0.49	26.57	42.13	0.63	0.31	0.28	9.50	2.55	4.99	1.11	2.06	1.17
PS40r	847.45	0.83	1.06		0.49	26.17	46.59	0.56	0.28		9.49	2.54		1.11	2.03	1.30
PS39	847.67	0.80	0.92	0.43	0.49	23.43	44.67	0.52	0.29	0.43	9.20	2.21	3.81	1.11	1.81	1.24
PS38	848.64	0.78	1.05	0.58	0.50	30.53	40.92	0.75	0.32	0.31	8.90	2.52	5.20	1.14	2.37	1.14
PS45	849.32	0.75	1.04	0.58	0.47	25.22	44.10	0.57	0.29	0.32	8.61	2.50	5.22	1.08	1.95	1.23
PS44	849.69	0.76	1.05	0.57	0.48	28.79	41.32	0.70	0.31	0.25	8.73	2.52	5.12	1.10	2.23	1.15
PS44r	849.69	0.72	1.04		0.49	29.41	44.80	0.66	0.29		8.23	2.50		1.10	2.28	1.25
PS43	850.50	0.66	0.87	0.39	0.50	26.76	41.24	0.65	0.31	0.35	7.62	2.09	3.53	1.14	2.07	1.15
PS42	851.17	0.52	0.76	0.33	0.47	22.31	43.67	0.51	0.30	0.41	5.95	1.82	2.96	1.08	1.73	1.22
PS48	852.01	0.62	0.88	0.43	0.47	23.38	45.54	0.51	0.28	0.34	7.06	2.11	3.84	1.07	1.81	1.27
PS47	852.60	0.88	1.02	0.54	0.54	27.17	54.95	0.49	0.23	0.42	10.13	2.45	4.86	1.23	2.10	1.53
PS49	853.00	0.70	1.00	0.52	0.49	26.79	42.08	0.64	0.31	0.32	8.06	2.41	4.66	1.11	2.08	1.17
PS49r	853.00	0.64	0.92		0.49	25.77	43.52	0.59	0.30		7.33	2.21		1.11	2.00	1.21
PS46	853.46	0.79	0.94	0.49	0.53	24.94	39.82	0.63	0.32	0.40	9.10	2.26	4.35	1.19	1.93	1.11
PS53	854.04	1.19	1.09	1.05	0.58	27.54	28.36	0.97	0.46	0.60	13.63	2.61	9.44	1.33	2.13	0.79
PS52	854.26	0.55	0.79	0.44	0.50	23.61	39.28	0.60	0.33	0.46	6.32	1.90	3.92	1.13	1.83	1.09
PS51	854.74	1.37	0.76	0.92	0.75	34.94	16.95	2.06	0.76	1.44	15.70	1.82	8.28	1.70	2.71	0.47
PS50	855.63	2.59	0.81	3.45	2.47	118.47	20.44	5.80	0.63	3.04	29.72	1.95	30.92	5.62	9.18	0.57
PS57	856.26	0.29	0.62	0.50	0.52	27.37	42.06	0.65	0.31	0.85	3.34	1.50	4.48	1.17	2.12	1.17
PS56	857.01	0.19	0.47	0.21	0.44	19.92	43.19	0.46	0.30	1.09	2.21	1.13	1.84	1.00	1.54	1.20
PS55	857.81	0.18	0.53	0.48	0.52	39.65	37.95	1.04	0.34	0.66	2.10	1.27	4.29	1.18	3.07	1.06
PS54	858.28	0.55	0.75	0.67	0.61	28.12	43.79	0.64	0.29	1.11	6.26	1.80	6.04	1.38	2.18	1.22
P19	25.99	0.38	0.73	0.50	0.55	23.38	42.22	0.55	0.31	0.55	4.32	1.74	4.48	1.26	1.81	1.18
P20	26.22	0.46	0.72	0.47	0.54	22.35	40.93	0.55	0.32	0.52	5.29	1.72	4.21	1.22	1.73	1.14
P21	27.01	0.46	0.57	0.26	0.56	18.26	36.26	0.50	0.36	1.20	5.28	1.38	2.33	1.28	1.41	1.01
P22	27.91	0.11	0.48	0.05	0.57	15.05	36.48	0.41	0.35	4.10	1.26	1.15	0.48	1.29	1.17	1.02
P23	29.38	0.18	0.48	0.06	0.47	15.39	35.60	0.43	0.36	0.76	2.02	1.14	0.55	1.06	1.19	0.99
P24	30.41	0.56	0.88	0.49	0.53	19.84	43.16	0.46	0.30	0.56	6.47	2.11	4.36	1.20	1.54	1.20
P24r	30.41	0.52	0.84		0.54	19.69	40.29	0.49	0.32		5.94	2.02		1.23	1.52	1.12
P25	31.27	0.81	0.45	0.06	0.87	16.59	32.42	0.51	0.40	15.06	9.29	1.08	0.55	1.98	1.29	0.90

Table B2. Continued.

Sample	Depth	Mo/Al	U/Al	Re/Al	Fe/Al	Sr/Al	Ba/Al	Sr/Ba^{o}	Sr/Ba^{c}	S/TOC	Mo EF^{a}	U EF	Re EF	Fe EF	Sr EF	Ba EF
	m	µg/g/%	µg/g/%	ng/g/%	-	µg/g/%	µg/g/%	-	-	-	-	-	-	-	-	-
P26	31.86	0.58	0.68	0.44	0.57	27.39	41.30	0.66	0.31	0.67	6.65	1.64	3.95	1.28	2.12	1.15
P27	32.23	0.17	0.52	0.07	0.58	14.06	37.08	0.38	0.35	2.81	2.00	1.25	0.60	1.31	1.09	1.03
P28	33.46	0.05	0.41	0.05	0.49	17.55	37.43	0.47	0.34	0.56	0.56	0.99	0.43	1.12	1.36	1.04
P13	33.73	0.12	0.46	0.06	0.57	14.08	36.90	0.38	0.35	3.39	1.33	1.09	0.53	1.29	1.09	1.03
P14	34.40	0.14	0.48	0.07	0.67	15.21	37.12	0.41	0.35	6.41	1.57	1.15	0.61	1.52	1.18	1.03
P15	35.13	0.18	0.51	0.08	0.62	14.15	38.89	0.36	0.33	4.53	2.06	1.23	0.73	1.42	1.10	1.08
P16	36.47	0.51	0.53	0.13	0.74	16.67	38.21	0.44	0.34	5.50	5.79	1.28	1.15	1.69	1.29	1.06
P16r	36.47	0.49	0.53	0.14	0.72	15.87	44.14	0.36	0.29		5.61	1.27	1.29	1.63	1.23	1.23
P17	36.84	0.16	0.48	0.07	0.49	16.19	37.90	0.43	0.34	0.74	1.83	1.14	0.65	1.12	1.25	1.06
P18	38.10	0.15	0.49	0.06	0.58	14.82	33.72	0.44	0.38	4.35	1.70	1.18	0.57	1.33	1.15	0.94
P7	38.70	0.12	0.48	0.07	0.49	15.40	36.00	0.43	0.36	0.60	1.37	1.16	0.64	1.10	1.19	1.00
P8	39.03	0.12	0.49	0.07	0.46	16.69	37.25	0.45	0.35	0.57	1.42	1.18	0.66	1.04	1.29	1.04
P9	40.02	0.14	0.46	0.08	0.48	15.95	35.71	0.45	0.36	0.69	1.56	1.10	0.68	1.09	1.24	0.99
P10	40.96	0.14	0.45	0.08	0.47	15.52	35.15	0.44	0.37	0.65	1.59	1.08	0.74	1.07	1.20	0.98
P11	41.45	0.09	0.44	0.07	0.47	14.48	34.82	0.42	0.37	0.29	0.99	1.05	0.66	1.06	1.12	0.97
P12	42.54	0.47	0.56	0.13	0.60	13.43	35.75	0.38	0.36	1.19	5.37	1.34	1.19	1.36	1.04	1.00
P12r	42.54	0.47	0.56		0.63	13.61	36.88	0.37	0.35		5.43	1.36		1.42	1.05	1.03
P1	43.34	0.56	0.78	0.13	0.59	12.90	33.56	0.38	0.38	1.38	6.39	1.86	1.18	1.34	1.00	0.93
P1r	43.34	0.49	0.75	0.13	0.59	12.39	35.35	0.35	0.37		5.65	1.81	1.19	1.35	0.96	0.98
P2	44.49	1.63	1.05	2.69	1.07	79.23	40.75	1.94	0.32	0.82	18.70	2.52	24.11	2.43	6.14	1.14
P3	45.29	0.40	0.81	1.65	0.56	117.80	43.76	2.69	0.30	0.33	4.57	1.95	14.74	1.27	9.12	1.22
P4	45.78	1.88	1.38	2.99	0.86	120.55	39.34	3.06	0.33	0.63	21.61	3.31	26.78	1.95	9.34	1.10
P4r	45.78	1.70	1.41	2.78	0.81	121.34	41.19	2.95	0.31		19.49	3.37	24.87	1.85	9.40	1.15
P5	46.24	0.88	1.11	2.86	0.61	186.65	35.01	5.33	0.37	0.35	10.14	2.66	25.61	1.38	14.46	0.98
P6	46.24	0.68	0.87	2.62	0.50	177.87	39.19	4.54	0.33	0.22	7.77	2.09	23.49	1.13	13.78	1.09
LC1	105.73	0.66	0.74	1.50	0.56	24.06	38.08	0.63	0.34	0.37	7.52	1.77	13.41	1.27	1.86	1.06
LC2	106.26	0.77	0.82	1.70	0.87	45.41	44.22	1.03	0.29	0.47	8.79	1.97	15.20	1.99	3.52	1.23
LC3	106.81	0.77	0.91	2.19	0.78	41.50	36.61	1.13	0.35	0.29	8.81	2.17	19.65	1.77	3.21	1.02
LC4	107.34	1.21	1.28	2.11	0.93	75.70	38.48	1.97	0.34	0.32	13.86	3.07	18.94	2.12	5.86	1.07
LC5	107.73	1.14	1.36	2.95	0.60	62.12	41.40	1.50	0.31	0.20	13.10	3.27	26.44	1.36	4.81	1.15
LC5r	107.73	1.10	1.33	3.08	0.56	59.67	39.72	1.50	0.33		12.56	3.20	27.55	1.28	4.62	1.11

Table B2. Continued.

Sample	Depth	Mo/Al	U/Al	Re/Al	Fe/Al	Sr/Al	Ba/Al	Sr/Ba^{o}	Sr/Ba^{c}	S/TOC	Mo EF^{a}	U EF	Re EF	Fe EF	Sr EF	Ba EF
	m	µg/g/%	µg/g/%	ng/g/%	-	µg/g/%	µg/g/%	-	-	-	-	-	-	-	-	-
LC6	108.01	1.17	1.45	2.87	0.75	49.58	41.14	1.21	0.31	0.30	13.45	3.47	25.70	1.71	3.84	1.15
LC7	108.51	3.35	2.25	4.85	0.60	98.17	41.93	2.34	0.31	0.16	38.43	5.41	43.42	1.37	7.60	1.17
LC8	108.94	2.67	2.41	3.99	0.63	180.92	42.53	4.25	0.30	0.15	30.63	5.78	35.75	1.44	14.01	1.18
LC9	109.43	2.22	2.32	4.17	0.52	169.33	45.20	3.75	0.29	0.14	25.49	5.57	37.37	1.19	13.12	1.26
LC10	110.08	1.28	1.58	1.53	0.50	292.73	43.84	6.68	0.29	0.15	14.67	3.80	13.74	1.14	22.67	1.22
LC11	110.68	1.68	1.44	2.81	0.54	178.92	40.54	4.41	0.32	0.12	19.24	3.45	25.20	1.22	13.86	1.13
LC12	110.86	1.81	1.48	2.49	0.68	209.66	40.38	5.19	0.32	0.13	20.70	3.56	22.33	1.54	16.24	1.12
LC13	111.27	1.19	1.39	1.70	0.60	302.30	47.62	6.35	0.27	0.15	13.65	3.34	15.18	1.36	23.41	1.33
LC14	111.67	2.37	1.76	2.91	0.46	93.64	41.70	2.25	0.31	0.11	27.13	4.23	26.05	1.05	7.25	1.16
LC14r	111.67	2.30	1.90	2.84	0.47	97.10	43.86	2.21	0.29		26.36	4.57	25.47	1.06	7.52	1.22
LC15	112.12	1.47	1.28	2.46	0.61	84.36	43.80	1.93	0.29	0.13	16.84	3.07	22.04	1.38	6.53	1.22
SJ1	134.88	0.41	0.47	0.34	0.60	10.87	37.17	0.29	0.35	0.88	4.75	1.13	3.07	1.37	0.84	1.04
SJ2	135.67	0.40	0.48	0.35	0.60	8.63	31.28	0.28	0.41	1.05	4.61	1.16	3.12	1.37	0.67	0.87
SJ3	136.48	0.35	0.48	0.52	0.53	9.95	36.32	0.27	0.36	0.68	4.07	1.14	4.66	1.21	0.77	1.01
SJ4	138.36	0.06	0.39	0.16	0.56	12.39	42.27	0.29	0.31	1.24	0.65	0.93	1.48	1.28	0.96	1.18
SJ5	139.84	0.09	0.39	0.20	0.57	10.86	37.36	0.29	0.35	1.22	1.02	0.93	1.82	1.29	0.84	1.04
SJ6	142.09	0.12	0.42	0.18	0.58	9.14	36.92	0.25	0.35	1.42	1.40	1.01	1.61	1.32	0.71	1.03
SJ6r	142.09	0.14	0.43	0.23	0.60	9.46	37.48	0.25	0.34		1.60	1.02	2.04	1.36	0.73	1.04
SJ7	143.38	0.13	0.40	0.18	0.55	8.26	35.98	0.23	0.36	1.28	1.44	0.96	1.62	1.25	0.64	1.00
SJ8	144.39	0.13	0.38	0.20	0.54	9.92	37.87	0.26	0.34	1.03	1.43	0.92	1.78	1.24	0.77	1.05
SJ9	145.54	0.17	0.40	0.28	0.54	9.83	37.60	0.26	0.34	0.93	1.97	0.96	2.52	1.23	0.76	1.05
SJ10	146.14	0.25	0.44	0.32	0.55	9.88	39.19	0.25	0.33	1.00	2.81	1.05	2.88	1.25	0.77	1.09
SJ11	148.11	0.24	0.40	0.27	0.52	9.95	34.73	0.29	0.37	0.89	2.74	0.97	2.38	1.19	0.77	0.97
SJ12	150.09	0.29	0.44	0.25	0.50	9.28	36.29	0.26	0.36	0.84	3.36	1.05	2.27	1.13	0.72	1.01
SJ12r	150.09	0.28	0.48	0.30	0.56	9.38	37.80	0.25	0.34		3.25	1.16	2.66	1.27	0.73	1.05
SJ13	150.81	0.27	0.47	0.26	0.53	9.64	38.67	0.25	0.33	1.00	3.06	1.13	2.36	1.20	0.75	1.08
SJ14	152.00	0.30	0.47	0.34	0.50	10.06	37.36	0.27	0.35	0.78	3.46	1.12	3.01	1.13	0.78	1.04
SJ15	153.14	0.28	0.51	0.45	0.56	10.84	39.09	0.28	0.33	0.76	3.22	1.22	4.07	1.28	0.84	1.09
SJ16	154.31	0.23	0.44	0.49	0.53	11.10	41.53	0.27	0.31	0.76	2.63	1.05	4.42	1.20	0.86	1.16
SJ17	155.88	0.19	0.48	0.36	0.60	10.12	39.97	0.25	0.32	1.20	2.16	1.16	3.25	1.36	0.78	1.11
SJ18	157.10	0.39	0.53	0.65	0.54	11.83	39.04	0.30	0.33	0.63	4.52	1.27	5.80	1.23	0.92	1.09

Table B2. Continued.

Sample	Depth	Mo/Al	U/Al	Re/Al	Fe/Al	Sr/Al	Ba/Al	Sr/Ba^{o}	Sr/Ba^{c}	S/TOC	Mo EF^{a}	U EF	Re EF	Fe EF	Sr EF	Ba EF
	m	µg/g/%	µg/g/%	ng/g/%	-	µg/g/%	µg/g/%	-	-	-	-	-	-	-	-	-
SJ19	157.98	0.54	0.64	1.86	0.64	16.61	35.89	0.46	0.36	0.31	6.19	1.53	16.66	1.46	1.29	1.00
SJ20	159.02	1.01	1.15	3.16	0.52	147.53	40.23	3.67	0.32	0.12	11.54	2.77	28.29	1.17	11.43	1.12
SJ20r	159.02	0.92	1.07	3.20	0.48	140.34	53.75	2.61	0.24		10.52	2.56	28.64	1.10	10.87	1.50
SJ21	159.18	1.41	1.23	4.53	0.51	133.09	48.95	2.72	0.26	0.12	16.13	2.95	40.54	1.16	10.31	1.36
SJ22	159.98	0.60	1.47	2.45	0.44	201.10	44.34	4.53	0.29	0.13	6.87	3.52	21.91	1.01	15.58	1.24
SJ23	160.78	0.90	1.44	2.53	0.53	152.09	46.18	3.29	0.28	0.14	10.36	3.46	22.66	1.21	11.78	1.29
SJ24	161.95	1.87	1.80	4.16	0.47	117.08	42.92	2.73	0.30	0.15	21.49	4.31	37.25	1.07	9.07	1.20
SJ24r	161.95	1.65	1.68	3.63	0.47	111.85	39.08	2.86	0.33		18.92	4.02	32.54	1.06	8.66	1.09
SJ25	163.78	1.38	1.88	2.83	0.52	206.92	54.95	3.77	0.23	0.12	15.80	4.51	25.33	1.19	16.03	1.53
SJ26	164.28	1.25	1.45	2.33	0.39	209.27	44.06	4.75	0.29	0.12	14.32	3.48	20.84	0.88	16.21	1.23
SJ27	165.08	1.75	1.25	2.30	0.65	271.07	58.55	4.63	0.22	0.22	20.07	2.99	20.64	1.48	21.00	1.63
SJ28	166.13	2.34	2.02	3.50	0.45	221.13	49.21	4.49	0.26	0.10	26.81	4.86	31.32	1.01	17.13	1.37
SJ29	167.31	1.71	1.50	2.48	0.50	157.54	47.54	3.31	0.27	0.13	19.64	3.60	22.26	1.14	12.20	1.32
SJ30	168.24	1.31	1.07	2.06	0.56	70.98	43.74	1.62	0.30	0.16	15.06	2.56	18.44	1.26	5.50	1.22
F1	464.09	0.18	0.50	0.36	0.58	21.13	39.68	0.53	0.33	0.75	2.07	1.20	3.22	1.32	1.64	1.11
F2	464.83	0.14	0.48	0.22	0.57	17.00	40.82	0.42	0.32	1.37	1.63	1.14	1.93	1.29	1.32	1.14
F3	465.87	0.18	0.50	0.28	0.58	20.46	39.98	0.51	0.32	1.03	2.08	1.21	2.49	1.31	1.58	1.11
F4	466.77	0.12	0.46	0.27	0.56	19.70	38.82	0.51	0.33	1.06	1.41	1.11	2.44	1.28	1.53	1.08
F5	467.75	0.18	0.53	0.35	0.60	26.39	40.97	0.64	0.32	0.92	2.03	1.26	3.12	1.35	2.04	1.14
F6	468.65	0.16	0.50	0.25	0.61	22.79	40.81	0.56	0.32	0.99	1.87	1.21	2.26	1.38	1.77	1.14
F7	469.14	0.15	0.51	0.29	0.56	24.45	39.50	0.62	0.33	0.66	1.73	1.23	2.59	1.27	1.89	1.10
F8	470.34	0.15	0.48	0.21	0.65	24.80	45.88	0.54	0.28	1.66	1.74	1.15	1.89	1.48	1.92	1.28
F9	471.38	0.12	0.48	0.34	0.57	27.91	39.58	0.71	0.33	0.90	1.33	1.16	3.07	1.29	2.16	1.10
F9r	471.38	0.15	0.47		0.67	24.70	48.59	0.51	0.27		1.73	1.14		1.51	1.91	1.35
F10	471.82	0.11	0.40	0.07	0.49	32.58	39.50	0.82	0.33	0.89	1.29	0.95	0.64	1.12	2.52	1.10
F11	472.22	0.17	0.54	0.41	0.58	26.53	40.88	0.65	0.32	0.71	1.98	1.29	3.64	1.31	2.05	1.14
F12	473.20	0.12	0.50	0.18	0.55	21.94	39.44	0.56	0.33	0.81	1.32	1.20	1.59	1.25	1.70	1.10
F13	473.88	0.16	0.52	0.26	0.56	26.52	41.13	0.64	0.31	0.72	1.84	1.25	2.32	1.27	2.05	1.15
F14	474.84	0.12	0.43	0.23	0.53	17.89	38.42	0.47	0.34	0.93	1.37	1.02	2.03	1.21	1.39	1.07
F15	475.96	0.23	0.49	0.22	0.55	25.38	38.73	0.66	0.33	0.60	2.62	1.18	1.99	1.25	1.97	1.08
F16	476.57	0.22	0.43	0.12	0.57	14.07	36.71	0.38	0.35	1.82	2.50	1.04	1.07	1.29	1.09	1.02

Table B2. Continued.

Sample	Depth	Mo/Al	U/Al	Re/Al	Fe/Al	Sr/Al	Ba/Al	Sr/Ba^{o}	Sr/Ba^{c}	S/TOC	Mo EF^{a}	U EF	Re EF	Fe EF	Sr EF	Ba EF
	m	µg/g/%	µg/g/%	ng/g/%	-	µg/g/%	µg/g/%	-	-	-	-	-	-	-	-	-
MF1	476.80	0.21	0.51	0.37	0.65	31.45	37.09	0.85	0.35	0.62	2.37	1.22	3.29	1.48	2.44	1.03
MF2	477.36	0.48	0.85	1.90	0.50	150.19	38.87	3.86	0.33	0.11	5.55	2.04	17.00	1.13	11.63	1.08
MF2r	477.36	0.57	0.94	1.93	0.49	153.38	37.55	4.08	0.34		6.57	2.24	17.26	1.12	11.88	1.05
MF4	478.45	0.07	0.63	0.71	0.58	220.58	44.46	4.96	0.29	0.18	0.85	1.52	6.37	1.31	17.09	1.24
MF5	479.18	0.03	0.74	1.33	0.58	665.75	41.14	16.18	0.31	0.06	0.39	1.77	11.94	1.33	51.57	1.15
MF6	480.36	0.12	0.69	0.93	0.59	742.15	40.03	18.54	0.32	0.25	1.37	1.66	8.37	1.35	57.48	1.12
MF7	480.60	0.29	0.75	1.35	0.43	122.16	40.77	3.00	0.32	0.12	3.37	1.81	12.12	0.98	9.46	1.14
MF8	481.65	0.02	0.94	0.74	0.57	1166.36	46.61	25.02	0.28	0.07	0.28	2.25	6.65	1.31	90.34	1.30
MF10	482.25	0.15	0.69	0.77	0.41	361.26	39.03	9.26	0.33	0.07	1.73	1.66	6.94	0.92	27.98	1.09
MF11	482.45	0.25	1.43	2.05	0.45	422.56	37.03	11.41	0.35	0.23	2.86	3.42	18.39	1.03	32.73	1.03
MF11r	482.45	0.27	1.29	1.71	0.41	360.79	32.95	10.95	0.39		3.06	3.09	15.31	0.93	27.94	0.92
MF13	483.07	0.28	1.17	1.40	0.59	1075.26	40.62	26.47	0.32	0.05	3.19	2.80	12.57	1.34	83.29	1.13
MF14	483.78	0.21	0.92	1.29	0.60	1110.89	42.36	26.23	0.30	0.19	2.43	2.21	11.53	1.37	86.04	1.18
MF16	484.41	0.22	2.55	1.86	0.65	1598.79	38.47	41.56	0.34	0.24	2.57	6.12	16.64	1.47	123.84	1.07
MF17	484.84	0.14	1.40	2.18	0.53	976.02	52.53	18.58	0.25	0.13	1.65	3.37	19.51	1.21	75.60	1.46
MF18	485.21	0.26	1.26	1.49	0.50	905.03	35.44	25.54	0.36		2.96	3.02	13.37	1.13	70.10	0.99
MF18r	485.21	0.25	1.17	1.37	0.49	843.19	34.35	24.54	0.38		2.90	2.81	12.25	1.12	65.31	0.96
MF20	485.69	0.28	0.97	1.63	0.45	722.21	35.77	20.19	0.36		3.16	2.33	14.60	1.02	55.94	1.00
MF22	487.32	0.19	0.99	0.96	0.47	730.05	91.61	7.97	0.14		2.12	2.38	8.64	1.07	56.55	2.55
MF23	487.73	0.06	0.88	0.89	0.59	854.15	39.06	21.86	0.33		0.65	2.11	7.97	1.34	66.16	1.09
CW1	43.35	0.06	0.45	0.19	0.66	16.46	42.71	0.39	0.30	1.78	0.71	1.07	1.67	1.49	1.27	1.19
CW2	44.58	0.22	0.58	0.41	0.77	15.54	40.67	0.38	0.32	1.13	2.51	1.40	3.71	1.75	1.20	1.13
CW2r	44.58															
CW3	46.05	0.03	0.43	0.13	0.67	17.11	43.30	0.40	0.30		0.34	1.02	1.19	1.52	1.33	1.21
CW4	47.81	0.21	0.45	0.92	0.70	15.52	37.61	0.41	0.34	0.82	2.40	1.09	8.22	1.58	1.20	1.05
CW5	49.18	0.07	0.44	0.07	0.63	14.01	38.98	0.36	0.33		0.83	1.06	0.66	1.42	1.08	1.09
CW6	51.06	0.44	0.59	1.44	0.66	14.82	40.47	0.37	0.32	0.82	5.02	1.43	12.94	1.51	1.15	1.13
CW7	52.65	0.38	0.49	0.82	0.56	12.91	33.41	0.39	0.39	0.70	4.36	1.17	7.33	1.28	1.00	0.93
CW7r	52.65	0.37	0.51	0.83	0.61	14.71	36.16	0.41	0.36		4.29	1.22	7.46	1.39	1.14	1.01
CW8	54.44	0.45	0.50	0.55	0.57	15.52	39.16	0.40	0.33	0.88	5.21	1.19	4.95	1.29	1.20	1.09
CW9	55.38	0.12	0.45	0.10	0.68	14.03	38.75	0.36	0.33		1.32	1.09	0.92	1.54	1.09	1.08

Table B2. Continued.

Sample	Depth	Mo/Al	U/Al	Re/Al	Fe/Al	Sr/Al	Ba/Al	Sr/Ba[o]	Sr/Ba[c]	S/TOC	Mo EF[a]	U EF	Re EF	Fe EF	Sr EF	Ba EF
	m	µg/g/%	µg/g/%	ng/g/%	-	µg/g/%	µg/g/%	-	-	-	-	-	-	-	-	-
CW10	57.35	0.48	0.71	0.57	0.70	12.94	34.80	0.37	0.37	0.67	5.49	1.69	5.07	1.59	1.00	0.97
CW10r	57.35															
CW11	58.53	0.30	0.56	0.65	0.59	14.76	39.64	0.37	0.33	0.81	3.42	1.35	5.80	1.33	1.14	1.10
CW12	59.73	0.39	0.64	0.67	0.60	17.68	40.59	0.44	0.32	0.70	4.45	1.54	6.02	1.37	1.37	1.13
CW13	61.56	0.31	0.52	0.50	0.59	15.75	37.67	0.42	0.34	0.91	3.54	1.24	4.49	1.34	1.22	1.05
CW14	62.76	0.37	0.57	0.53	0.59	14.14	38.13	0.37	0.34	0.75	4.27	1.36	4.73	1.33	1.10	1.06
CW15	64.74	0.54	0.95	0.53	0.61	17.82	39.81	0.45	0.32	1.12	6.20	2.28	4.75	1.39	1.38	1.11
CW16	65.89	0.45	0.68	0.48	0.78	21.97	38.67	0.57	0.33	0.56	5.12	1.63	4.28	1.77	1.70	1.08
CW16r	65.89	0.45	0.76	0.53	0.74	22.32	47.23	0.47	0.27		5.20	1.83	4.78	1.68	1.73	1.32
CW17	67.48	0.19	0.44	0.49	0.69	18.15	37.93	0.48	0.34	1.85	2.23	1.05	4.40	1.56	1.41	1.06
CW18	68.99	0.26	0.57	0.45	0.57	21.39	45.06	0.47	0.29	0.70	2.96	1.37	4.04	1.30	1.66	1.26
CW19	70.55	0.24	0.60	0.63	0.54	22.96	40.37	0.57	0.32	0.53	2.74	1.44	5.60	1.22	1.78	1.12
CW20	72.24	0.22	0.50	0.37	0.65	30.27	40.87	0.74	0.32	0.70	2.56	1.19	3.32	1.48	2.34	1.14
CW21	72.98	0.48	0.95	0.61	0.98	50.01	36.49	1.37	0.35	0.74	5.55	2.29	5.48	2.24	3.87	1.02
CW21r	72.98															
CW22	73.13	1.17	1.13	4.50	0.46	91.19	35.85	2.54	0.36	0.09	13.45	2.71	40.28	1.04	7.06	1.00
CW23	73.68	0.55	0.90	3.84	0.47	117.08	38.24	3.06	0.34	0.10	6.32	2.17	34.43	1.07	9.07	1.07
CW27	76.11	0.15	0.76	1.06	0.55	638.66	42.04	15.19	0.31	0.45	1.68	1.82	9.49	1.26	49.47	1.17
CW28	77.16	0.48	0.84	1.26	0.66	992.79	47.16	21.05	0.27	0.21	5.53	2.01	11.32	1.50	76.90	1.31
CW29	77.95	0.19	0.85	1.04	0.49	280.42	43.28	6.48	0.30	0.18	2.15	2.03	9.31	1.11	21.72	1.21
CW29r	77.95	0.18	0.82	1.07	0.46	271.89	42.15	6.45	0.31		2.09	1.97	9.55	1.05	21.06	1.17
CW30	78.79	0.11	0.79	0.92	0.49	504.98	61.02	8.28	0.21	1.74	1.23	1.89	8.21	1.11	39.11	1.70

[a] Trace element (TE) enrichment factors (EF) are calculated as: TE EF = $(TE/Al)_{sample}/(TE/Al)_{local\ detrital\ background}$; local detrital backgrounds are from Table 2 and see text for details.

[b] Molar ratios of C_{org}:P are calculated as C_{org}:P = (TOC/12.01)/(P/30.97)

[o] Sr/Ba ratios are calculated based on elemental data from Table 1

[c] Sr/Ba ratios are corrected for carbonate-associated Sr by $Sr_{carb\text{-}corrected} = (Sr/Al)_{background} \times Al_{sample}$

Table B3. Sedimentary Fe speciation data for the Collingwood Member and Rouge River Member.

Sample	Fe_{carb} (%)	Fe_{ox} (%)	Fe_{mag} (%)	S_{py} (%)	Fe_{py} (%)	Fe_T (%)	Fe_{HR} (%)	Fe_{HR}/Fe_T	Fe_{PY}/Fe_{HR}
LC1	0.17	0.16	0.10	0.82	0.71	3.19	1.14	0.36	0.63
LC3	0.33	0.12	0.10	0.31	0.27	3.71	0.82	0.22	0.33
LC4	0.48	0.12	0.09	0.36	0.31	3.56	1.01	0.28	0.31
LC7	0.14	0.04	0.03	0.16	0.14	2.03	0.35	0.17	0.40
LC9	0.13	0.04	0.02	0.14	0.12	1.34	0.31	0.23	0.39
LC11	0.28	0.05	0.07	0.03	0.03	1.24	0.43	0.34	0.06
LC14	0.24	0.04	0.04	0.10	0.09	1.29	0.41	0.32	0.21
LC15	0.25	0.05	0.07	0.09	0.08	1.54	0.45	0.29	0.17
SJ19	0.18	0.14	0.15	0.40	0.35	3.70	0.82	0.22	0.42
SJ21	0.17	0.05	0.04	0.04	0.03	1.39	0.29	0.21	0.12
SJ24	0.07	0.04	0.01	0.08	0.07	1.63	0.19	0.12	0.36
SJ26	0.08	0.03	0.01	0.06	0.05	0.92	0.18	0.19	0.29
SJ28	0.08	0.03	0.01	0.07	0.06	0.83	0.18	0.22	0.33
SJ30	0.17	0.05	0.08	0.16	0.14	1.72	0.44	0.26	0.32
CW15	0.13	0.12	0.07	0.82	0.71	3.59	1.04	0.29	0.69
CW18	0.14	0.12	0.08	0.14	0.12	4.61	0.46	0.10	0.27
CW21	0.47	0.15	0.26	0.08	0.07	4.15	0.95	0.23	0.07
CW22	0.18	0.05	0.04	1.01	0.88	1.83	1.15	0.63	0.76
CW23	0.16	0.05	0.03	0.59	0.51	1.93	0.75	0.39	0.69
CW27	0.15	0.04	0.03	<0.01	0.00	0.68	0.22	0.33	0.00
CW29	0.15	0.06	0.04	<0.01	0.00	1.29	0.26	0.20	0.00
PS30	0.10	0.07	0.05	0.47	0.41	3.77	0.62	0.17	0.66
PS44	0.21	0.09	0.06	0.21	0.18	3.58	0.54	0.15	0.34
PS40	0.17	0.09	0.05	0.36	0.31	3.50	0.63	0.18	0.50
PS38	0.18	0.09	0.07	0.36	0.31	3.57	0.65	0.18	0.48
PS35	0.21	0.11	0.04	0.69	0.60	4.03	0.97	0.24	0.62
PS33	0.66	0.20	0.26	0.24	0.21	4.69	1.32	0.28	0.16
PS29	0.13	0.07	0.05	0.57	0.50	3.82	0.75	0.20	0.66
PS47	0.17	0.10	0.07	0.52	0.45	3.95	0.79	0.20	0.57
PS52	0.16	0.09	0.07	0.53	0.46	3.98	0.78	0.20	0.59
PS56	0.18	0.11	0.07	0.45	0.39	3.54	0.75	0.21	0.53
P26	0.16	0.08	0.11	0.99	0.86	4.85	1.22	0.25	0.71
P15	0.10	0.09	0.04	1.37	1.19	5.55	1.42	0.26	0.84
P8	0.14	0.10	0.07	<0.01	0.00	4.19	0.30	0.07	0.00
P12	0.12	0.07	0.05	1.52	1.32	5.63	1.56	0.28	0.85
P2	0.78	0.20	0.14	0.54	0.47	5.63	1.58	0.28	0.30
P3	0.23	0.09	0.05	0.12	0.10	2.79	0.48	0.17	0.22
P5	0.22	0.06	0.04	0.18	0.16	2.48	0.47	0.19	0.33

Table B4. Carbon and oxygen isotope compositions of the Collingwood Member.

	$\delta^{13}C$ (‰)	Repeat	$\delta^{18}O$ (‰)	Repeat
MF4	-0.4	-0.3	-8.9	-8.8
MF6	-0.6		-7.7	
MF8	-0.3		-8.2	
MF11	-0.4		-8.1	
MF14	-0.7		-6.0	
MF17	-0.7	-0.7	-7.1	-7.0
MF18	-1.0		-7.2	
MF20	-0.8		-6.3	
MF22	-0.9		-6.4	
MF23	-0.9	-0.7	-6.3	-6.1
CW21	0.0		-9.0	
CW22	-1.4		-8.8	
CW23	-1.0		-8.6	
CW27	-0.6		-8.2	
CW28	-0.8		-9.3	
CW29	-0.7		-8.5	
CW30	-0.8	-0.7	-7.6	-7.5
SJ21	-0.9		-9.2	
SJ24	-0.2	-0.2	-7.8	
SJ26	-0.4		-8.3	
SJ28	-0.5	-0.5	-7.5	-7.5
SJ30	0.0	-0.1	-10.5	-10.6
LC3	-0.4		-10.8	
LC5	-1.4	-1.6	-9.2	-9.0
LC7	-1.2		-9.1	
LC9	-1.1		-8.9	
LC14	-0.9		-9.3	-9.2

Table B5. Uranium isotope compositions using different leaching acids and calculated $\delta^{238}U$ of non-detrital and non-detrital-carbonate components.

		d238U	2SD measured	2SD reported	n	Al (ug/g)	Mg (%)	Ca (%)	Ti (ug/g)	U (ug/g)
LC5	0.8M acetic	-0.42	0.08	0.08	3	241.1	0.3	10.2	0.0	0.6
	0.5M HCl	-0.48	0.20	0.20	3	1148.3	0.6	11.8	5.7	1.9
	1M HCl	-0.48	0.08	0.08	3	1610.3	0.6	10.5	8.4	1.9
	bulk	-0.45	0.02	0.08	2					
	non-detrital	-0.50		0.08						
	non-detrital-carbonate*	-0.55		0.11						
SJ24	0.8M acetic	-0.43	0.07	0.08	3	185.9	0.2	12.7	0.2	0.7
	0.5M HCl	-0.46	0.15	0.15	2	579.5	0.3	14.9	5.4	2.0
	1M HCl					838.7	0.4	16.2	7.3	2.3
	bulk	-0.43	0.00	0.08	2					
	non-detrital	-0.47		0.08						
	non-detrital-carbonate	-0.48		0.17						
SJ26	0.8M acetic	-0.36	0.07	0.08	3	162.8	0.3	18.8	0.3	0.6
	0.5M HCl	-0.38	0.03	0.08	3	437.9	0.5	21.8	4.9	1.3
	1M HCl	-0.41	0.11	0.11	3	524.2	0.4	21.4	5.9	1.3
	bulk	-0.33	0.06	0.08	2					
	non-detrital	-0.34		0.08						
	non-detrital-carbonate	-0.27		0.14						
CW21	1M HCl	-0.52	0.04	0.08	3	1849.6	3.9	10.9	16.9	0.7
	bulk	-0.49	0.05	0.08	2					
	non-detrital	-0.64		0.08						
	non-detrital-carbonate	-0.69		0.11						
CW29	1M HCl	-0.64	0.08	0.08	2	1270.8	0.9	22.2	12.8	0.6
	bulk	-0.53	0.06	0.08	2					
	non-detrital	-0.62		0.08						
	non-detrital-carbonate	-0.59		0.11						

*calculated based on local detrital background and carbonate U data with 1N HCl; 0.5N HCl carbonate U data is used for SJ24

Table B6. Uranium isotope compositions for the Collingwood Member and Rouge River Member.

Drillcore	Formation	Sample	$\delta^{238}U$ (‰)	$2SD_{measured}$ (‰)	n	$\delta^{238}U_{non\text{-}detrital}$ (‰)	$2SD_{reported}$ (‰)
Chatham	RR	C43	-0.31	0.01	3	detrital	0.08
	RR	C38	-0.35	0.04	3	-0.54	0.08
	RR	C29	-0.34	0.08	3	-0.48	0.08
	RR	C30	-0.27	0.10	3	-0.13	0.10
	RR	C20	-0.27	0.14	3	-0.16	0.14
	RR	C20r	-0.31	0.05	2		
	RR	C17	-0.30	0.04	2	-0.29	0.08
	RR	C7	-0.32	0.11	2	-0.36	0.11
	RR	C10	-0.34	0.00	3	-0.56	0.08
	RR	C1	-0.31	0.10	3	-0.32	0.10
Port Stanley	RR	PS2	-0.35	0.02	3	-0.44	0.08
	RR	PS16	-0.35	0.07	3	-0.44	0.08
	RR	PS25	-0.30	0.02	2	-0.30	0.08
	RR	PS25r	-0.27	0.00	2		
	RR	PS22	-0.36	0.09	2	-0.41	0.09
	RR	PS23	-0.27	0.07	3	-0.23	0.08
	RR	PS27	-0.31	0.03	3	-0.31	0.08
	RR	PS30	-0.20	0.15	3	-0.11	0.15
	RR	PS35	-0.23	0.07	2	-0.17	0.08
	RR	PS40	-0.26	0.02	3	-0.24	0.08
	RR	PS38	-0.34	0.12	2	-0.37	0.12
	RR	PS44	-0.30	0.03	3	-0.29	0.08
	RR	PS49	-0.25	0.02	2	-0.21	0.08
	RR	PS53	-0.32	0.11	2	-0.33	0.11
	RR	PS51	-0.28	0.03	2	-0.25	0.08
Little Current	CW	LC1	-0.31	0.02	2	-0.32	0.08
	CW	LC3	-0.41	0.04	2	-0.50	0.08
	CW	LC5	-0.45	0.02	2	-0.51	0.08
	CW	LC7	-0.26	0.03	2	-0.25	0.08
	CW	LC7r	-0.26	0.03	2		
	CW	LC9	-0.31	0.10	2	-0.31	0.10
	CW	LC14	-0.34	0.08	2	-0.35	0.08

Table B6. Continued.

Drillcore	Formation	Sample	$\delta^{238}U$ (‰)	$2SD_{measured}$ (‰)	n	$\delta^{238}U_{non\text{-}detrital}$ (‰)	$2SD_{reported}$ (‰)
St. Joseph	RR	SJ6	-0.29	0.08	2	detrital	
	RR	SJ10	-0.31	0.03	2	detrital	
	RR	SJ19	-0.34	0.12	3	-0.42	0.12
	CW	SJ21	-0.39	0.04	2	-0.43	0.08
	CW	SJ24	-0.43	0.00	2	-0.47	0.08
	CW	SJ24r	-0.37	0.03	2		
	CW	SJ26	-0.33	0.06	2	-0.34	0.08
	CW	SJ28	-0.24	0.08	3	-0.23	0.08
	CW	SJ30	-0.47	0.02	2	-0.58	0.08
Collingwood Member No.7A	RR	CW15	-0.27	0.12	2	-0.24	0.12
	RR	CW18	-0.32	0.05	2	-0.35	0.08
	CW	CW21	-0.49	0.05	2	-0.64	0.08
	CW	CW22	-0.45	0.01	2	-0.53	0.08
	CW	CW22r	-0.46	0.08	2		
	CW	CW23	-0.44	0.02	2	-0.55	0.08
	CW	CW29	-0.53	0.06	2	-0.62	0.08
	CW	CW29r	-0.46	0.10	3		

Table B7. Elemental data and U isotope compositions of the Collingwood Member leached with 1N HCl

Sample Name	Mg %	Al ug/g	K %	Ca %	Ti ug/g	V ug/g	Mn ug/g	Fe %	Sr ug/g	Mo ng/g	Th ng/g	U ug/g	Mn/Sr	Mg/Ca	Sr/Ca	Mo/U	U/Al ug/g/%	$\delta^{238}U_{carb}$ (‰)	2SD measured (‰)	2SD reported (‰)	n
MF4	1.65	1749.69	0.12	17.66	15.49	8.39	612.19	0.80	590.00	38.33	2642.78	0.49	1.04	0.09	0.003	0.08	2.80	-0.67	0.08	0.08	3
MF6	0.49	660.09	0.05	28.41	6.87	4.94	296.11	0.23	830.74	52.82	1091.77	0.31	0.36	0.02	0.003	0.17	4.70	-0.79	0.10	0.10	3
MF8	0.49	844.02	0.06	30.30	8.67	5.00	270.83	0.25	1109.29		962.48	0.52	0.24	0.02	0.004	0.00	6.16	-0.60	0.07	0.08	3
MF11	0.51	1320.47	0.10	23.69	9.99	4.50	258.73	0.24	867.68	126.30	2963.81	1.41	0.30	0.02	0.004	0.09	10.71	-0.85	0.03	0.08	3
MF14	0.36	284.98	0.03	32.83	3.04	2.98	141.53	0.09	562.12	5.74	419.62	0.23	0.25	0.01	0.002	0.03	7.96	-0.56	0.05	0.08	3
MF17	0.38	477.98	0.04	32.31	4.68	3.60	181.15	0.12	591.99	38.53	547.50	0.45	0.31	0.01	0.002	0.09	9.33	-0.84	0.03	0.08	3
MF18	0.31	426.16	0.04	29.69	3.15	4.58	206.65	0.14	582.36	1.52	586.39	0.40	0.35	0.01	0.002	0.00	9.37	-0.75	0.03	0.08	3
MF20	0.34	576.41	0.05	30.60	4.14	3.64	172.80	0.13	578.38	18.27	723.64	0.40	0.30	0.01	0.002	0.05	7.01	-0.75	0.07	0.08	3
MF22	0.34	582.68	0.05	30.12	4.91	4.08	145.22	0.13	626.12	24.71	733.68	0.39	0.23	0.01	0.002	0.06	6.66	-0.91	0.05	0.08	3
MF23	0.32	546.47	0.05	28.23	4.12	3.83	135.18	0.12	580.83	29.71	705.74	0.35	0.23	0.01	0.002	0.08	6.45	-0.68	0.06	0.08	3
MF23r	0.37	464.61	0.05	32.40	3.42	3.48	170.82	0.12	505.76		515.91	0.25	0.34	0.01	0.002		5.44	-0.69	0.03	0.08	3
CW21	3.56	1832.28	0.12	9.91	16.91	12.49	1254.40	1.59	191.06	520.69	2254.20	0.63	6.57	0.36	0.002	0.83	3.43	-0.52	0.04	0.08	3
CW27	0.53	823.00	0.07	27.35	6.32	5.08	255.02	0.25	863.85	68.90	1131.08	0.45	0.30	0.02	0.003	0.15	5.48	-0.58	0.12	0.12	3
CW28	0.48	885.81	0.07	29.53	7.93	5.43	233.22	0.22	973.92	156.40	1002.99	0.33	0.24	0.02	0.003	0.47	3.75	-0.63	0.09	0.09	3
CW29	0.84	1258.94	0.09	20.15	12.81	6.14	321.99	0.35	615.41	137.09	2136.44	0.52	0.52	0.04	0.003	0.26	4.14	-0.64	0.08	0.08	3
CW30	0.61	880.14	0.07	25.25	8.14	5.19	301.18	0.26	748.65	58.09	1439.37	0.43	0.40	0.02	0.003	0.14	4.86	-0.63	0.02	0.08	3
CW30r	0.60	882.88	0.07	25.22	7.04	5.14	297.94	0.26	742.29	29.85	1366.79	0.41	0.40	0.02	0.003	0.07	4.59	-0.67	0.06	0.08	3
CW22	0.44	1052.11	0.08	14.67	7.64	5.09	610.39	0.32	313.85	677.82	1898.56	1.27	1.94	0.03	0.002	0.53	12.10				
CW23	0.49	1031.41	0.08	20.64	7.38	3.53	511.39	0.33	490.83	154.48	1940.54	1.27	1.04	0.02	0.002	0.12	12.33				
SJ21	0.80	599.13	0.06	24.50	7.36	10.60	545.71	0.34	360.98	579.57	1226.11	1.64	1.51	0.03	0.001	0.35	27.34				
SJ21r	0.79	589.14	0.06	24.15	6.05	10.50	540.15	0.34	352.03	595.91	1218.81	1.56	1.53	0.03	0.001	0.38	26.51				
SJ28	0.53	339.92	0.04	23.97	4.30	5.91	170.37	0.13	420.41	395.83	1063.29	2.25	0.41	0.02	0.002	0.18	66.07				
SJ30	4.10	548.84	0.07	15.77	9.24	12.08	480.09	0.68	181.39	476.74	1599.34	1.33	2.65	0.26	0.001	0.36	24.21				
LC3	4.21	959.61	0.10	10.09	16.96	18.12	870.50	1.51	160.43	501.34	2095.72	1.18	5.43	0.42	0.002	0.42	12.32				
LC7	0.59	606.81	0.07	19.90	6.42	16.93	421.95	0.32	312.25	1965.74	1159.48	3.40	1.35	0.03	0.002	0.58	56.00				
LC9	0.62	601.05	0.06	22.70	6.82	11.85	312.39	0.26	457.45	1111.83	1373.23	3.25	0.68	0.03	0.002	0.34	54.05				
LC14	1.39	407.85	0.05	17.33	6.13	13.18	333.11	0.39	255.07	1102.40	1267.56	2.36	1.31	0.08	0.001	0.47	57.88				

Appendix C. Supplementary materials for Chapter 4

Table C1. Comparison of U isotope compositions in carbonates using different leaching agents.

Sample	Acid	Al (μg/g)	U (μg/g)	Ca (%)	Mg (μg/g)	Ti (μg/g)	$\delta^{238}U$ (‰)	2SD (measured)	2SD (reported)	n
L7346	0.8M acetic acid	27.1	0.12	35.2	1915.1	0.03	-0.34	0.04	0.09	3
	0.5M HCl	92.7	0.22	37.3	2017.1	0.49	-0.37	0.05	0.09	3
	1M HCl	111.6	0.22	35.4	1924.3	0.42	-0.4	0.07	0.09	3
C5253	0.8M acetic	27.1	0.42	35.0	2834.6	0.04	-0.59	0.06	0.09	3
	0.5M HCl	135.3	0.60	35.9	3473.4	0.98	-0.52	0.03	0.09	3
	1M HCl	164.1	0.60	36.5	3490.1	1.13	-0.55	0.03	0.09	3
SP5399	0.8M acetic acid	8.2	0.37	30.1	1771.7		-0.36	0.09	0.09	3
	0.5M HCl	87.9	0.91	33.7	2013.1	1.90	-0.41	0.04	0.09	3
	1M HCl	129.5	0.90	32.9	2058.1	2.20	-0.39	0.03	0.09	3
SP5388	0.8M acetic acid	1.9	0.17	34.5	2444.8	0.01				
	0.5M HCl	12.1	0.21	35.2	2541.1	0.52	-0.76	0.06	0.09	3
	1M HCl	15.1	0.22	35.2	2541.7	0.48	-0.75	0.05	0.09	3

Table C2. Geochemical data of carbonate samples from the three carbonate sections in the Great Basin, western USA.

Locations	Sample ID#	Depth* (m)	Composite depth* (m)	$\delta^{13}C_{carb}$* (‰)	$\delta^{18}O_{carb}$* (‰)	$\delta^{34}S_{CAS}$* (‰)	I/Ca* (μmol/mol)	TOC^ (%)	$\delta^{238}U$ (‰)	2SD (measured)	2SD (reported)	n
IB	LDN7339	71.60	71.60				0.21	*0.005*	-0.60	0.08	0.09	3
IB	LDN7346	82.60	82.60				0.14		-0.40	0.10	0.10	3
IB	LDN7354	94.50	94.50			28.29	0.00	0.036	-0.70	0.08	0.09	3
IB	LDN7358	100.60	100.60			29.54	0.15		-0.44	0.02	0.09	3
IB	LDN7365	111.28	111.28	-0.60	-8.91	34.77	0.26	0.022	-0.44	0.12	0.12	5
IB	LDN7373	123.47	123.47	-0.80	-8.69		0.17		-0.48	0.02	0.09	3
IB	LDN7376	128.05	128.05			33.55	0.12		-0.42	0.07	0.09	3
IB	LDN7379	132.62	132.62				0.00	*0.021*	-0.46	0.07	0.09	3
IB	LDN7381	135.67	135.67	-0.88	-8.81	36.49	0.02					
IB	LDN7383	138.72	138.72	-0.71	-9.04	33.61	0.00	*0.020*	-0.40	0.09	0.09	3
IB	LDN7385	141.77	141.77	-0.72	-8.64	42.95	0.03		-0.59	0.09	0.09	3
IB	LDN7387	144.82	144.82	-0.94	-9.14	34.15	0.17	*0.016*	-0.46	0.11	0.11	5
IB	B-TOP7397	146.01	146.01	-1.10	-9.05	28.51	0.24		-0.56	0.10	0.10	4
IB	LDN7389	147.86	147.86	-0.27	-8.81		0.21		-0.42	0.14	0.14	5
IB	B-TOP7401	149.01	149.01	-0.17	-8.71	28.20	0.20	*0.032*	-0.49	0.08	0.09	3
IB	B-TOP7403	150.51	150.51	-0.42	-8.93		0.03		-0.59	0.06	0.09	3
IB	LDN7391	150.91	150.91	0.02	-8.96	36.72	0.07	*0.011*	-0.59	0.06	0.09	3
IB	LDN7392	152.44	152.44				0.00		-0.42	0.07	0.09	3
IB	B-TOP7409	155.01	155.01			43.28	0.10	0.047	-0.69	0.04	0.09	3
IB	B-TOP7411	156.51	156.51	0.77	-9.06		0.15	*0.047*	-0.78	0.05	0.09	3
IB	LDN7395	157.01	157.01	1.03	-8.94	32.39	0.36	*0.028*	-0.53	0.10	0.10	3
IB	B-TOP7414	158.76	158.76			48.29	0.05		-0.63	0.01	0.09	3
IB	C65-7533	160.06	160.06	0.91	-8.41	47.62	0.10	0.023	-0.70	0.04	0.09	3
IB	B-TOP7420	163.26	163.26	1.06	-8.57	52.15	0.16	0.045	-0.90	0.03	0.09	3

Table C2. Continued.

Locations	Sample ID#	Depth* (m)	Composite depth* (m)	$\delta^{13}C_{carb}$* (‰)	$\delta^{18}O_{carb}$* (‰)	$\delta^{34}S_{CAS}$* (‰)	I/Ca* (µmol/mol)	TOC^ (%)	$\delta^{238}U$ (‰)	2SD (measured)	2SD (reported)	n
IB	B-TOP7424	166.26	166.26	1.36	-8.90	46.36	0.27		-0.72	0.08	0.09	3
IB	B-TOP7427	168.51	168.51			43.96	0.16	*0.011*	-0.60	0.04	0.09	3
IB	B-TOP7430	170.76	170.76			46.86	0.20		-0.56	0.11	0.11	4
IB	C65-5253	175.30	175.30	-0.50	-9.48	43.95	0.07	0.026	-0.52	0.08	0.09	4
IB	C65-5254	178.35	178.35	-0.88	-9.11	45.28	0.02		-0.55	0.08	0.09	3
IB	C65-5256	185.06	185.06	-2.60	-9.26	46.54	0.05	0.025	-0.64	0.08	0.09	4
IB	C65-5258	189.94	189.94	-0.86	-8.58	41.61	0.10		-0.44	0.06	0.09	3
IB	C65-5260	196.95	196.95	-1.49	-9.29		0.14	0.033	-0.48	0.04	0.09	3
IB	C65-5262	202.74	202.74	-2.54	-9.41	37.98	0.12		-0.64	0.09	0.09	3
IB	C65-5263	205.79	205.79	0.25	-8.57	29.51	0.37	*0.014*	-0.68	0.07	0.09	3
IB	C65-5265	212.50	212.50	0.51	-8.79	30.64	0.28		-0.52	0.02	0.09	3
SP	SP5143	90.00	128.25	-0.57	-9.92	32.86	0.34	*0.014*	-0.51	0.07	0.09	3
SP	SP5376	99.00	137.25	-0.88	-13.03	31.01	0.00		-0.43	0.10	0.10	5
SP	SP5378	105.00	143.25	-0.71	-9.69	32.17	0.17	0.014	-0.47	0.14	0.14	4
SP	SP5380	110.50	148.75	-0.91	-11.56	32.99	0.30	0.015	-0.55	0.09	0.09	3
SP	SP5380r								-0.62	0.04	0.09	3
SP	SP5381	114.00	152.25	-1.26	-10.11	32.91	0.32		-0.61	0.08	0.09	3
SP	SP5383	117.50	155.75	-0.50	-9.88	33.44	0.00	0.019	-0.62	0.11	0.11	5
SP	SP5385	120.00	158.25	-0.39	-11.12	32.29	0.13		-0.45	0.03	0.09	3
SP	SP5388	124.50	162.75	0.49	-9.55	36.46	0.00	0.020	-0.75	0.05	0.09	3
SP	SP5390	128.00	166.25	0.45	-11.69	37.41	0.00	0.013	-0.55	0.14	0.14	5
SP	SP5392	131.25	169.50	-0.17	-10.14	39.72	0.09	0.016	-0.55	0.06	0.09	3
SP	SP5394	134.00	172.25	0.31	-9.96	40.51	0.15	0.013	-0.57	0.11	0.11	5
SP	SP5397	138.01	176.26	-0.45	-10.13	39.18	0.01	0.024	-0.53	0.10	0.10	3

Table C2. Continued.

Locations	Sample ID#	Depth* (m)	Composite depth* (m)	$\delta^{13}C_{carb}$* (‰)	$\delta^{18}O_{carb}$* (‰)	$\delta^{34}S_{CAS}$* (‰)	I/Ca* (µmol/mol)	TOC^ (%)	$\delta^{238}U$ (‰)	2SD (measured)	2SD (reported)	n
SP	SP5399	141.01	179.26	-0.66	-12.05	36.33	0.17		-0.41	0.10	0.10	3
SP	SP5401	143.70	181.95	-0.34	-11.31	36.78	0.12		-0.33	0.14	0.14	5
SP	SP5404	148.50	186.75	-1.49	-10.02	39.85	0.13	0.018	-0.50	0.10	0.10	3
SP	SP5407	153.70	191.95	-1.34	-9.65	39.63	0.19		-0.49	0.05	0.09	3
SP	SP5411	159.00	197.25	-1.24	-9.85	36.49	0.43	0.031	-0.63	0.10	0.10	4
SP	SP5415	165.30	203.55	-1.39	-9.58	42.71	0.29		-0.53	0.04	0.09	3
SP	SP5418	171.30	209.55	-1.14	-15.95	34.52	0.16	0.020				
SP	SP7551	180.00	218.25			40.18	0.19		-0.48	0.07	0.09	3
MP	MP290	48.00	131.26	-0.89	-9.38	32.05	0.56	0.035	-0.54	0.09	0.09	4
MP	MP292	54.00	137.26	-1.34	-9.50	15.74	0.25		-0.51	0.06	0.09	3
MP	MP294	60.00	143.26	-1.38	-9.02	16.91	0.17	0.051	-0.40	0.09	0.09	3
MP	MP296	66.00	149.26	-1.58	-8.86	13.94	0.06	0.027	-0.47	0.05	0.09	3
MP	MP298	72.00	155.26	-1.03	-8.57	31.35	0.00	0.019	-0.55	0.11	0.11	4
MP	MP301	81.00	164.26	0.17	-8.84	37.94	0.00		-0.37	0.02	0.09	3
MP	MP303	87.00	170.26	-0.02	-7.75	29.72	0.07		-0.47	0.03	0.09	3
MP	MP303r								-0.44	0.02	0.09	3
MP	MP306	96.00	179.26	-0.69	-8.53	25.03	0.02	0.015	-0.26	0.07	0.09	3
MP	MP309	105.00	188.26	-0.77	-8.97	30.76	0.12	0.021	-0.36	0.03	0.09	3
MP	MP311	111.00	194.26	-0.96	-8.93	31.64	0.13	0.012	-0.46	0.07	0.09	3
MP	MP314	120.00	203.26	-1.07	-9.60	35.39	0.12	0.024	-0.39	0.10	0.10	5

Table C2. Continued.

Sample ID#	U (ng/g)	Na (µg/g)	Mg (%)	P (%)	Al (µg/g)	K (µg/g)	Ca (%)	V (µg/g)	Mn (µg/g)	Fe (%)	Co (µg/g)	Zn (µg/g)	Sr (µg/g)	Mo (ng/g)
LDN7339	205.2	62.4	0.2	0.08	44.8	68.2	30.7	0.5	159.8	0.06	0.3	1.2	273.7	41.5
LDN7346	222.7	82.9	0.2	0.08	47.1	99.8	33.8	0.7	73.6	0.06	0.4	2.0	328.5	41.5
LDN7354	416.9	126.0	0.3	0.06	170.7	87.5	34.1	0.3	951.2	0.11	2.9	15.3	509.0	55.8
LDN7358	360.6	134.6	0.2	0.07	194.5	81.8	33.6	0.3	774.7	0.16	4.1	3.7	559.8	37.3
LDN7365	426.5	47.7	0.2	0.03	68.9	85.4	35.4	0.3	48.6	0.04	0.4	2.1	401.2	13.0
LDN7373	307.8	101.8	0.3	0.08	104.0	192.6	30.1	0.3	311.8	0.06	0.5	1.8	372.2	29.2
LDN7376	1489.9	61.6	0.3	0.09	72.7	83.1	36.3	1.9	169.9	0.05	0.5	2.3	372.9	96.6
LDN7379	382.0	45.4	0.2	0.03	76.6	90.1	33.4	0.7	214.8	0.06	0.3	1.2	350.8	21.9
LDN7381	566.8	44.5	0.2	0.06	51.9	73.4	33.9	0.4	431.3	0.06	0.3	1.0	346.7	36.7
LDN7383	460.4	34.7	0.2	0.02	67.4	80.0	34.1	1.3	344.4	0.05	0.4	1.0	343.8	157.9
LDN7385	198.4	34.0	0.3	0.05	17.5	223.2	36.0	0.1	446.1	0.07	0.2	0.5	345.9	27.7
LDN7387	435.2	134.3	0.3	0.04	211.1	223.4	32.3	0.8	325.1	0.06	0.3	1.6	366.8	144.4
B-TOP7397	279.7	94.5	0.3	0.07	227.3	233.9	32.3	0.3	295.2	0.07	0.3	6.0	383.8	23.7
LDN7389	270.1	60.7	0.3	0.02	214.9	263.9	33.5	0.3	364.4	0.06	0.2	0.9	382.1	65.5
B-TOP7401	247.4	86.0	0.5	0.03	129.7	257.2	33.1	0.2	317.0	0.06	0.4	2.5	471.0	0.2
B-TOP7403	323.0	84.5	0.3	0.09	103.6	287.5	35.7	0.3	989.9	0.05	0.3	1.6	386.2	46.3
LDN7391	77.9	63.7	0.3	0.02	27.4	58.4	32.6	0.3	1281.9	0.04	0.4	0.5	550.6	106.6
LDN7392	139.8	49.4	0.2	0.05	23.0	407.7	39.7	0.3	978.3	0.05	0.3	1.0	376.7	42.2
B-TOP7409	118.0	41.8	0.3	0.12	54.9	196.7	36.0	0.1	897.2	0.05	0.2	1.0	392.3	9.8
B-TOP7411	115.8	43.7	0.3	0.04	33.5	175.3	36.6	0.1	1045.7	0.05	0.4	2.2	384.9	47.5
LDN7395	167.9	30.3	0.3	0.00	25.8	189.3	36.7	0.3	939.5	0.04	0.2	0.9	397.1	92.2
B-TOP7414	251.2	65.8	0.4	0.13	108.2	213.8	35.1	0.7	1084.8	0.05	0.2	1.4	459.3	26.7
C65-7533	275.5	51.4	0.2	0.12	40.9	200.0	35.5	0.3	1403.8	0.06	0.2	0.8	414.9	57.6
B-TOP7420	205.8	58.8	0.3	0.14	63.7	198.3	37.2	0.2	1816.5	0.07	0.3	1.3	425.7	6.8

Table C2. Continued.

Sample ID#	U (ng/g)	Na (µg/g)	Mg (%)	P (%)	Al (µg/g)	K (µg/g)	Ca (%)	V (µg/g)	Mn (µg/g)	Fe (%)	Co (µg/g)	Zn (µg/g)	Sr (µg/g)	Mo (ng/g)
B-TOP7424	274.1	46.1	0.3	0.06	77.1	206.5	34.6	0.2	491.5	0.06	0.3	1.0	370.8	13.0
B-TOP7427	408.8	51.8	0.3	0.06	52.9	212.5	35.5	0.5	558.9	0.07	0.2	0.7	353.3	20.2
B-TOP7430	439.8	68.1	0.3	0.16	145.4	221.3	34.7	0.5	297.1	0.05	0.3	2.7	401.7	19.3
C65-5253	634.3	59.7	0.3	0.09	177.5	242.3	35.0	0.7	194.3	0.08	0.4	3.0	396.8	20.8
C65-5254	721.7	68.7	0.3	0.22	185.2	197.8	34.7	0.7	222.1	0.08	0.5	9.4	431.5	26.4
C65-5256	516.9	81.4	0.3	0.16	235.5	201.9	35.1	0.9	237.7	0.08	0.7	20.2	385.3	41.6
C65-5258	473.2	47.7	0.3	0.05	196.6	230.8	31.2	0.3	184.8	0.07	0.3	3.2	326.0	25.3
C65-5260	506.5	65.6	0.3	0.05	536.4	250.3	29.2	0.5	174.5	0.10	0.4	3.4	334.0	46.3
C65-5262	697.6	100.3	0.3	0.24	366.0	201.3	32.4	0.6	258.5	0.10	0.9	30.0	376.9	120.9
C65-5263	73.0	48.4	0.3	0.01	87.6	175.6	33.8	0.2	152.6	0.06	0.3	1.6	419.9	16.8
C65-5265	256.0	90.5	0.3	0.03	112.5	199.2	33.3	0.2	141.7	0.08	0.3	3.1	400.1	28.3
SP5143	379.4	77.7	0.2	0.13	68.7	104.3	33.2	0.6	222.2	0.01	0.2	0.4	278.8	19.2
SP5376	802.3	92.1	0.2	0.21	36.5	140.1	32.8	1.1	239.6	0.02	0.2	0.3	230.0	227.7
SP5378	496.7	112.6	0.8	0.16	13.4	126.7	33.8	1.3	264.8	0.02	0.2	1.0	227.5	47.5
SP5380	1148.8	112.2	0.5	0.19	44.3	153.8	34.2	1.8	706.4	0.03	0.2	3.9	222.1	59.9
SP5380r														
SP5381	688.8	143.3	0.2	0.30	43.0	175.2	34.8	0.6	806.6	0.02	0.2	0.5	226.4	32.1
SP5383	445.5	84.7	0.2	0.16	6.0	153.5	35.6	0.6	1045.9	0.02	0.2	0.3	278.7	34.1
SP5385	359.7	78.6	0.2	0.14	50.0	183.9	32.6	0.3	1182.4	0.02	0.2	0.2	262.5	23.3
SP5388	234.4	77.3	0.2	0.08	10.8	130.7	36.4	0.2	1815.6	0.08	0.3	3.4	290.0	38.3
SP5390	353.0	86.3	0.2	0.16	40.8	195.9	34.0	0.8	507.7	0.06	0.4	8.8	259.0	15.5
SP5392	545.7	108.1	0.2	0.17	56.5	175.2	35.5	0.5	415.8	0.08	0.5	2.1	347.4	94.7
SP5394	816.5	127.2	0.3	0.22	179.9	105.3	35.0	0.9	268.6	0.07	0.3	2.6	365.4	52.5
SP5397	598.0	104.9	0.2	0.10	31.6	100.2	34.1	0.6	162.9	0.07	0.2	2.3	299.6	52.4

Table C2. Continued.

Sample ID#	U (ng/g)	Na (µg/g)	Mg (%)	P (%)	Al (µg/g)	K (µg/g)	Ca (%)	V (µg/g)	Mn (µg/g)	Fe (%)	Co (µg/g)	Zn (µg/g)	Sr (µg/g)	Mo (ng/g)
SP5399	967.7	99.0	0.2	0.20	112.0	188.8	32.6	1.4	191.4	0.07	0.3	7.5	266.4	13.4
SP5401	295.3	39.7	0.2	0.02	4.6	77.1	34.0	0.4	140.3	0.06	0.2	1.1	257.5	43.9
SP5404	532.9	88.2	0.2	0.10	189.0	118.8	31.4	0.6	196.6	0.09	0.3	12.2	293.8	39.0
SP5407	460.8	69.6	0.4	0.04	56.8	89.1	34.7	0.4	217.3	0.10	0.2	1.2	305.0	19.6
SP5411	388.4	56.8	0.2	0.06	125.6	351.1	31.9	0.4	177.9	0.07	0.3	2.6	317.5	22.1
SP5415	227.8	66.5	0.8	0.06	74.5	117.8	30.1	0.4	325.3	0.16	0.2	2.3	308.8	24.6
SP5418	1528.8	19.7	0.1	0.05	35.1	103.2	36.4	1.8	196.6	0.04	0.2	0.7	140.3	23.4
SP7551	545.4	64.2	0.3	0.04	72.8	124.7	35.4	0.4	143.8	0.08	0.5	1.3	379.4	18.4
MP290	4185.8	181.9	0.3	0.60	596.7	433.9	31.9	2.8	686.7	0.20	1.8	7.8	285.5	71.8
MP292	486.2	45.3	0.2	0.05	587.3	507.5	22.8	0.9	184.7	0.14	0.6	4.1	233.3	39.4
MP294	429.1	66.9	0.2	0.07	868.4	768.4	20.9	1.3	172.3	0.14	0.6	7.4	182.6	58.3
MP296	267.8	38.8	0.1	0.04	318.2	443.6	22.1	0.5	173.7	0.11	0.3	1.7	168.6	46.4
MP298	381.8	98.1	0.2	0.05	214.8	267.8	30.5	0.3	423.2	0.09	0.5	3.9	243.6	7.3
MP301	75.3	102.1	0.5	0.01	40.1	127.4	33.7	0.3	219.1	0.06	0.5	2.4	460.3	12.5
MP303	797.4	81.9	0.4	0.07	99.2	143.4	34.2	0.6	267.4	0.13	0.4	1.7	238.1	28.0
MP303r														
MP306	399.4	81.9	0.1	0.03	41.2	81.8	32.1	0.2	109.5	0.05	0.3	0.8	237.9	8.5
MP309	499.2	46.2	0.2	0.05	93.6	150.3	32.7	0.4	126.5	0.05	0.8	1.9	233.5	7.0
MP311	761.0	44.3	0.1	0.03	26.6	90.2	36.9	0.2	277.8	0.05	0.3	0.8	221.1	14.3
MP314	315.5	34.6	0.2	0.03	17.8	76.5	38.2	0.3	194.2	0.07	0.4	1.8	316.5	

Table C2. Continued.

Sample ID#	La (ng/g)	Ce (ng/g)	Pr (ng/g)	Nd (ng/g)	Sm (ng/g)	Gd (ng/g)	Dy (ng/g)	Er (ng/g)	Tl (ng/g)
LDN7339	3576.4	9585.4	842.8	3324.5	648.5	668.0	718.6	410.4	5.1
LDN7346	2223.7	4603.4	479.3	1799.6	348.9	351.9	376.6	266.5	6.9
LDN7354	7934.8	25240.1	3367.7	15265.0	3050.2	2711.3	1807.2	804.1	8.1
LDN7358	11087.1	34170.2	4415.7	19546.7	3828.2	3537.7	2398.5	1195.2	9.0
LDN7365	1808.8	3400.9	395.6	1468.6	273.9	268.7	239.5	142.9	2.3
LDN7373	3004.3	5725.7	645.6	2353.2	400.2	416.9	395.9	225.5	9.0
LDN7376	1767.9	3219.2	353.9	1327.6	240.6	239.2	202.6	126.5	3.0
LDN7379	2049.5	3914.8	432.4	1636.6	310.1	292.3	263.5	158.9	2.5
LDN7381	1571.3	2887.0	305.5	1086.7	210.1	223.0	184.6	120.6	3.8
LDN7383	2337.3	4696.4	533.0	1936.5	367.0	362.8	300.8	187.8	6.5
LDN7385	1343.8	2274.7	219.5	792.7	143.5	138.4	126.2	74.5	2.3
LDN7387	3026.2	5567.7	605.2	2187.8	422.9	390.7	369.6	198.5	26.7
B-TOP7397	4624.3	8975.8	1022.8	3828.7	781.6	659.0	595.0	352.6	10.9
LDN7389	3258.4	6736.7	721.1	2631.6	515.8	452.9	394.8	245.6	7.3
B-TOP7401	4144.2	8644.7	924.8	3495.7	570.0	559.7	494.8	261.1	4.1
B-TOP7403	1934.9	3543.9	349.9	1308.2	235.3	228.9	213.2	137.1	7.1
LDN7391	1092.3	1974.9	202.4	710.3	134.2	126.9	115.9	80.1	6.4
LDN7392	672.2	1119.6	120.4	448.9	97.4	82.7	76.1	54.2	4.5
B-TOP7409	1384.1	2651.8	304.0	1117.2	178.3	199.1	175.2	82.5	4.3
B-TOP7411	1257.9	2396.5	276.5	1040.1	191.8	206.4	134.0	95.4	6.4
LDN7395	1426.0	2555.8	281.5	948.3	185.9	173.5	144.0	96.0	8.3
B-TOP7414	6151.1	13682.1	1378.5	5070.5	900.9	906.7	627.7	343.6	2.1
C65-7533	5641.4	13318.7	1264.7	4647.7	949.0	877.9	745.5	402.2	4.1
B-TOP7420	2626.4	5006.3	498.4	1793.9	344.9	353.2	279.4	163.9	3.6
B-TOP7424	4134.2	8978.4	937.6	3372.7	667.3	613.8	490.1	311.2	4.4
B-TOP7427	4209.5	7604.3	697.6	2324.0	386.1	430.1	360.2	202.6	5.2
B-TOP7430	5591.8	11162.3	1041.7	3778.4	672.5	692.3	511.1	256.2	5.0
C65-5253	5590.7	10525.2	1029.7	3455.2	568.9	589.4	474.9	281.4	3.9
C65-5254	8415.5	15677.9	1478.4	5187.6	802.8	906.9	684.9	366.9	1.9
C65-5256	10294.8	18653.9	1817.1	6609.3	1062.9	1086.1	714.1	359.0	1.7
C65-5258	6680.1	12304.5	1322.0	4665.1	749.1	656.4	460.1	262.2	4.0
C65-5260	8695.6	17440.9	1925.0	7004.2	1296.4	1070.1	658.0	313.4	7.1
C65-5262	17984.8	36662.7	4120.1	15012.2	2623.2	2326.5	1359.4	622.6	10.2
C65-5263	2272.7	4225.9	443.8	1602.0	286.7	262.7	159.4	80.5	3.7
C65-5265	4804.2	8594.1	858.4	2935.1	465.7	396.5	289.3	134.9	8.5

Table C2. Continued.

Sample ID#	La (ng/g)	Ce (ng/g)	Pr (ng/g)	Nd (ng/g)	Sm (ng/g)	Gd (ng/g)	Dy (ng/g)	Er (ng/g)	Tl (ng/g)
SP5143	1686.1	3626.3	352.9	1406.7	263.3	336.5	315.0	176.4	9.5
SP5376	2175.1	5121.3	530.3	2083.9	388.2	469.6	379.3	229.4	9.8
SP5378	1791.4	4064.5	401.2	1683.2	349.5	321.7	320.7	205.5	7.6
SP5380	2222.7	5165.3	528.7	1897.5	407.8	433.3	401.6	249.0	12.2
SP5380r									
SP5381	2482.9	5820.0	591.3	2359.1	515.0	528.8	459.3	283.6	5.1
SP5383	1921.1	4016.6	429.8	1662.8	285.0	332.7	261.3	165.6	6.9
SP5385	3069.6	7292.7	733.3	2879.4	604.6	559.1	480.3	307.9	6.7
SP5388	4217.8	7986.7	779.9	2870.0	413.0	487.5	379.7	207.0	25.6
SP5390	8926.0	17938.3	1673.5	5884.7	1016.1	1031.0	749.0	415.2	34.7
SP5392	8958.5	16125.7	1671.4	6023.2	1016.8	1038.9	583.3	304.3	12.3
SP5394	10722.5	19725.0	1934.3	6913.8	1030.5	1146.5	665.5	357.9	5.8
SP5397	6133.9	12270.5	1161.3	4251.9	728.1	792.5	620.1	411.7	19.1
SP5399	5429.5	11091.1	1107.1	3927.1	697.4	723.2	587.0	347.1	13.8
SP5401	3591.1	7116.2	653.1	2316.2	385.4	391.0	314.1	183.0	13.7
SP5404	9088.7	19342.9	1901.2	6850.1	1168.5	1127.6	777.1	419.6	7.5
SP5407	5084.5	8634.2	835.0	2971.5	472.7	484.5	308.0	163.5	8.3
SP5411	5877.4	10848.4	1100.8	3814.4	651.6	648.9	433.0	209.1	11.5
SP5415	7200.7	14228.8	1476.0	5308.8	904.8	836.9	539.0	270.1	7.1
SP5418	3348.3	5786.8	597.4	2099.7	367.5	394.2	314.8	201.8	6.4
SP7551	3438.7	5774.7	566.7	1966.1	312.1	303.7	217.3	125.4	6.0
MP290	16251.7	26417.9	3018.4	11026.2	1751.3	1783.9	1259.6	643.2	21.6
MP292	12052.6	23484.0	2696.7	9798.3	1561.9	1429.9	899.7	458.8	11.2
MP294	12078.7	24715.3	2830.2	10188.9	1834.2	1480.3	1002.0	516.9	14.0
MP296	9808.8	19589.9	2145.0	7809.3	1386.4	1134.8	776.9	409.6	29.3
MP298	9349.0	18872.2	2028.9	7536.7	1267.8	1153.9	774.8	422.4	10.1
MP301	1936.7	3462.0	391.5	1406.4	222.2	216.8	142.9	78.7	3.2
MP303	10411.9	19879.7	2133.5	7855.9	1237.7	1094.4	606.7	324.6	2.4
MP303r									
MP306	6035.5	13241.6	1297.6	4961.8	849.9	853.0	614.0	363.9	6.6
MP309	8905.1	18875.5	1960.2	7424.6	1338.3	1219.8	969.1	534.4	2.8
MP311	3222.4	6509.9	630.2	2276.7	382.3	372.3	314.3	207.6	1.2
MP314	4758.3	8166.3	891.0	3269.5	530.3	597.7	490.9	321.0	2.3

Table C2. Continued.

Sample ID#	U/Al (ng/µg)	Mg/Ca	Mn/Sr	Sr/Ca	Mo/U	Mo/Al (ng/µg)	C_{org} : P (molar ratio)
LDN7339	4.58	0.006	0.58	0.001	0.20	0.93	0.16
LDN7346	4.73	0.005	0.22	0.001	0.19	0.88	
LDN7354	2.44	0.008	1.87	0.001	0.13	0.33	1.55
LDN7358	1.85	0.006	1.38	0.002	0.10	0.19	
LDN7365	6.19	0.007	0.12	0.001	0.03	0.19	1.68
LDN7373	2.96	0.009	0.84	0.001	0.09	0.28	
LDN7376	20.49	0.008	0.46	0.001	0.06	1.33	
LDN7379	4.99	0.007	0.61	0.001	0.06	0.29	2.14
LDN7381	10.91	0.007	1.24	0.001	0.06	0.71	
LDN7383	6.83	0.006	1.00	0.001	0.34	2.34	2.44
LDN7385	11.31	0.007	1.29	0.001	0.14	1.58	
LDN7387	2.06	0.008	0.89	0.001	0.33	0.68	0.94
B-TOP7397	1.23	0.008	0.77	0.001	0.08	0.10	
LDN7389	1.26	0.008	0.95	0.001	0.24	0.30	
B-TOP7401	1.91	0.015	0.67	0.001	0.00	0.00	2.69
B-TOP7403	3.12	0.007	2.56	0.001	0.14	0.45	
LDN7391	2.84	0.008	2.33	0.002	1.37	3.89	1.49
LDN7392	6.08	0.006	2.60	0.001	0.30	1.83	
B-TOP7409	2.15	0.007	2.29	0.001	0.08	0.18	1.03
B-TOP7411	3.46	0.007	2.72	0.001	0.41	1.42	2.79
LDN7395	6.50	0.007	2.37	0.001	0.55	3.57	16.58
B-TOP7414	2.32	0.013	2.36	0.001	0.11	0.25	
C65-7533	6.74	0.007	3.38	0.001	0.21	1.41	0.48
B-TOP7420	3.23	0.009	4.27	0.001	0.03	0.11	0.82
B-TOP7424	3.55	0.009	1.33	0.001	0.05	0.17	
B-TOP7427	7.73	0.008	1.58	0.001	0.05	0.38	0.47
B-TOP7430	3.03	0.009	0.74	0.001	0.04	0.13	
C65-5253	3.57	0.009	0.49	0.001	0.03	0.12	0.74
C65-5254	3.90	0.008	0.51	0.001	0.04	0.14	
C65-5256	2.19	0.010	0.62	0.001	0.08	0.18	0.41
C65-5258	2.41	0.008	0.57	0.001	0.05	0.13	
C65-5260	0.94	0.012	0.52	0.001	0.09	0.09	1.73
C65-5262	1.91	0.010	0.69	0.001	0.17	0.33	
C65-5263	0.83	0.010	0.36	0.001	0.23	0.19	3.25
C65-5265	2.28	0.010	0.35	0.001	0.11	0.25	

Table C2. Continued.

Sample ID#	U/Al (ng/µg)	Mg/Ca	Mn/Sr	Sr/Ca	Mo/U	Mo/Al (ng/µg)	C_{org} : P (molar ratio)
SP5143	5.52	0.005	0.80	0.001	0.05	0.28	0.29
SP5376	21.98	0.006	1.04	0.001	0.28	6.24	
SP5378	37.14	0.024	1.16	0.001	0.10	3.55	0.23
SP5380	25.95	0.016	3.18	0.001	0.05	1.35	0.20
SP5380r							
SP5381	16.03	0.005	3.56	0.001	0.05	0.75	
SP5383	73.98	0.006	3.75	0.001	0.08	5.67	0.31
SP5385	7.20	0.006	4.50	0.001	0.06	0.47	
SP5388	21.65	0.007	6.26	0.001	0.16	3.54	0.69
SP5390	8.66	0.005	1.96	0.001	0.04	0.38	0.21
SP5392	9.67	0.007	1.20	0.001	0.17	1.68	0.24
SP5394	4.54	0.008	0.74	0.001	0.06	0.29	0.15
SP5397	18.93	0.006	0.54	0.001	0.09	1.66	0.62
SP5399	8.64	0.006	0.72	0.001	0.01	0.12	
SP5401	64.24	0.006	0.54	0.001	0.15	9.55	
SP5404	2.82	0.008	0.67	0.001	0.07	0.21	0.45
SP5407	8.12	0.011	0.71	0.001	0.04	0.35	
SP5411	3.09	0.008	0.56	0.001	0.06	0.18	1.43
SP5415	3.06	0.027	1.05	0.001	0.11	0.33	
SP5418	43.59	0.003	1.40	0.000	0.02	0.67	1.06
SP7551	7.49	0.008	0.38	0.001	0.03	0.25	
MP290	7.02	0.009	2.40	0.001	0.02	0.12	0.15
MP292	0.83	0.009	0.79	0.001	0.08	0.07	
MP294	0.49	0.008	0.94	0.001	0.14	0.07	1.83
MP296	0.84	0.006	1.03	0.001	0.17	0.15	1.88
MP298	1.78	0.006	1.74	0.001	0.02	0.03	0.98
MP301	1.88	0.015	0.48	0.001	0.17	0.31	
MP303	8.04	0.012	1.12	0.001	0.04	0.28	
MP303r							
MP306	9.69	0.005	0.46	0.001	0.02	0.21	1.36
MP309	5.33	0.005	0.54	0.001	0.01	0.07	0.99
MP311	28.63	0.004	1.26	0.001	0.02	0.54	0.92
MP314	17.70	0.004	0.61	0.001			2.13

Samples in gray occur within the $\delta^{13}C$ excursion (gray boxes in Figures. 2–4) from Edwards et al. (2018)

* Data from Edwards et al. (2018)

^ Italic fond TOC are from Edwards and Saltzman (2016)

IB = Ibex; SP = Shingle Pass; MP = Meiklejohn Peak.